# Study, measurement, and modeling of the propagation of conducted emissions due to on-board chargers in grids with various earthing systems

Mohsen Seddighi

## To cite this version:

Mohsen Seddighi. Study, measurement, and modeling of the propagation of conducted emissions due to on-board chargers in grids with various earthing systems. Electric power. Université Paris-Saclay, 2024. English. NNT : 2024UPAST087 . tel-04861197

**HAL Id: tel-04861197**

**https://theses.hal.science/tel-04861197v1**

Submitted on 2 Jan 2025

université
PARIS-SACLAY

# Study, measurement, and modeling of the propagation of conducted emissions due to on-board chargers in grids with various earthing systems

*Étude, mesure et modélisation de la propagation des émissions conduites dues aux chargeurs embarqués dans les réseaux avec différents systèmes de mise à la terre*

**Thèse de doctorat de l'université Paris-Saclay**

École doctorale n°575, Electrical, Optical, Bio-physics and Engineering (EOBE)
Spécialité de doctorat : Génie Électrique
Graduate School : Sciences de l'ingénierie et des systèmes. Référent : ENS Paris-Saclay

Thèse préparée dans l'unité de recherche **SATIE** (Université Paris-Saclay, ENS Paris-Saclay, CNRS), sous la direction de **Francois COSTA**, le co-encadrement de **Pierre-Etienne LÉVY**,

**Thèse présentée et soutenue à Paris-Saclay, le 11/07/2024, par**

## Mohsen SEDDIGHI

### Composition du Jury

Membres du jury avec voix délibérative

| | |
|---|---|
| **Nadir IDIR**<br>Professeur des Universités, Université de Lille, L2EP | Rapporteur et examinateur |
| **Christian VOLLAIRE**<br>Professeur des Universités, Ecole Centrale de Lyon, Ampère | Rapporteur et examinateur |
| **Francois DE DARAN**<br>Senior EMC Expert, Safran Tech | Examinateur |
| **Francoise PALADIAN**<br>Professeur des Universités, Université Clermont Auvergne | Examinatrice |
| **Jean-Luc SCHANEN**<br>Professeur des Universités, Grenoble INP, G2ELab | Examinateur et président |

THÈSE DE DOCTORAT

NNT : 2024UPAST087

université PARIS-SACLAY
DOCTORAL SCHOOL
Electrical, Optical, Bio:
Physics and Engineering
(EOBE)

**Titre :** Étude, mesure et modélisation de la propagation des émissions conduites dues aux chargeurs embarqués dans les réseaux avec différents systèmes de mise à la terre

**Mots clés :** CEM, Electronique de puissance, véhicules électriques (VE)

**Résumé :** La transition vers le véhicule électrique (VE), motivée par les politiques de décarbonation des transports et les avancées technologiques significatives en matière de stockage et de conversion de l'énergie électrique va se poursuivre dans les décennies à venir. En outre, les futurs chargeurs embarqués (Onboard Charger - OBC) bidirectionnels en puissance vont contribuer à une plus grande stabilité du réseau, à l'effacement des pointes, voire même à améliorer l'intégration des ressources énergétiques renouvelables : on parle du concept "véhicule-à-réseau" (V2G). Cela signifie que non seulement le nombre de VE augmentera, mais aussi leurs temps de charge et de décharge connectés au réseau. Les besoins de compacité des équipements, favorisés par la disponibilité de composants à grande vitesse de commutation (SiC GaN) ont incité les constructeurs à accroitre les fréquences de fonctionnement des chargeurs embarqués (> 50-100 kHz) avec comme corrolaire l'augmentation de leurs émissions électromagnétiques conduites et rayonnées. En conséquence, ces sources de bruit restent connectées au réseau et fonctionnent durant des périodes prolongées, ce qui rend nécessaire d'anticiper de potentiels problèmes de compatibilité électromagné-tique (CEM) dans les réseaux d'énergie : c'est le propos général de ce travail. L'un des objets de cette thèse concerne la méthode normalisée de mesure des émissions conduites dans laquelle l'impédance de mesure du bruit via le réseau de stabilisation de l'impédance de ligne (RSIL) n'est pas toujours représentative de l'impédance du réseau BT, ni évidemment de ses possibles fluctuations. Ainsi, les différents systèmes de mise à la terre fournissent des chemins présentant des impédances HF différentes qui peuvent modifier le niveau des émissions. Par conséquent, l'écart entre la configuration normative avec RSIL et l'impédance réelle au point d'accès du réseau électrique peut impacter l'efficacité du filtrage CEM, entraînant de potentiels dysfonctionnements dans les systèmes voisins et/ou connectés sur le même réseau. Le besoin d'analyse des variations d'impédance et les conséquences sur CEM nous ont conduit à développer et mettre en œuvre une méthodologie pour mesurer l'impédance HF de la terminaison de bruit en fonctionnement sous tension réseau nominale et en l'absence du RSIL. Cette approche permet de mesurer l'impédance en ligne de divers équipements et alimentations, en particulier le réseau de distribution. Partant de ces observations, l'étude de l'impact de l'impédance réelle du réseau sur le volume optimisé d'un filtre CEM a été abordé au travers de scénarios où différents niveaux normatifs ont été considérés. Afin d'examiner les émissions conduites causées par notre prototype de chargeur embarqué bidirectionnel dans un environnement contrôlé sans RSIL, un micro-réseau relié au réseau réel via un transformateur d'isolation a été réalisé. Ceci nous a permis de contrôler ses paramètres : impédance de source, longueur des câbles, système de mise à la terre et de maîtriser les variations d'impédance dues aux charges localement connectées. Les émissions conduites ont été ensuite mesurées et analysées en différents points du micro-réseau selon différentes configurations (régime de terre et différentes charges sur le micro-réseau). Parallèlement, un modèle fréquentiel du micro-réseau a été établi avec une nouvelle approche basée sur l'utilisation d'un solveur de type SPICE et sur l'acquisition expérimentale d'impédances élémentaires, permettant une simulation plus rapide pour des grands systèmes. Ce travail a été suivi par des procédures de vérification rigoureuses pour assurer la précision et la fidélité du modèle. Un modèle comportemental de type « boîte noire » a été développé pour l'OBC, définissant la source de bruit et ses impédances. Il est ainsi possible de simuler les niveaux de courant parasites en tout point du micro-réseau, quelque soit les charges connectées Par conséquent, le modèle de l'ensemble du système nous a permis d'analyser les variations d'impédance et les émissions conduites dans une version élargie du système réalisé. La thèse présentera une synthèse des résultats expérimentaux et de simulation que nous avons obtenus.

**Title:** Study, measurement, and modeling of the propagation of conducted emissions due to on-board chargers in grids with various earthing systems

**Keywords:** EMC, Power Electronics, Electric Vehicles (EVs)

**Abstract:** The transition to electric vehicles (EVs), driven by policies to decarbonize transport and significant technological advances in electrical energy storage and conversion, will continue over the coming decades. What is more, future on-board chargers (OBCs) with bidirectional power supply will contribute to greater grid stability, peak-shaving and even improved integration of renewable energy resources: we’re talking about the “vehicle-to-grid” (V2G) concept. This means that not only will the number of EVs increase, but also their charging and discharging times when connected to the grid.

The need for compact equipment, favored by the availability of high-speed switching components (SiC GaN), has prompted manufacturers to increase the operating frequencies of OBCs (> 50-100 kHz), with the corollary of increasing their conducted and radiated electromagnetic emissions. As a result, these noise sources remain connected to the grid and operate for extended periods, making it necessary to anticipate potential Electromagnetic Compatibility (EMC) problems in energy networks: this is the general aim of this work.

One of the subjects of this thesis concerns the standardized method of measuring conducted emissions, in which the noise measurement impedance via the Line Impedance Stabilization Network (LISN) is not always representative of the impedance of the LV network, nor of course of its possible fluctuations. Thus, different grounding systems provide paths with different HF impedances, which can alter the level of emissions. Consequently, the discrepancy between the normative configuration with LISN and the actual impedance at the point of access to the power network can impact the effectiveness of EMC filtering, leading to potential malfunctions in neighboring systems and/or those connected to the same network.

The need to analyze impedance variations and their consequences on EMC filters led us to develop and implement a methodology for measuring the RF impedance of the noise termination while operating at nominal mains voltage and in the absence of the LISN. This approach makes it possible to measure the line impedance of various equipment and power supplies, in particular, the distribution network. Based on these observations, the study of the impact of actual network impedance on the optimized volume of an EMC filter was approached through scenarios where different normative levels were considered.

In order to examine the conducted emissions caused by our prototype bidirectional on-board charger in a controlled environment without LISN, a microgrid connected to the real net-work via an isolation transformer was built. This enabled us to control its parameters: source impedance, cable length, grounding system and to control impedance variations due to locally connected loads. Conducted emissions were then measured and analyzed at various points on the microgrid according to different configurations (grounding regime and different loads on the microgrid).

In parallel, a frequency model of the microgrid was established using a new approach based on the use of a SPICE-type solver and the experimental acquisition of elementary impedances, enabling faster simulation for large systems. This work was followed by rigorous verification procedures to ensure model accuracy and fidelity. A “black box” behavioral model has been developed for the OBC, defining the noise source and its impedances. This makes it possible to simulate parasitic current levels at any point in the microgrid, whatever the connected loads.

As a result, the model of the entire system has enabled us to analyze impedance variations and conducted emissions in an extended version of the realized system. The thesis will present a synthesis of the results.

# ACKNOWLEDGMENTS

First of all, I would like to thank my thesis supervisors at the SATIE laboratory: François COSTA and Pierre-Etienne LÉVY, for their guidance, commitment and the various technical and scientific exchanges we've had over the years. Your encouragements were instrumental in the completion of this work.

I would like to extend my heartfelt thanks to Mickaël PETIT and Dounia OUSTAD for their invaluable support and advice that enabled me to reach this level.

I would also like to extend my thanks to the jury members. Thank you for agreeing to be part of my thesis jury. I am also grateful for all your relevant and interesting remarks and suggestions.

I am also grateful to the lab staff and fellow PhD students for their assistance and camaraderie. A special thanks to my dear friend, Said BENSEBAA, whose unwavering support helped me through some of the toughest moments.

To my friends and family, your love and encouragement have been my anchor. I am especially grateful to my wife, for her incredible support in raising our daughter while I focused on my work. To my mother who taught me to believe in myself and always encouraged me to strive for excellence.

Thank you all for being an essential part of this journey.

# RESUME DETAILLE EN FRANÇAIS

La transition vers le véhicule électrique (VE), motivée par les politiques de décarbonation des transports et les avancées technologiques significatives en matière de stockage et de conversion de l’énergie électrique, se poursuivra dans les décennies à venir. De plus, les futurs chargeurs embarqués bidirectionnels (On Board Chargers - OBC) contribueront à une plus grande stabilité du réseau, à l’effacement des pointes, et à une meilleure intégration des ressources énergétiques renouvelables, dans le cadre du concept de "véhicule-à-réseau" (V2G). Cela signifie que non seulement le nombre de VE augmentera, mais aussi les temps de charge et de décharge lorsqu'ils seront connectés au réseau.

La nécessité de concevoir des équipements compacts, facilitée par la disponibilité de composants à commutation rapide (SiC, GaN), a conduit les fabricants à augmenter les fréquences de fonctionnement des OBC (> 100 kHz), ce qui, en contrepartie, accroît les émissions électromagnétiques conduites et rayonnées. Ces sources de bruit, connectées au réseau pour des périodes prolongées, posent des défis en matière de compatibilité électromagnétique (CEM) dans les réseaux énergétiques.

L’un des thèmes centraux de cette thèse porte sur la méthode standardisée de mesure des émissions conduites, où l'impédance de mesure via le réseau de stabilisation d'impédance de ligne (RSIL) ne représente pas toujours fidèlement l'impédance du réseau basse tension, ni ses fluctuations possibles. Différents systèmes de mise à la terre peuvent modifier les niveaux d'émissions en offrant des chemins avec des impédances HF variées. La différence entre la configuration normative avec RSIL et l'impédance réelle au point d'accès au réseau peut affecter l'efficacité des filtres CEM, entraînant d'éventuelles perturbations dans les systèmes voisins et/ou connectés au même réseau.

Pour répondre à ce défi, dans le deuxième chapitre, nous avons développé et mis en œuvre une méthodologie de mesure de l'impédance RF de la terminaison de bruit, en opérant à une tension secteur nominale et en l'absence du RSIL. Cela permet de mesurer l'impédance des lignes de divers équipements et alimentations, en particulier du réseau de distribution, comme présenté dans la Figure A.

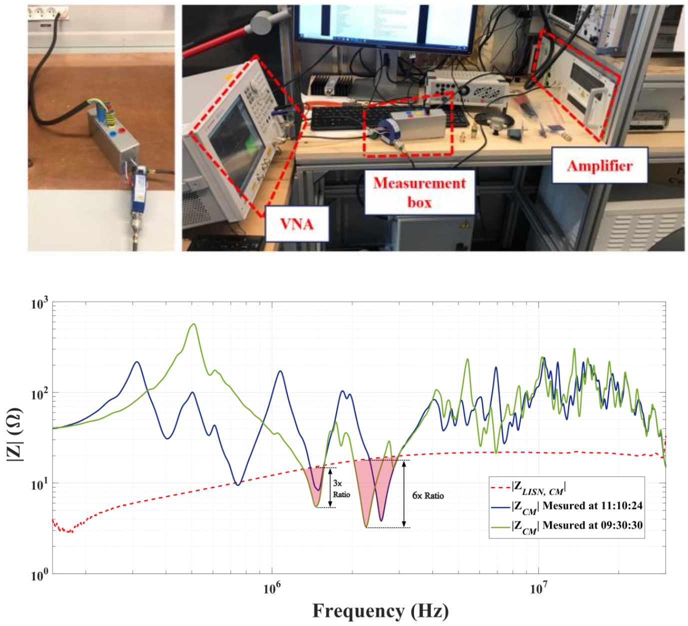

*Figure A* *Le banc d'essai et la comparaison de l'impédance MC mesurée entre LISN et le réseau à l'une des stations de recharge du parking de l'ENS.*

À partir de ces observations, l'impact de l'impédance réelle du réseau sur le volume optimisé d'un filtre CEM a été étudié à travers un cas d'étude et différents scénarios. Par exemple, dans l'un de ces scénarios, une augmentation de 111,1 % du volume du filtre a été observée.

Dans le troisième chapitre, la description de l'environnement de recharge est présentée, y compris notre prototype d'OBC bidirectionnel et le micro-réseau, qui ont été réalisés afin de fournir un environnement contrôlé pour analyser les émissions conduites causées par l'OBC sans le RSIL, comme présenté dans la Figure B.

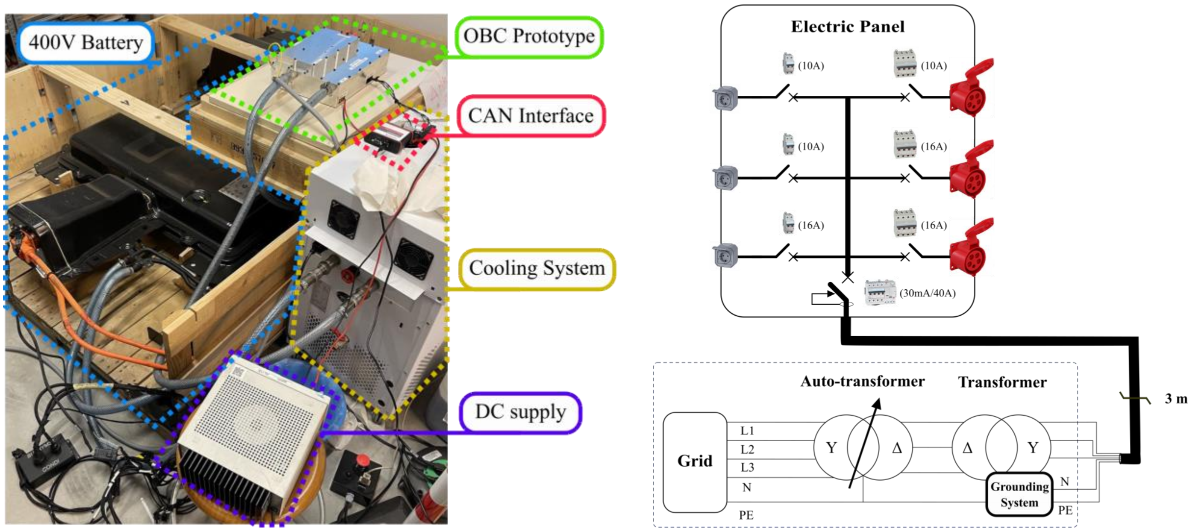

(a) (b)

*Figure B* *(a) Le banc d'essai pour le prototype d'OBC (b) la structure du micro-réseau réalisé.*

Ensuite, l'accent est mis sur la modélisation des différents éléments du système. Un modèle HF du micro-réseau a été établi dans le domaine des fréquences à l'aide d'une nouvelle approche basée sur un solveur de type SPICE et l'acquisition expérimentale d'impédances, permettant une simulation plus rapide pour les grands systèmes. Ce modèle comprend les câbles, le transformateur d'isolation avec différents systèmes de mise à la terre et les disjoncteurs. La méthodologie de modélisation et les résultats de l'impédance pour deux cas sont présentés dans la Figure C.

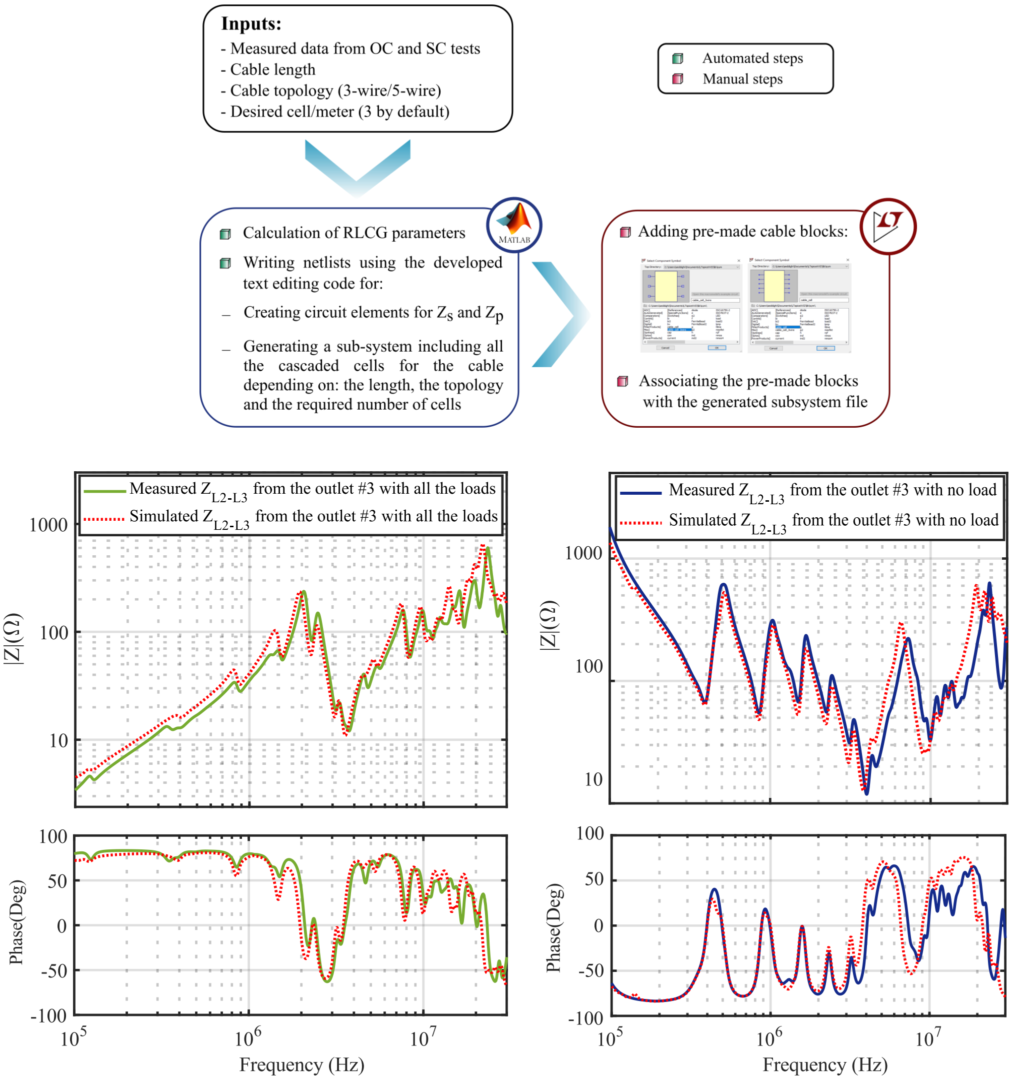

*Figure C La méthode de modélisation des câbles et la comparaison entre les résultats d'impédance mesurés et simulés dans le micro-réseaux réalisé.*

De plus, un modèle comportemental avec une approche "boîte noire" a été développé pour l'OBC, définissant la source de bruit et ses impédances. Enfin, l'ensemble du modèle d'environnement de charge développé est utilisé pour prédire les niveaux d'émissions conduites dans le système. L'utilisation de ce modèle permet de simuler les niveaux de courants parasites en tout point du micro-réseau, quelles que soient les charges connectées, comme l'illustre la Figure E pour un cas. Nous sommes également allés plus loin en créant un modèle pour une version étendue du système mis en œuvre, afin d'examiner les émissions conduites dans un environnement de recharge plus vaste.

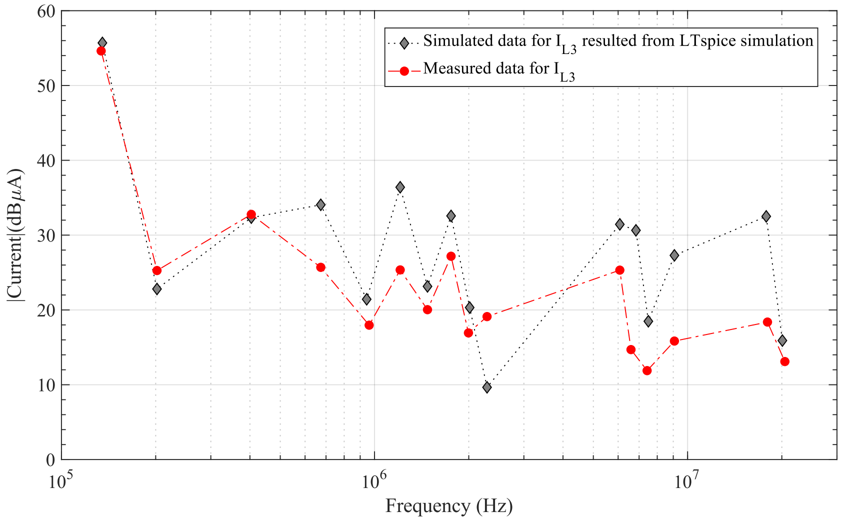

*Figure E* *Comparaison entre les données mesurées et simulées sur le courant L3 du côté AC de l'OBC#1 lorsqu'il est la seule charge connectée au micro-réseau avec le système de mise à la terre ITR.*

En outre, une étude d'impact a été menée pour examiner l'influence des paramètres du réseau et de la charge sur les émissions conduites. Une partie des résultats est présentée dans la Figure F.

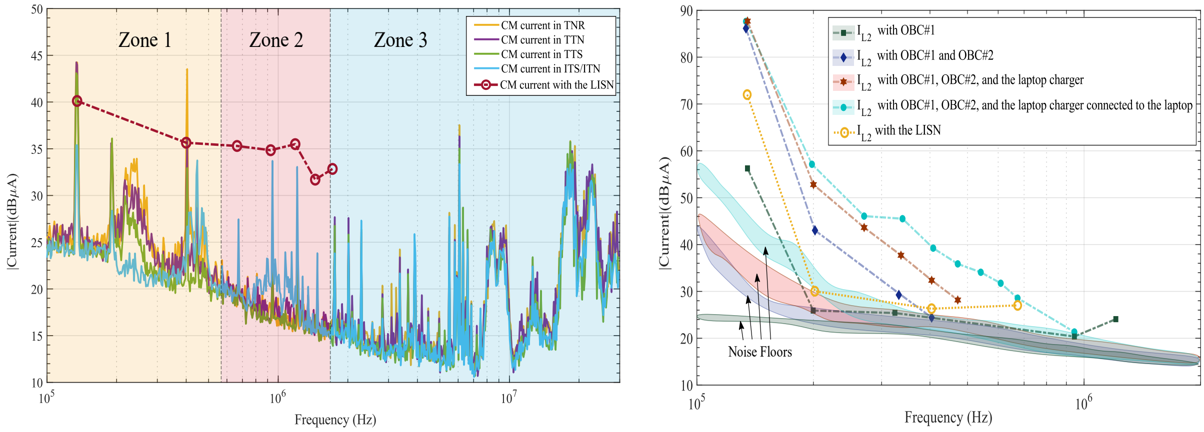

*Figure F* *Le courant MC dans différents systèmes de mise à la terre et l'évolution du courant L2 en connectant des charges au micro-réseau.*

Diverses perspectives ont été identifiées sur la base des limitations rencontrées au cours de la thèse, qui pourraient contribuer à l'amélioration de la prédiction des émissions conduites, comme présenté dans les points ci-dessous :

- La mesure de la phase des courants parasites avec des configurations plus avancées est une perspective essentielle pour une étude plus approfondie. L'utilisation d'un analyseur de signaux capable de fournir à la fois la phase et l'amplitude du signal améliorerait la précision de la caractérisation du bruit et permettrait d'obtenir un modèle plus prédictif.
- Développer un modèle de convertisseur basé sur des données de phase plus précises et moins d'hypothèses, avec des performances améliorées lorsqu'il est connecté à des systèmes asymétriques tels que le modèle de micro-réseau discuté dans cette recherche. Cette avancée pourrait améliorer la précision du modèle dans la prévision des émissions conduites dans diverses conditions de fonctionnement, en particulier dans des environnements électriques complexes.
- Utiliser le modèle développé pour effectuer une analyse statistique des émissions conduites dans des scénarios avec plusieurs OBC ayant des phases aléatoires connectées au réseau. Cette approche impliquerait l'établissement de surfaces de probabilité pour les niveaux de courant, offrant une compréhension plus complète de la variabilité et des extrêmes potentiels des émissions conduites dans des systèmes complexes..

# TABLE OF CONTENTS

# LIST OF FIGURES

# LIST OF TABLES

# LIST OF ABBREVIATIONS

### *A*

AC
    Alternating Current · 7
AMN
    Artificial Mains Network · 22
AN
    Artificial Network · 22

### *B*

BCI
    Bulk Current Injection · 42
BEV
    Battery Electric Vehicle · 4

### *C*

CAN
    Controller Area Network · 73
CISPR
    Comité International Spécial des Perturbations Radioélectriques/International Special Committee on Radio Interference · 21
CM
    Common Mode · 18

### *D*

DAB
    Dual Active Bridge · 12
DC
    Direct Current · 7
DER
    Distributed Energy Resources · 11
DM
    Differential Mode · 18
DUT
    Device Under Test · 22

### *E*

EM
    Electromagnetic · 47
EMC
    Electromagnetic Compatibility · 3
EMI
    Electromagnetic Interferences · 16
ESA
    Electronic Sub-assembly · 11
ESD
    Electrostatic Discharge · 11
ESO
    European Standardization Organization · 21
EUT
    Equipment Under Test · 18
EV
    Electric Vehicle · 3
EVSE
    Electric Vehicle Supply Equipment · 7

### *H*

HDV
    Heavy-duty Vehicle · 4
HF
    High Frequency · 28
HV
    High Voltage · 13

# GENERAL INTRODUCTION

The research work presented in this dissertation was conducted within the framework of a CIFRE PhD through a collaboration between the SATIE laboratory (Laboratoire des Systèmes et Applications des Technologies de l'Information et de l'Energie) at the École Normale Supérieure de Paris-Saclay – Paris-Saclay University, and Stellantis (formerly PSA Group), from September 2020 to July 2024. This work was supported by the OpenLab Electrical Engineering for Mobility, Stellantis, France, and co-financed by the ANRT association, and it contributes to the optimal design of EMC filters by studying and modeling the propagation of conducted emissions from on-board chargers in grids with various earthing systems in the absence of the LISN.

## Scope of the work

The transition to Electric Vehicles (EVs) is a critical component of global efforts to decarbonize transport and address the growing environmental challenges posed by carbon emissions. This shift is driven by both stringent regulatory policies and significant advancements in the fields of energy storage and power electronics. As a result, the deployment of EVs has surged, accompanied by the proliferation of On-board Chargers (OBCs). The demand for compact and efficient systems necessitates the rise in operating frequencies of these devices, which has led to increased electromagnetic emissions and, consequently, larger EMC filters. This highlights the importance of addressing potential Electromagnetic Compatibility (EMC) issues, particularly in the context of conducted emissions.

Traditional EMC measurement setups often rely on the Line Impedance Stabilization Network (LISN) to standardize the measurement environment. However, this approach may not accurately reflect the diverse impedance characteristics of real-world power grids, which can vary significantly based on many factors, such as grounding systems and load configurations. Consequently, there is a critical need to develop and implement methodologies for assessing conducted emissions in more realistic scenarios by analyzing the grid's high-frequency impedance. Through experimental measurements and modeling, the research aims to bridge the gap between standardized EMC testing and the actual conditions encountered in different grid configurations.

## Chapter preview

In this context, this dissertation is divided into four chapters:

**Chapter 1:** This chapter introduces the research context by reviewing the different charging systems and related standards, with a focus on the OBCs and their structure. It addresses the issues associated with EMC standard conducted emissions measurement. Finally, different grounding systems and their characteristics are presented.

**Chapter 2:** The chapter provides an overview of grid impedance measurement techniques. The selected technique is then implemented, allowing for measurements at the ENS Paris-Saclay EV parking facility. Moreover, it investigates the impact of deviations between the impedances of LISN and the grid behind it on the volume of the filter in a case study using a developed volume optimization technique.

**Chapter 3:** This chapter introduces the OBC prototype and the microgrid to which it will be connected during the tests. It details the modeling process for each element of the charging system, dividing it into a grid impedance model and a converter black box model.

**Chapter 4:** The chapter analyzes the measured conducted emission generated by the OBC on the grid with different parameters. It then exploits the developed models by predicting the conducted emissions followed by a section dedicated to the grid HF impedance analysis.

# CHAPTER 1

## Context

With the dramatic rise in the number of Electric Vehicles (EVs) being charged on the grids all over the world on the one hand and the progress of wide-bandgap component technologies that allow power conversion at a higher switching frequency on the other hand, Electromagnetic Compatibility (EMC) is becoming a growing concern. This chapter gives an introduction to the context of the thesis subject. First, the charging environment of electric vehicles is presented, and then the issue associated with the EMC standard conducted emissions measurement will be addressed. Finally, different grounding systems and their importance in the perturbations generated by an On-board Charger (OBC) will be pointed out.

## 1.1 EVs Charging System

With the growing environmental concerns and the alarming consequences of increased carbon emissions, and also due to the fact that approximately one-quarter of the entire $CO_2$ emissions originate from transportation powered by fossil fuels, governments worldwide have started to implement different policies such as incentives, refunds, and stricter emissions standards to encourage the adoption of EVs as a sustainable solution [1]. Figure 1-1 presents the mandates and legislation worldwide regarding the transport decarbonization policy for Light-duty Vehicle (LDV) and Heavy-duty Vehicle (HDV) segments up to 2050.

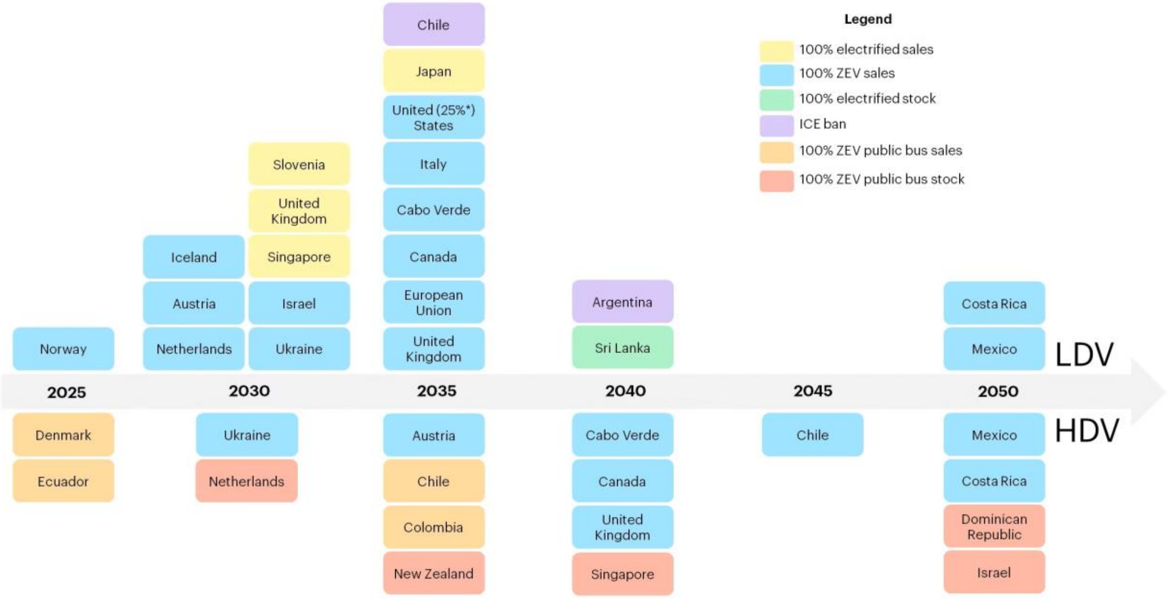

*Figure 1-1 Global Zero-emission Vehicle (ZEV) mandates and Internal Combustion Engine (ICE) bans (Electrified vehicles include Battery Electric Vehicles (BEVs), Plug-in Hybrid Electric Vehicles (PHEVs), and Hybrid Electric Vehicles (HEVs), while ZEVs include BEVs, PHEVs as well as Fuel Cell Electric Vehicles (FCEVs)) [2].*

In addition, technological advancements in all the related domains, such as batteries, power electronics, electric motors, and so forth, led to improved efficiency, as the comparison presented in Figure 1-2 shows, and a decline in EV pricing that consequently boosted market acceptance. For example, the kWh price of Li-ion batteries (which represents approximately 25% of the EV price in the case of Renault ZOE) has been decreasing by around 20% each year since 2010 [3]. Moreover, the specific energy of Li-ion batteries has increased from 80 Wh/kg to around 300 Wh/kg since first commercialized by Sony in 1991, resulting in a more extended driving range [4]. Forecasts suggest that the specific energy of batteries and so the driving range of EVs will continue to improve through advancements in battery technology as new materials and structures come into existence, like Lithium Air Battery (LAB) that propose a theoretical high specific energy of 11,140 Wh/kg comparable to that of gasoline 12,700 Wh/kg [5].

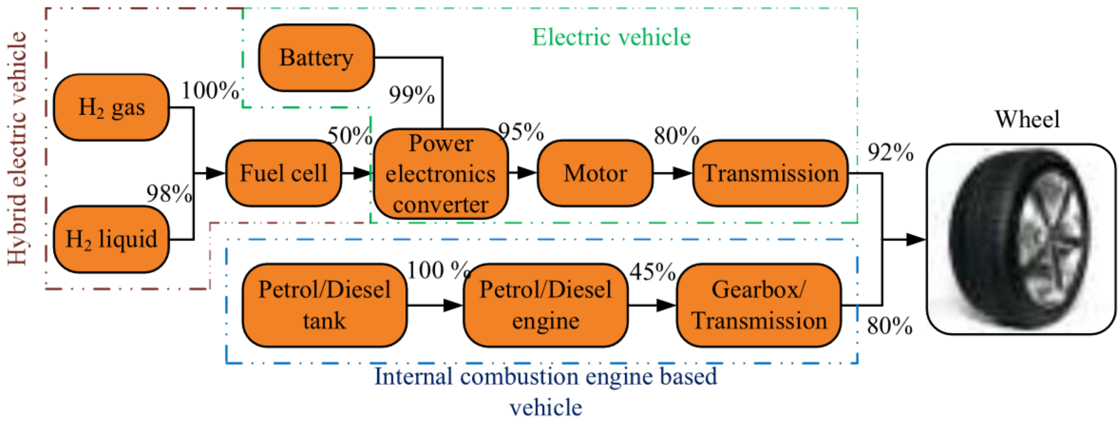

*Figure 1-2 The tank-to-wheel energy efficiency comparison among FCEVs, BEVs, and ICEs [1].*

The result of transport decarbonization policies and technological progress has been a remarkable transformation toward EVs in the automotive industry over the last decade. The number of BEV and PHEV sales combined has increased from 320 thousand in 2014 to about 14 million in 2023, and the market share has risen from 0.4% to about 16% in 2023, as can be seen in Figure 1-3. Many forecasts, presented in [6], project that transport electrification will continue to grow and will experience a sharp rise over the upcoming decades as well.

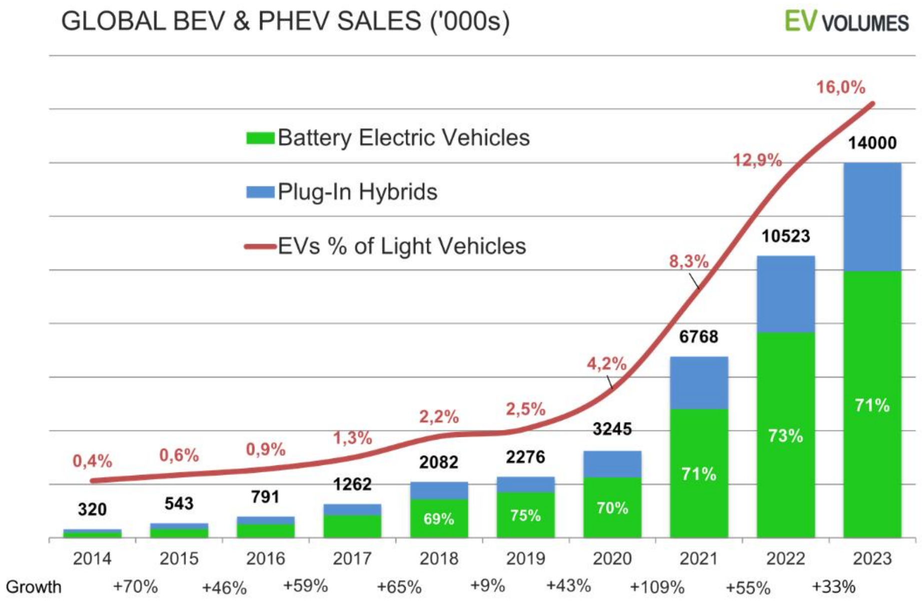

*Figure 1-3 Global BEV and PHEV sales and market share of light-duty vehicles evolution in the last decade [6].*

All these ever-increasing BEVs must be charged by the electric grid, and to meet this demand and to make them more accessible for consumers, governments and private entities have invested in developing the charging infrastructure. Regardless, today, one of the main obstacles preventing all-electric vehicles from dominating the market, besides their shorter driving range, is their longer charging time compared to the refueling time of ICEs. Therefore, it is of utmost importance to tackle the complications associated with EV charging.

EV charging techniques can be categorized depending on the manner in which they transfer power (conduction, induction, and battery swapping), the type of transferred power (AC or DC), where the charger is located (on-board or off-board), or the rate of power. The most inclusive EV charging methods classification, which has been suggested in the literature [7], [8], [9] is presented in Figure 1-4.

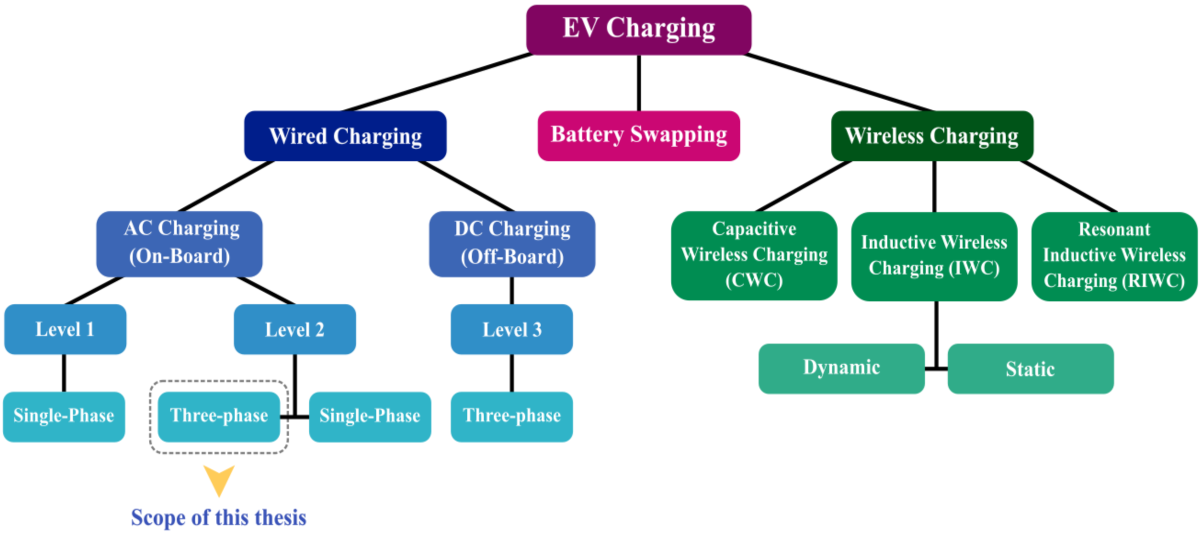

*Figure 1-4 Classification of EV charging techniques.*

The wireless or cordless method, also known as Wireless Power Transfer (WPT), has two types, which are determined by the movement of EVs. Static wireless charging applies when the EV is at a standstill, while dynamic wireless charging can be achieved while the vehicle is in motion, aided by an appropriate control strategy and with speed restrictions [10]. WPT systems have already managed to transfer energy across air gaps of 200 mm, with efficiencies of about 96% [11]. However, the energy efficiency of wireless charging is still lower than conductive or wired charging, and numerous studies, including [12], [13], [14], aim to improve the efficiency and distance between the transceiver and receiver coil by employing appropriate power electronics circuits and suitable compensation networks. It is worth mentioning that the SAE J2954 standard, which is related to wireless charging, imposes a minimum energy efficiency of around 80% [3].

Battery swapping is an alternative approach to recharging the existing battery. This technique has been mostly adopted by Chinese automakers, for example, NIO, who claimed that they have built 1,383 power swap stations in China and Europe, with a fully automated replacement procedure that needs only about three minutes [15].

The wired, conductive, or plug-in method sets up the physical connection between the AC grid and the EV, and it is the method that is broadly utilized nowadays as it is more efficient and requires less time for charging compared to the wireless method. As depicted in Figure 1-5, an EV battery charger is mostly composed of two stages,

- an AC/DC rectifier with an active Power Factor Correction (PFC) feature, and
- a DC/DC converter providing the DC voltage level required for the battery.

This power conversion process can be conducted within the EV by means of an On-board Charger (OBC) or externally through an off-board charger in an Electric Vehicle Supply Equipment (EVSE), more commonly referred to as a charging station or a charge point. The latter is a general term that can be used for nonconductive charging methods as well. In this classification, the level 1 category applies to single-phase wall outlets at home or workplace limited to 1.9 kW; level 2 can be single-phase or three-phase private or public EVSE limited to 19.2 kW; level 3 signifies DC fast charging stations with power rates over 50 kW.

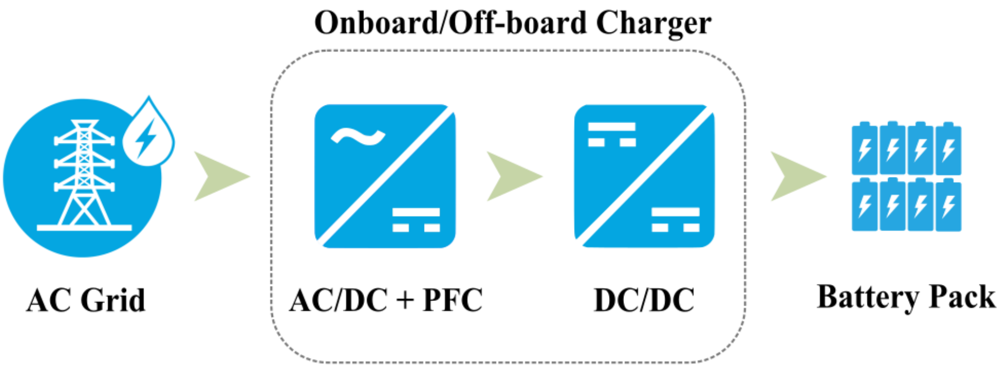

*Figure 1-5 The basic concept of power conversion in the conductive EV charging method.*

Being stationary, EVSEs do not require adhering to strict volume and weight design limitations, unlike OBCs, and consequently, conductive off-board chargers can deliver energy in a DC form directly to the battery at significantly higher power rates.

### 1.1.1 EV Conductive Charging Standards

Through the implementation of global standards, cross-manufacturer compatibility is achievable and thereby promotes the widespread adoption of electric vehicles. Concerning EV conductive charging, there are several standards all around the world, most notably:

- SAE: The Society of Automotive Engineers or SAE International, which is a US-based organization with a focus on transport industries, defined a set of regulations for conductive charging method in the SAE J1772 standard [16].
- IEC: The International Electrotechnical Commission develops and releases global standards for all electrical, electronic, and related domains, including transport electrification with the IEC 61851 series on EV conductive charging systems and the IEC 62196 series on plugs, socket-outlets, vehicle connectors, etc. [17].
- GB/T charging standard: Employed in China with GB/T 18487, which provides general requirements for conductive charging systems; GB/T 20234, which provides physical requirements for connectors and interfaces; and GB/T 27930, which provides communication requirements [18].

*Table 1-1 EV conductive charging levels defined by SAE J1772 [16],[19].*

| SAE J1772 Levels | Voltage (V) | | Maximum Current (A) | Maximum Power (kW) | Charger Location |
|---|---|---|---|---|---|
| **AC - Level 1** | 120 AC | 1 Φ | 16 AC | 1.9 | On-board – Residential |
| **AC - Level 2** | 208 AC | 3 Φ $V_{LL}$ | 80 AC | 16.6 | On-board – Private and commercial |
| | 240 AC | Split 1 Φ | | 19.2 | |
| **DC - Level 1** | Up to 1000 DC | | 80 DC | 80 | Off-board – Commercial |
| **DC - Level 2** | Up to 1000 DC | | 400 DC | 400 | Off-board – Commercial |

The SAE J1772, which is a North American standard, outlines four levels of charging, two for AC and two for DC, presented in Table 1-1; the dissimilarity between these levels is dependent on the power supply type, rules, and maximum power rate.

The standardization of the Tesla charging standard, also known as the North American Charging Standard (NACS), is currently in progress under SAE J3400 as well [20], [21].

The IEC standard also defines four distinct charging modes, as summarized in Table 1-2. As described in [3], the first mode is adapted to scooters or small vehicles, e.g., Renault Twizy recharging from a typical residential outlet, and it is not recommended for EVs.

In Mode 2, a control mechanism in the charger cable verifies the outlet type, and if it is reinforced, it allows a maximum direct current of 16 A. Mode 3 requires a particular type of charging outlet, commonly referred to as Wall Box, and the power can be delivered with a maximum rate of 7.4 kW in single-phase and 22kW in three-phase. Finally, the voltage and current limits in DC fast charging are described in mode 4.

*Table 1-2 EV conductive charging modes defined by IEC 61851 [3].*

| IEC 61851 Modes | Voltage (V) | | Maximum Current (A) | Maximum Power (kW) | Charger Location and Connector Type |
|---|---|---|---|---|---|
| **Mode 1** | 230 AC | 1 Φ | 8 AC | 1.8 | On-board – Residential outlet |
| **Mode 2** | 230 AC | 1 Φ | 16 AC | 3.7 | On-board – Reinforced outlet (e.g. Green'up) |
| **Mode 3** | 230 AC | 1 Φ | 32 AC | 7.4 | On-board – Private or Commercial Specific outlet (e.g. Wall Box) |
| | 400 AC | 3 Φ / Y | 16 AC | 11 | |
| | | | 32 AC | 22 | |
| **Mode 4** | 400 - 1000 DC | | 400 DC | 400 | Off-board – Commercial EVSE (CCS Combo 2) |

### 1.1.2 On-board Chargers

On-board chargers enable users to charge the battery conveniently from their residences, thus making recharging more accessible while simultaneously decreasing the expenditure on infrastructure. Moreover, by simply bypassing the OBC, the vehicle can be charged from a DC fast-charging EVSE, as presented in Figure 1-6.

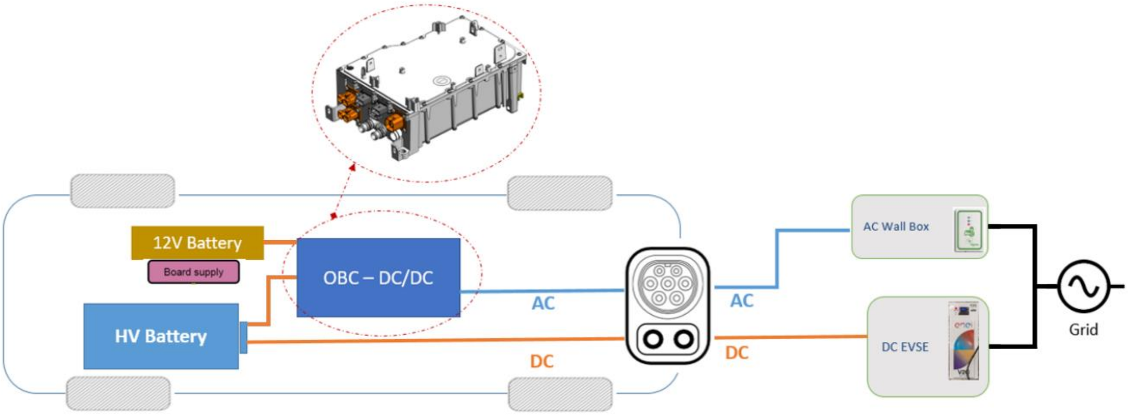

*Figure 1-6 A simple diagram of EV battery DC and AC charging (related to mode 3 and mode 4).*

In spite of concerns about battery degradation and the cost of OBCs, they are increasingly being developed to sustain bidirectional power flow by employing active bidirectional switches to be able to operate in Vehicle-to-Everything (V2X) functionality modes, such as Vehicle-to-Load (V2L), Vehicle-to-Vehicle (V2V), and particularly Vehicle-to-Grid (V2G), which will be discussed in more detail in the 1.1.3 section.

The majority of OBCs employed in the automotive industry are typically two-stage architecture, as demonstrated in Figure 1-5. Nevertheless, single-stage configurations have been suggested in the literature, such as [22], [23], for lower power rates (usually up to 3.3 kW for single-phase) to achieve a reduced number of active components, leading to cost reduction and a potential power density and durability gain by eliminating the electrolytic capacitor between the two stages. From another point of view, OBCs can also be divided into non-integrated or propulsion system integrated. [24] presents a review of 70 research papers on different types of integrated OBC topologies. The Renault ZOE’s Chameleon charger, protected by patent [25], is a commercial example of the bidirectional propulsion system integrated topologies supporting power levels up to 43 kW.

OBCs, like many other converters, used to utilize Si-based switches, but lately, they have been revolutionized by one key technology that has emerged, which is the utilization of

Wide-Band Gap (WBG) components, such as silicon carbide (SiC) and gallium nitride (GaN). These components offer significant benefits in terms of efficiency and power density by the ability to switch at even higher frequencies. However, these benefits come at a cost; as the switching frequency rises, so does the rate of change in voltage and current, resulting in a decline in the system's EMC performance and requiring a larger EMC filter.

#### 1.1.2.1 PFC Stage

Table 1-3 presents a summary of many standards regarding the development of OBCs gathered from [19] and [26]. Standards related to power quality restrict the maximum current and voltage Total Harmonic Distortion (THD) between 5-10%, which cannot be accomplished without an active PFC stage, as the conventional voltage rectifiers generate a highly distorted current.

*Table 1-3 An overview of the regulations relevant to OBC development.*

| Classification | Standards | Description |
|---|---|---|
| **Power Quality** | IEEE 519<br>IEC 61000-3<br>SAE J2894<br>GB/T 14549 | Limits of the harmonics injected into the grid from the EVSE |
| **EMC** | CISPR 25 | Radiated/conducted electromagnetic emissions limit |
| | IEC 61851-21 | On-board charger EMC requirements for conductive connection to an AC/DC supply |
| | ISO 11542 | Radiated/conducted electromagnetic immunity |
| | ISO 10605 | Electrostatic Discharge (ESD) susceptibility |
| **Environmental Conditions** | ISO 16750 | Environmental conditions and testing for Electronic Sub-assemblies (ESAs) |
| **Safety** | ISO 26262 | Functional safety assessment |
| | UL 2202<br>IEC 60950<br>ISO 6469 | Electrical safety tests |
| **V2G** | ISO 15118<br>IEEE 1547<br>UL1741 | Vehicle-to-grid (V2G) operation's communication interface specifications/ Interconnection between the grid and Distributed Energy Resources (DER) |

When it comes to three-phase bidirectional OBCs, which we are more focused on, the prominent PFC converters are the full-bridge converter and three-level T-type converter, as illustrated in Figure 1-7. One of the most widespread bidirectional rectifiers is the former due to its ease of control and higher power level capability. This topology has been employed commercially by the BYD EV as part of the bidirectional OBC’s front-end PFC converter, allowing for vehicle-to-load (V2L) via bypassing one leg and employing the converter like an H-bridge inverter to charge other loads at up to 3.3 kW [26].

The T-type converter, a bi-directional adaptation of the well-known “Vienna” converter, offers advantages like low conduction and switching losses in middle switches, a straightforward operation principle, and lower switch stress [27].

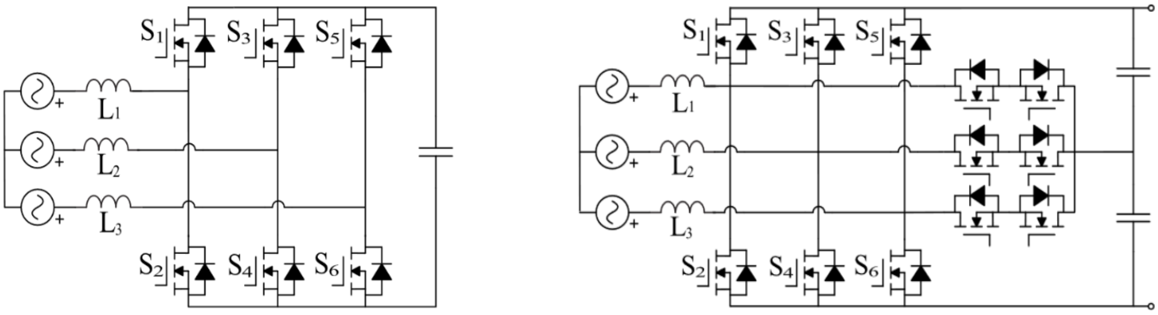

(a) (b)

*Figure 1-7 Bidirectional three-phase PFC topologies: (a) full-bridge PFC converter. (b) T-type PFC converter [26].*

#### 1.1.2.2 DC/DC Stage

The second stage, the DC/DC converter, guarantees the suitable voltage level for the battery and DC bus, providing galvanic isolation and enabling control over the direction of power flow thanks to the Dual Active Bridge (DAB) converters. The most common commercial bidirectional DC/DC converter topologies are demonstrated in Figure 1-8 and can all achieve an efficiency higher than 98%. The LLC resonant converter, depicted in Figure 1-8-a, is the least preferable because of the asymmetrical configuration.

The phase-shifted DAB converter, shown in Figure 1-8-b, is particularly favored for its relatively simple control and design. In contrast, CLLC resonant topology necessitates a more complex control and design since this converter usually has a variable switching frequency.

However, it yields higher power density and operates with a much broader soft-switching region, particularly in light load scenarios [26].

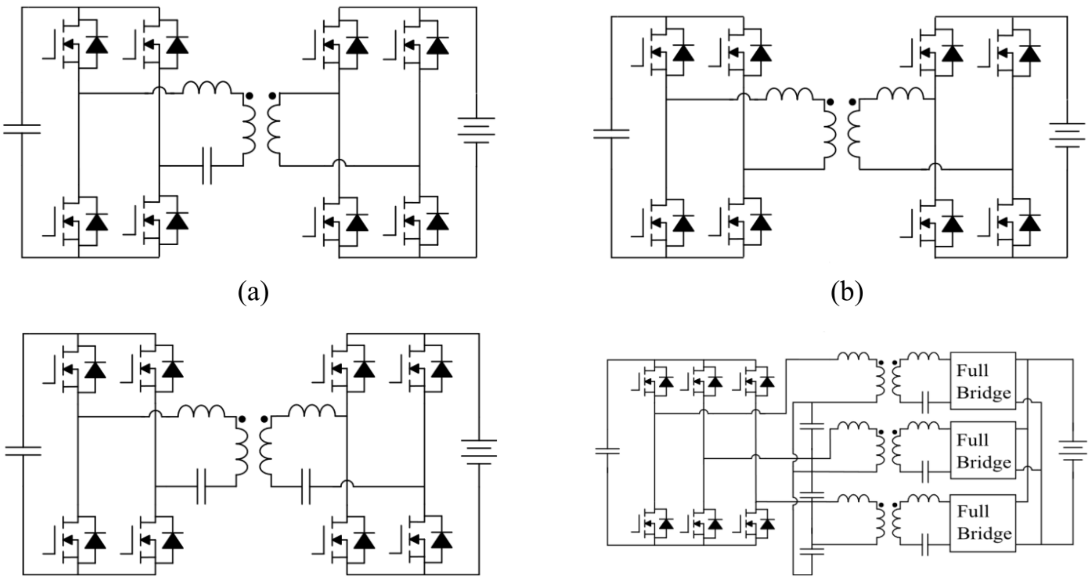

(a) (b) (c) (d)

*Figure 1-8 Bidirectional DC/DC topologies: (a) Single-phase LLC. (b) Single-phase phase-shifted DAB. (c) Single-phase CLLC. (d) Three-phase CLLC [26].*

Regarding the output voltage level, 400 V HV battery architectures have been the most common for electric vehicles for many years. Nevertheless, with the emergence of wide band gap (WBG) active components capable of withstanding higher voltage stress, such as SiC, it is set to change, and 800 V and 900 V systems have been introduced lately in specific models from car manufacturers, including the Hyundai Ioniq 5, Audi e-tron GT, Chevrolet CAMARO eCOPO and Porche Taycan. This is due to the fact that higher voltage systems can reduce the energy loss in the battery, cables, electric machine, and traction inverter, leading to a higher global efficiency [28]. This trend is expected to persist up to 1500 V systems, as the Japanese standard CHAdeMO 3.0/Chaoji, released in 2020, defined the prerequisites and conditions for an ultra-high-power DC charging up to 900 kW and 1500 V. In addition to the advantages already mentioned, the rise in voltage has its limits and presents a variety of issues, including the necessity for a greater clearance and creepage distance to prevent insulation failure and partial discharge that may result in an increase in the size of the system [19].

### 1.1.3 Vehicle to Grid (V2G)

The large-scale adoption of plug-in electric vehicles (PEVs), which include BEVs and PHEVs, if charging is uncontrolled, can have multiple negative impacts on the existing distribution network, such as augmented peak demand, voltage instability, increased power loss, transformer overheating, and overloading. However, since the average operating time for PEVs as a means of transportation is only 5%, and they remain idle 95% of the time, the bidirectional power flow feature can provide grid operators with the opportunity to employ the fleet of PEVs as a massive mobile energy storage reservoir, and this gave rise to the vehicle-to-grid (V2G) concept. Through V2G, EVs can be utilized for various purposes beyond transportation, such as contributing to grid stability, improving renewable distributed energy resources integration, and enabling additional functionalities [29], [30], [31], [32], [33].

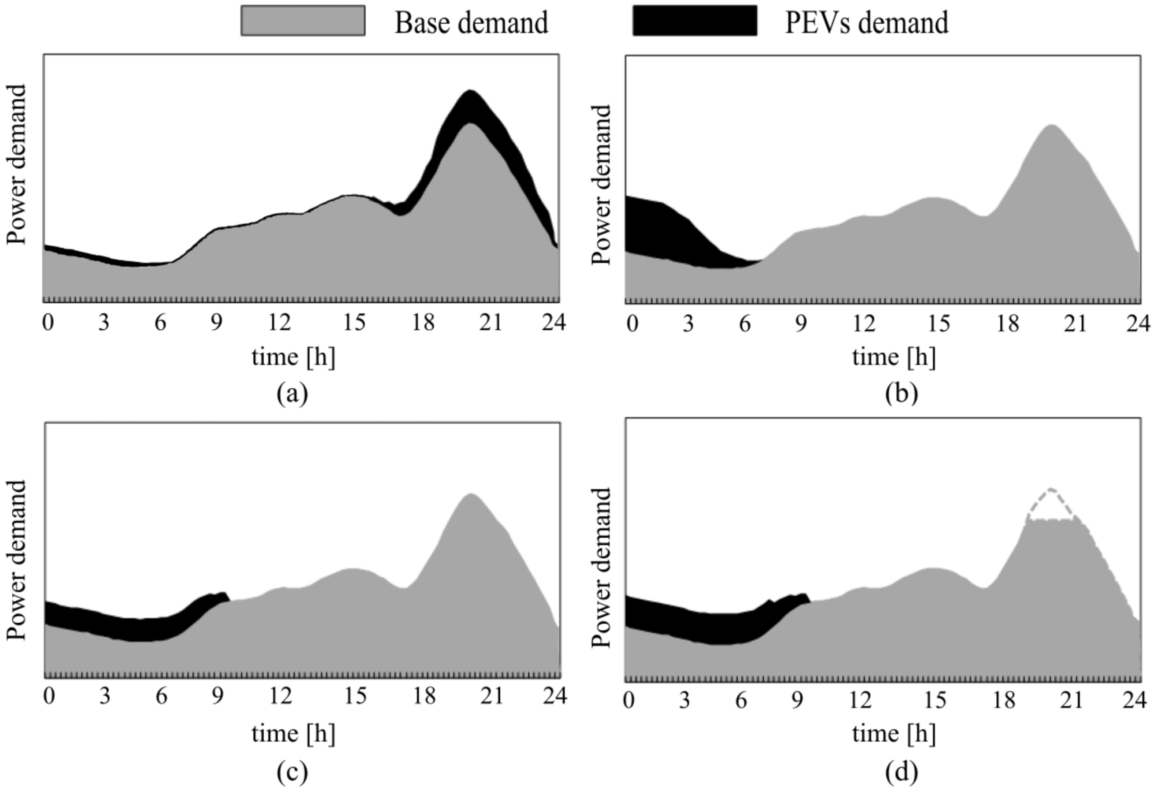

*Figure 1-9 Total power demand profile with different charging and discharging strategies: (a) Uncontrolled charging, (b) Delayed charging, (c) Controlled charging, and (d) V2G [34].*

Figure 1-9 presents the total power demand in four different scenarios for charging and discharging the fleet of PEVs. As the marginal power generated during the peak demand is generally costly and CO2 intensive, it is ideal to maintain power demand as flat as possible throughout the day [35]. Therefore, the worst scenario is uncontrolled charging, also referred to as dumb charging or unregulated charging. Using this method will not only accelerate the need for infrastructure upgrades but also make the mentioned negative impacts on distribution networks inevitable. In delayed charging, an optimal design of electricity tariff prices during the day can incentivize a large number of EV owners to charge at off-peak times. However, it can cause a second peak if the pricing is poorly managed. In controlled charging, also called smart charging, PEVs act as controllable load units, and the charging time and power depend on some distribution network parameters like total power demand, transformer loading, etc., or to minimize the charging cost. This can be achieved through a centralized or decentralized control architecture. In centralized control, the control entity or aggregator is responsible for managing directly the charge of all PEVs under its region. Although this method can use the network's capacity to its fullest, it requires expensive communication infrastructure, and its complexity increases with the number of PEVs. In contrast, the decision-making in decentralized control resides in each PEV, i.e., in each owner, rather than in an external entity as the aggregator, which implies that each PEV must have some intelligence to decide based on its conditions like SoC and also base on the real-time electricity prices received from the aggregator [32]. In the first three scenarios, uncontrolled charging, delayed charging, and controlled charging, power flow is unidirectional, and even in the best case, only the total demand valleys can be filled. However, in the V2G case, the peak demand can also be shaved, resulting in a flatter total demand, as can be seen in Figure 1-9-d.

The potential benefits for both parties make this technology likely to become widely adopted, leading to an increase in the number of connected OBCs to the grid, which implies a proliferation in the number of sources of electromagnetic interference, thus making it crucial to address potential issues such as EMC concerns. Furthermore, as we examine a bidirectional OBC in this research, we will also delve into the comparison of EMC performance between V2G and G2V modes in the following chapters.

## 1.2 Electromagnetic Compatibility

Most electronic devices generate and emit some form of electromagnetic waves and are susceptible to malfunction if exposed to them. Therefore, in today’s world of pervasive electronic systems, the Electromagnetic Compatibility (EMC) discipline emerges as a critical aspect in the framework of technological development, as lives can certainly be at risk if a system fails to function correctly, especially in the automotive context. EMC constitutes the systematic study and application of principles to ensure that electronic devices can coexist within close spatial proximity without disturbing one another, causing system malfunctions. Hence, systems should not disrupt others by generating excessive Electromagnetic Interferences (EMI), and at the same time, they must be resilient to a certain level of these emissions [36]. The reason for delving into the subject of EMC stems from the need to meet extra design goals for electronic systems to be electromagnetically compatible with their environment, on top of the essential requirements for system functionality.

The main sources and culprits for electromagnetic perturbations are usually the high di/dt loops and high dv/dt nodes. The origin can be different from Electrostatic Discharge (ESD) to lightning, and in power electronics, fast switching converters.

These emissions can be transferred from the source to the victim in two ways:

- Conducted emissions that propagate through power supply or interconnection cables and wires existing in the system.
- Radiated emissions that transfer energy through the electric field and magnetic field.

Therefore, the study of the EMC aspects of a system, an OBC, for example, can be divided into four different categories: Conducted emission, conducted immunity, radiated emission, and radiated immunity. The work in this thesis concerns the first category.

It is important to note that there exists a significant correlation between the level of conducted emissions and the radiated emissions. Notably, studies such as [37] and [38] have demonstrated that in energy conversion systems utilizing shielded cables, radiated emissions exhibit a strong correlation with the common mode current passing through the ground plane and the shield. This correlation arises only with CM current because the DM current passing through the cables is shielded. However, in the context of EV charging, the cables on the grid side are not shielded. As a result, both DM and CM currents contribute to the radiated emissions. However, in single-phase systems, the DM contribution is relatively limited due to the close proximity of the two conductors carrying currents with inverse polarity.

Both government agencies and product manufacturers enforce EMC requirements on electronic systems. The regulations mandated by government agencies are legally binding and typically cannot be exempted. Meeting these EMC requirements does not necessarily ensure the product will not interfere with other devices. Instead, it controls the amount of electromagnetic pollution created by the product. For example, one of the main Directives of CE marking, which is mandatory for a product that will be marketed in Europe, is EMC Directive 2014/30/EU, which lays down the essential EMC requirements. The conformity assessment procedure can be either self-certification or the responsibility lies with the manufacturer to involve a recognized third-party body that will evaluate technical files and the evidence of conformity in accordance with a particular procedure determined by the relevant Directive [39]. the EMC requirements that manufacturers willingly place on their products are designed to satisfy customers and are often more rigorous in order to ensure a dependable, high-quality product and to preserve a positive reputation.

Effective management of EMC in the production process requires early consideration when the degree of design freedom is much higher, which allows for more cost-effective solutions since EMC failure and countermeasures are exponentially more costly as the project timeline progresses. Having a reliable model of the system in the design stage prevents future problems and also significantly reduces the cost and time in the event of a design re-spin.

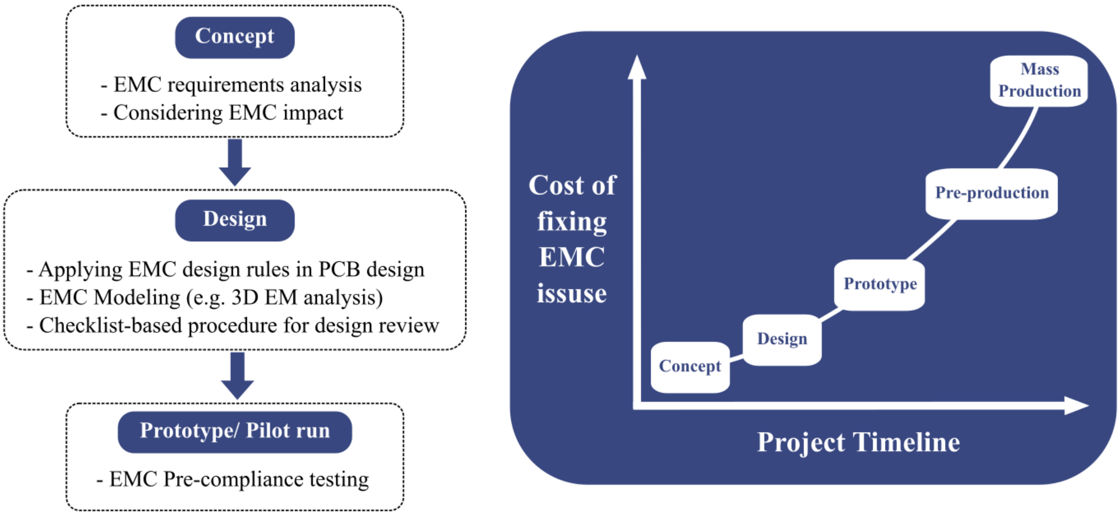

*Figure 1-10 EMC management strategies in different production stages and cost of EMC failure in different phases.*

Various methods exist to address EMC issues. One common approach involves implementing effective shielding techniques, such as enclosures or conductive coatings, to contain generated electromagnetic emissions and prevent external interference. Another common practice is designing passive, active, or hybrid EMC filters at the system's input and output stages to attenuate emissions and enhance the overall EMC performance. By implementing passive filtering, we establish an additional pathway for high-frequency noises to limit the polluted area between input and output filters.

In active filtering, we detect the noise and compensate it by generating a signal using active components. However, due to the limited bandpass, active filtering is more suited for lower frequencies. Therefore, generally, a combination of passive and active filtering can be an optimal solution for attenuating the noises, reducing the volume and mass of the filters [40]. The OBC prototype that we work on has only passive input and output filters.

### 1.2.1 Conducted Emissions

#### 1.2.1.1 Propagation Modes in Single-phase and Three-phase Systems

In the context of studying EMC in a system, conducted emissions are considered to propagate in two modes, common mode (CM) and differential mode (DM) , which are defined as the following equations in symmetric single-phase systems:

$$\boldsymbol{I_{CM} = I_1 + I_2} \tag{1-1}$$

$$\boldsymbol{I_{DM} = \frac{I_1 - I_2}{2}} \tag{1-2}$$

Where $I_1$ and $I_2$ are the currents flowing in power lines between LISN and EUT, as shown in Figure 1-11. The CM current goes through both the phase and the neutral lines and returns from the ground, while the DM current goes through the phase line and returns from the neutral line.

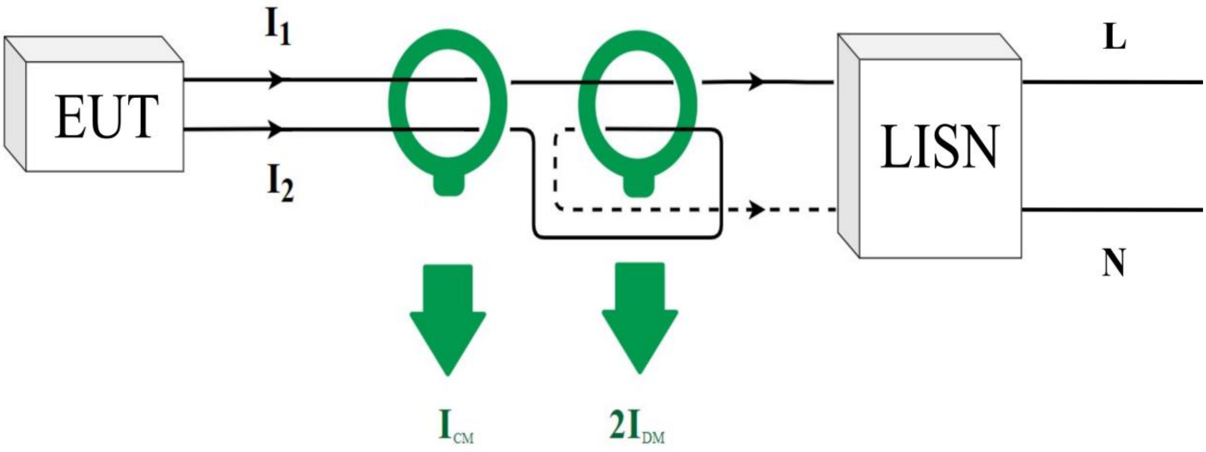

*Figure 1-11 Common mode and differential mode current in single-phase systems.*

In order to extract CM and DM currents in single-phase systems, two current sensors can be inserted in the test setup, as demonstrated in Figure 1-11.

Moreover, regarding CM and DM decomposition in three-phase systems, [41] describes a general asymmetric three-phase three-wire arrangement in Figure 1-12-a where $v_i$ indicates noise source of phase $i$, $Z_i$ noise source impedance, and $Z_0$ capacitive coupling to ground. By assuming that the system is symmetric we have:

$$\boldsymbol{Z_a = Z_b = Z_c = Z} \qquad 1\text{-}3$$

Therefore, the leakage current to ground is equally distributed in each phase driven by the CM voltage source:

$$\boldsymbol{i_{CM} = i_a + i_b + i_c} \qquad 1\text{-}4$$

$$\boldsymbol{v_{CM} = \frac{1}{3}(v_a + v_b + v_c)} \qquad 1\text{-}5$$

And thus, DM voltage sources can be defined as follows:

$$\boldsymbol{v_{i,DM} = v_i - v_{CM}} \qquad 1\text{-}6$$

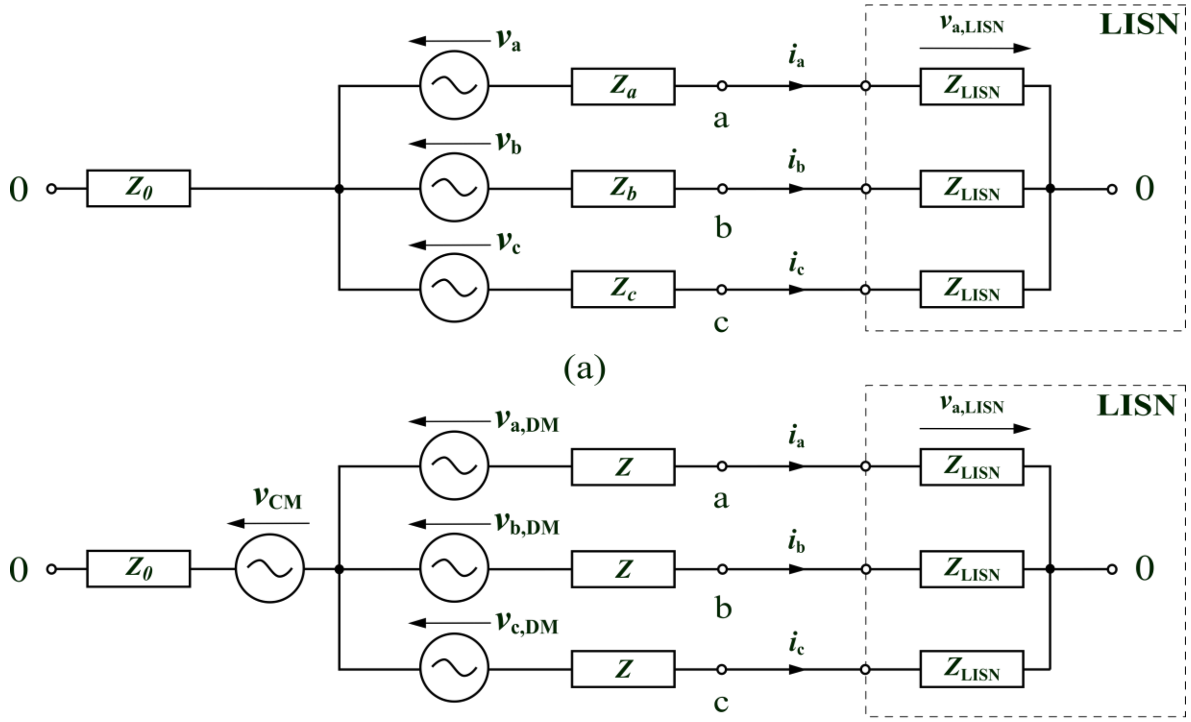

(a)

(b)

*Figure 1-12 (a) Equivalent circuit of the three-phase three-wire converter with inner noise source impedances connected to the LISN and (b) decomposition into CM and DM [41].*

Similarly, the typical asymmetric configuration for the three-phase four-wire systems, including the one under examination in chapter III of this thesis, can be delineated as depicted in Figure 1-13-a.

Depending on whether a switching leg is present on the neutral, as is the case with four-leg inverters, the source $v_n$ can be present, though it is typically uncommon, especially within the scope of this study. Consequently, under the assumption of system symmetry and the absence of a fourth switching leg, $v_n$ is considered zero, resulting in the system being described as illustrated in Figure 1-13-b, with the CM current equally distributed in each of four wires:

$$\boldsymbol{i_{CM} = i_a + i_b + i_c + i_n} \tag{1-7}$$

$$\boldsymbol{v_{CM} = \frac{1}{3}(v_a + v_b + v_c)} \tag{1-8}$$

Hence, DM voltage sources can be identified as:

$$\boldsymbol{v_{i,DM} = v_i - v_{CM}} \tag{1-9}$$

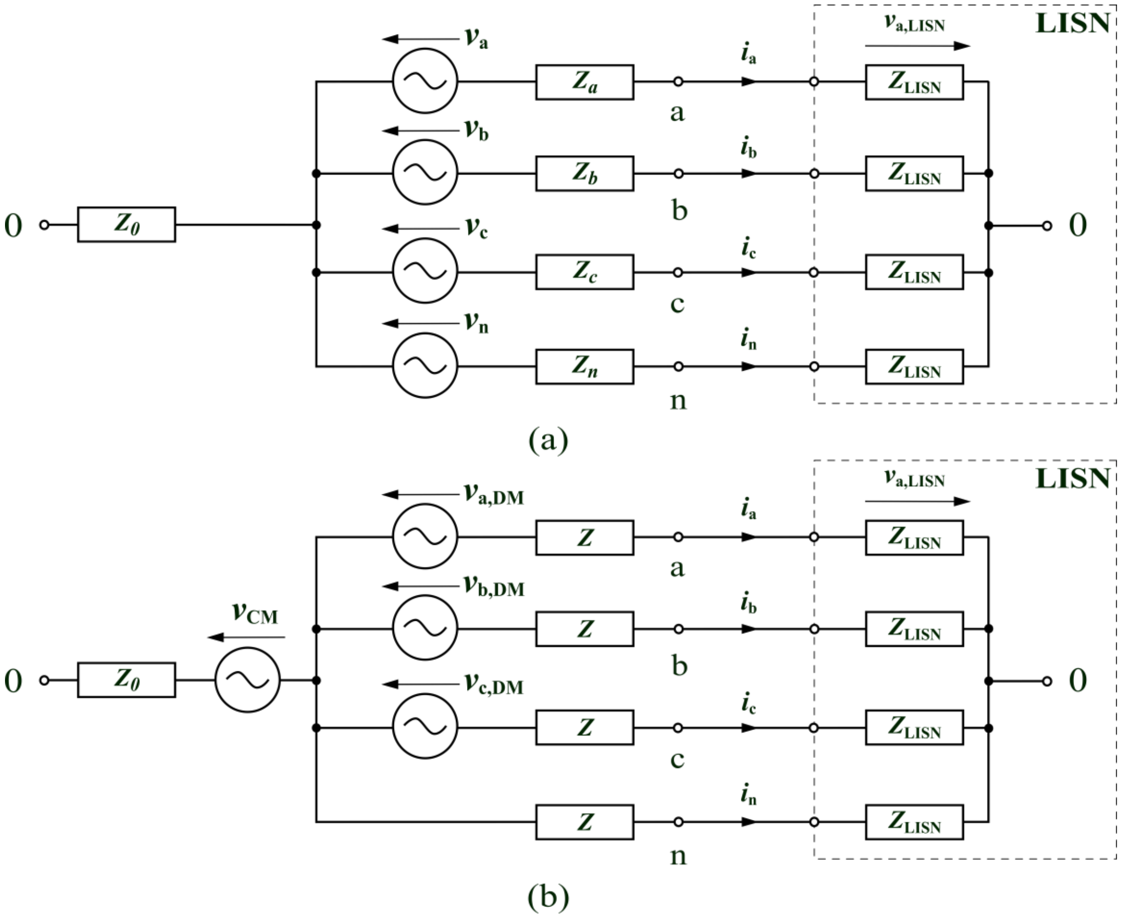

*Figure 1-13 Equivalent circuit of the three-phase four-wire converter with inner noise source impedances connected to the LISN and (b) decomposition into CM and DM.*

#### 1.2.1.2 Conducted Emissions Standards

Many regulatory bodies enforce the allowable thresholds of conducted emissions emitted from an end product, and these EMC standards are defined by various organizations, including the Federal Communication Commission (FCC) in the USA, “Comité International Spécial des Perturbations Radioélectriques” (CISPR) in Europe, and Radio Technical Commission for Aeronautics (RTCA). In the automotive industry, the vital conducted emissions tests and limits that apply to automotive components and modules are outlined in CISPR 25/EN55025 [42]. This standard is the only exception to CISPR-based test standards, as it allows for conducted emissions measurements up to 108 MHz, while all other standards have limits up to 30MHz. It is worth mentioning that European Standardization Organizations (ESOs) define and develop EU harmonized standards, and the European Committee for Electrotechnical Standardization (CENELEC) is one of the ESOs that EMC-related “EN550xx” standards come from.

Figure 1-14 present the relevant limit lines for peak and average detectors for Class 5, which is the strictest requirement from CISPR 25. Although there is a possibility for increased noise spikes in the intervals between frequency bands, automobile manufacturers have the liberty to extend these frequency ranges as per their specific needs.

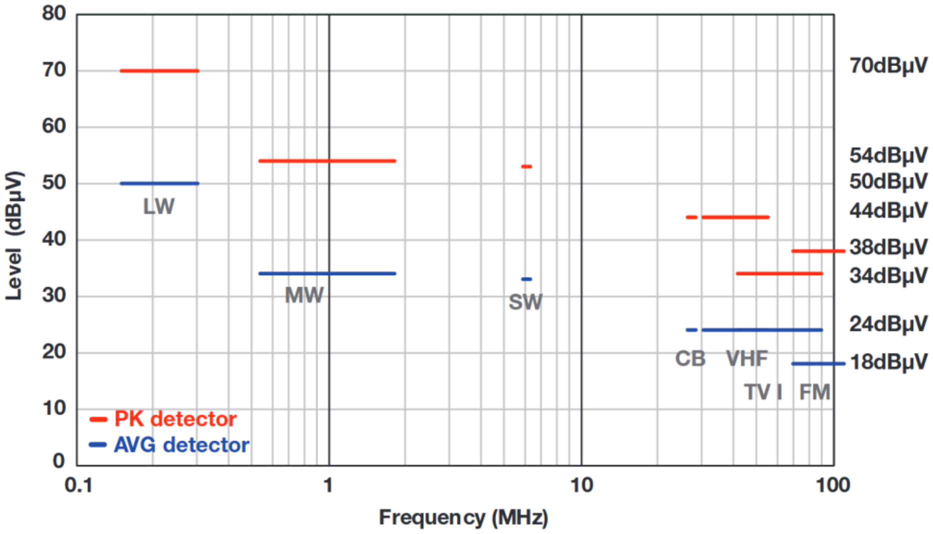

*Figure 1-14 CISPR 25 Class 5 conducted emission limits [42].*

Regarding OBCs, the IEC 61851-21-1 standard defines the EMC requirements for conductive connection to the supply, referring to many other normative texts such as CISPR 25, CISPR 22, CISPR 16, etc. The scope of this regulation is limited to OBCs, and their testing must be done either on the complete vehicle or on the charging system component level (ESA - electronic subassembly).

#### 1.2.1.3 The Issue Associated with Line Impedance Stabilization Network

When it comes to EMC conducted emissions measurements, Line Impedance Stabilization Network (LISN), also referred to as Artificial Network (AN) 5 µH/50 Ω network used for DC power supplies or Artificial Mains Network (AMN) 50 µH/50 Ω network used only for AC power mains based on CISPR standards, is an essential part of the test setup that must be inserted between the device under test and the power source during testing procedures. The commercial LISN structure is presented in Figure 1-15. This device is designed to achieve several aims. It eradicates the high-frequency link (over the regulatory frequency range of 150 kHz–30 MHz) between the DUT and the power supply using $L_1$, ensuring that external conducted emissions that may exist in the AC distribution system have no impact on the measurements. The LISN also protects the AC grid and the loads connected in the vicinity from the generated conducted emissions by the product under test. Moreover, proper shielding of the LISN makes the measurement immune against possible external radiated emissions. It also provides a fixed impedance, seen by the product looking into its source, to avoid the inevitable variations in line impedance from location to location, helping the repeatability of the measurements.

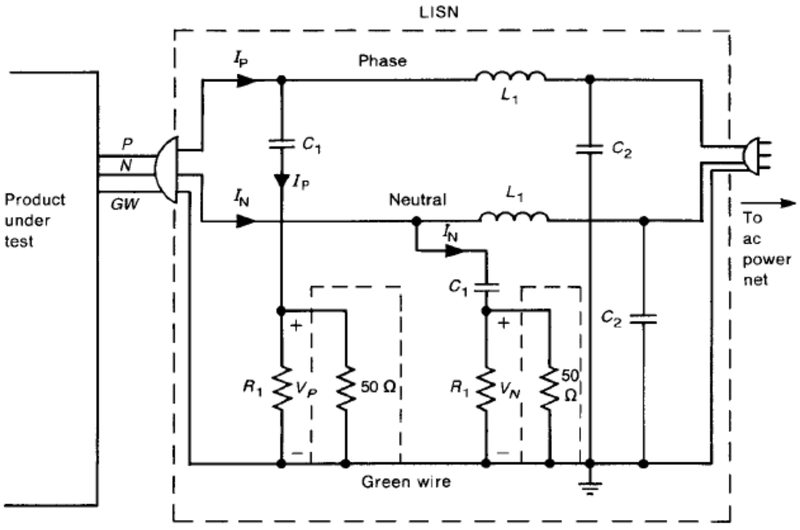

*Figure 1-15 The structure of an LISN used for the measurement of conducted emissions [36].*

The LISN is designed so that its impedance is statistically representative of both the mains' CM impedance (between a line and the ground) and the mains' DM impedance (between two lines/between each line and neutral) [43]. However, as the grid impedance can vary from site to site depending on the grid parameters such as the grounding system, cable length, and also depending on the loads connected to the grid in the vicinity of the measurement point, the disparity between the source or grid impedance and the LISN impedance can potentially impact the accuracy of conducted emission measurements and lead to the EMC filter performance drop as the impedance of noise termination can affect insertion loss of the passive filter [44], [45], [46]. In the second chapter, the influence of this impedance deviation on the volume of EMC filters will be investigated.

## 1.3 Grounding Systems

In the absence of LISN, one of the grid parameters that can affect the level of conducted emissions is the grounding or earthing system of the facility. The Low Voltage (LV) grounding system describes the grounding configuration of the secondary of the last transformer (MV/LV or LV/LV) and the approach utilized for grounding the installation frames. The three LV grounding systems, as defined in IEC 60364 and French standard NF C 15-100, are:

- **TT**: transformer neutral is grounded, and the frame is connected to the ground as well;
- **IT**: transformer neutral is isolated from the ground while the frame is attached to the ground;
- **TN**: the neutral of the transformer is connected to the ground, while the body or frame of the electrical load is linked to neutral.

According to IEC 60364, the TN system is composed of multiple sub-systems:

- **TN-C**: when there is only one conductor (PEN) instead of the Neutral (N) and Protective Earth (PE)/ground conductors;
- **TN-S**: when the N and PE neutral conductors are separate;
- **TN-C-S**: employing a TN-S after a TN-C (it is worth mentioning that using TN-S-C, a TN-C downstream of a TN-S, is prohibited).

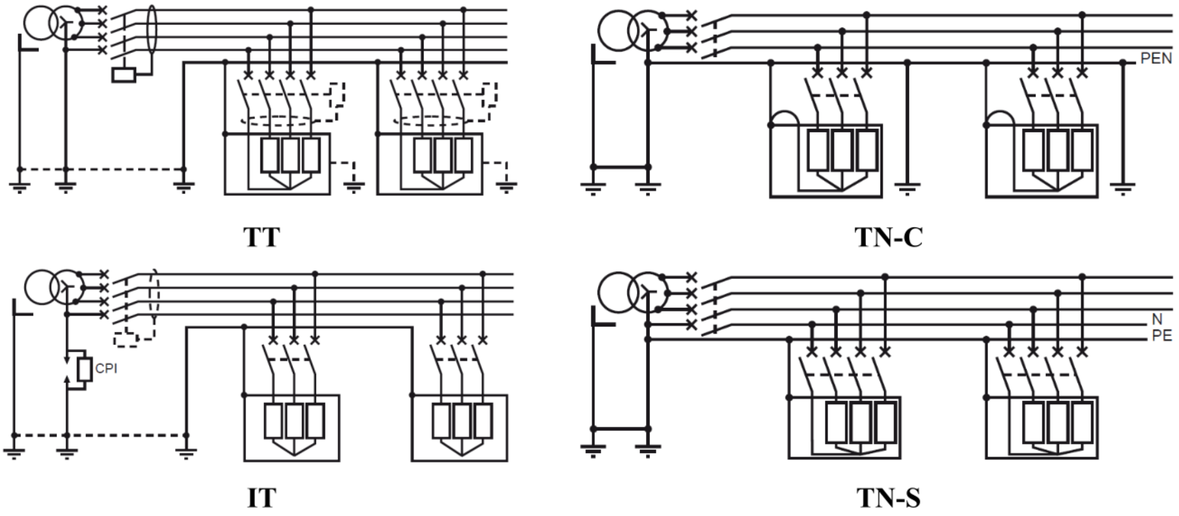

**TT** **TN-C**

**IT** **TN-S**

*Figure 1-16 TT, TN-S, TN-C, IT grounding systems [47].*

In certain cases, the LV neutral can be connected to the last transformer frame and the substation's earth connection, as presented in Figure 1-17. In France, in these cases, as in standard NF C 13-100, the third letter in the systems' names determines the type of connection:

- **R** indicates that all the frames are connected to each other, as in TNR and ITR;
- **N** means the Neutral frame is linked to the substation frame, as in TTN and ITN;

- **S** signifies all the frames' ground connections are separated, as in TTS and ITS.

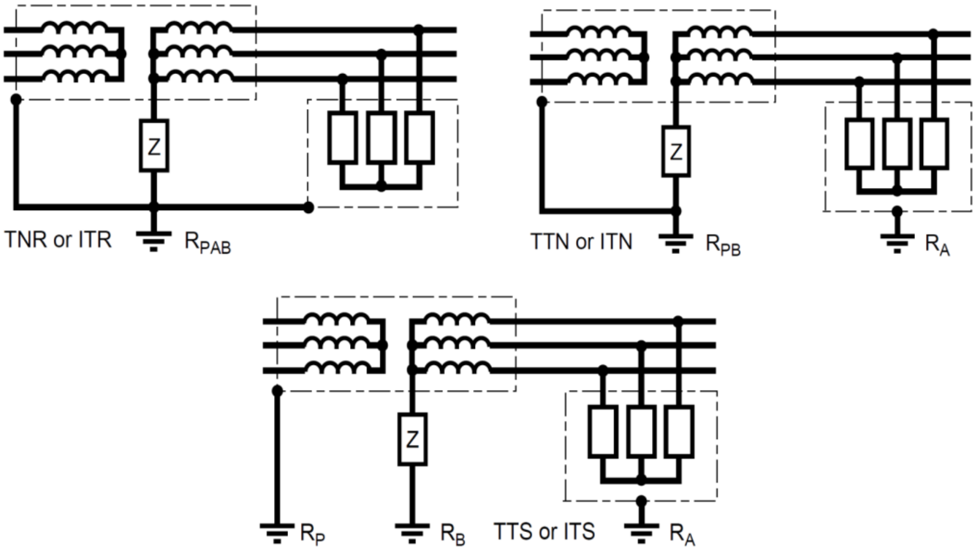

*Figure 1-17 Different ground connections of the substation frames and LV neutral [48].*

Each of these different grounding connections can impact the noise termination high-frequency impedance and, consequently, the conducted emissions levels.

### 1.3.1 Characteristics of Grounding Systems

Although all grounding systems, demonstrated in Figure 1-16, offer the same level of protection of persons against indirect contact, they have different features and thus are used depending on the necessities and local standards. For example, in France, the TN system is forbidden in mines and quarries, and the IT system is mandatory in hospitals, operating theaters, and wherever safety circuits subject to the workers' protection decree, such as emergency exit lighting, are mandated. Furthermore, legal restrictions prevent the use of TN-C in buildings that may present a risk of explosion [49]. In the following sections, we explore the characteristics of each of these grounding systems.

#### 1.3.1.1 TT

The TT system is widely recognized as the simplest solution to design and install, and thus, it is recommended in facilities with more frequent modifications and upgrades. In TT systems, as depicted in Figure 1-18, in the presence of an insulation fault, the resistance of ground connections ($R_a$ and $R_b$) are the primary factor limiting fault current (5A < $I_d$ < 50A) [48]. Therefore, the fire hazard in the TT system is less than in TN and higher than in IT. The fault voltage ($U_d$) that appears on the application's frame is around half of the nominal phase-to-neutral voltage ($U_0$), as the resistance of both grounding connections is typically low and of the same order of magnitude. Hence, this voltage in both single-phase and three-phase networks (230/400 V) is deemed unsafe as it surpasses the permissible limit, even in dry atmospheric conditions (50V for 1000 Ω human body, which is for a bare foot to hand contact based on IEC 479-1 [50]) and thus the first insulation fault will trigger a network shutdown. However, it can be limited locally to the faulty circuit by using multiple selective Residual Current Devices (RCDs) in series or parallel [47].

Regarding the installation, unlike other systems that have interconnected ground connections, the TT system needs a minimum of two separate grounding connections, and consequently, it ranks lowest in terms of ground lightning immunity performance, as there could be discrepancies in voltage surges on each grounding connection. The use of RCDs is necessary, but unlike the IT system, it does not require continuous monitoring during operation (only periodic checking of RCDs may be necessary).

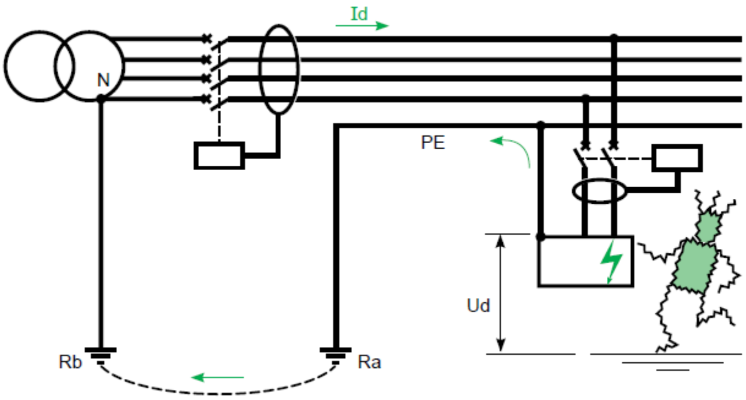

*Figure 1-18 First isolation fault in the TT system [48].*

#### 1.3.1.2 TN

The TN system allows for cost savings in the installation process by removing the need for a switchgear pole and a conductor (in TN-C). However, when an insulation fault occurs, as demonstrated in Figure 1-19, since the current limiting factors are only the resistances of the conductors, the magnitude of the fault current is high ($1\text{kA} < I_d < 100\text{kA}$) and can lead to greater damage to the installation, such as deterioration in the windings of rotating machines [47]. As the insulation fault current magnitude is similar to that of a phase-neutral short-circuit in this case, breaking can be accomplished by the Short-Circuit Protection Device (SCPD), and as long as the specified breaking time is respected, RCDs are unnecessary.

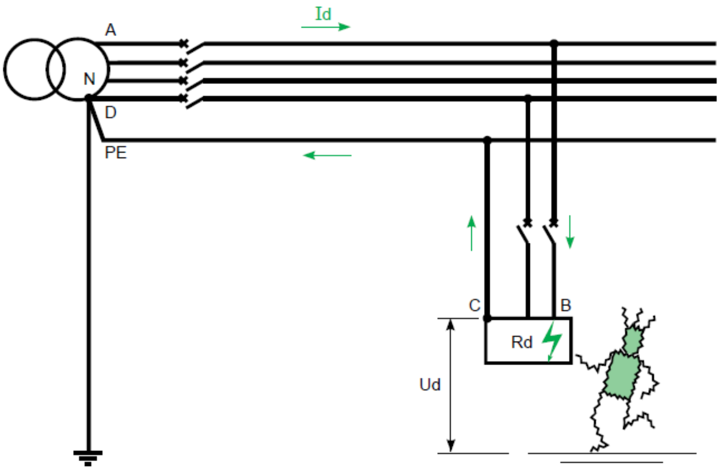

*Figure 1-19 First isolation fault in the TN system [48].*

#### 1.3.1.3 IT

In regular operation (in the absence of insulation failures), the network is connected to the ground through its leakage impedance. In the event of an insulation fault, Figure 1-20-a, the fault current is equal to some of the leakage currents ( $I_d < 1$A), and since the fault voltage is low, it poses no danger, and the installation can remain in operation. In this case, the Insulation Monitoring Device (IMD), which is obligatory in the IT system and permanently monitors the insulation resistance to ground by injecting a DC current between them, will signal the first insulation fault. Once the failure is reported, it is crucial to promptly detect and remove it before a second fault occurs in order to systematically prevent any disruptions in power supply. Otherwise, the second insulation fault, whose impact depends on the conductor involved in the fault, can be a short-circuit, and the danger of electric shock is equivalent to that observed in the TN system, see Figure 1-20-b.

The IT system is the most reliable in terms of service continuity, making it the preferred choice in database applications. Nevertheless, the maintenance process requires vigilant monitoring to prevent a potential shutdown caused by a second isolation fault.

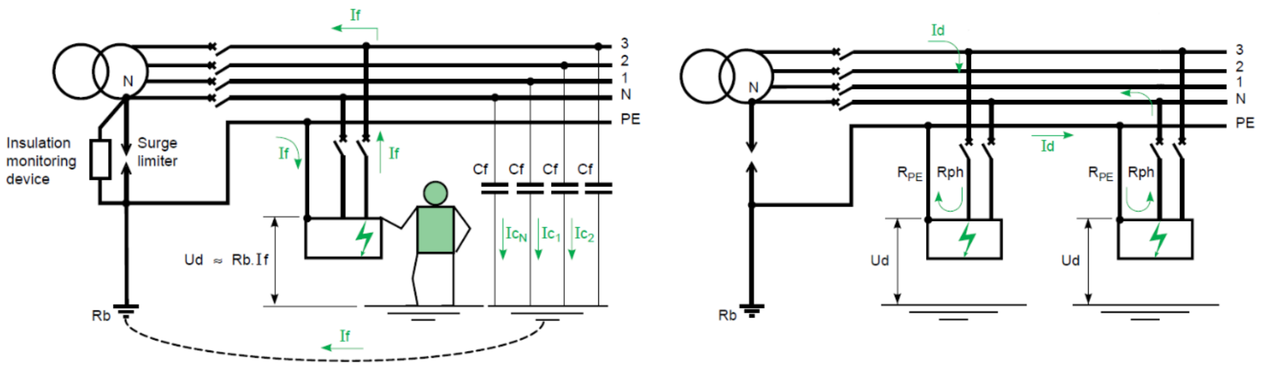

(a) (b)

*Figure 1-20 (a) First isolation fault and (b) Second isolation fault in the IT system [48].*

### 1.3.2 Installation of Grounding Systems

Regarding the installation of grounding connections, there are various types available depending on many factors, such as the site's ground condition (soil nature, soil moisture, etc.). The purpose of the ground termination connection is to provide a low LF impedance pathway for both electrical faults and lightning discharge currents to safely dissipate into the ground. The main types of earthing electrodes are:

- solid copper earth plates, loops, or lattice mats, which are considered the preferred solution for new constructions and must be in contact with the iron framework of the building foundation;

- solid or copper-bonded earth rods, which is specifically for buildings that already exist or even to enhance the existing grounding connection.

While numerous standards specify a maximum allowable DC resistance (or LF impedance) for any type of grounding connection installation, the AC resistance can still exceed this limit depending on the type of installation due to skin and proximity effects, especially in the EMC concerned frequency range.

On the other hand, as depicted in Figure 1-21, there are many EMC recommendations regarding cable management in facilities, such as duct size and shape or separation of bundles either by shielding or by placing the cables in separate ducts, etc., although adherence to these guidelines is not compulsory. As in most cases, the cables are not shielded, their HF behavior heavily relies on whether or not they respect the mentioned recommended actions.

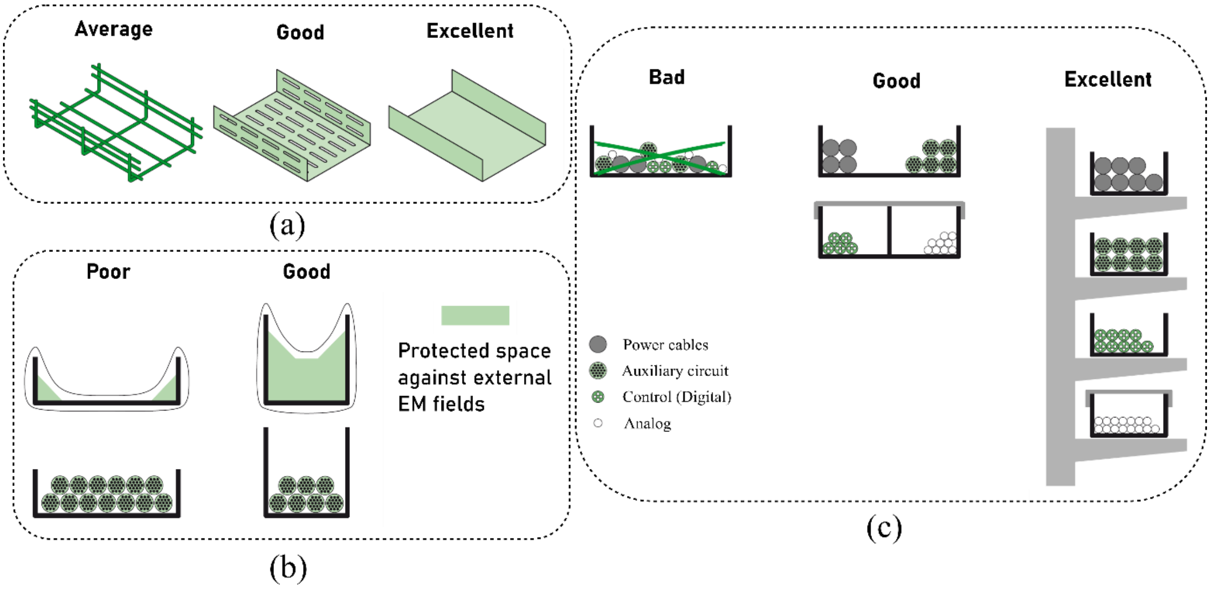

*Figure 1-21 Some of EMC guidelines regarding cable management [47].*

### 1.3.3 Electric Power Systems Across the Globe

The development of these different LV grounding systems has been the result of a long and continuous search for enhanced personnel protection and elimination of the danger of electric shock or electrocution for individuals. The main objectives have been regulating the electrical potential between live conductors and the ground during standard operation, restricting voltage between electrical equipment frames and the ground, installing safety mechanisms, limiting rises in potential due to MV faults, and increasing continuity of service and availability of electrical power [51].

In public and industrial MV, unless under certain special conditions, the neutral and the protective conductor (PE) is not distributed between substations or between a substation and the MV load. Many countries require the substation (MV/LV transformer frame) and LV neutral to have distinct ground connections (TTS or ITS) except if the ground connection resistance is very low (less than 1 Ω). However, in a few countries, such as the USA, the ground connections of the MV/LV substation and LV neutral are always linked.

LV networks and loads are grounded in all industrialized countries. Table 1-4 gathers the most common LV grounding systems across the world. The data presented in this table indicates that TN is predominantly utilized in Anglo-Saxon countries, while the TT system is more commonly employed in other parts of the world. A select few countries, notably Norway, opt for the IT system.

*Table 1-4 Public distribution examples worldwide - LV earthing systems [51].*

| **Country** | **LV grounding system** | |
|---|---|---|
| **France** | 230/400 V | TT |
| **Great Britain** | 240/415 V | TT (Rural areas)<br>TN (Town areas) |
| **USA** | 120/240 V | TN-C |
| **Germany** | 230/400 V | TT and TN (more common) |
| **Norway** | 230/400 V | IT |
| **Spain** | 230/400 V | TT |
| **Italy** | 230/400 V | TT |
| **Japan** | 100/200 V | TT |
| **Belgium** | 230/400 V | TT |

Electric vehicle charging installations can have different grounding systems as well, depending on the country they are located. Local standards in many countries define a set of rules for EV charging points. For example, in the UK, the BS 7671 standard prevents a Protective Multiple Earthing (PME) system, which is similar to a TN-C-S system with a PEN conductor tied down to the ground at several points along its route, from being used as earthing for a charging point located outdoors. Moreover, in a PME system, the same standard mandates additional protection based on voltage monitoring, which must be installed if there is no local grounding electrode [52].

## 1.4 Conclusion

This first chapter, serving as the contextual and introductory framework, allowed us firstly to show the importance of the OBC development through the growth of EVs in the transportation sector and also to situate the studied OBC prototype between the different charging systems.

The problematic side of using an LISN in the standard method of conducted emissions measurements, which is this thesis's primary focus, has been addressed in the first chapter. In the second chapter, we will explore this issue by first verifying the HF impedance deviation using the Two-Probe (TP) technique and then showing how conducted emission and the volume of the EMC filter required for limiting these emissions will be affected in a case study when the impedance of the LISN that is not representative of the power supply impedance.

Analyzing the impact of grounding systems on conducted emissions levels when an LISN is not included is necessary because, although all grounding systems offer users a certain level of safety, they have different traits regarding EMC as each of these systems defines a distinct path for CM and DM currents with a distinct HF propagation impedance which also significantly varies from LF impedance of the system. Our focus will shift to this subject in the third chapter, along with the "Black box" modeling of the prototype in order to anticipate its behavior in all types of grids with different parameters and with the presence of other loads.

# CHAPTER 2

# Impact of Standardized Method of Conducted EMI Measurement on EMC Filters Volume

This chapter focuses on the quantitative assessment of volume variations in an EMC filter under diverse scenarios. Specifically, the investigation addresses variations resulting from the presence or absence of an LISN in the measurement setup, as well as those due to the adjustment of EMC standards stringency. In order to conduct this analysis, in the first part of this chapter, a methodology is developed for measuring the HF impedance of the noise termination in the absence of the LISN, providing an understanding of the HF characteristics of any type of power supply, especially the distribution grid impedance. Subsequently, an algorithm was developed to design a performant EMC filter optimized for volume. By employing these two methodologies, this chapter effectively demonstrates the variations in EMC filter volume across different testing scenarios, thereby contributing to the broader comprehension of EMC filter performance in real-world applications.

## 2.1 Power Supply HF Impedance Measurement During Operation

In the absence of the LISN, the termination impedance for noise changes to the high-frequency impedance of the power supply, which is the AC grid in the case of an OBC. Given the variability of this impedance across different sites, depending on the characteristics of the local power grid and connected loads in the vicinity, it becomes critical to establish a reliable method for its measurement.

The initial part of this chapter is dedicated to a comprehensive exploration of methodologies employed for grid impedance measurement. Subsequently, we introduce and expound upon the characteristics and implementation aspects of the Two-Probe (TP) method, which has been used multiple times in different stages of this thesis.

### 2.1.1 State of Art on Grid Impedance Measurement Techniques

Carrying out the measurement of the grid impedance without galvanic isolation and with a direct electrical connection, also called direct measurement, poses challenges due to the sensitivity of impedance measuring instruments to high-voltage conditions, such as impedance analyzers and vector network analyzers that are designed for off-state impedance measurement. Therefore, these instruments cannot be utilized for on-state or on-line measurements under nominal voltage. However, such instruments remain valuable for comparison purposes to assess the accuracy of techniques capable of both on-state and off-state impedance measurements.

In this section, we will succinctly compare and analyze the characteristics of different methods employed in the current state of the art for grid impedance measurement. Impedance measurement methods can be classified in many ways, considering different criteria. In our study, one important aspect is the maximum frequency a method can reach, as well as its precision, which is a crucial criterion due to the impact of measurement band-width on the accuracy level. Therefore, studied impedance measurement methods are divided into three main categories based on their frequency capabilities: low-frequency methods (under 10 kHz), medium-frequency methods (up to 500 kHz), and high-frequency methods (up to 100 MHz).

#### 2.1.1.1 Low-frequency methods

Online low-frequency impedance data are commonly utilized to ensure compliance with anti-islanding standard regulations (e.g., IEEE1574, IEEE929, and VDE0126) and for adaptive control of grid-connected converters, particularly in distributed renewable energy resources.

Generally, within the scope of grid impedance measurement approaches, the current state of the art categorizes methods into two principal classifications: passive or noninvasive and active or invasive. The former primarily uses pre-existing non-characteristic signals within the system and is limited to frequencies below 2 kHz [53]. Nonetheless, in many cases, the measurement of these background distortions becomes challenging or unfeasible due to insufficient amplitude or repetition rate, thus failing to provide an acceptable Signal-to-Noise Ratio (SNR).

In contrast, active methods deliberately introduce disturbances into the power supply network, subsequently followed by acquisition and signal processing procedures. For frequencies higher than 2 kHz these invasive methods represent the sole viable solution.

Various approaches exist for perturbing the network; thus, active methods can be divided into two major categories as well: transient methods and steady-state methods. Steady-state methods typically inject a periodically known distortion into the network and then make the analyses in the steady-state period as can be seen in [54], [55], [56], [57].

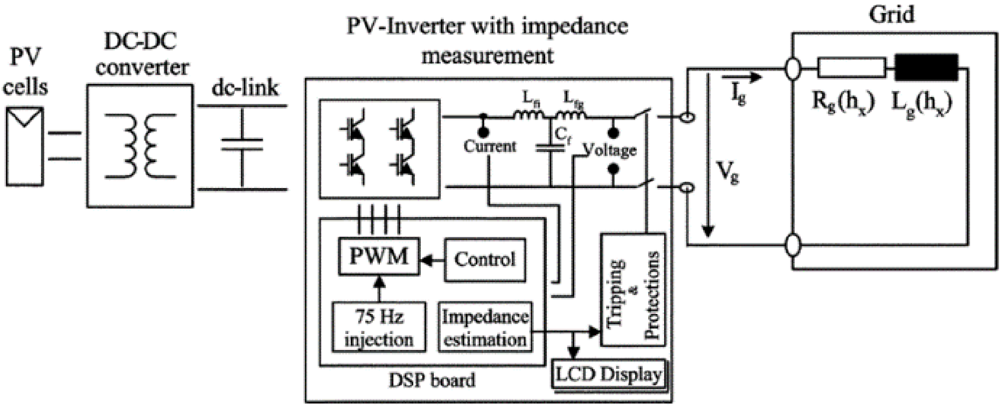

*Figure 2-1 Principle diagram of the PV-inverter that includes the grid impedance measuring method [54].*

In transient methods, as its name suggests, a transient current spike will be injected into the network (e.g., a resistive short-circuit), and then the grid voltage and current will be measured at two different time instants, before and after the impulse occurrence. The impulse will provide a wide harmonic spectrum that, afterward, should be analyzed to calculate the impedance [55]. However, transient methods are not popular due to their main drawback, which is concerns about exceeding system ratings.

#### 2.1.1.2 Medium-frequency methods

Medium-frequency methods are generally used in the analysis of access impedance for Narrowband Power Line Communication (NB-PLC) channels. In [58], three different active methods in this range of frequency have been reviewed. The first method was developed by the Institute of Systems Engineering at HES-SO Valais-Wallis (also called IGOR-Meter) and, while being expensive, has the capacity to measure very low-level signal levels, even in a noisy environment; the second one was developed by the University of the Basque Country (UPV/EHU) which is portable, inexpensive and based on commercial devices, and the last one is proposed by Dresden University of Technology (TUD) which has better low-frequency range performance.

Although all these methods have the same concept, which is the active perturbation of the grid, they propose distinct setups and signal processing units, resulting in varying features and functionalities. Table 2-1 presents a brief comparison between their main features.

*Table 2-1 Summary of the main characteristics of the medium-frequency methods.*

| | **HES-SO** (Haute École Spécialisée de Suisse Occidentale) | **UPV/EHU** (University of the Basque Country) | **TUD** (Technische Universität Dresden) |
|---|---|---|---|
| **Frequency range** | 9 kHz – 500 kHz | 20 kHz – 500 kHz | DC to 200 kHz |
| **Coupling to grid** | Direct connection | Via capacitive coupler | Direct connection |
| **Other features** | • No need for mains synchronization<br>• Measure On-line grid and equipment impedances<br>• Plugged | • No need for mains synchronization<br>• Fast measurement (a few seconds)<br>• Battery powered | • Synchronized to mains<br>• Direct connection to the grid<br>• Plugged |

#### 2.1.1.3 High-frequency methods

In our study, the designated frequency range of interest spans from 150 kHz to 30 MHz, aligning with the frequency range specified for conducted emission requirements across EMC standards, with the exception of CISPR25. Consequently, our study primarily focuses on high-frequency methods due to their relevance within the specified frequency range of interest. However, it is crucial to acknowledge the importance of investigating the frequency band between 10 kHz and 150 kHz as well. Since the phenomena observed in the EMC frequency range of interest often stem from the continuity of effects of phenomena occurring in the previous decade band.

An approach for the measurement of the grid access impedance in Broadband Power Line Communications (BB-CLP) Mode 1 (2 MHz to 7 MHz) is proposed by [59]. This method relies on simultaneously measuring the voltage and current generated by a signal generator introduced into the grid within the frequency range under test, which is from 20 kHz to 10 MHz, as demonstrated in Figure 2-2.

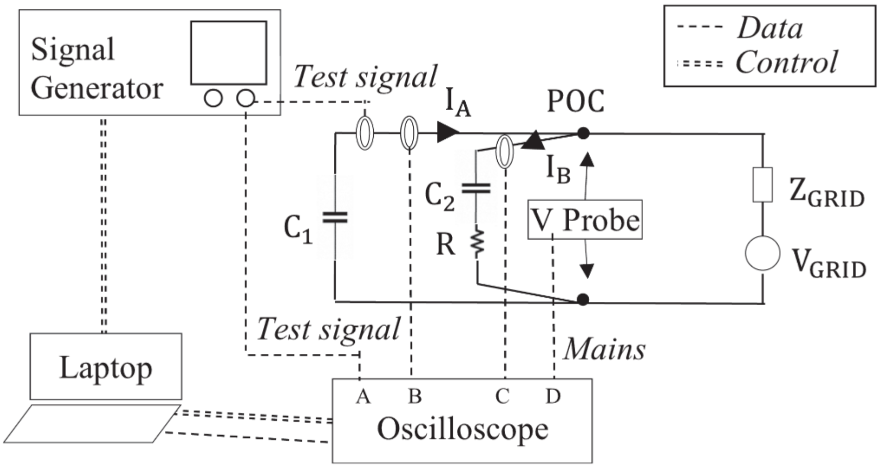

*Figure 2-2 Measurement setup for characterizing the electrical grid impedance proposed by [59].*

The post-processing analysis of the recorded data in this method, using Fourier analysis implemented in MATLAB, enables the spectral characterization of the voltage, current, and grid impedance complex values, providing both amplitude and phase or real and imaginary components. However, the frequency span offered by this method covers only part of the frequency range concerned by EMC standards. Moreover, synchronization between the signal generator and the oscilloscope makes the post-processing task challenging.

Another method for measuring a load impedance under its normal operating condition (when connected to the power supply) is proposed by [60], called the Two-Probe (TP) measurement approach. This method utilizes an injection and a monitoring clamp-on current probe and a Vector Network Analyzer (VNA) as both the source of the introduced perturbation and the receiver. The fundamental setup for measuring the unknown impedance $Z_x$ within a closed circuit that has the potential to carry both high voltage and high current is illustrated in Figure 2-3 (a). This setup entails a VNA and two probes, an injecting current probe and a receiving current probe, that are coupled to the circuit via inductive couplings, avoiding direct connection to the loop.

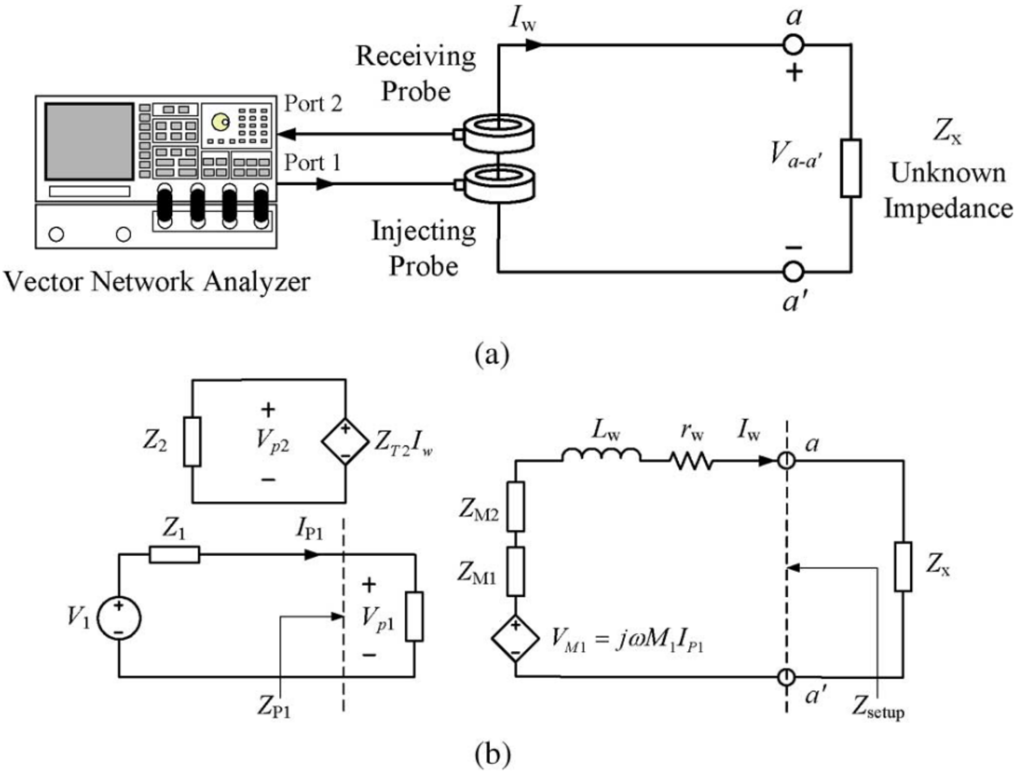

*Figure 2-3* *(a) Conceptual two-probe in-circuit measurement setup; (b) Equivalent circuit of the measurement setup [60].*

Figure 2-3 (b) presents the equivalent circuit of the setup, where $Z_{M1}$ and $Z_{M2}$ denote the equivalent impedances of the injecting and receiving probes, respectively. For example, $Z_{M2}$ consists of a small insertion resistance and a reduction in inductance. The latter happens because the secondary ampere-turns cancel the magnetic flux generated by the primary current in the space occupied by the magnetic core; thus, less flux links the circuit than when the current monitor is not present. $V_{M1}$ represents the induced signal voltage in the circuit loop from port 1 of the VNA through the injecting probe. The loop wire variables, namely the loop inductance and resistance denoted by $L_w$ and $r_w$, respectively, must be reduced to the minimum extent possible in order to achieve a higher level of precision. Based on [60], $Z_{setup}$ is defined as the sum of all impedances in the loop except the unknown impedance, and therefore, by writing Kirchhoff's voltage law in the main loop, we will have:

$$\boldsymbol{V_{M1}=(Z_{M1}+Z_{M2}+r_w+j\omega L_w+Z_x)\ I_w=\left(Z_{setup}+Z_x\right)\ I_w} \tag{2-1}$$

On the other hand, the induced voltage can be written as:

$$\boldsymbol{V_{M1}=\left(j\omega M_1\right)\ I_{p1}} \tag{2-2}$$

where $M_1$ is the mutual inductance between the injecting probe and the coupling loop. By applying Kirchhoff's voltage law to the bottom loop, which is associated with the injecting probe, the following equation is obtained:

$$\boldsymbol{I_{P1}=\left(\frac{V_1}{Z_{p1}+Z_1}\right)=\frac{V_{p1}}{Z_{p1}}} \tag{2-3}$$

$V_1$ and $Z_1$ represent VNA port one's Thévenin equivalent voltage source and impedance, respectively, and $Z_{p1}$ is the input impedance of the injecting probe. By replacing Equation 2-3 in Equation 2-2 we will have:

$$\boldsymbol{V_{M1}=j\omega M_1\frac{V_{p1}}{Z_{p1}}} \tag{2-4}$$

The received signal at port 2 of the VNA depends on the $I_w$ current measured by the current monitor and its transfer impedance ($Z_{T2}$); thus, the $I_w$ can be expressed as:

$$\boldsymbol{I_w=\frac{V_{p2}}{Z_{T2}}} \tag{2-5}$$

Finally, by substituting Equations 2-4 and *2-5* into Equation 2-1, the unknown impedance to be measured can be calculated as follows:

$$\boldsymbol{Z_x=K\left(\frac{V_{p1}}{V_{p2}}\right)-Z_{setup}} \tag{2-6}$$

where $K$ is a coefficient depending on the probes' parameters and the frequency given by:

$$\boldsymbol{K = \frac{j\omega M_1 Z_{T2}}{Z_{p1}}} \tag{2-7}$$

and, as presented in Appendix A, the ratio between the voltages can be determined by scattering parameters obtained from the VNA:

$$\boldsymbol{\frac{V_{p1}}{V_{p2}} = \frac{1 + S_{11}}{S_{21}}} \tag{2-8}$$

A premeasurement calibration procedure for this technique is also proposed in [61] to obtain *K* and $Z_{setup}$ that consists of measuring two known impedances and is easy to apply. On the other hand, [62] introduced another calibration by suggesting a three-port network pre-calibration, which claimed to extend the highest measurement frequency; however, it necessitates a VNA equipped with a minimum of three ports, and it also increases the complexity of the data processing step.

An improved version is proposed by [63], adding an RF amplifier in addition to an attenuator to improve the SNR and protect the VNA against overvoltage. Figure 2-4 illustrates the modified setup aimed at achieving a higher SNR.

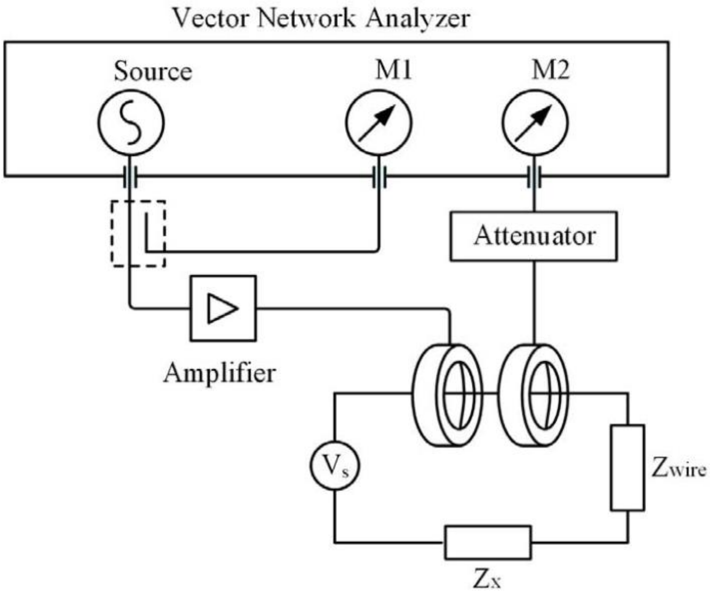

*Figure 2-4 The setup for improved version of two-probe method proposed by [63].*

The two-probe technique later has been used for DM and CM grid impedance measurements by [64] in the EMC context due to its capacity to obtain information on both amplitude and phase of the impedance up to 100 MHz, covering the EMC frequency range of interest, depending on the setup and impedance amplitude order of the load.

This approach offers the capability to attain results at high frequencies with an acceptable margin of error facilitated by the use of a VNA. Moreover, it has an uncomplicated calibration process, thus streamlining the measurement procedure.

A comparison between the two introduced HF impedance measurement methods is presented in Table 2-2.

*Table 2-2 Summary of the main characteristics of the high-frequency methods.*

| | **Two-Probe Method** | **Method Proposed by [59]** |
|---|---|---|
| **Frequency Range** | 100 kHz – 30 MHz | 20 kHz to 10 MHz |
| **Other Features** | • Using a VNA that simplifies the process with more accuracy<br>• Utilizes two probes<br>• LF limitation due to the VNA | • Using a signal generator, laptop, and oscilloscope that adds more complexity<br>• Utilizes four probes<br>• Offers improved LF performance. |

#### 2.1.1.4 Conclusion

The preceding sections outlined various methodologies for grid impedance measurement, each carrying its own set of merits and demerits tailored to specific applications. To select a method from the mentioned techniques within the context of EMC, it is essential to note that low-frequency and medium-frequency approaches can be disregarded. Thus, our focus narrows down to high-frequency methods. In pursuit of our objectives, we prioritized criteria such as frequency range and ease of implementation. Based on the aforementioned advantages in Table 2-2, the two-probe method was employed in our study for the measurement of both grid impedance and in-circuit on-state equipment impedance.

In the following section, we will present the implementation of this methodology for the measurement of grid impedance, including insights into our setup configuration.

### 2.1.2 TP Technique Implementation for Grid Impedance Measurement

With the aim of monitoring grid impedance variations in the absence of an LISN in the circuit, the two-probe method has been selected for measuring grid impedance. This method enables the acquisition of both magnitude and phase of impedance without requiring direct electrical contact. The following subsections will delve into the specifics of the test bench setup and the accuracy assessment of this method.

#### 2.1.2.1 Test setup description

The initial step of establishing the test setup for TP impedance measurement technique involved identifying the most suitable pair of probes for our study. To accomplish this, seven injecting and monitoring probes (refer to Appendix B) were characterized, with the setup presented in Figure 2-5 using the Agilent E5061B VNA gain-phase ports. In this arrangement, the equivalent impedance observed from the LF port is set to 50 Ω to match the source impedance. The currents flowing in the two branches are equal. Thus, the voltage of the R port is 50 times the input current of the probe. The T port, on the other hand, represents the output voltage of the probe. Therefore, the transfer function can be determined using the T/R ratio.

$$\boldsymbol{\frac{V_T}{V_R} = \frac{V_{output}}{50\, I_{input}} = \frac{TF}{50}} \tag{2-9}$$

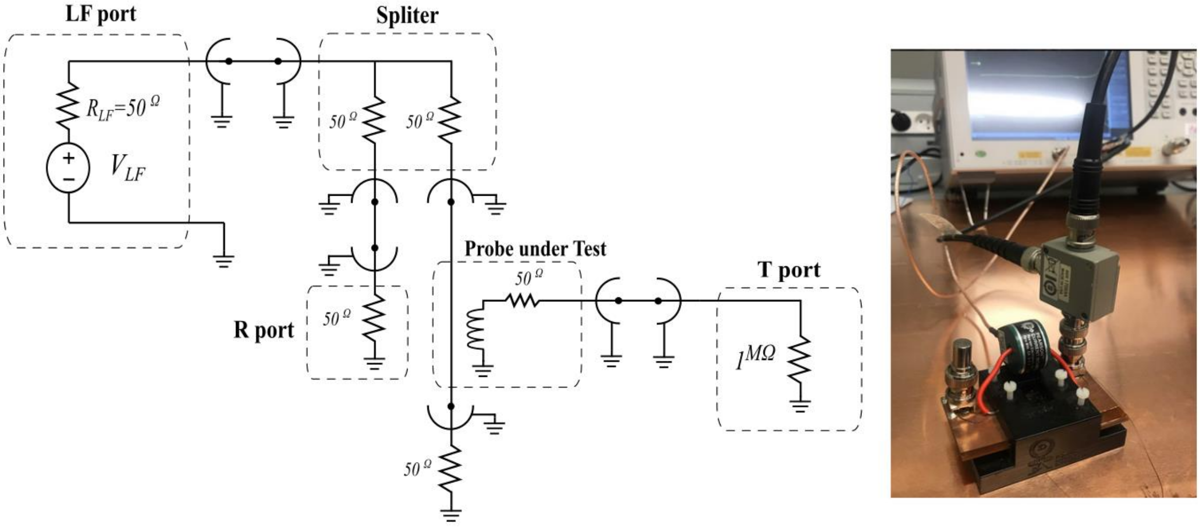

(a) (b)

*Figure 2-5 probes characterization setup.*

Subsequently, multiple measurements were conducted on a known impedance. The selection process was not solely driven by probe performance; other factors like size were also considered. For example, the PRANA Bulk Current Injection (BCI) probe is relatively large, requiring a longer loop length. Consequently, the increased parasitic inductance of the loop wire results in a lower SNR. Finally, the RF BCI probe COM-Power CLCE-400 and the Pearson 2877 current monitor have been selected as the injection and monitoring probes, respectively.

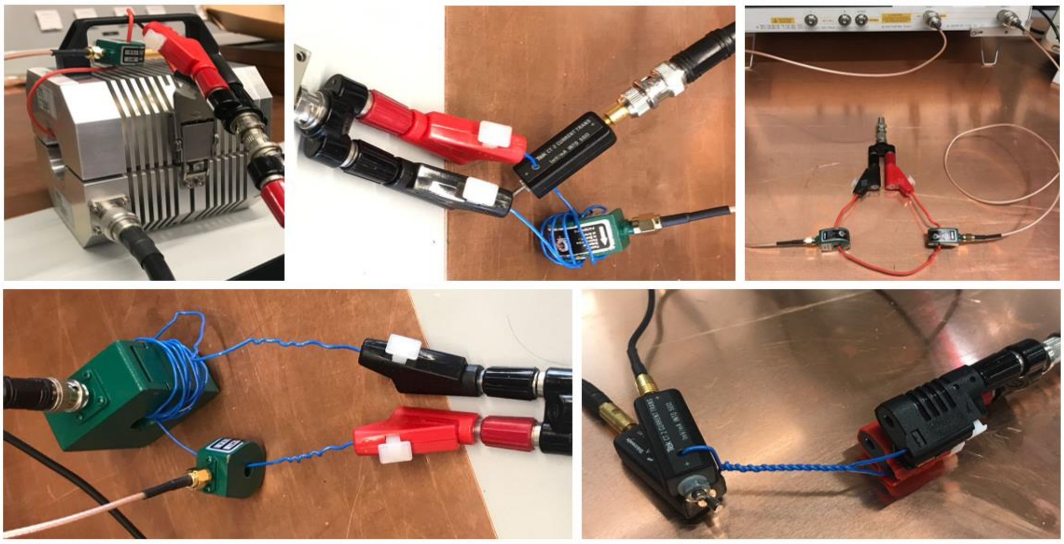

*Figure 2-6 Conducting tests with different pairs of probes to find the most precise pairing.*

The Agilent E5061B VNA, alongside a broadband power amplifier (PRANA DT-70), which provides a constant gain of 48 dB in a wide frequency range (10 kHz – 1000 MHz) that includes our range of interest, was used to extract the S-parameters. Since the output power of VNA is adjustable, the inclusion of an attenuator was not required. Therefore, the output power was configured to ensure that even in short-circuited loop, the maximum power level for the VNA port (20 dBm) would not be exceeded.

The two-probe impedance measurement technique evaluates the loop's impedance, with a notable decrease in SNR as the order of amplitude of the loop's impedance increases. Consequently, as depicted in Figure 2-3-a, when employing the two-probe technique for impedance measurement, it is advantageous to short-circuit the unknown impedance with the shortest wire length possible in order to measure the unknown impedance and the minimized setup impedance. However, when measuring the grid impedance, short-circuiting the grid is clearly not a viable option as it generates a low-frequency current of significant amplitude. Consequently, the challenge lies in effectively limiting LF current while concurrently offering a low-impedance path for HF signals. This can be achieved by employing capacitors as terminations instead of short-circuited terminations. In order to select the most suitable capacitor values for both DM and CM measurement setups, it is crucial to carefully assess the constraints imposed by LF current. These constraints include:

- Maximum allowable induced voltage on the VNA ports: The current flowing within the loop induces a voltage on the VNA ports via clamp probes. In addition to the RF power limit of 20 dBm, there is a voltage limit of 7 V for low-frequency and DC components imposed on the VNA ports to prevent damage to the device.
- Thermal limit: Maximum current is limited by the SCPD, and this restriction is the least stringent.
- Maximum allowable differential current by the RCD: The amount of current allowed to flow to the ground is severely restricted for safety reasons. However, this strict constraint is only applied when measuring the CM impedance.
- Probes saturation: depending on the manufacturer, the maximum current capable of saturating the core of these RF probes can be given directly for a specific low-frequency range, or it may be provided in the form I/F figure parameter that corresponds to the maximum peak of a sine-wave current divided by the frequency. Exceeding this maximum current threshold can cause a waveform distortion.

When conducting DM impedance measurements on the grid, the Pearson current monitor core saturation is the strictest constraint in our case, with an I/F figure of 0.0025 Peak Amperes/Hz.

$$\boldsymbol{I_{sat,peak}} = \mathbf{0.0025}\,\boldsymbol{f} = \mathbf{125\ mA} \qquad 2\text{-}10$$

This means that a peak current of more than 125 mA in 50 Hz can distort the waveform, which corresponds to a capacitor of 1.22 µF considering a 230 V AC grid:

$$\mathbf{C} = \frac{\boldsymbol{I_{sat,peak}}}{\boldsymbol{2\pi f V_{peak}}} = \mathbf{1.22}\ \mu\mathbf{F} \qquad 2\text{-}11$$

In order to avoid the saturation problem, a capacitor with a maximum value of 1.22 µF is needed to limit the DM current. Therefore, to ensure compliance with the constraint and remain well below the threshold, a 0.15 µF capacitor was selected for the DM measurement setup.

For CM measurements on the grid, while similar constraints to those in DM measurements apply, the strictest limitation comes from the differential protection by the RCD. Consequently, the CM current was restricted to less than 1 mA, aligning with the safety protocols within the laboratory with a safety margin.

It is noteworthy to mention that the restriction on the low-frequency fundamental current (50 Hz), as discussed earlier, is specifically relevant in the context of power supply impedance measurement and is not applicable when measuring the in-circuit impedance of equipment in the on-state. In the latter case, the saturation of the probes becomes a more critical constraint for impedance measurements.

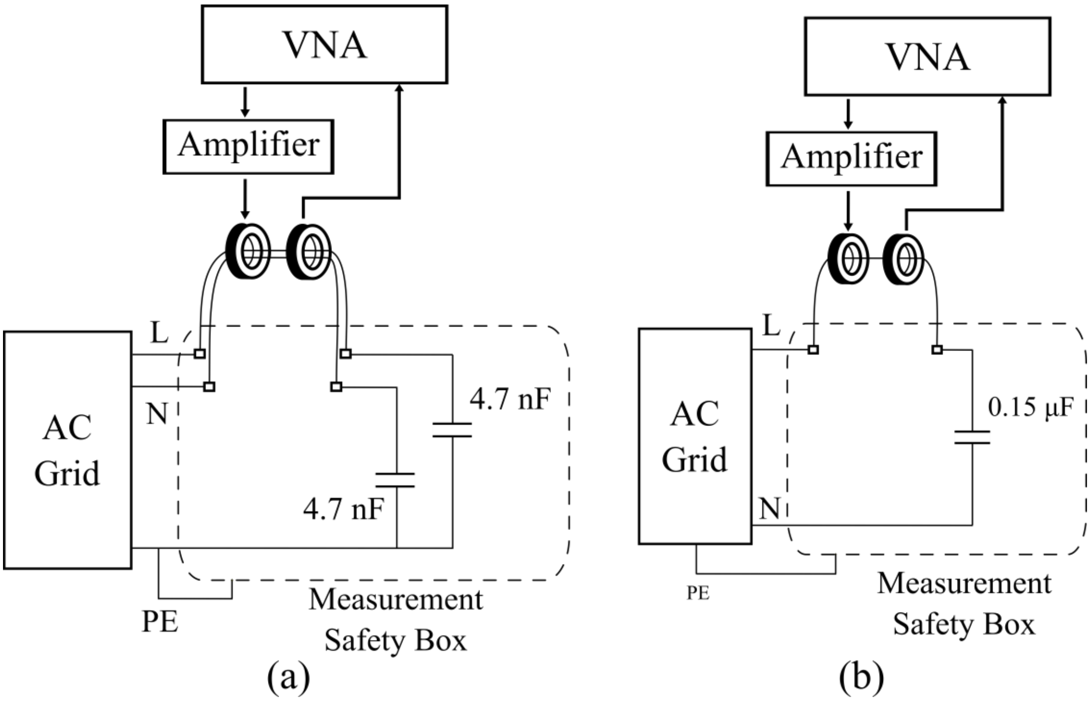

*Figure 2-7 Electrical schematics of the measurement setup: (a) Common-Mode circuit (b) Differential-Mode circuit.*

Figure 2-7 presents the electrical schematics of the measurement setup for DM and CM impedance measurements. A metallic measurement safety box has been made not only for the user’s protection against the grid’s high voltage since it will be connected to the grid but also to fix the probes’ position and help the repeatability of measurements. Two different pairs of ports have been embedded for DM and CM measurement separately and each of them is connected to their related capacitor.

As for calibration, the method proposed by [61] is selected due to its ease of implementation. This global calibration procedure consists of two measurements for each configuration with two known impedances, depending on the expected order of the unknown impedance.

In our case, 50 Ω and short are selected and measured with both configurations, as shown in Figure 2-8. By replacing the *2-8* equation inside the *2-6* equation and doing the two measurements, two following equations are obtained:

$$\boldsymbol{Z_x}|_{\boldsymbol{Z_x=50\Omega}} = \boldsymbol{K}\left(\frac{\boldsymbol{1+S_{11}}}{\boldsymbol{S_{21}}}\right)\Bigg|_{\boldsymbol{Z_x=50\Omega}} - \boldsymbol{Z_{setup}} \qquad 2\text{-}12$$

$$\boldsymbol{Z_x}|_{\boldsymbol{Z_x=\text{short}}} = \boldsymbol{K}\left(\frac{\boldsymbol{1+S_{11}}}{\boldsymbol{S_{21}}}\right)\Bigg|_{\boldsymbol{Z_x=\text{short}}} - \boldsymbol{Z_{setup}} \qquad 2\text{-}13$$

Hence, by solving the *2-12* and *2-13* equations, the setup impedance and the frequency-dependent parameter K can be calculated, as shown in Figure 2-9 for both CM and DM configurations. Once these two parameters are found, we can measure any impedance with the setup.

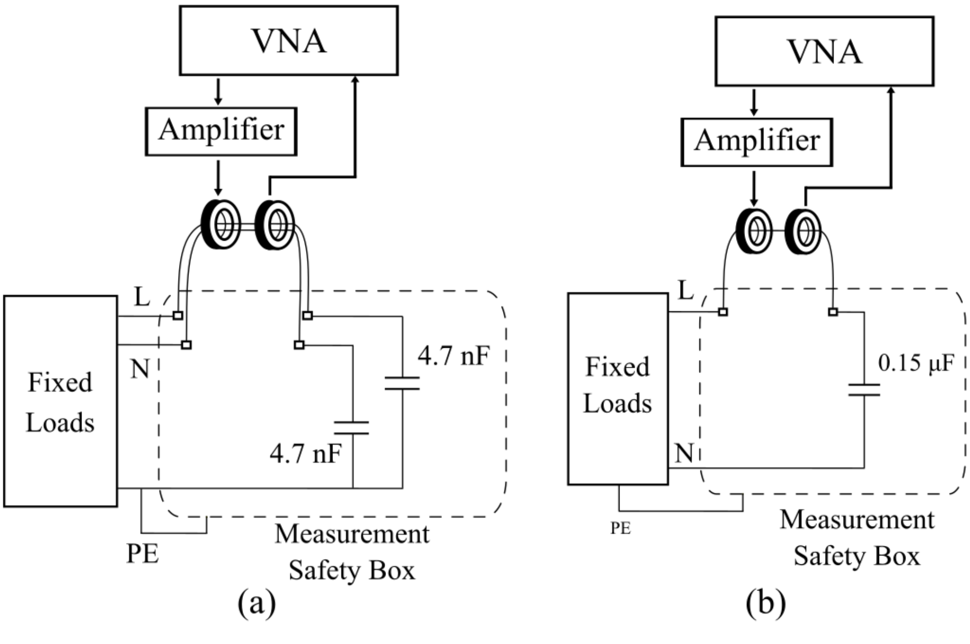

*Figure 2-8 Measurement configuration related to global calibration and accuracy assessment using fixed loads for: (a) Common-Mode circuit (b) Differential-Mode circuit.*

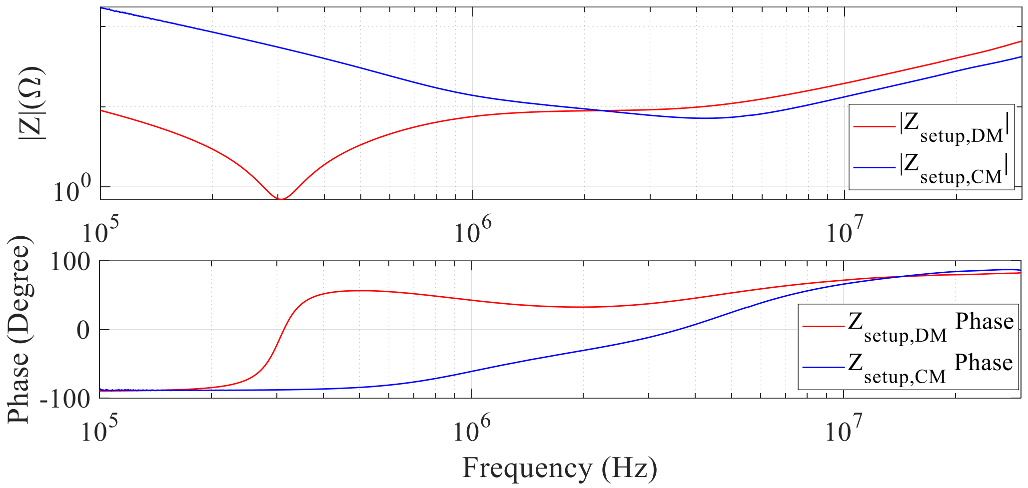

*Figure 2-9 The impedance of the DM and CM setups calculated with global calibration process.*

Finally, the test setup for grid impedance is presented in the Figure 2-10. The subsequent section is dedicated to the evaluation of the accuracy of this method.

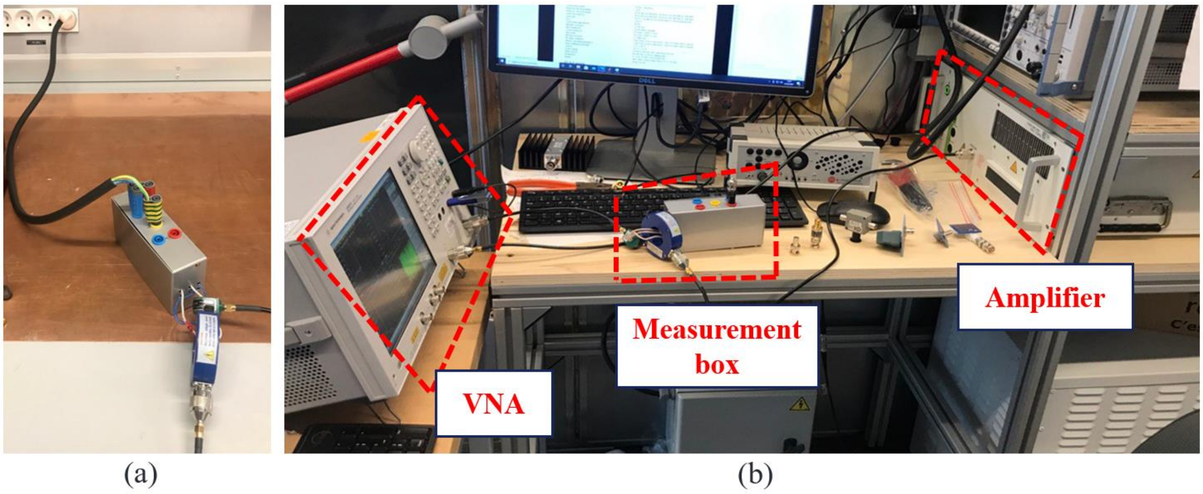

(a) (b)

*Figure 2-10 Grid impedance measurement test bench: (a) on grid, (b) during calibration procedure.*

#### 2.1.2.2 Accuracy of the TP method

The IEC 61557-3 [65] standard determines a maximum measurement uncertainty of ± 30 % for the whole frequency range and for the wide range of impedances expected to be found in the LV grid. These requirements are applicable to equipment for measuring the loop impedance between a line conductor and protective conductor, between a line conductor and neutral, or between two line conductors for the sake of protective measures and electrical safety. In this study, the primary objective of grid impedance measurements is to predict the EMI level. Although not as critical as protective measurements, achieving a high certainty while measuring the in-circuit on-state impedance of equipment can lead to better HF models for the charging environment and more accurate prediction of EM perturbations afterward.

Since the TP method has been employed multiple times throughout this study, it is imperative to assess its accuracy across various frequencies and impedance orders of magnitude. The objective of this section is to provide an error map in an impedance amplitude/phase-frequency plane, which effectively illustrates the accuracy across the plane within the expected frequency range and across different orders of magnitude by showing the approximate error for each region.

In the first step, some known loads included resistances of 3 Ω, 10 Ω, 25 Ω, 100 Ω, 470 Ω, 1000 Ω, and a 100 µH inductor in parallel with a 470 Ω resistance spanning a range of amplitudes expected for grid impedance, were measured using the E4990A impedance analyzer to serve as a reference for assessing the accuracy of the measurements. Each component was soldered onto a PCB and connected to a BNC connector to ensure consistent connection and minimize wiring parasitic inductance. Figure 2-11 presents a comparison between measurement results of the RL load, as an example, obtained using the impedance analyzer and those derived from the TP method in a 22 cm long loop configuration without the limiting capacitors.

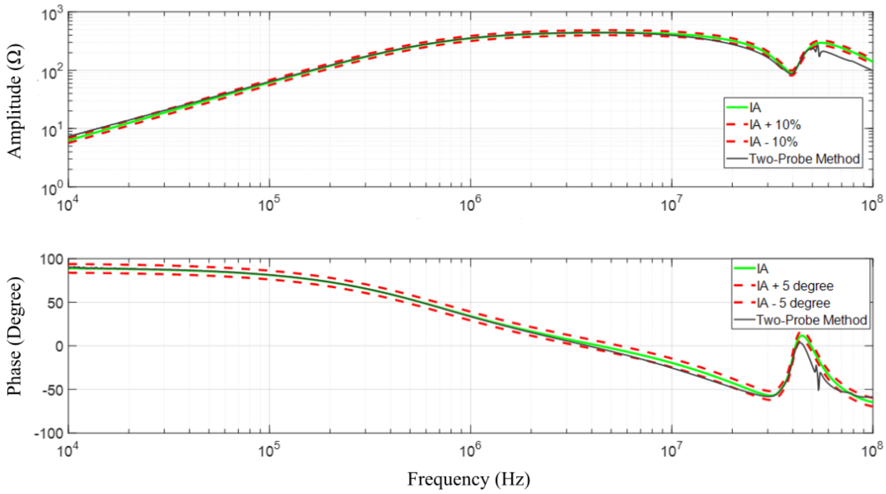

*Figure 2-11 The RL load impedance amplitude and phase comparison between the measured results via TP method and using the E4990A impedance analyzer.*

Since the TP method measures the impedance of the loop, meaning the sum of the unknown impedance and the setup impedance, which can be variable depending on the length of the loop wire and the used LF current limiting capacitor, the accuracy of the measured unknown impedance highly depends on the order of magnitude of the impedance setup.

Therefore, the error maps for CM and DM configurations are different and must be calculated separately.

The accuracy of our version of the TP method with the configuration presented in Figure 2-8 was assessed by comparing the impedance measurement results of the known loads obtained via the TP method in each configuration with those obtained using the impedance analyzer.

To determine the total error for each data point in a configuration, CM setup here, the error of the impedance analyzer, provided by the manufacturer as presented in Figure 2-12, is added as follows:

$$\boldsymbol{Er_{amp,CM,total}}=\left(\frac{|Z_{IA}|-|Z_{VNA,CM}|}{|Z_{IA}|}\right)\times 100+\boldsymbol{Er_{amp,IA}} \qquad \text{2-14}$$

$Er_{amp,IA}$ and $Er_{amp,CM,total}$ denote the amplitude error of the impedance measured by E4990A and the total amplitude error of the impedance measured by the TP approach in CM setup, respectively. Both errors are quantified in percentage units. $Z_{\mathrm{VNA,CM}}$ is calculated from the measured S-parameters using the global calibration with 50 Ω and short terminations.

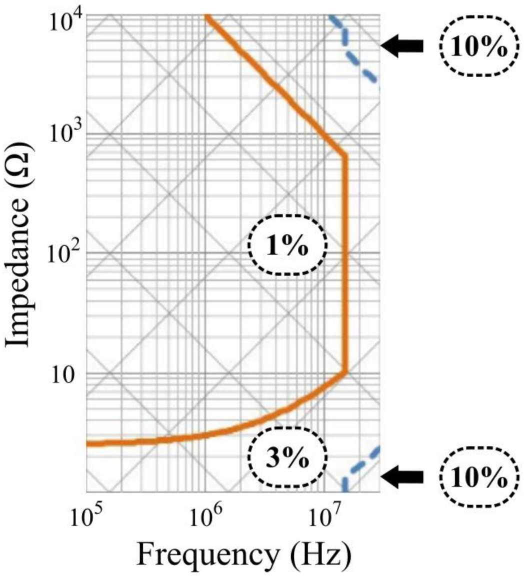

*Figure 2-12 Impedance measurement accuracy at test port of the Keysight 42941A impedance probe connected to the E4990A impedance analyzer [66].*

Similarly, the total error of the amplitude of the measured impedance by the TP approach in the DM setup can be expressed as follows:

$$Er_{amp,DM,total}=\left(\frac{|Z_{IA}|-|Z_{VNA,DM}|}{|Z_{IA}|}\right)\times 100+Er_{amp,IA} \qquad 2\text{-}15$$

After calculating the total error in each data point the error maps are generated by Triangulation-based linear interpolation with $C^0$ continuity as illustrated in Figure 2-13. This can be done for any configuration only by measuring and replacing the $|Z_{VNA}|$ data.

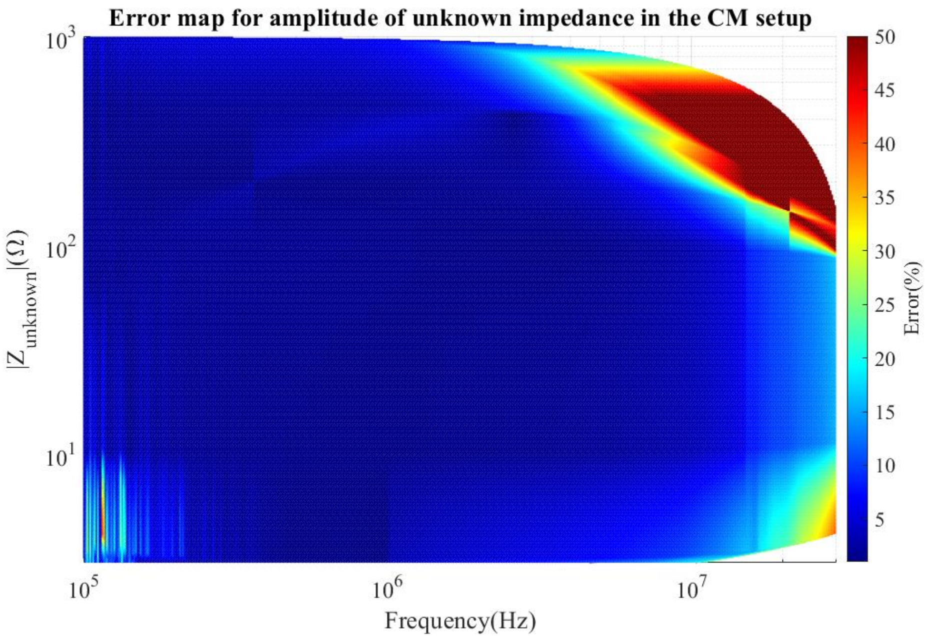

(a)

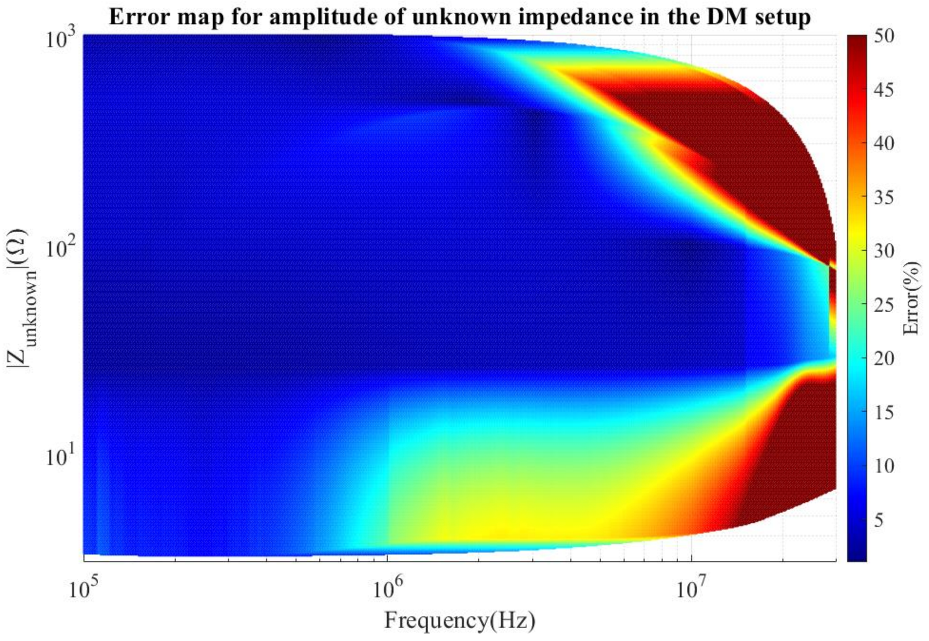

(b)

*Figure 2-13 The error map for amplitude of the measured impedance via TP method (a) in the CM and (b) in the DM configurations.*

The accuracy of the error map can be enhanced by increasing the number of known loads. Therefore, with knowledge about the approximate order of magnitude of the target unknown impedance, the known impedances can be strategically limited.

It is worth noting that the nominal values of selected resistors are valid only at low frequencies; at high frequencies, inductive and capacitive effects play a significant role, and thus, a broader range of impedance values are covered, extending beyond those offered by perfect resistors. In addition to that, the RL load was selected so that it is similar to a typical grid impedance to improve the coverage even at low frequencies.

The error maps indicate that generally, in both very high or low orders of magnitude, as well as at higher frequencies, the error increases, and the performance of the TP approach decreases. The HF performance of this measurement method in the specified configurations is primarily affected by the capacitors' HF behavior, which stems from their imperfections and parasitic elements. At very low orders of magnitude, the unknown impedance becomes negligible compared to the setup impedance. Conversely, at very high orders of magnitude, the signal in the loop becomes highly attenuated, making it difficult to differentiate it from the noise.

However, within the frequency range and magnitude range of the grid impedance, the Two-Probe approach performs adequately and meets the requirements outlined in the IEC 61557-3 across most regions of the plane.

#### 2.1.2.3 LV grid impedance results

Initially, a measurement was conducted using the described setup, with a transformer and auto-transformer implemented as precautionary measures for the initial grid measurement connection. Subsequently, measurements were performed at various locations within the lab premises, including my office and the testing room.

These measurements were iteratively conducted at each location, using Python programming, where a trigger signal was sent to the VNA every 30 minutes to measure the grid impedance and automatically save the data over the course of a day. As anticipated, the results revealed significant variations in both DM and CM impedances from one place to another. However, the fluctuation during the 24-hour period was minimal at a specific location, due to the insignificant change in loads connected nearby, especially during nighttime.

It is anticipated that altering the loads connected to the grid cause variations in the grid impedance. To validate this anticipated impedance fluctuation and find the magnitude of this potential variation, measurements were conducted in the testing room for both CM and DM impedances. Two sets of measurements were performed: one before and one after connecting several loads commonly used during a typical day in the testing room, such as a soldering machine, a drill press, and oscilloscopes.

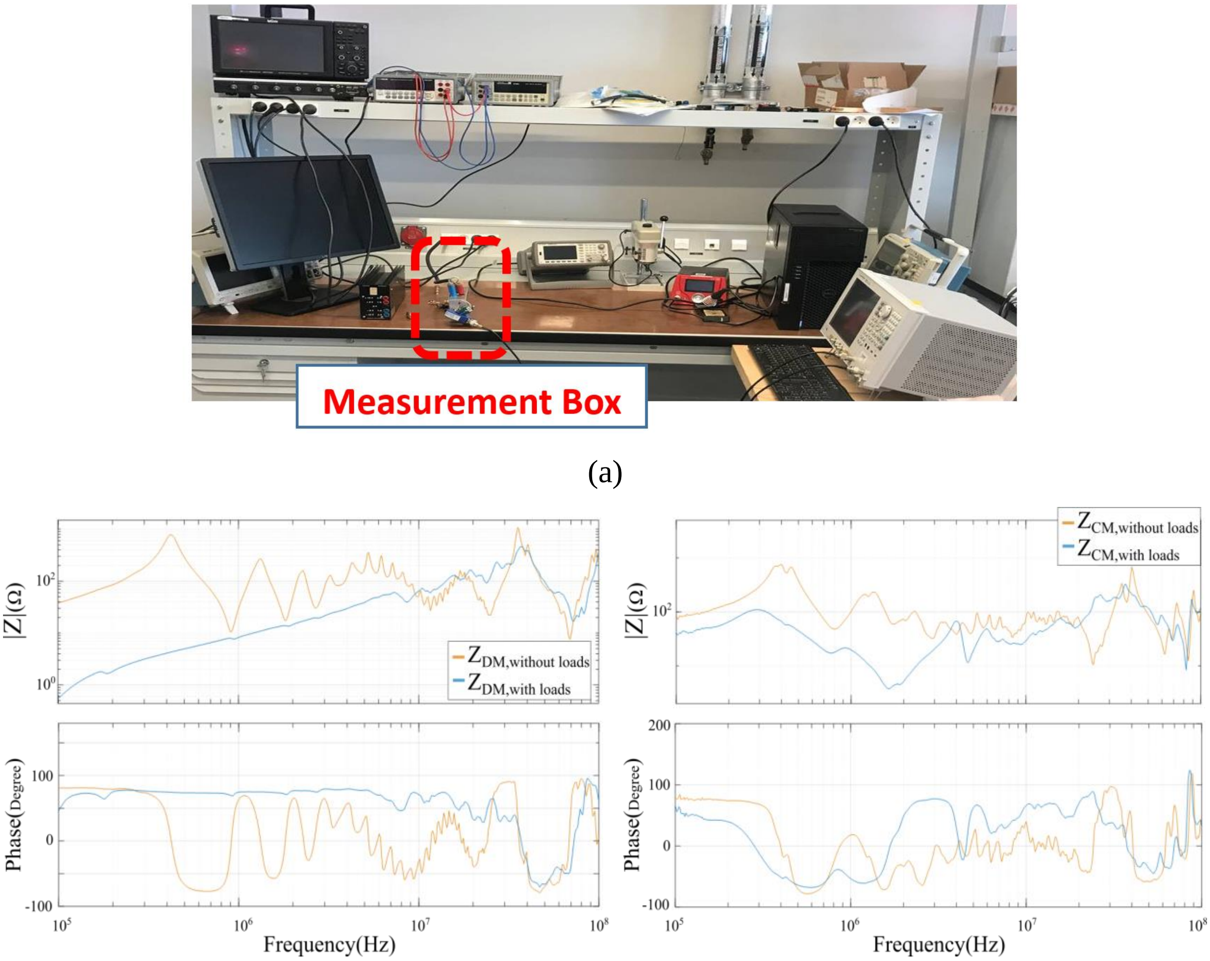

(a)

(b) (c)

*Figure 2-14 Variation of the grid impedance observed at experimentation room in the presence and absence of connected loads (a) measurement setup and loads (b) DM impedance (c) CM impedance.*

The results of impedance measurements at testing room before and after connecting several loads for both CM and DM impedances are presented in Figure 2-14. In the absence of the nearby loads, the resonances observed in measured impedance, especially in DM, closely aligns with the resonances that are signature of cables impedance, indicating their dominance.

Upon adding nearby loads, it becomes evident that the impedance seen from the measurement point is primarily influenced by the impedance of the loads in close proximity. Moreover, at lower frequencies in both CM and DM impedance a more significant impedance difference before and after adding the loads is observed. The general observed trend within both CM and DM impedances indicates as frequency increases the impedance difference between values before and after the load decreases.

This observation led us to consider that the measured impedance results for future experiments involving a particular OBC under test could be affected if someone was working on another bench in the testing room. Consequently, it becomes imperative to establish our own grid-connected microgrid to ensure a controlled experimental environment. Furthermore, it prompted us to consider that when demonstrating the influence of impedance mismatch between the LISN and the grid in an automotive context, it is crucial to observe the impedance fluctuations in real-world scenarios, which means in related grids, such as an EV parking facility, where typical loads (OBCs) are connected and disconnected over a period of time.

In order to monitor the actual HF impedance fluctuations than would be seen by an OBC a 14-day long measurement campaign was launched to extract the HF impedance of the grid at ENS parking facility, which offers 40 designated spots exclusively for EVs each equipped with reinforced Green'up outlet. Due to the setup limitations, the CM and DM impedance measurements cannot be conducted simultaneously. As a result, we divided the measurement campaign, allocating half for DM impedance measurements and the other half for CM impedance measurements.

Measurements were conducted at 15-minute intervals from approximately 8:00 AM to 8:00 PM for both DM and CM impedances using the portable testing bench described at 2.1.2.1 section, as shown in Figure 2-15. These measurements were carried out in a frequency range spanning from 100 kHz to 30 MHz, with an IF bandwidth set to 10 Hz and a measurement time of 159 seconds. The maximum data points possible in the E5061B VNA (1601 points) were utilized. In order to prevent any influence on the parking grid impedance, the testing setup powering plug was connected to another point outside the parking facility using an extension cord reel.

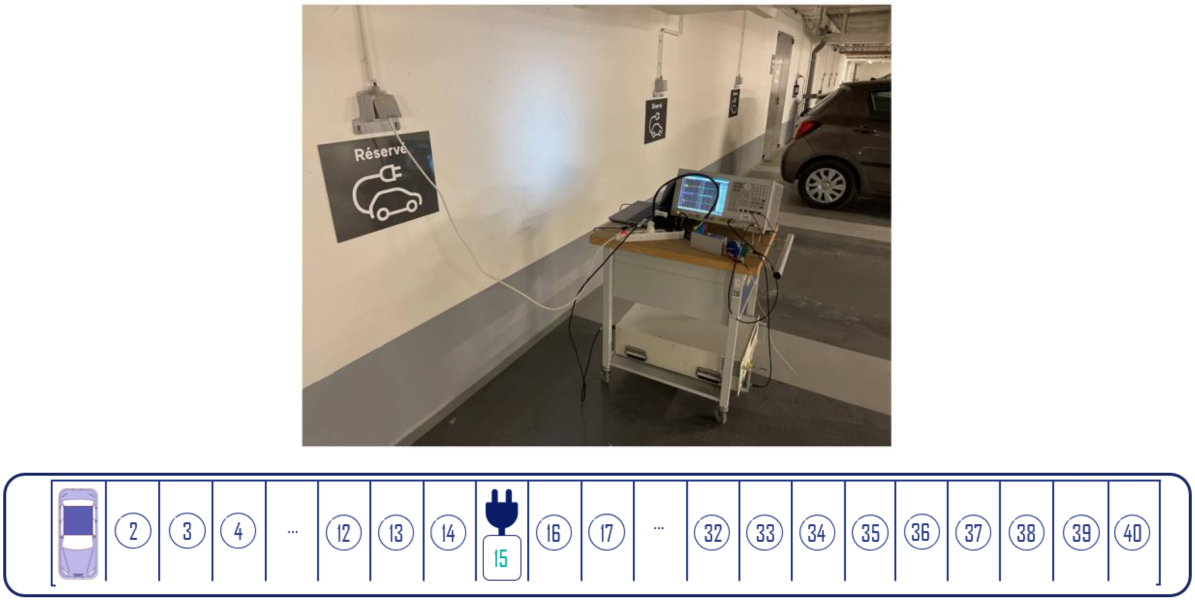

*Figure 2-15 The portable testing bench at the ENS parking facility connected on place #15.*

Figure 2-16 presents the measured results for amplitude and phase of CM impedance measured at place #15, serving as an example, over the course of a day. Notably, significant fluctuations in peak amplitudes are observed, particularly at lower frequencies within the range, alongside discernible shifts in frequency in certain peaks. It is worth mentioning that even at the maximum observed occupancy during the measurement campaign, approximately half of the 40 parking EV outlets were occupied.

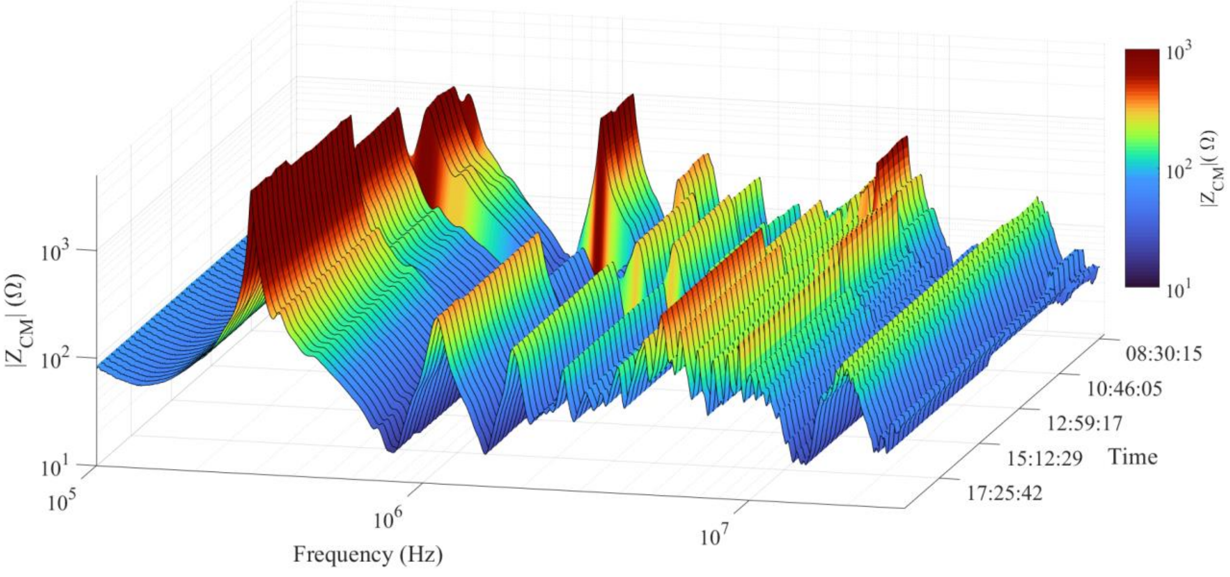

(a)

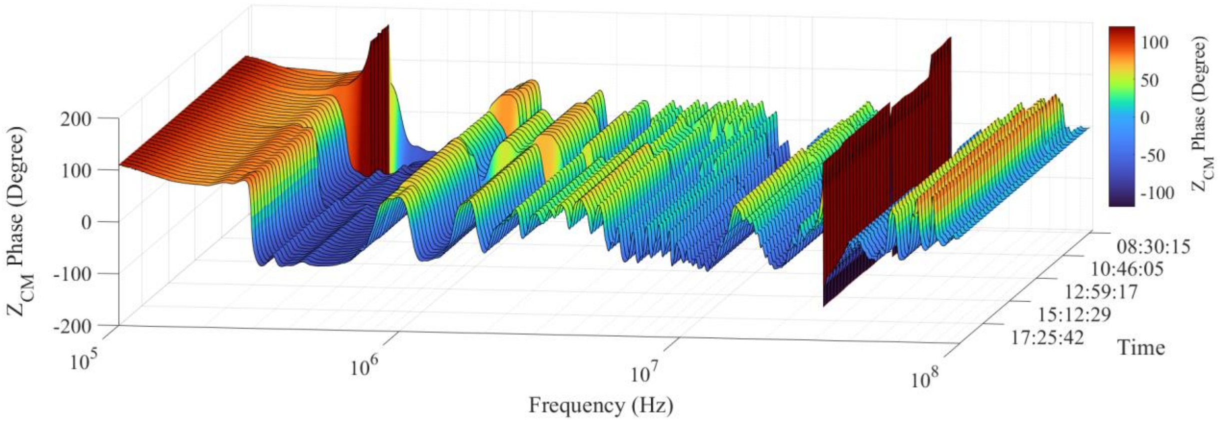

(b)

*Figure 2-16 The CM impedance measured by TP method at ENS parking from place #15 (a) amplitude (b) phase.*

Another sample of the obtained data is presented in Figure 2-17, where two measured grid CM impedances at place #25 at two different times in one day are compared to the CM impedance of the LISN. It is observed that throughout the day, the impedance of the grid can fluctuate depending on the loads connected nearby and it may lead to instances where the grid impedance falls below the LISN impedance, highlighted as the red marked regions. Furthermore, as it can be seen, the frequency range and depth of these red areas changes dynamically throughout the day.

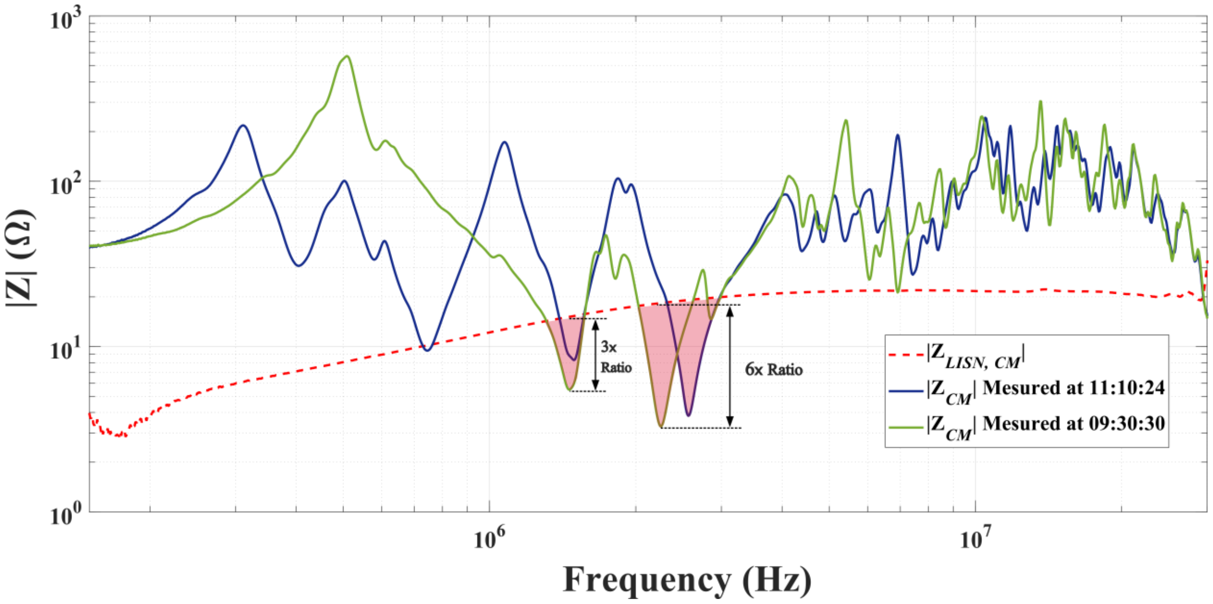

*Figure 2-17 CM impedance comparison between LISN and the grid at ENS parking place #25.*

If the frequency of any noise peaks happens to be within the red areas, the amplitude of the noise will surpass what is predicted by the LISN in compliance tests. In other words, in real-world applications where the noise termination impedance is changed, and the LISN impedance is substituted with the grid impedance, for example, with the green curve in Figure 2-17, depending on the noise source impedance, the noise current amplitude can be up to 6 times higher than the expected level by the standardized measurement method in the worst-case scenario, and consequently, it disturbs the environment more than it is supposed to do and can cause a malfunction in systems nearby.

The red areas become broader in DM as a consequence of the LISN's DM impedance amplitude being approximately four times greater than its CM impedance. Figure 2-18 presents the comparison of DM grid impedance amplitude measured at place #17 at two distinct time points with that of the LISN. The measured impedance, when the portable test bench supply is connected to the same grid nearby, indicates a significant deviation, particularly at low frequencies, where a maximum impedance ratio of 30 times was observed. This emphasizes the importance of having knowledge about the loads that can be connected to the LV grid under study.

In the following section, we undertake a quantitative assessment of this impedance deviation's effect on the EMI level and, consequently, on the volume of EMC filters.

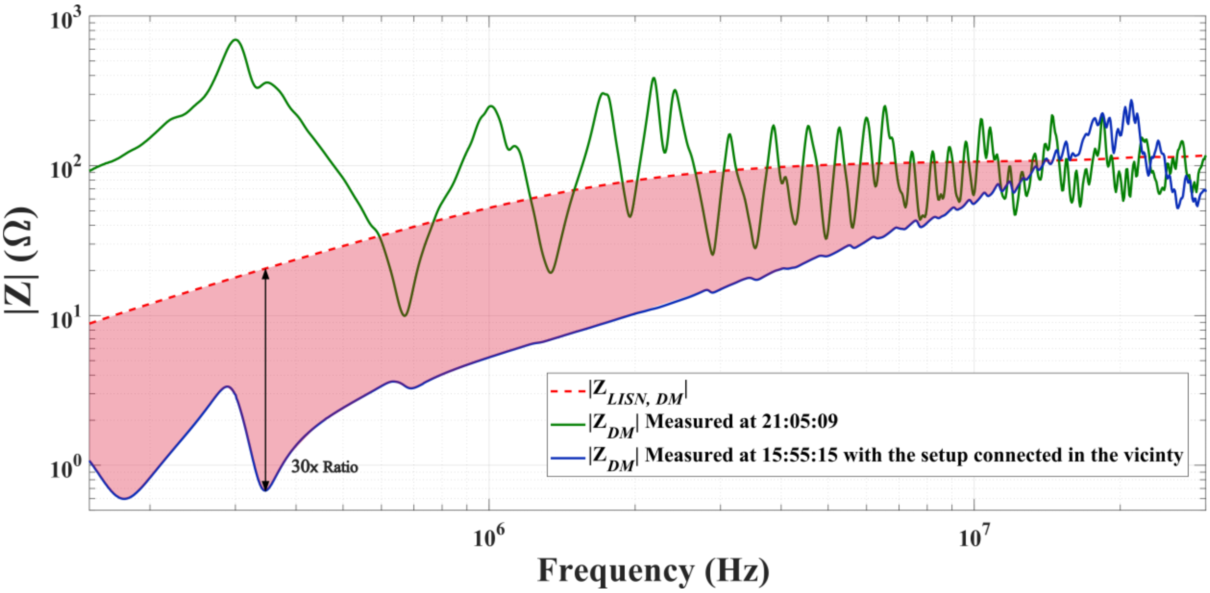

*Figure 2-18 DM impedance comparison between LISN and the grid at ENS parking place #17.*

## 2.2 Impact of the Standardized Method on the Sizing of EMC Filters

The observed impedance deviation in the previous section implies that filters designed based on conducted EMI measurements with the LISN may provide insufficient attenuation in real-world applications if the noise termination impedance is smaller than the LISN impedance in its absence. In such cases, to ensure the performance of filters, they must be designed based on the worst-case scenario, meaning the EMI level observed at the lowest possible noise termination impedance in an application.

It is important to emphasize that our intention in this study is not to undermine existing standards; rather, this is solely a theoretical study aimed at examining potential undesired outcomes in specific circumstances and exploring possible solutions to avoid them, as well as assessing the consequences and impacts of each solution on EMC filter performance and size. Exploring imaginary solutions can provide valuable insights into potential ways to tackle such complex problems.

Therefore, to address the question of “How much will the EMC filter volume vary?”, two hypothetical approaches can be considered: firstly, defining and enforcing new types of LISNs for different applications based on the worst-case scenario derived from power supply impedance measurements in the targeted application; secondly, maintaining the existing LISNs and adjusting the standard limit levels based on the maximum impedance deviation from comparing the worst-case scenario and LISN’s impedance. In both cases, it is certain that the filter size, which depends on various parameters of the circuit, will vary compared to previous configurations. Here, we aim to quantitatively assess this change from both of these approaches in volume within a specific setup.

By considering these hypothetical approaches, a deeper understanding of the challenges and opportunities involved in addressing the issue of EMC filter performance degradation on the grid can be gained. Additionally, such imaginative exercises can hopefully spark innovation and creativity, leading to novel ideas and strategies for real-world implementation.

In this section, an algorithm is developed to design a performant EMC filter optimized for volume in the first step. Subsequently, the impact of the LISN removal, as well as modifying the standard levels, will be investigated.

### 2.2.1 Filter Optimization Method

A methodology, proposed by [67], has been adapted to determine the product of capacitance and inductance values of two second-order low-pass filters for differential mode and common mode. The structure assumed for EMC filters is composed of an inductor as common mode choke and two different kinds of capacitors for DM and CM filters, as indicated in Figure 2-19. In this method, these filters are considered separately based on the assumption that the common-mode propagation channels are symmetrical.

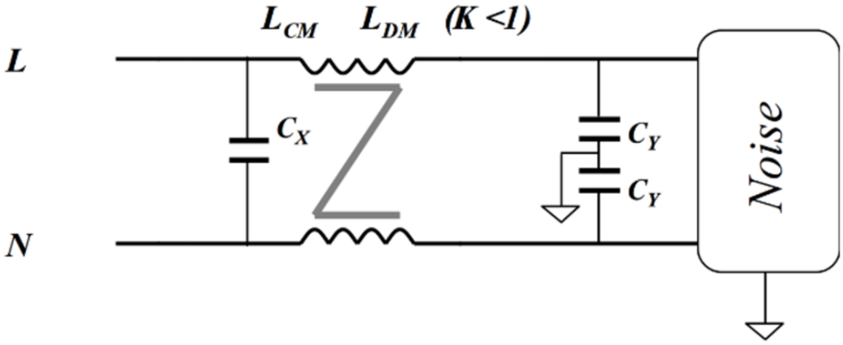

*Figure 2-19 Typical passive EMC filter structure.*

In order to find the maximum cutoff-frequency of each of these second-order filters and subsequently the minimum components values, following equations have been used for CM and DM filters design, as proposed in [67].

$$2C_y\,.\,(L_{CM}+0.5L_{DM}) = \left(\frac{10^{\frac{S_{M_{CM}}-G_{M_{CM}}}{40}}}{2\pi.f_{M_{CM}}}\right)^2 \qquad 2\text{-}16$$

$$(C_x+0.5C_y).2L_{DM} = \left(\frac{10^{\frac{S_{M_{DM}}-G_{M_{DM}}}{40}}}{2\pi.f_{M_{DM}}}\right)^2 \qquad 2\text{-}17$$

Here, $f_M$ represents the frequency of the maximum deviation from the standard limit in related spectrum, $S_M$ is maximum level of the related spectrum within a particular frequency range (with considering that filter has an attenuation of 40 dB/dec) and $G_M$ is the limit level in same frequency defined by the standard (both in dBμA or dBμV).

Obtaining the optimum volume for differential and common mode filters cannot be done separately, due to the fact that the chosen structure does not contain any individual component for differential mode inductor. In this case, the leakage inductance of the common mode inductor plays the role of a differential mode inductor. Therefore, the process of finding the optimum volume for these two filters are entangled with one another and the optimum solution must include optimizing the volume of these filters simultaneously.

Here, the objective function is the total volume, which means sum of the components volume. In CM filter, capacitors are mostly from Multi-Layer Ceramic Capacitor (MLCC) type and the DM filter capacitor is often from film capacitor type. In [68], an approximation formula has been proposed for estimating the capacitor volume. However, in this study, volume of the capacitors come from data provided by the manufacturers.

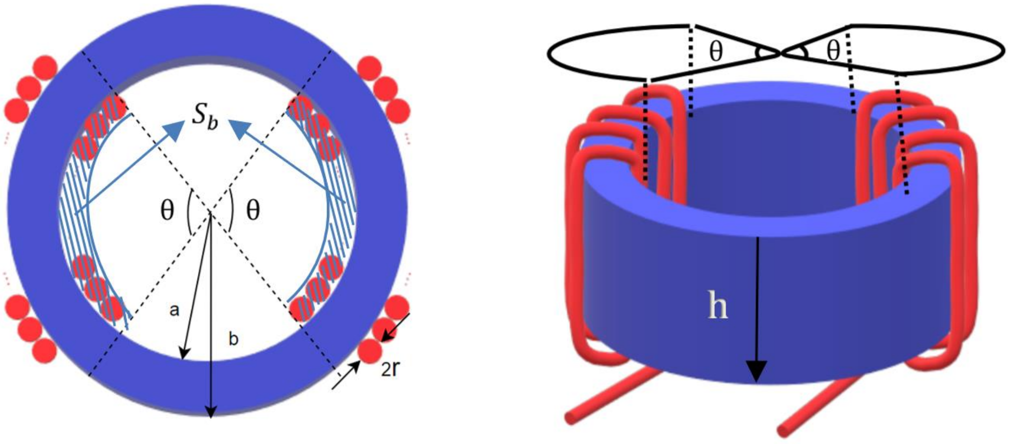

*Figure 2-20 Geometric parameters of the common mode inductor.*

The volume of the common mode inductor, which has two windings in same direction around a toroidal core, with the geometric parameters presented in Figure 2-20, can be expressed by the following formula,

$$\boldsymbol{V_L = k_{CM} \,.\, (A_e \,.\, S_b)^{\frac{3}{4}}} \tag{2-18}$$

where $S_b$ is the internal coiling area, for a single-layer inductor; $A_e$ is the cross-section of the magnetic core, and $k_{CM}$ geometric factor defined as follow.

$$\boldsymbol{k_{CM} = \frac{\pi \,.\left(\frac{b}{a} + \frac{2}{\alpha}\right)^2 .\left(\frac{h}{a} + \frac{4}{\alpha}\right)}{\left[\left(\frac{b}{a} - 1\right)\left(\frac{h}{a}\right)\frac{\pi.\theta}{\alpha^2}\right]^{\frac{3}{4}}}} \tag{2-19}$$

In this formula, $\theta$ represents the coiling angle, α signifies the ratio of inner radius of the core to the radius of the coil (r). the height of the core is represented by the variable $h$, and a $a$

and $b$ are inner and outer radiuses, respectively. The inductance of a single-layer toroid inductor can be calculated using the following equation.

$$\boldsymbol{L_{CM} = \frac{\mu.h.N^2}{2\pi}\,ln\left(\frac{b}{a}\right)} \qquad 2\text{-}20$$

Here, permeability of the core is signified as $\mu$, and $N$ represent the number of turns. This choke has a leakage flux that can be modeled as the DM inductance which depends on $\theta$ and effective permeability $\mu_{DM}$. As detailed in [69], effective permeability can be expressed as a function of Γ, the length-to-diameter (or equivalent diameter in the case of square cross section) ratio of the equivalent rod, with a set of curves for different core materials. However, for typical values of Γ, $\mu_{DM}$ is independent of the core permeability and then the following expression can be employed.

$$\boldsymbol{\mu_{DM} = 2.5\,\Gamma^{1.45}} \qquad 2\text{-}21$$

Hence, by having the effective rod length ($l_e$), the leakage inductance can be approximated using the following equation.

$$\boldsymbol{L_{DM} = \mu_{DM}\,\frac{\mu_0\,N^2\,A_e}{l_e\cdot\sqrt{\frac{\theta}{2\pi}+\frac{sin\frac{\theta}{2}}{\pi}}}} \qquad 2\text{-}22$$

Therefore, after determining the wire diameter ($D_{wire}$) based on flowing current using current density (δ), optimal inner and outer radiuses of the core, along with the number of turns and height can be achieved for a specific $L_{CM}$ and $\theta$. In order to obtain optimized geometric parameters of $L_{CM}$, two simple minimization steps are performed: one on the length of the wire and another on core inner and outer radiuses ratio. Finally, the volume will be calculated for a specific $L_{CM}$ and $\theta$, and this procedure will be repeated for different values of $L_{CM}$ and θ. During each repetition, the constraints will be checked, to find a valid optimal volume for the inductor and thus for the filter. For better comprehension, a simplified flowchart of the program is depicted in Figure 2-21.

The primary inputs of this optimization program include the products of L and C for CM and DM filters, which depend on the required cut-off frequencies. Additionally, the material of the core, expressed by the maximum flux density ($B_M$) and the relative permeability ($\mu_r$), as well as the RMS current flowing in the wires must be provided as inputs. A database containing information on capacitors, magnetic cores, and wire diameters available in the market was gathered and utilized. Additionally, an option to create a larger inductor by stacking two cores was incorporated into the optimization process.

It is worth mentioning that the parasitic elements of the components are not initially considered in the filter calculations and structure. However, during the final model verification step prior to fabrication, the parasitic elements of the filter components were taken into account.

The first constraint of this optimization is that the components of the filter are limited to those available in the market. This ensures that the filter can be realized without adding several components in series or parallel, which would introduce unwanted parasitic effects. Therefore, in each step after the calculation of a parameter, the nearest existing value is selected. The other constraint that should be taken into account is the saturation problem. In common mode choke, the only current that can saturate the core is CM current, so it is also considered as an input.

Ultimately, by exhaustively exploring all possible combinations of capacitance and inductance values within a defined range and identifying the minimum solution that satisfies the constraints, the optimal components of the EMC filter can be determined. It’s important to highlight that by establishing realistic limits, the optimization process can be completed in less than a minute.

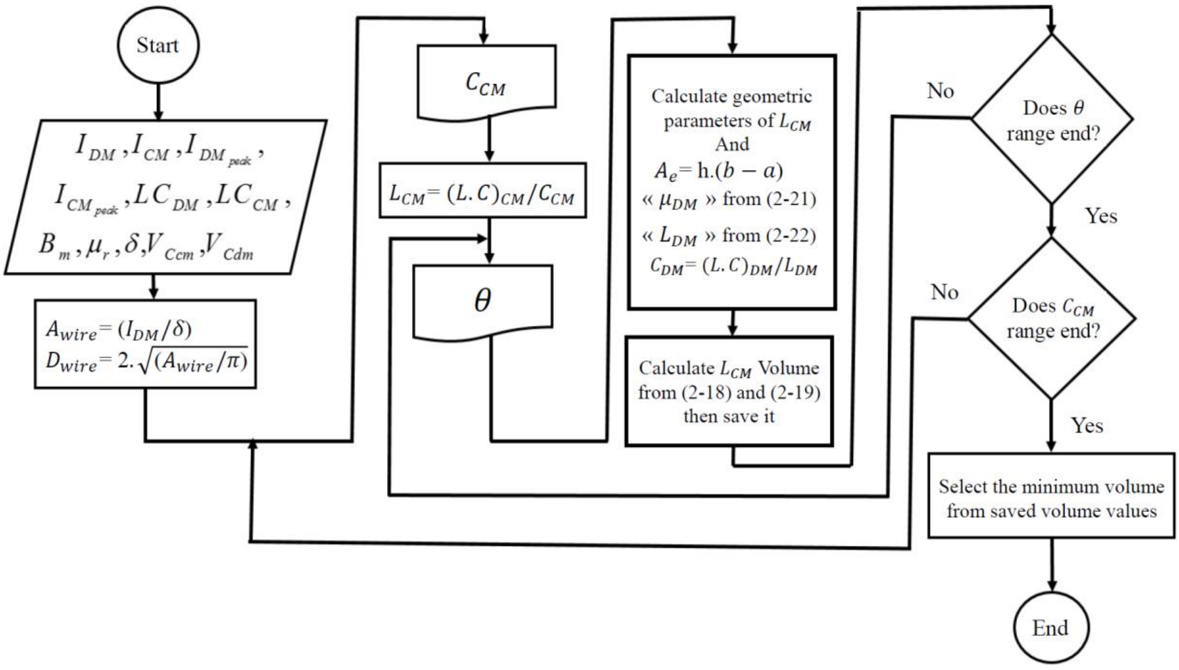

*Figure 2-21 A simplified flowchart of the proposed volume optimization method.*

### 2.2.2 LISN Removal Impact on EMC Filters Volume

In order to examine the influence of the absence of the LISN or its replacement with a hypothetical LISN whose impedance matches the power supply impedance on EMC filter volume, a typical test setup has been employed, including a half-bridge inverter system for feeding a resistive-inductive load, from a DC source. The selection of this setup is predicated on the anticipated significant disparity between the impedance of the DC source and that of the LISN. With such a notable impedance deviation, the impact on the filter would be more pronounced and easily observable.

Additionally, advancements in semiconductor devices and converter architectures have facilitated the transition to higher voltages, leading to the increased adoption of DC grids across various sectors, including distributed generation, marine vessels, and aerospace applications. Despite the inherent challenges associated with their protection systems, DC grids offer notable advantages in terms of flexibility, efficiency, and power density, making it pertinent to analyze the variation in filter size within such systems [70], [71].

The diagram in Figure 2-22-a illustrates the inverter system, which employs bipolar sinusoidal pulse width modulation (SPWM). This configuration is realized for experimental verification, as shown in Figure 2-22-b. Two identical LISNs (type 6516- 5-TS-10-BNC) from Solar Electronics adapted for various standards, such as DO-160F, are used for each phase. The details of the main parameters are provided in Table 2-3.

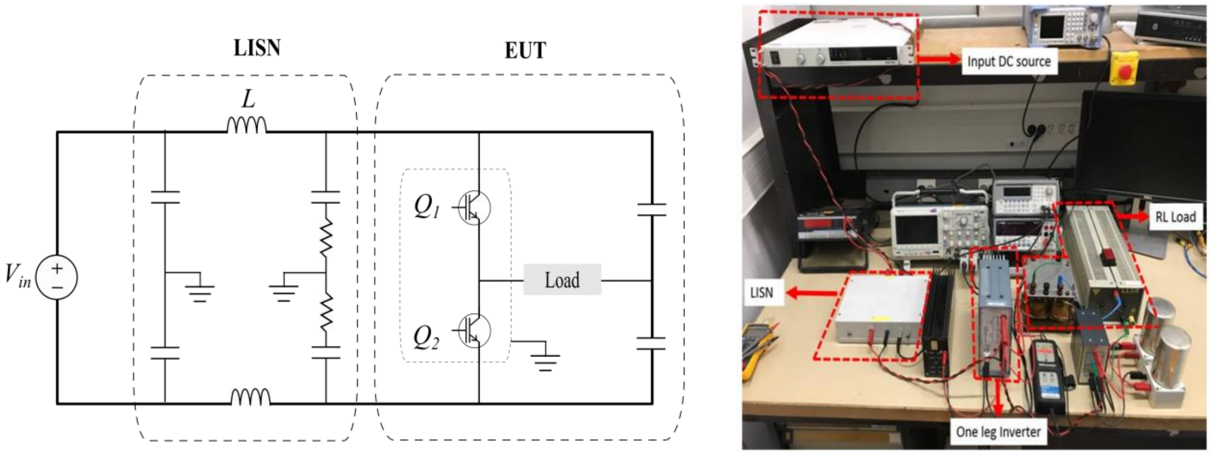

(a) (b)

*Figure 2-22 The conducted emissions measurement setup (a) equivalent circuit diagram; (b) test workbench.*

*Table 2-3 Test setup details.*

| Parameters | Value | Unit |
|---|---|---|
| Load Power | 100 | W |
| Input Source Voltage | 100 | V |
| Switching Frequency | 16 | kHz |
| Fundamental Frequency | 400 | Hz |

In this case, after removing the LISN, the noise termination impedance varies from the impedance of the LISN to the actual value of the DC source impedance. Therefore, the CM and DM impedances of both the LISN and the DC source are measured in a range from 150 kHz to 30 MHz using the same setup described in section 2.1.2.1, which was originally used for LV grid impedance measurement.

The four configurations are presented in Figure 2-24. The measured results for magnitudes of impedances for both cases are indicated in Figure 2-24. As was expected from the LISN structure, presented in Figure 1-15, the DM and CM impedances, after the inductive range, reach approximately 100 Ω and 25 Ω at high frequency, respectively. However, $Z_{\text{DC Source, DM}}$ has a lower magnitude compared to $Z_{\text{LISN, DM}}$ in the low-frequency range, which will lead to a higher DM emission. The behavior of $Z_{\text{DC Source}}$ and the resonances that can be seen in DM and CM at high-frequency originate mainly from the DC source output LC filter and its regulation stage.

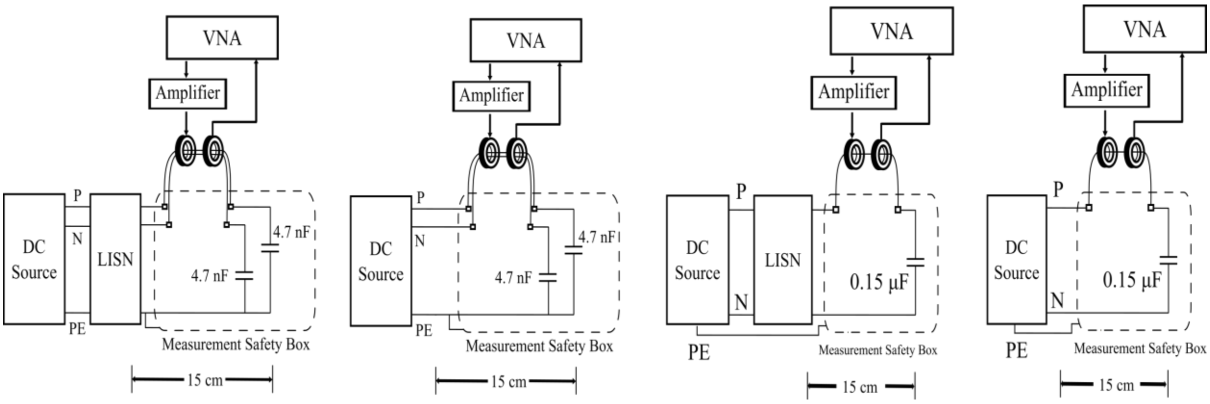

(a) (b) (c) (d)

*Figure 2-23 Measurement configurations for extraction of (a) CM impedance of the LISN, (b) CM impedance of the DC source, (c) DM impedance of the LISN, (d) DM impedance of the DC source.*

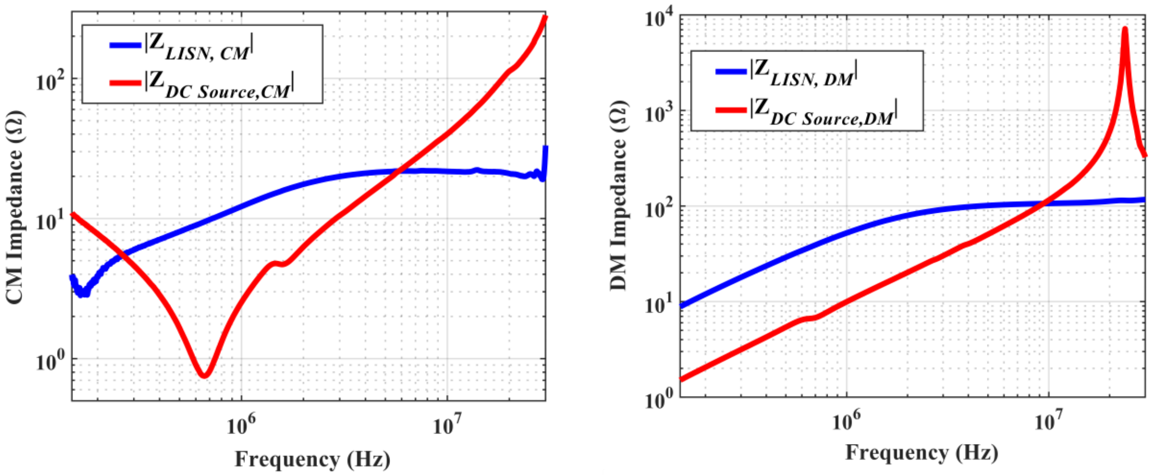

(a) (b)

*Figure 2-24 Magnitudes of measured impedances (a) CM, (b) DM*

The conducted emissions in a 100 W single-leg inverter system are measured in the anechoic chamber without a filter in a range of 150 kHz to 50 MHz, as indicated in Figure 2-25, using an R&S ESU EMI test receiver with a resolution bandwidth (RBW) of 9 kHz, video bandwidth (VBW) of 2 kHz, the positive peak detector, and a Pearson 8585C monitoring probe with the configuration illustrated in Figure 1-11.

The results demonstrate that neither CM nor DM currents satisfy the DO-160F norm in both cases, and for each case, an EMC filter is required to comply with the standard. In the context of this setup's intended application within the aeronautics field, the relevant standard selected for comparison is DO-160F from RTCA.

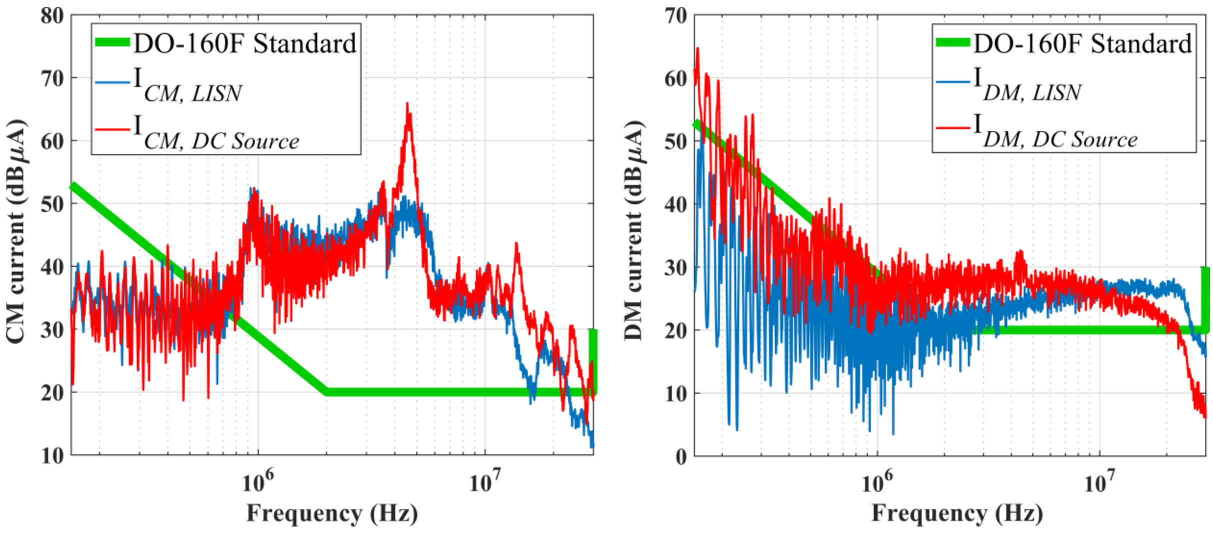

(a) (b)

*Figure 2-25 Comparison of measured conducted emissions for the two cases (a) CM, (b) DM.*

In the two cases, compared in Figure 2-25, all aspects of the setup remain the same except for the LISN, including the load, inverter switching frequency, ground connections and other parameters. Therefore, the internal high-frequency impedance of the converter (the noise source) and its parasitic elements remain approximately the same. Consequently, particularly in the case of DM, the difference in the amplitude of conducted emissions between two scenarios primarily depends on the noise termination impedance, whether it's the LISN or the DC source. However, in CM, this isn't the main determining factor as a large portion of the noise can circulate between the lines and ground plane via bodies of the devices within the setup. Generally, the lower frequency range of the EMC spectrum, typically from 150 kHz to 1 or 2 MHz, has a more pronounced impact on filter design and the filter volume basically depends on conducted emissions level in this range. Here, in the absence of the LISN, especially in the differential mode, emissions measured at lower frequencies within this range tend to be significantly higher, leading to a larger filter size. By employing the filter optimization methodology developed in the 2.2.1 section, two filters for the two cases were designed and then compared in terms of volume. The components' value and the total volume of the components for the two filters are presented in Table 2-4.

As expected, the filter designed for the DC power supply is significantly larger than the filter designed for the LISN. The highest conducted emissions deviation can reach 16 dB and it leads to a 111.1% increase in the volume of the required filter. In other words, the filter designed with LISN will be ineffective (assuming that no margin was considered in the design process) in a real situation where the LISN is absent.

*Table 2-4 Designed filters' components values and total volume.*

| | **LISN** | **DC source** | **Variation** |
|---|---|---|---|
| ***$L_{CM}$ (µH)*** | 60 | 178 | +196.7% |
| ***$C_{CM}$ (nF)*** | 13.9 | 4.5 | -67.6% |
| ***$L_{DM}$ (µH)*** | 1 | 3 | +200% |
| ***$C_{DM}$ (nF)*** | 1200 | 3300 | +175 % |
| Components total volume (cm$^3$) | 4.5 | 9.5 | +111.1% |

Since the low-frequency emissions level in differential mode with the DC source is higher than the case with LISN, the components' value of the DM filter designed for the DC source has increased more than those of the CM filter. However, as the chosen structure does not contain any individual component for the $L_{DM}$, the common mode choke value, and consequently its volume, is increased to provide the required leakage inductance.

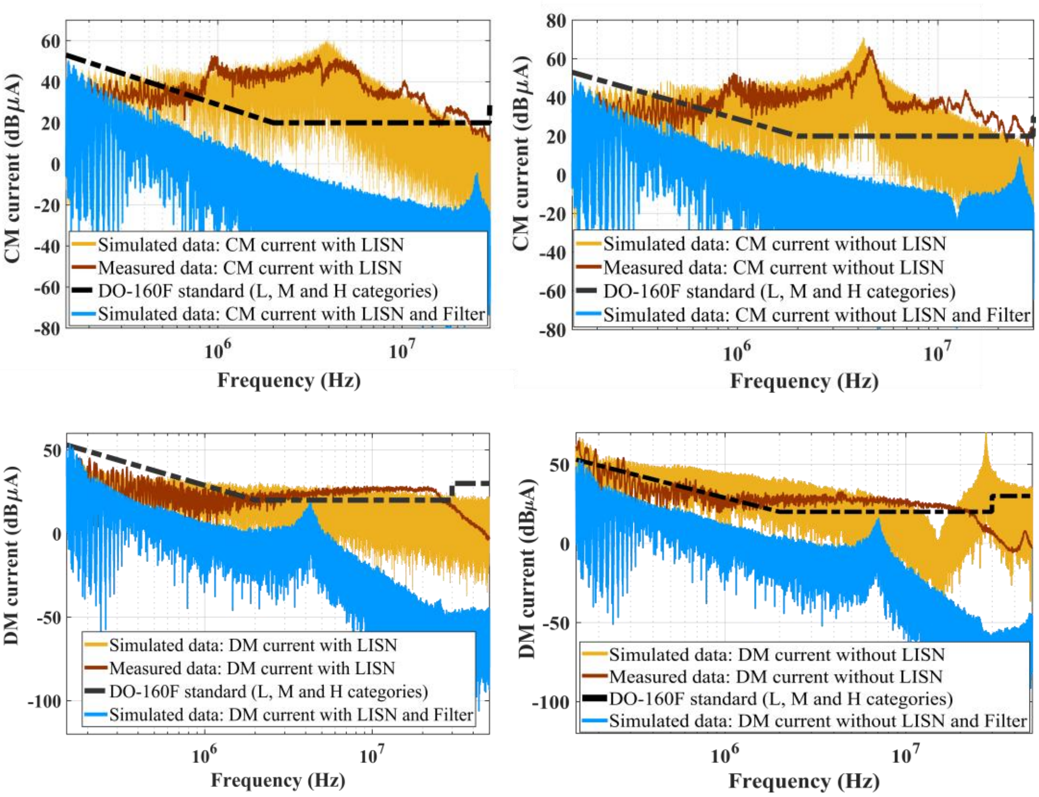

*Figure 2-26 Comparison between measured and simulated conducted emissions before and after adding the filter w/o LISN for both CM and DM.*

The test setup is modeled in MATLAB Simulink in the time domain for a duration of 5 ms with a sample time of 3.125 ns to verify the filter performance before fabrication. The designed filters of Table 2-4 have also been modeled and added to the setup model. Results derived from the simulations are compared in the frequency domain: FFT of the calculated values are compared to measured conducted emission data, as shown in Figure 2-26. Due to the model imperfection, in particular in heat sink capacitance modeling and in IGBT switches modeling, more deviation between the measured and simulated results may be seen in high frequencies. Fortunately, the low-to-medium frequency range is relevant for the filter design; thus, the high-frequency deviation has no effect on the filter components' values and the volume. The results verify the performance of the designed filters and show that in all cases, the conducted emissions levels, after the insertion of filters into the model, are inferior to the standard limit, but the volume of the EMC filter has significantly increased in the design without the LISN, corresponding to the DC power supply.

### 2.2.3 Modified Standard Levels Impact on EMC Filters Volume

To assess the impact of modifying the standard profile on the optimized volume of EMC filters, a similar test setup to what is presented in Figure 2-22 has been employed with the LISN. This time, the system is modeled at three different power rates: 100 W, 750 W, and 3 kW, and the low-power system was implemented for experimental verification. In order to define our modified standards, various modifications were applied to the DO160-F standard.

*Table 2-5 Modified standards description.*

| No. | Description |
|---|---|
| 1 | DO-160F (L, M and H categories) |
| 2 | DO-160F (L, M and H categories) with +10 (dB) vertical shift |
| 3 | DO-160F (L, M and H categories) with -10 (dB) vertical shift |
| 4 | DO-160F (L, M and H categories) with +15 (dB) vertical shift |
| 5 | DO-160F (L, M and H categories) with + 20 (dB) vertical shift, or DO-160F (B category) |
| 6 | DO-160F (L, M and H categories) with +50 (kHz) horizontal shift from starting point (150kHz) |
| 7 | DO-160F (L, M and H categories) with -50 (kHz) horizontal shift from starting point (150kHz) |

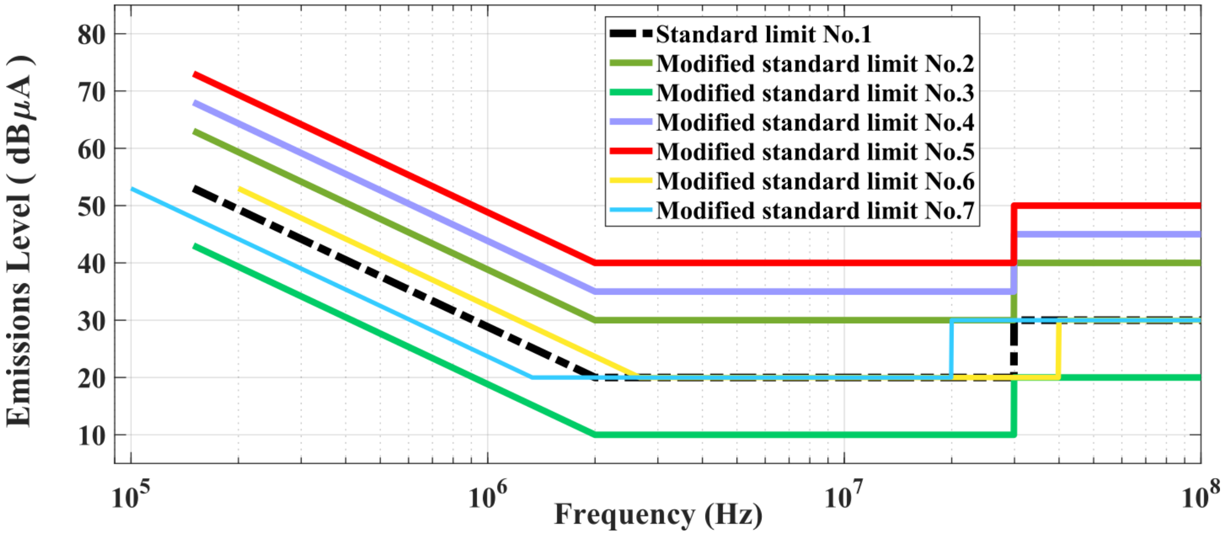

*Figure 2-27 Modified standards described in Table 2-5.*

The original DO-160F standard, along with its modified versions, is detailed in Table 2-5 and depicted in Figure 2-27. Utilizing the optimization program outlined in the 2.2.1 section, seven filters for the seven standards were designed for each low-power (100 W), medium-power (750 W), and high-power (3 kW) system to comply with the related modified standard. Then, their volumes have been calculated for inductive and capacitive components separately. Figure 2-28 presents the total volume of designed filters for the low-power system.

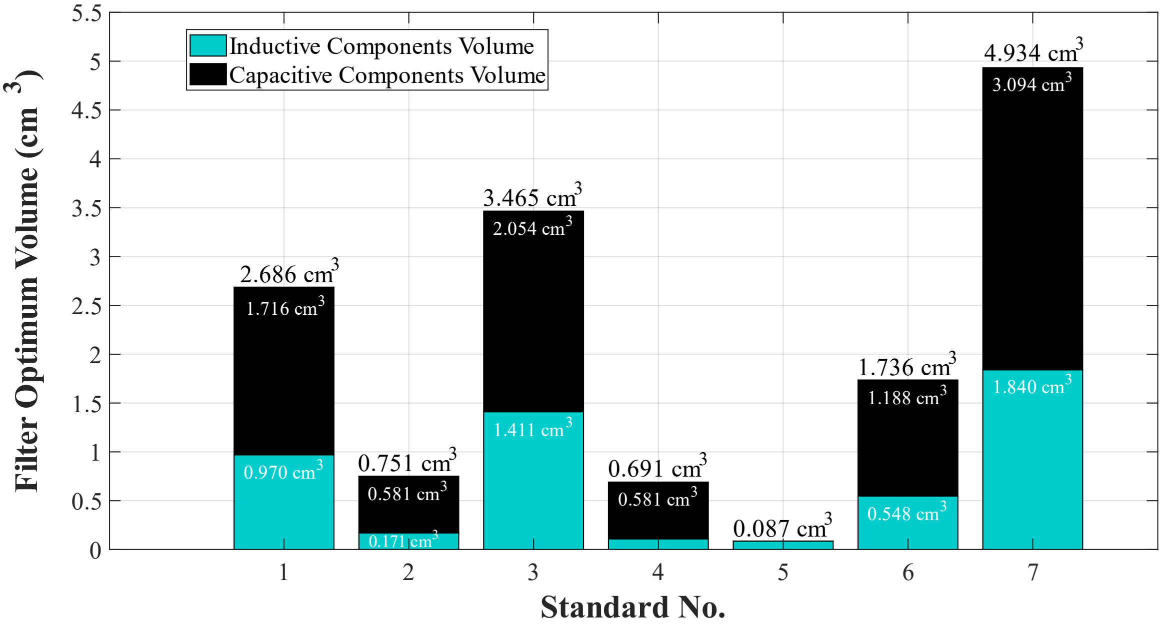

*Figure 2-28 The optimal volumes of filters designed for each modified standard ($P_{out}$=100 W).*

In order to compare the results, considering the volume of the filter designed for DO-160F (standard No.1) as the reference, volume variations for all the power ratings are depicted in Figure 2-29.

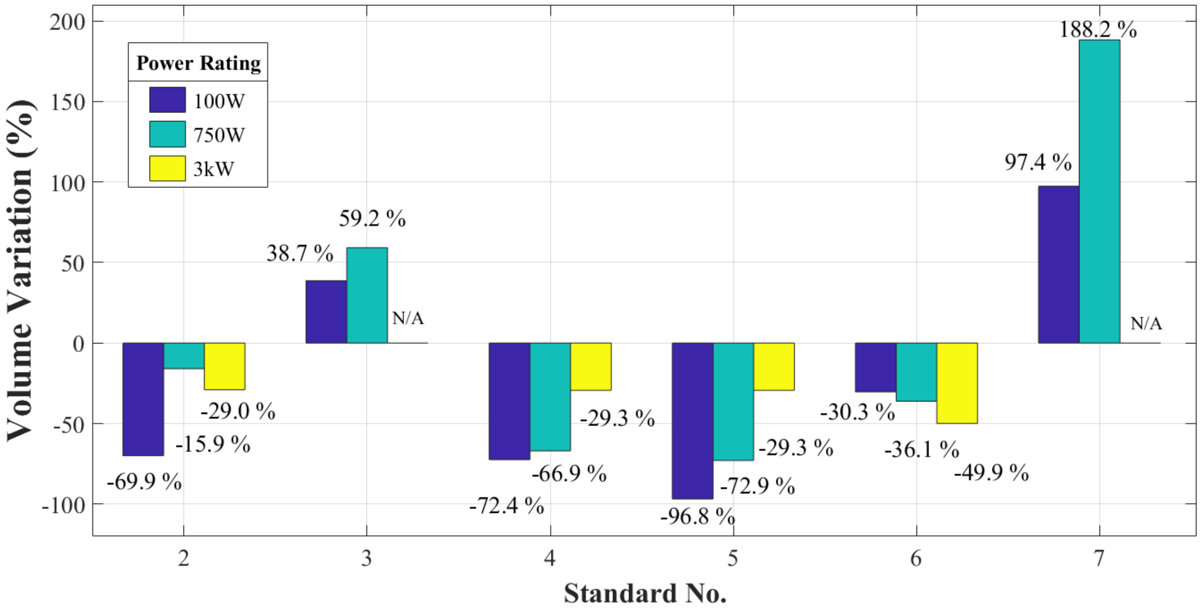

*Figure 2-29 Volume variations of filters designed for each modified standard.*

For the high-power system, the algorithm was not able to find a valid solution for modified standards No. 3 and No. 7 using the predefined filter structure. However, the problem can be solved by changing the structure and using separate $L_{DM}$ elements.

As can be seen in Figure 2-29, a larger volume gain has been observed in the low-power system compared to the high-power system when only the level of standard is changed by a vertical shift in the same frequency as DO-160F, such as No.2, No.4, and No.5. However, when the standard is horizontally shifted to the higher frequencies, the trend is reversed and highest volume gain has been detected for the high-power system. In addition, the large increase in standard no. 7 shows the significant impact of low-frequency harmonics on filter sizing.

Furthermore, in the case of filter No. 5 for the 100 W system, the maximum gain is observed due to the elimination of $C_{DM}$, as the DM emission level is lower than the limit even without a DM filter. This implies that the volume gain does not always follow a linear relationship with the emissions level; instead, a notable increase in volume gain occurs at certain thresholds.

In order to verify the performance of the designed filters, seven filters related to the low-power system, were realized. The components' value and the total volume of the components for each filter are presented in Table 2-6. As an example, the filter related to standard No. 3 is indicated in Figure 2-30.

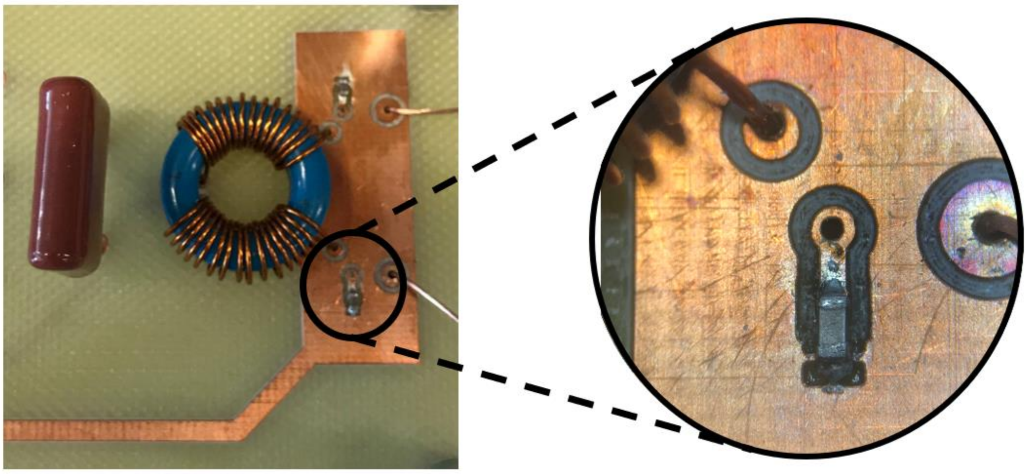

*Figure 2-30 Designed filter related to standard No. 3.*

The conducted emissions are again measured using an R&S ESU EMI test receiver after placing the filters between the LISN and the EUT in order to check if the emission levels are below the level of the related standard.

The designed filters are also modeled in MATLAB Simulink and are added to the modeled system. The results obtained from the simulations and the measurements show that in all the cases the level of conducted emissions, after adding the filter, is below the level of the related defined standard. In Figure 2-31, as an example, the experimental results for some cases, along with the simulation results, are presented.

*Table 2-6 Realized filters' components values and total volume for the seven cases. (P=100 W)*

| Standard No. | 1 | 2 | 3 | 4 | 5 | 6 | 7 |
|---|---|---|---|---|---|---|---|
| **$L_{CM}$ (μH)** | 565 | 45 | 600 | 21.2 | 2 | 235 | 1027 |
| **$C_{CM}$ (nF)** | 1.5 | 15 | 2.7 | 27 | 27 | 1.8 | 1.8 |
| **$L_{DM}$ (μH)** | 4.6 | 0.4 | 5.8 | 0.2 | 0.02 | 1.95 | 8.6 |
| **$C_{DM}$ (nF)** | 390 | 68 | 680 | 68 | N/A | 270 | 1200 |
| Components total volume (cm$^3$) | 2.5 | 0.75 | 3.46 | 0.69 | 0.09 | 1.74 | 4.93 |

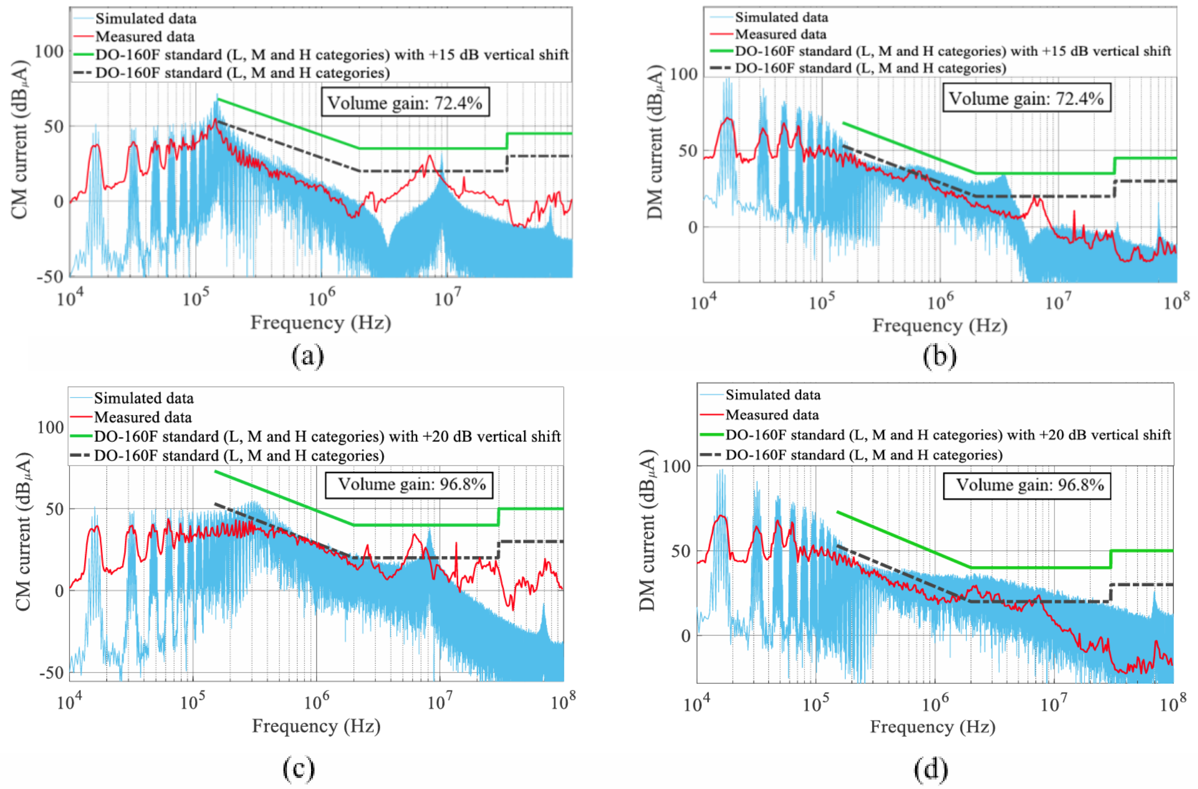

*Figure 2-31 Conducted emissions after adding the designed filter to the system (P =100 W): (a) CM current for case No. 4, (b) DM current for case No.4, (c) CM current for case No. 5, (d) DM current for case No. 5.*

## 2.3 Conclusion

In summary, this chapter has presented a comprehensive overview of the current state-of-the-art for assessing the high-frequency impedance of the LV grid. A methodology was implemented that enabled us to measure not only the impedance of the LV grids but also that of any power source or device under voltage. Hence, the variation of impedance in a typical day at an EV parking facility could be captured, illustrating why EMC filters in real-world applications may not always perform as effectively as expected.

Furthermore, a thorough examination of volume variations in EMC filters under diverse testing scenarios was conducted. The provided knowledge about the external noise termination impedance using the TP method led to a clearer understanding of the relationship between this impedance variation and the filter volume. It also showed that the influence of impedance variation in the external noise termination is more pronounced on the DM current compared to the CM current.

In the forthcoming chapter, we will delve into the EV charging environment under test, including both the OBC and the associated grid infrastructure to which it is connected. To establish a precise model of the entire system valid for high-frequency, each part of the system will be modeled, and rigorous verification procedures will be undertaken to ensure the accuracy and fidelity of the model representations.

# CHAPTER 3

# HF Modeling of the EV Charging Environments

This chapter is firstly dedicated to the charging environment description, including our prototype bidirectional OBC and the microgrid, which is realized in order to provide a controlled environment while analyzing the conducted emissions caused by the OBC without the LISN. Following this, the focus shifts toward modeling different elements of the system. An HF model of the microgrid was established in the frequency domain using a new approach based on a SPICE-type solver and the experimental acquisition of impedances, enabling faster simulation for large systems. This model includes the cables, the isolation transformer with different grounding systems, and the circuit breakers. Additionally, a behavioral model with a "black box" approach is developed for the OBC, defining the noise source and its impedances. By providing the model for the entire system, this chapter enables the simulation of parasitic current levels at any point in the microgrid.

## 3.1 The Charging Environment Description

In this section, we will provide a comprehensive description of the charging environment, which includes the EUT we aim to analyze for conducted emissions – our bidirectional OBC prototype – as well as the microgrid to which the EUT will be connected in the absence of the LISN.

### 3.1.1 The EUT: Bidirectional OBC Prototype

The bidirectional OBC prototype structure, as presented in Figure 3-2, contains a three-phase full-bridge PFC converter and a DC-DC stage using single-phase phase-shifted DAB topology both presented in section 1.1.2. As detailed in Table 3-1, the prototype utilizes both SiC MOSFET and GaN HEMT switches, enabling it to deliver a maximum of 11 kW from the grid to load, and vice versa.

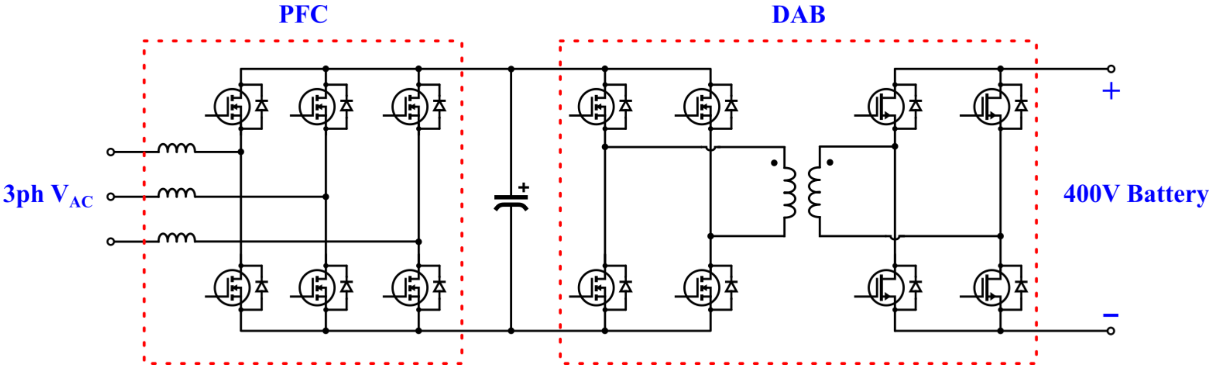

*Figure 3-1 Simplified schematic of the bi-directional OBC prototype.*

It is important to mention that the prototype is provided by Stellantis according to a set of specifications defined by the company. Since it is a sealed prototype delivered with very few documentation, we are unable to perform internal measurements of the prototype, and we also lack full understanding of its functioning, especially regarding the digital control. These considerations orientated the choice for the modeling methodology, which will be presented later in this chapter.

As presented in Figure 3-2-a, the load in this setup is an EV battery composed of 216 NMC cells – lithium-Nickel-Manganese-Cobalt-oxides – arranged in a 2P6S configuration, where six cells are connected into series strings, then the two strings are paralleled together, providing a voltage range from 270 V to 453 V.

*Table 3-1 Bi-directional OBC prototype specifications.*

| | **Description** |
|---|---|
| PFC Switching Frequency | 67.5 kHz |
| DAB Switching Frequency | 135 kHz |
| PFC switches | SiC MOSFET 1200 V |
| DAB primary switches | SiC MOSFET 650 V |
| DAB secondary switches | GaN 650 V |
| Maximum power | 11 KW |
| Efficiency (at $P_{max}$) | ~97% |

The test setup is also equipped with a VN1630A Vector CAN (Controller Area Network) interface enabling operational control of both the battery and OBC through the CANalyzer software.

The OBC incorporates EMC filters on both its input and output sides to limit the polluted area. These filters occupy a substantial portion of the overall volume and mass of the OBC prototype, accounting for approximately half of its circuit board space, as illustrated in Figure 3-2-b.

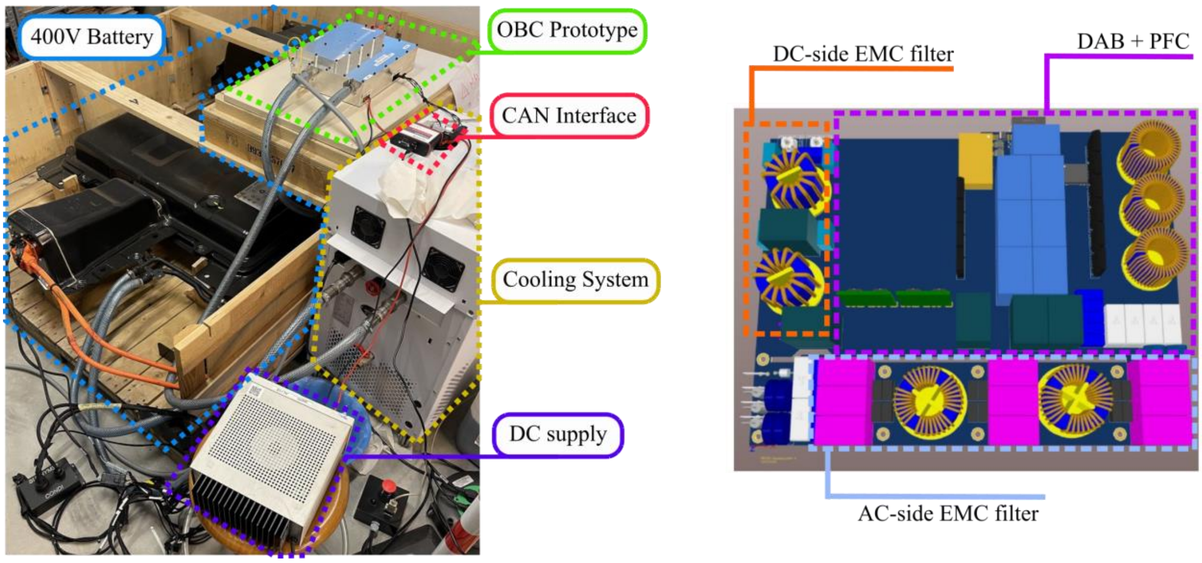

(a) (b)

*Figure 3-2 Bi-directional OBC prototype: (a) Test setup, (b) OBC board with EMC filters.*

### 3.1.2 The Grid-tied Microgrid

The grid impedance fluctuation at any given point over time depending on the loads connected nearby the measurement point, as addressed in chapter II, results in variations in conducted emission levels if an LISN is not utilized. As discussed in the first chapter, the use of an LISN serves not only to ensure consistent emission levels over time at a single measurement location but also to maintain consistent results when measurements are taken at different locations. This standardization of measurements guarantees repeatability regardless of the testing environment. Therefore, if conducted emission measurements are to be performed without an LISN at a specific point, the first step is to ensure that the results remain consistent over time at that specific location.

As suggested in [72], in the case where an isolation transformer is connected to the grid, generally, the grid impedance is relatively small compared to the impedance of the transformer, and the high-frequency impedance seen from the secondary of the transformer is dominated by the leakage inductance and parasitic capacitances between the windings of the transformer so that the variations of the grid behind it do not affect the impedance seen from the secondary side. This statement will be validated in our case in the forthcoming section dedicated to the modeling of the transformer.

Therefore, in order to mitigate the undesired and uncontrolled variations of the grid impedance and to have a controlled environment, a grid-tied microgrid was realized, as depicted in Figure 3-3, including the following elements:

- ❒ An isolation transformer, in order to stabilize the impedance as explained above;
- ❒ A variable autotransformer, in order to adjust the voltage level as our OBC prototype requires a gradual voltage ramp-up;
- ❒ An electric panel, with six outlets, half of which are single-phase and the other half three-phase;
- ❒ Seven circuit breakers with different ratings, as detailed in Table 3-2, in order to verify the HF impedance of circuit breakers with different current ratings.

*Table 3-2 Microgrid circuit breakers details.*

| | Current Rate | Quantity |
|---|---|---|
| Three-phase Residual Current Breaker with Overcurrent protection (RCBO) | 40 A / 30 mA | 1 |
| Three-phase Miniature Circuit Breaker (MCB) | 16 A | 2 |
| | 10 A | 1 |
| Single-phase MCB | 16 A | 1 |
| | 10 A | 2 |

Furthermore, the transformer not only stabilizes the impedance but also allows for the implementation of different grounding systems by changing the connection of neutral and protective earth conductors. Hence, it enables us to analyze the variation in conducted emissions due to different grounding systems. In cases where implementing a grounding system requires two or more grounds, such as ITS and TTN, which were described in Figure 1-17, since we have only one actual ground connection of the facility, the other grounds are emulated by placing a resistor between them. However, it is worth noting that this emulation does not fully represent the high-frequency behavior of a ground connection.

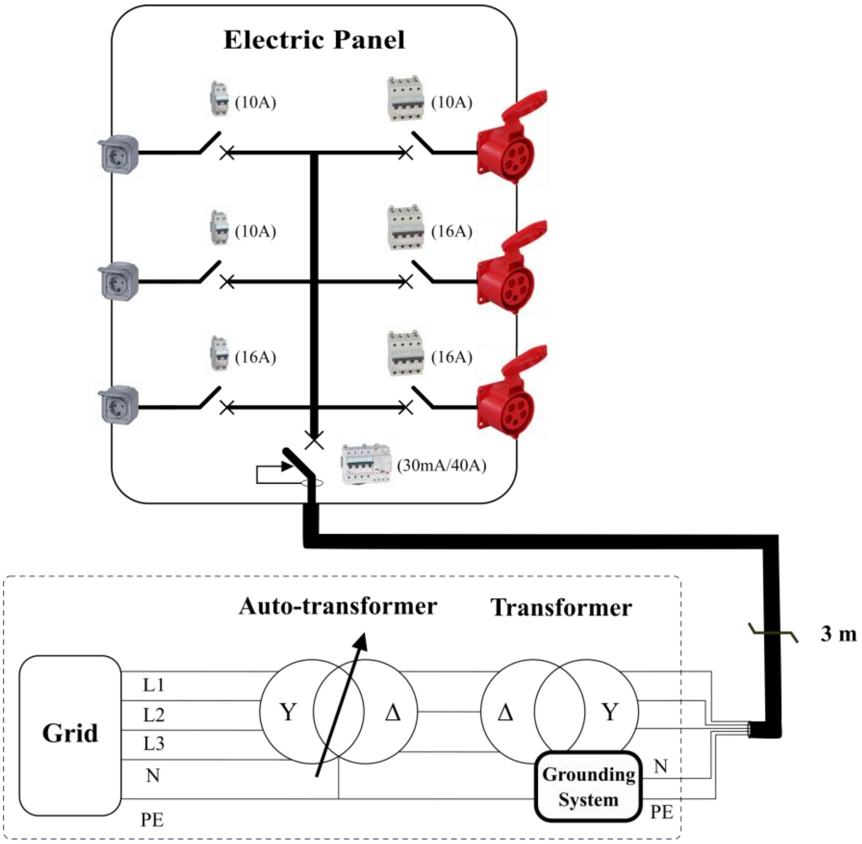

*Figure 3-3 The realized microgrid structure.*

In addition to the advantages mentioned above, the microgrid allows us to perform the conducted emission measurements at any desired point in the system regarding the distance from the last transformer, making it possible to analyze the impact of cable length on the level of emissions.

Eventually, in order to analyze conducted emissions at various operating points under different grid parameters, such as cable length and grounding system, the OBC prototype will undergo charging and discharging cycles on the microgrid. Subsequent sections of this chapter will delve into the development of a high-frequency model representing the entire system by individually modeling each element.

## 3.2 The Charging Environment HF model

The objective of developing the charging environment HF model in this study is to contribute to the design of effective EMC filters for the OBC by exploring external noise termination impedance variation in real-world scenarios in the absence of LISN. Specifically, the aim is to predict conducted emission levels at different points within a large-scale system, such as a parking facility, which involves perturbation sources – OBCs – and external noise terminations – the microgrid – modeling.

Regarding HF modeling of energy conversion systems involving power converters, two main approaches are typically utilized: exhaustive and behavioral modeling. The former is the conventional method, where the circuit model of the converter and other parts of the system are elaborately developed in the time domain. This includes detailed representations of the control system, the switching of active components, and the high-frequency parasitic effects by inserting additional passive circuit elements, as presented in Figure 3-4.

Although time-domain simulation of systems modeled with the exhaustive approach can effectively predict the physical phenomena associated with switching, it becomes increasingly complex when applied to systems with complicated structures due to the proliferation of the number of components and the need for very high sampling frequencies. Additionally, when conducting simulations in the time domain, the results for conducted emissions must undergo the Fourier transformation plus a special signal treatment emulating the EMI analyzer to be compared with compliance standard limits specified in the frequency domain.

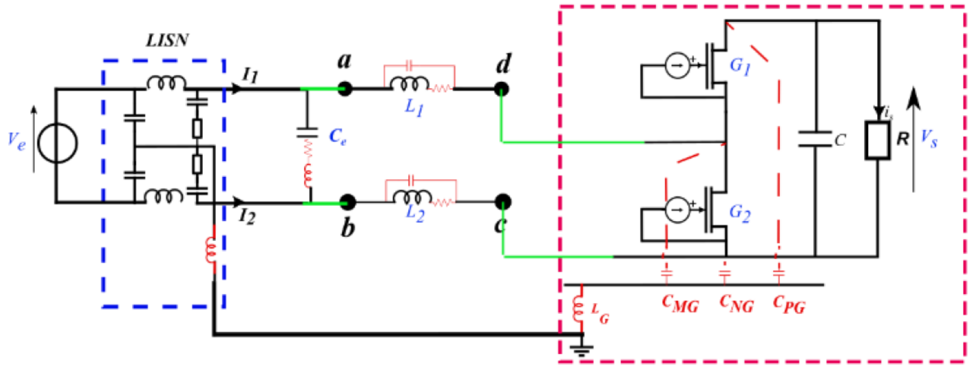

*Figure 3-4 Diagram of an exhaustive model of a boost converter considering the parasitic elements [40].*

On the other hand, the behavioral or system modeling approach involves developing an EMC model of the entire system by defining the perturbation sources and internal and external termination impedances. This method aims to represent the system's behavior without requiring detailed knowledge of its internal structure by a simplified equivalent model that encapsulates the circuit's characteristics using a reduced number of elements.

Behavioral EMC models can operate in the frequency domain, enabling faster calculations. Furthermore, in situations where, due to confidentiality, the details of the internal structures are unavailable, and information for constructing an exhaustive model is insufficient, the behavioral modeling approach proves invaluable, as is the case in this thesis.

Given the necessity of analyzing the signal spectrum in the context of EMC, frequency domain simulation was chosen as the preferred method. Moreover, due to the potential complexity of the system, depending on factors such as the number of EVs and the size of the parking facility, simplicity and calculation time were primary criteria during the modeling and simulation stages. Therefore, we opted to define our models in the frequency domain in a SPICE-type solver to ensure straightforward implementation. To achieve this, we utilized the capabilities of AC analysis in LTspice, enabling us to create circuit elements for sources and impedances based on measurement data. These elements display different amplitude and phase values across the frequency spectrum, unlike the typical usage of LTspice.

In the following sections, we first focus on modeling the constituents of the microgrid, and then our focus shifts to the methods of perturbation source modeling. More detailed information on the simulation method will be provided in the cable modeling section.

### 3.2.1 The Microgrid Elements Modeling

#### 3.2.1.1 Cable modeling

The behavior of a cable cannot be adequately described with a single lumped-element model when the signal's wavelength ($\lambda$) becomes significantly smaller (approximately one-tenth) than the length of the cable ($l$), in other words, when the line is electrically short ($10\lambda < l$) [73]. This occurs particularly when analyzing the high-frequency behavior of cables, such as in the EMC context, where the signals' wavelengths are relatively short.

However, a bifilar cable behavior can be described through the propagation of Transverse Electromagnetic (TEM) waves alongside the cable derived from a distributed-element model based on transmission line theory, which was initially developed to characterize signal behavior in very long lines where the line length even exceeds the wavelength of a low-frequency signal.

The transmission line theory proposes a lumped RLCG model of two conductors, also called the elementary cell equivalent model, by assuming that the length of the lumped segment is short relative to the wavelength of the signal. The theory of multiconductor transmission line, which is an extension of transmission line theory for more than two conductors, suggests the elementary cell with frequency-dependent parameters, as presented in Figure 3-5 for a 3-wire cable, and the model of the entire cable can be obtained by cascading these cells. This model is valid if the cross-section of cables and the distance between them are smaller than one-fourth of the shortest wavelength of the signal [74].

The circuit elements, demonstrated in Figure 3-5, change with frequency due to high-frequency effects such as dielectric loss and skin and proximity effects. The question here is how the circuit elements must be defined to address these high-frequency effects. The following section provides an overview of the existing cable RLCG parameters extraction techniques and approaches for modeling high-frequency effects.

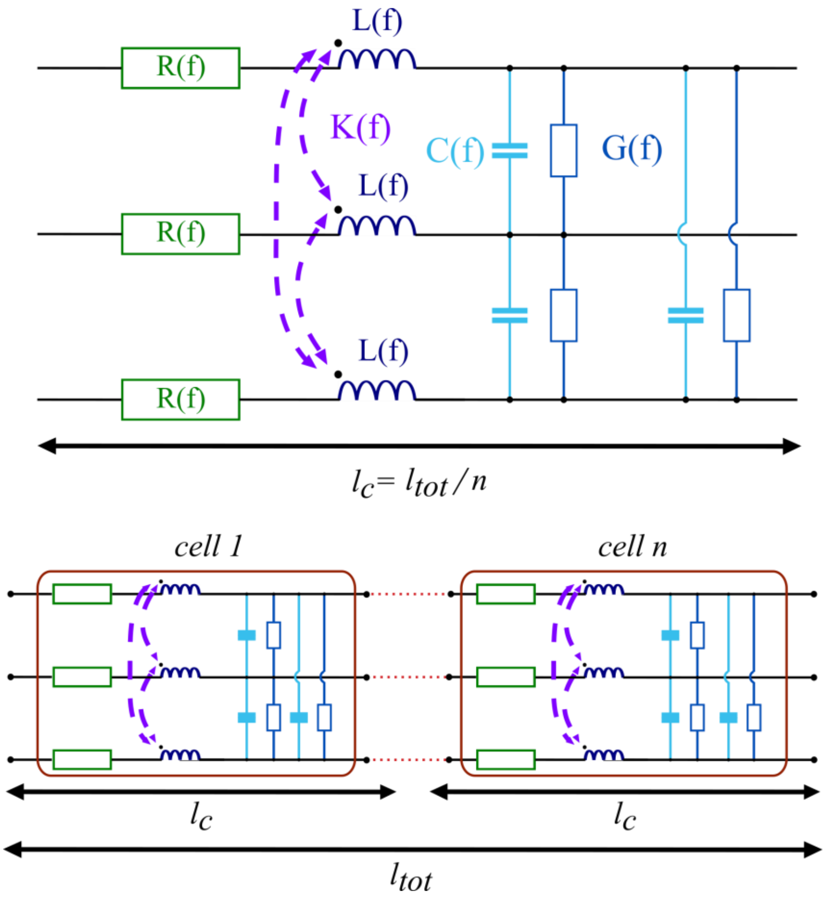

*Figure 3-5 The elementary cell model and the 3-wire cable equivalent circuit model resulted from n cascaded elementary cells.*

#### 3.2.1.1.1 Overview of the Cable Parameters Extraction Methods

Numerous research studies have been done on cable modeling and extracting per-unit length cable parameters. According to the state of the art, three main approaches can be considered when it comes to RLCG parameters extraction: analytical calculation, numerical calculation using finite-element method, and short cable measurements.

The analytic approach determines the cable parameters value depending on the geometric and physical characteristics of the cable by relying on Maxwell’s equations, as presented in [75]. However, some studies, such as [76] and [77], show that results derived from this method do not have acceptable accuracy, especially at high frequency, due to the simplifications that have been considered, and thus, some of the high-frequency effects are not taken into account.

In some studies, numeric methods such as the finite-element method are used to solve Maxwell’s equations using software such as FEMM or ASERIS-NET, as demonstrated in Figure 3-6. As presented in [78], the results for resistance and inductance, especially when conductors are modeled with strands, are accurate enough. However, the capacitance extraction with this method is so sensitive to the geometric definition, and a small error in dimensions will lead to a significant variation [77]. Moreover, a detailed model, such as a conductor with strands, will highly increase the simulation time.

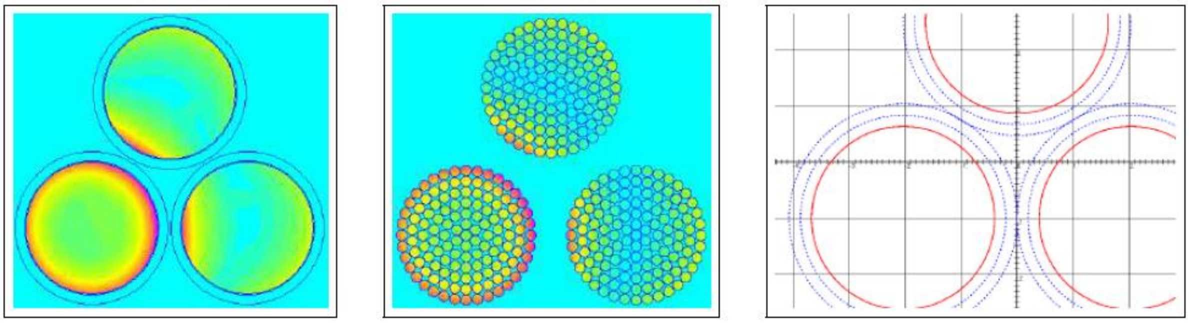

(a) (b) (c)

*Figure 3-6 Numerical methods for extraction of unshielded 3-wire cable parameters: (a) FEMM - solid conductors, (b) FEMM - conductors with strands, (c) ASERIS - solid conductors [78].*

The last method for the parameters' extraction is the experimental method, which involves conducting a set of measurements on a short piece of cable, the technique employed in several studies such as [79], [80], and [81].

In [82], a more complex elementary cell for bifilar cables is proposed to partly address certain high-frequency effects, aiming to make the model's parameters frequency-independent. A measurement method is then outlined to derive all frequency-independent parameters directly from open-circuit and short-circuit impedance measurements at only four different frequency points. However, due to certain simplifications, this method is limited to frequencies below several MHz, and is also restricted to cables with two conductors.

On the other hand, [83] presents a measurement procedure involving open-circuit and short-circuit measurements using an impedance analyzer to extract the frequency-dependent parameters of a basic elementary cell for shielded 3-wire cables that can be extended to become applicable to cables with more wires.

Following the determination of frequency-dependent per-unit parameters, several studies, including [77], [83], [84], [85], and [86], suggest employing RL and RC ladder or parallel networks to model the skin and proximity effects, as well as dielectric loss across different frequencies. These networks' component values can be calculated using curve fitting techniques and mathematical solver tools like APLAC and IC-EMC software.

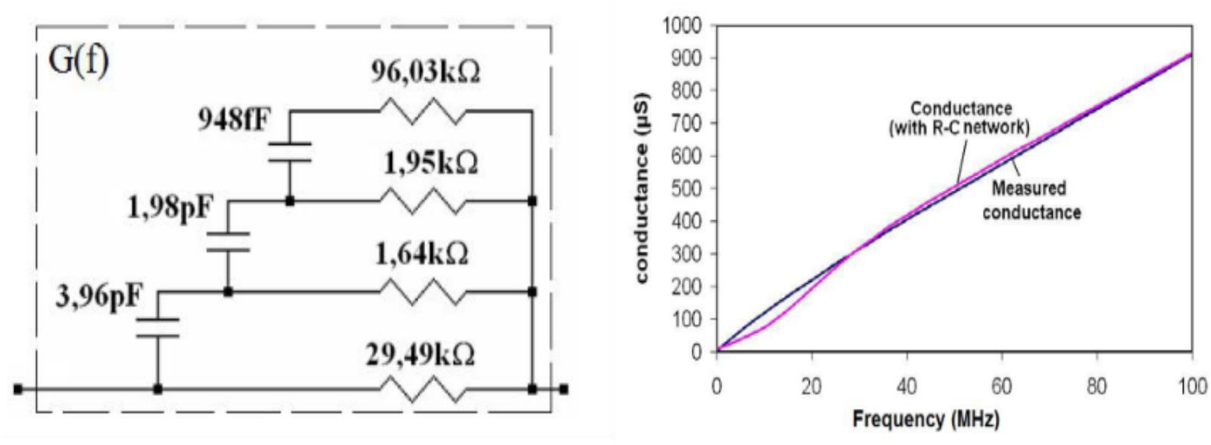

*Figure 3-7 An example of dielectric loss modeling by an RC network [77].*

An illustration of this modeling method is depicted in Figure 3-7, where an RC ladder network is proposed to represent dielectric loss. However, having a precise model that represents high-frequency effects with a limited number of components can be challenging, especially over a wide frequency range. As can be seen in the case shown in Figure 3-7, when attempting to model dielectric loss across a broad frequency spectrum (DC to 100 MHz), significant discrepancies between measured and simulated conductance emerge in the frequency range relevant to conducted emissions (150 kHz to 30 MHz). Although expanding the ladder network or employing more complex structures can potentially improve the alignment between modeled and measured results, this can lead to increased simulation time and greater difficulty in calculating network component values.

An example of an elementary cell comprising ladders and parallel networks for an unshielded 3-wire cable is presented in Figure 3-8-a, with a total of 60 circuit elements per cell. To achieve an accurate model for a 1-meter length of the cable in a frequency range from 100 kHz to 100 MHz, [87] suggests using 32 cells per meter, resulting in the simulated cable impedance shown in Figure 3-8-b. However, when applying this method to an unshielded 5-wire cable, which is the cable utilized in this study, the elementary cell structure requires 140 elements per cell.

In a large-scale system, such as an EV parking facility with just 100 meters of 5-wire cable, this translates to a staggering 444,800 circuit elements, which will significantly slow down the simulation process.

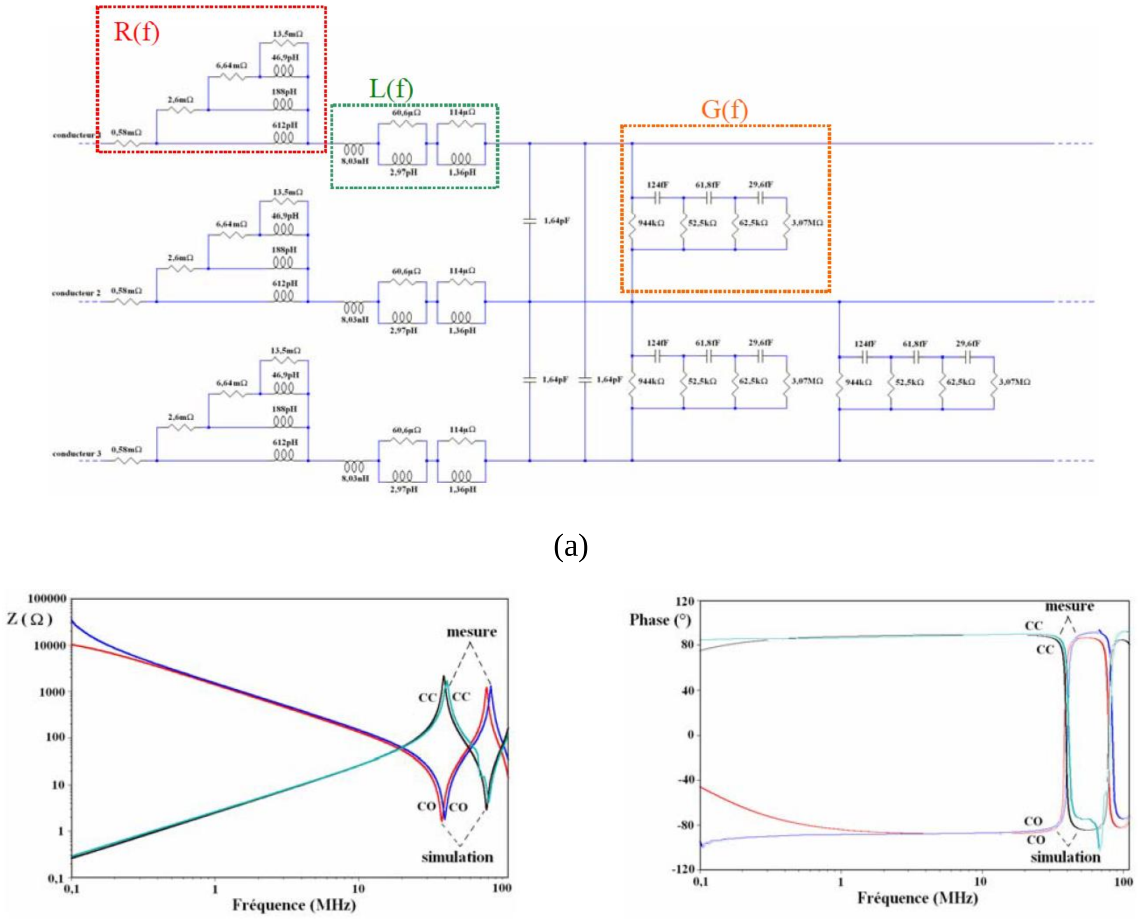

(a)

(b)

*Figure 3-8 (a) elementary cell of an unshielded 3-wire cable; (b) the simulation results for a 1-meter length of cable using 32 cells [87].*

In the simulation method mentioned above, there always exists a trade-off between the precision of the model and the complexity and the simulation time. In pursuit of a more streamlined approach, we have opted for an alternative simulation method, which will be detailed in the following section.

#### 3.2.1.1.2 The Cables Model and the Simulation Method

The cables employed in this study are unshielded 5-wire and 3-wire cables for three-phase and single-phase, respectively. They feature a conductor cross-section of 2.5 mm$^2$ and comply with the IEC 60245-4 type 66 standard.

For the extraction of frequency-dependent parameters of our unshielded 5-wire and 3-wire cables, an approach similar to that proposed by [83] for 3-wire shielded cables is adopted. The main difference lies in the inclusion of a third test to determine the coupling factor.

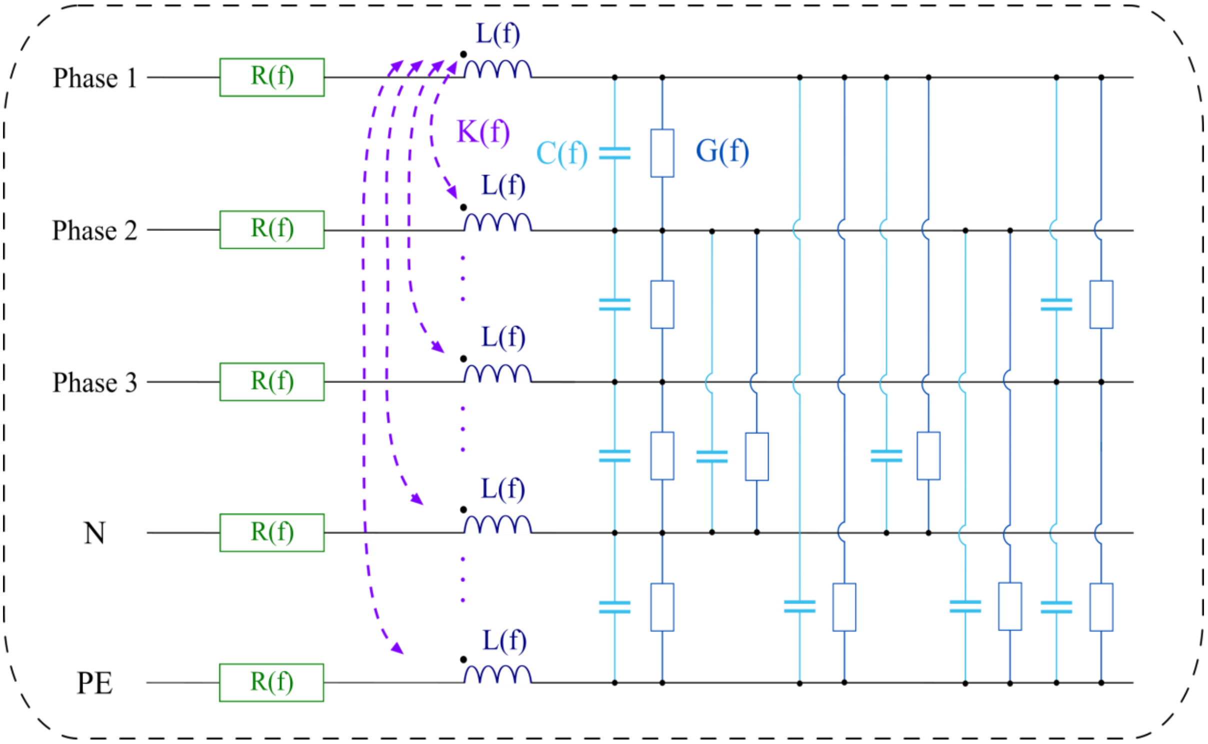

*Figure 3-9 The general equivalent model for the elementary cell of a 5-wire cable.*

The general equivalent circuit for the elementary cell of a 5-wire unshielded cable is presented in Figure 3-9. In order to extract the cell model parameters, we conduct three tests on a 33 cm length of cable using the E4990A impedance analyzer as follows:

- ❒ Short-circuit test #1, where all conductors are soldered together at one end, and the impedance is measured from the other end between one conductor and the other four conductors that are shorted together, indicated with "SC1" index;
- ❒ Short-circuit test #2, where all conductors are soldered together at both ends and the measurement is performed between the two ends, referred to with "SC2" index;
- ❒ Open-circuit test, where one cable end is left open, and the measurement is conducted from the other end between one conductor and the other four conductors shorted together, denoted with "OC" index.

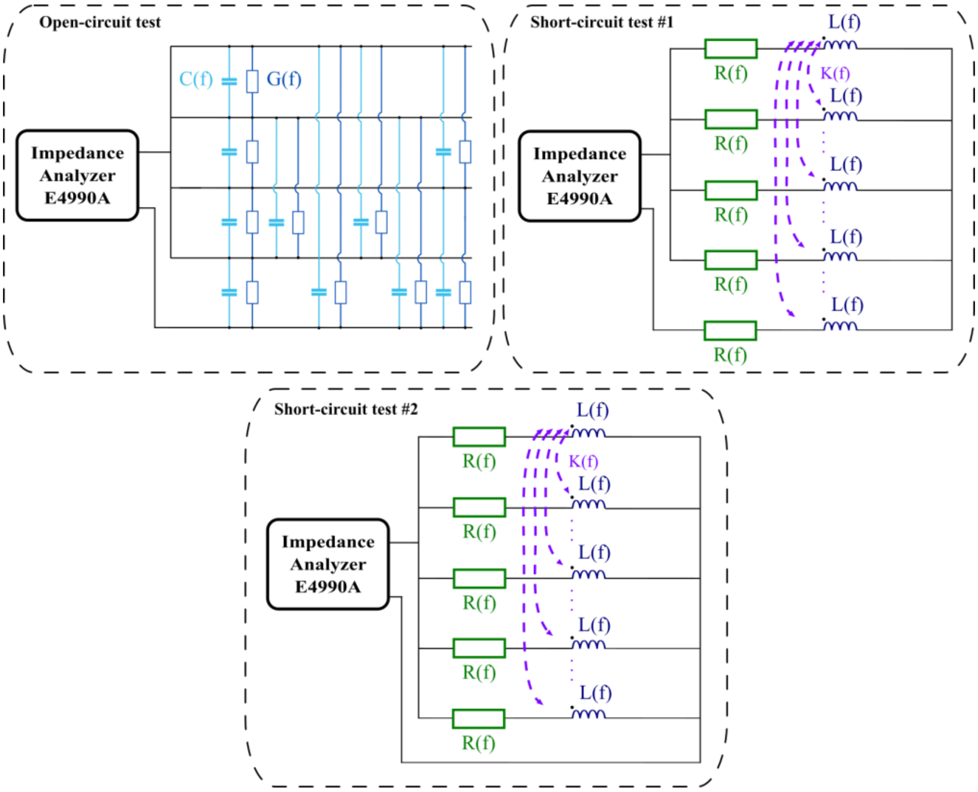

*Figure 3-10* *Parameter extraction measurements for the unshielded 5-wire cable: open-circuit and short-circuit tests.*

By applying KVL (Kirchhoff's Voltage Law) and KCL (Kirchhoff's Current Law) in the three test configurations illustrated in Figure 3-10 and converting it to the frequency domain for each the equivalent admittance in open-circuit configuration and equivalent impedances in the first and second short-circuit test arrangements, from the impedance analyzer point of view, can be calculated. The equivalent admittance and impedances are expressed in Equations 3-1, 3-2, and 3-3.

$$\boldsymbol{Y_{OC} = 4\,[G(f) + C(f).j\omega]} \tag{3-1}$$

$$\boldsymbol{Z_{SC1} = \frac{5}{4}\,[R(f) + L(f)(1 - K(f)).j\omega]} \tag{3-2}$$

$$\boldsymbol{Z_{SC2} = \frac{1}{5}\,[R(f) + L(f)(1 + 4K(f)).j\omega]} \tag{3-3}$$

Therefore, using equation *3-1*, the capacitance and the conductance can be calculated as follows:

$$\boldsymbol{C(f) = \frac{Im[Y_{OC}]}{4\omega}} \tag{3-4}$$

$$G(f) = \frac{Re[Y_{OC}]}{4} \tag{3-5}$$

The resistance can also be calculated by one of the short-circuit tests as follows:

$$R(f) = \frac{4}{5}\, Re[Z_{SC1}] \tag{3-6}$$

Equations *3-2* and *3-3* can also be expressed as

$$L(f)(1 - K(f)) = \frac{4}{5\omega} Im[Z_{SC1}] \tag{3-7}$$

$$L(f)(1 + 4\, K(f)) = \frac{1}{5\omega} Im[Z_{SC2}] \tag{3-8}$$

By solving the pair of equations above for the two unknowns – in this case, inductance and coupling factor – their values can be determined using the following expressions.

$$L(f) = \frac{1}{10\omega}[\, 4\, Im[Z_{SC1}] + Im[Z_{SC2}]] \tag{3-9}$$

$$K(f) = \frac{Im[Z_{SC2}] - 4\, Im[Z_{SC1}]}{Im[Z_{SC2}] + 16\, Im[Z_{SC1}]} \tag{3-10}$$

The RLCG parameters of our unshielded 5-wire cable, calculated based on the measurements explained above, are presented in Figure 3-11.

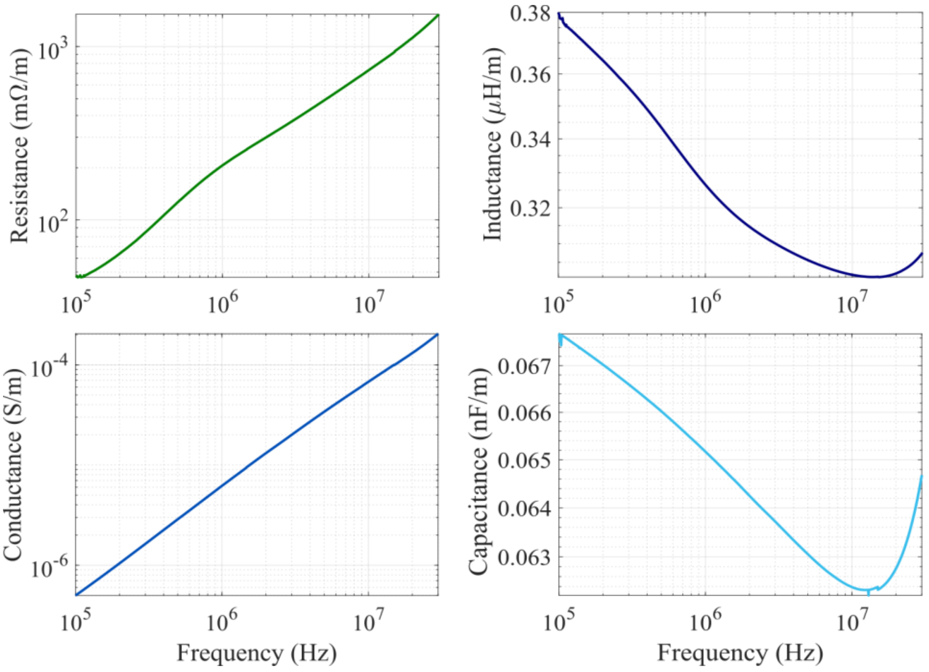

*Figure 3-11 Evolution of extracted RLCG parameters with frequency in the unshielded 5-wire cable.*

These results revealed that the coupling factor is negligible across the frequency range, with minimum and maximum values ranging from 0.045 to 0.089, and thus, can be disregarded. This approach was also employed for the calculation of the 3-wire unshielded cable cell parameters, the details of which are not provided here for the sake of brevity.

The simulation is carried out in the LTspice environment, operating in the frequency domain. The LTspice AC analysis allows for incorporating components defined based on an experimental acquisition of impedances, facilitating accurate modeling of high-frequency effects without the need for the ladder and parallel networks. The final simulated cell model with 15 components per cell is illustrated in Figure 3-12. This model is based on two defined impedances $Z_s$ and $Z_p$ that include the mentioned evolution of series and parallel parameters due to high-frequency effects. An example demonstrating this type of component definition in LTspice is provided in Appendix C.

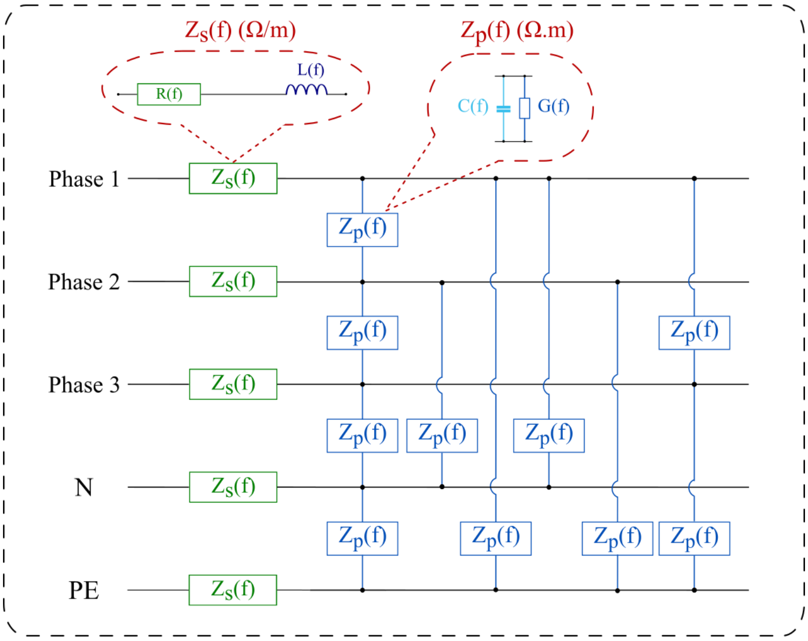

*Figure 3-12 Final modeled cell for the unshielded 5-wire cable.*

Figure 3-13 presents the step-by-step process of cable simulation using MATLAB and LTspice. Initially, MATLAB is utilized to compute the RLCG parameters, as previously described. Subsequently, two impedances ($Z_s$ and $Z_p$) are defined based on the obtained data. A text editing program is developed to automate the netlist writing process and ensure compatibility with the LTspice netlist syntax. Using this program and the provided inputs, the number of cells is calculated, and a subcircuit is generated based on the cell topology (3-wire or 5-wire), encompassing all cascaded cells. It is worth mentioning that a minimum of three cells is considered for cables shorter than one meter. Once the subcircuit file is automatically generated, a premade block is added to the LTspice schematic and associated with the generated subcircuit file.

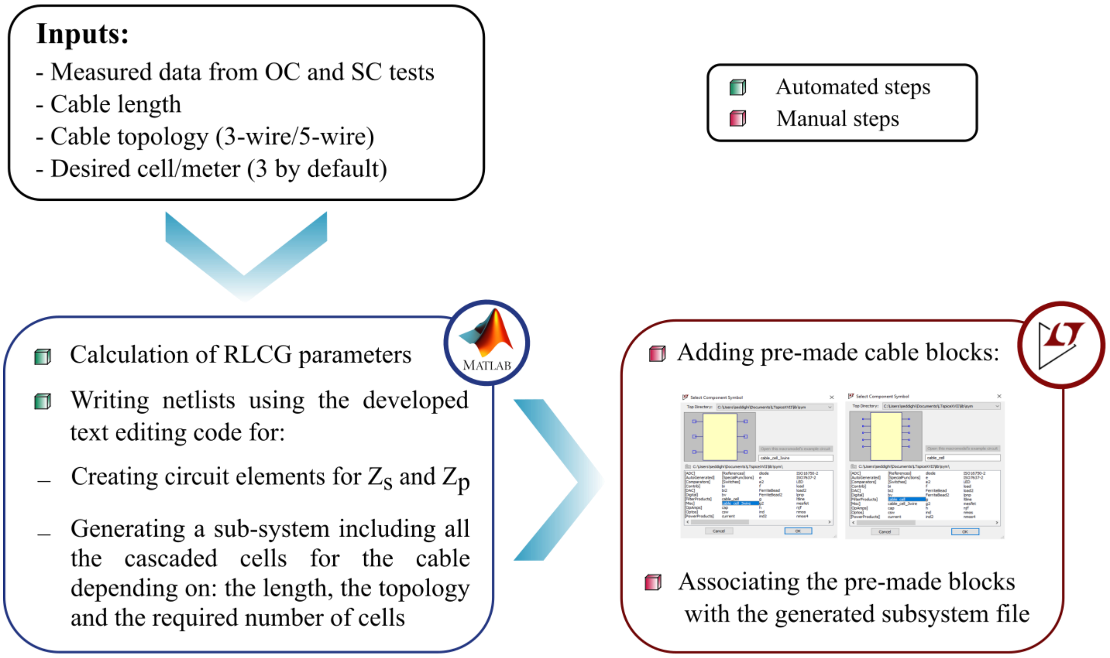

*Figure 3-13 Cable modeling and simulation method using MATLAB and LTspice.*

As an example, Figure 3-14 illustrates the simulated open-circuit impedance of a 10-meter-long unshielded 5-wire cable with a different number of cells per meter. The simulated impedance, employing one, three, and ten cells per meter, demonstrates that after three cells per meter, the results converge, indicating that additional cells are unnecessary. Therefore, the program defaults to employing three cells per meter as it strikes a balance between accuracy and computational efficiency.

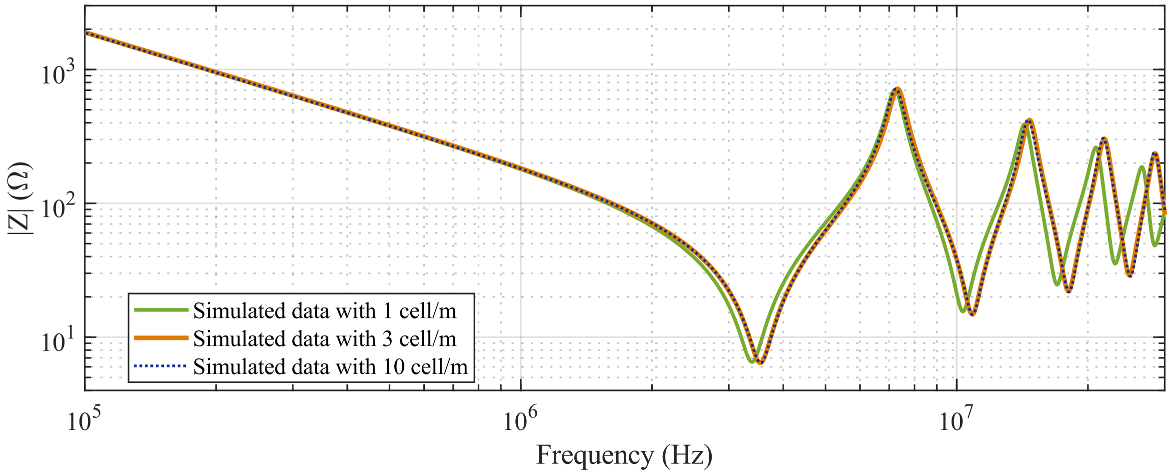

*Figure 3-14 Comparison between simulated data for the open-circuit impedance of the modeled cable of 10 meters with a different number of cells.*

The comparison between measured and simulated data for the open-circuit impedance of a 10-meter-long unshielded 5-wire cable is also illustrated in Figure 3-15.

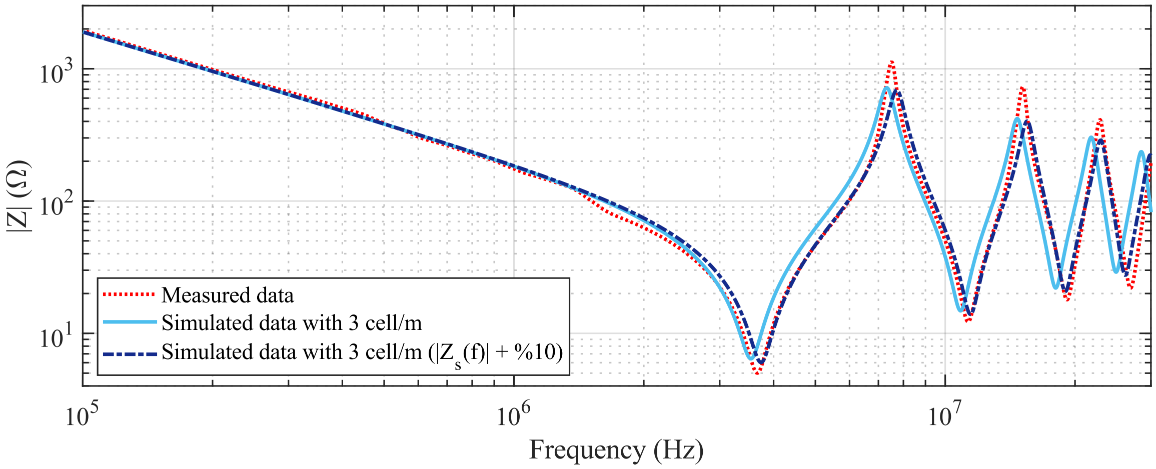

*Figure 3-15 Comparison between simulated and measured data for the open-circuit impedance of the modeled cable of 10 meters.*

In this method, the accuracy of the measurements becomes crucial as the results are sensitive to the defined components. For example, when simulating the case with three cells per meter and introducing a 10 percent error to $Z_s$, the discrepancy becomes evident. As can be seen in Figure 3-15, without considering the error, the simulated results show the first resonance frequency occurring several tens of kHz prior to the measured data. However, after applying this error, this frequency is shifted to several tens of kHz after the frequency observed in the measured data. In addition, the deviation between measured and simulated data can also be attributed to the placement and surroundings of the 10-meter-long cable during impedance measurement.

In comparison to the approach outlined in Figure 3-8, this simulation method reduced the number of components per elementary cell from 140 to 15. Additionally, adopting three cells per meter instead of 32 cells per meter decreased the total number of components by approximately 100-fold. Consequently, for a 100-meter cable, only 4500 components are utilized in total, as opposed to 448,000 components.

Indeed, achieving such a reduction in component count is highly beneficial for our objective of predicting conducted emissions levels in large-scale systems such as electric vehicle parking. Through accurate prediction and observation of the distribution of both DM and CM currents across various paths, we can improve the effectiveness of OBC’s EMC filters by preventing potential scenarios that may cause malfunctions. This not only ensures compliance with regulatory standards but also enhances the overall performance and reliability of the electric vehicle charging infrastructure.

It is essential to acknowledge that this approach lacks the capability for time-domain analysis. However, by prioritizing frequency-domain modeling, we can develop simpler and more efficient models. While time-domain analysis offers valuable insights, the ultimate goal often centers on interpreting the signal spectrum, especially since compliance standards are specified in the frequency domain. Therefore, focusing on frequency-domain modeling aligns well with the objective of assessing conducted emissions.

It is worth mentioning that the evolution of the RLCG parameters with frequency is relatively straightforward, as demonstrated in Figure 3-7 and Figure 3-11. Thus, it is feasible to model this evolution with sufficient accuracy using ladders and parallel networks. However, for cases that are more complicated and involve multiple resonances, this method can introduce a magnificent error. For instance, in [88], a motor winding impedance variation with frequency modeled with this approach exhibited a discrepancy of over 200% at frequencies near one of the resonances. This highlights the challenge of accurately modeling the complex impedance curves, particularly those with several resonances, as it requires more complex equivalent circuit structures and networks, which will eventually make the process of tuning the parameters extremely difficult, even using numerical curve fitting tools.

Therefore, while suitable for specific applications, this method may not be sufficient for modeling complex impedances such as transformer windings, as will be discussed in the following section.

#### 3.2.1.2 Grid, transformer, and autotransformer modeling

As mentioned previously, one of the objectives of the microgrid is to have a controlled environment. It was also stated that by employing a transformer and an autotransformer, the impedance variations in the grid behind them do not influence the impedance observed from the secondary side. To verify this statement in our case, two impedance measurements were done from the secondary side of the transformer:

- Firstly, as depicted in Figure 3-16 with the impedance analyzer, when the transformer and autotransformer are connected to each other without being connected to the grid, and the primary side of the autotransformer is short-circuited while its sliding brush is adjusted to the nominal voltage value. This configuration effectively shorted the magnetizing inductance, providing an approximate measurement of the leakage inductances of both the transformer and autotransformer.

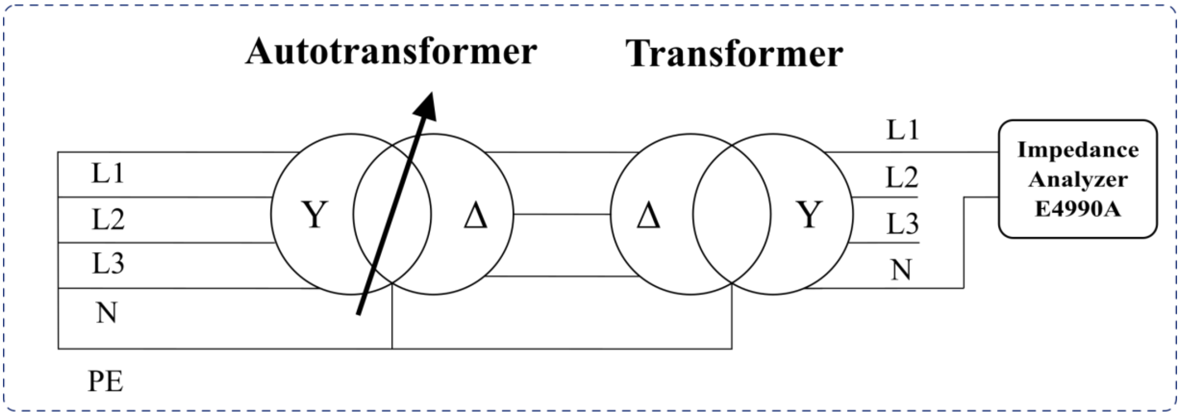

*Figure 3-16 The test configuration used for transformer secondary side impedance measurement with the IA.*

- Secondly, with the TP method using the DM configuration, when the transformer and autotransformer are connected to the grid and the sliding brush is set on the nominal voltage value, as demonstrated in Figure 3-17.

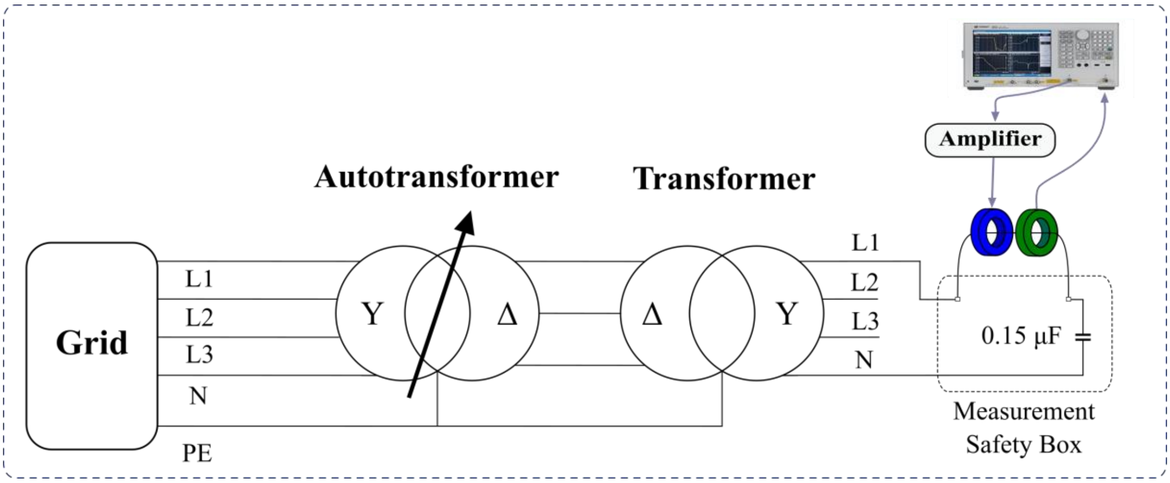

*Figure 3-17 The test configuration used for transformer secondary side impedance measurement with the TP method.*

Obtained results from these two measurements for one phase are presented in Figure 3-18. These data suggest that the impedance observed from the secondary of the transformer within the frequency range of interest predominantly corresponds to that of the transformer and autotransformer, and thus, the impedance of the grid behind it appears to have minimal to no impact. The slight difference observed between the two curves at frequencies exceeding

10 MHz is primarily attributed to the degraded accuracy of the TP method in this frequency range.

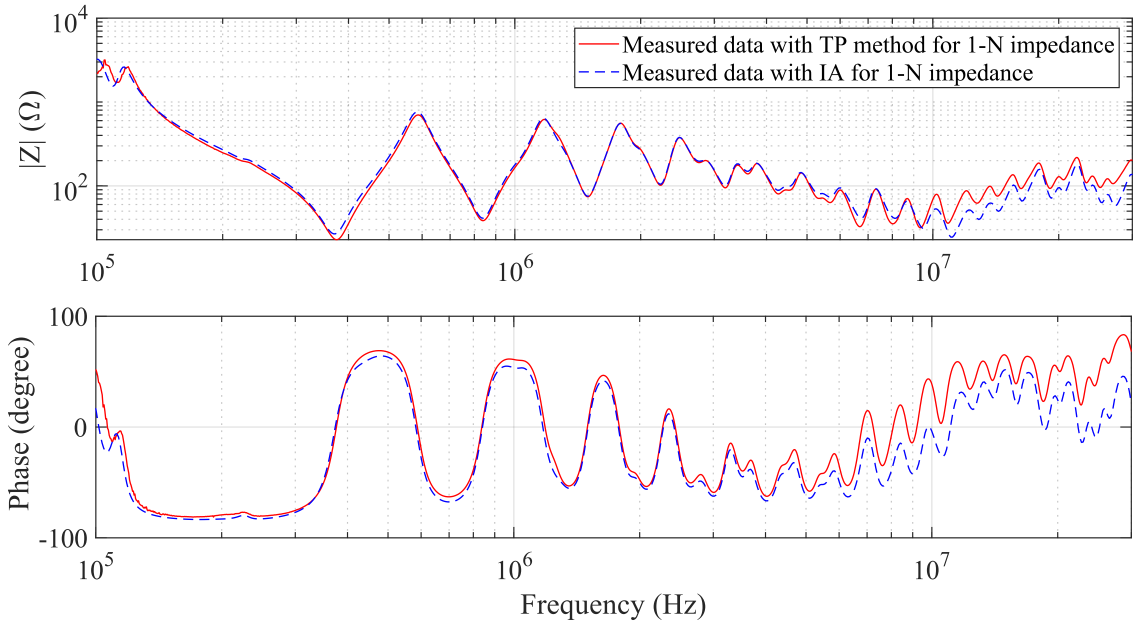

*Figure 3-18 Comparison between the measured transformer impedance from the secondary side perspective via IA and TP method.*

Given that variations in grid impedance do not affect the impedance from the secondary side of the transformer perspective, we can simplify our model by defining a T model, as illustrated in Figure 3-19, for the autotransformer, the transformer, and the grid altogether.

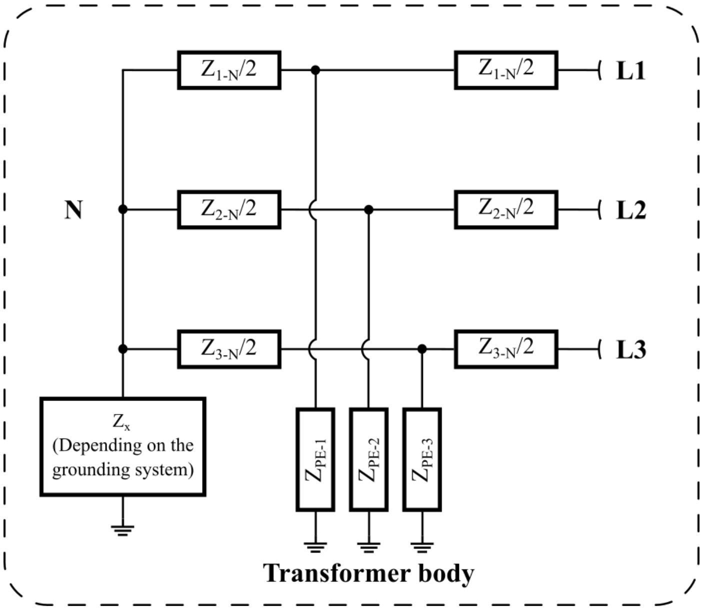

*Figure 3-19 Equivalent model for the grid, the autotransformer, and the transformer.*

While the autotransformer was primarily utilized for voltage level regulation, it also contributes to higher impedance stability due to its typically higher leakage inductance. It is also worth mentioning that this model is valid for a fixed position of the sliding brush since the impedance seen from the output is dependent on the sliding brush position, which, in our case, is set on the nominal voltage.

#### 3.2.1.3 Grounding systems modeling

The six grounding systems, presented in Figure 1-17, are modeled by the impedance of the neutral ($Z_N$) and the number of ground connections. Theoretically, $Z_N$ can be either zero or infinite. However, in reality, it manifests as either a short wire with inductive behavior or an Insulation Monitoring Device (IMD) with capacitive behavior, which is mandatory in IT systems.

Figure 3-20 presents the model of the TTS and ITS systems, featuring three separate ground connections. The ground connection to which the transformer body is connected is considered the reference and is the input ground coming from the building ground connection.

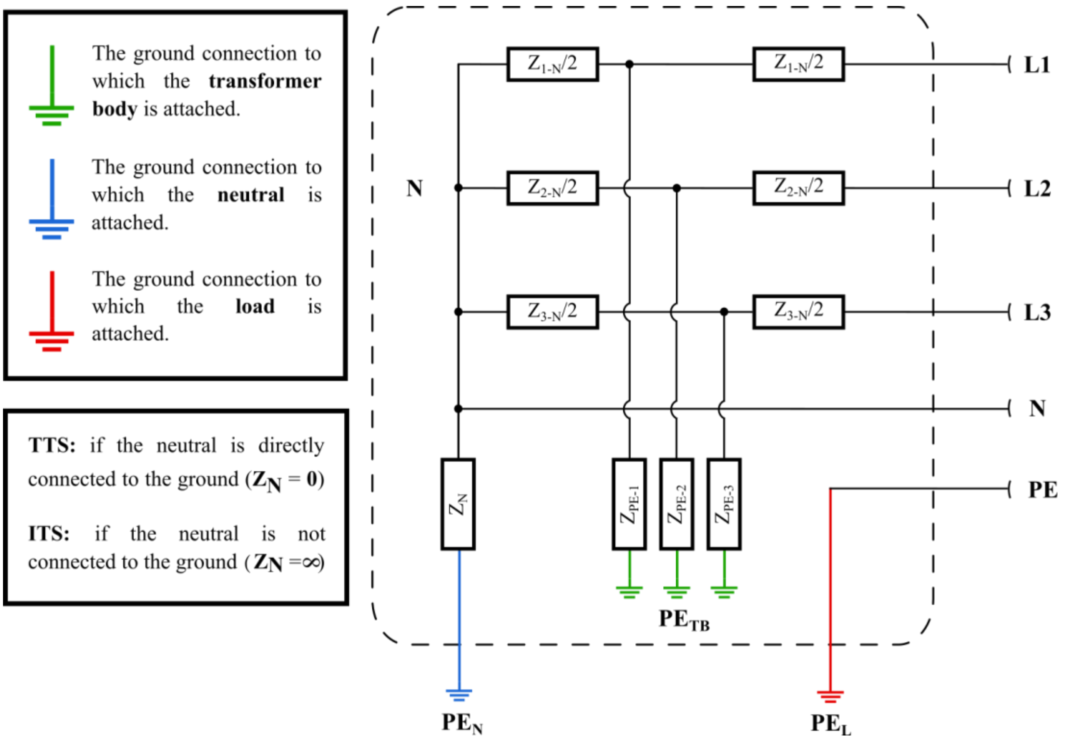

*Figure 3-20 Model of the TTS and ITS systems by three separate ground connections.*

In this case, as presented in Figure 3-21, the other two required grounds are emulated by inserting two resistors between the reference ground and each of the other ones since we could not establish physical ground connections.

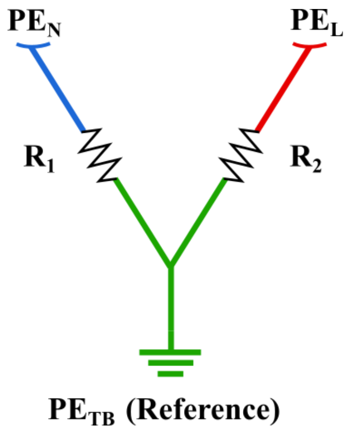

*Figure 3-21 The realization of three distinct grounds.*

The resistor values ($R_1$ =10 Ω and $R_2$ =7 Ω) are selected to be around the typical resistance of the earth (~10 Ω), which is mentioned in [48]. However, it is important to note that this emulation does not entirely represent the high-frequency behavior of an actual ground connection.

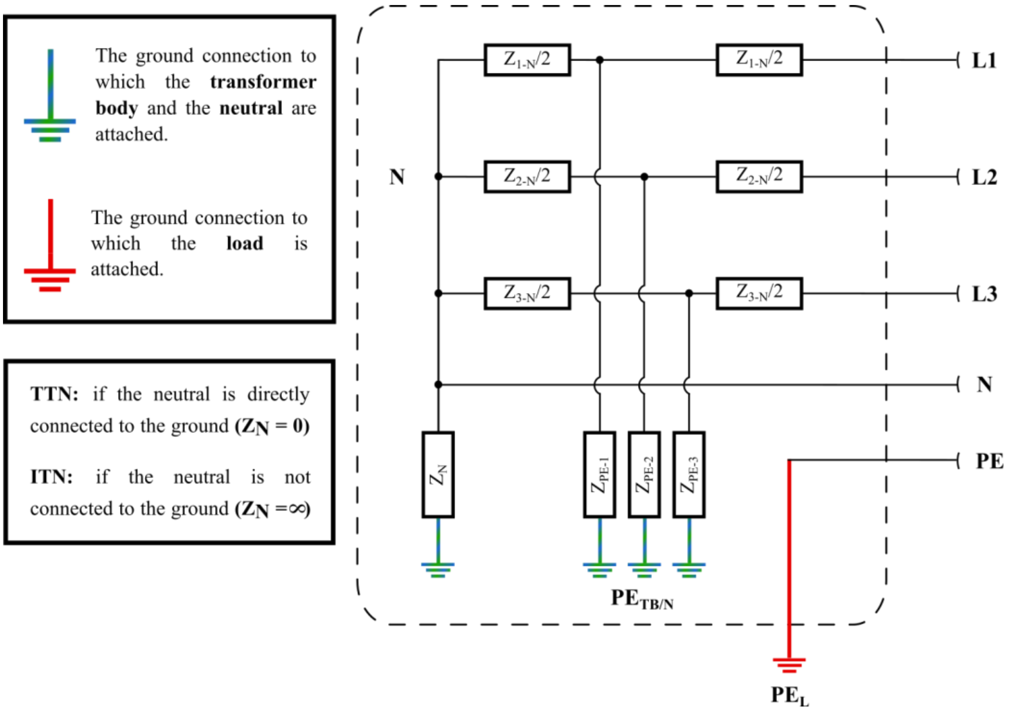
The ground connection to which the **transformer body** and the **neutral** are attached.

The ground connection to which the **load** is attached.

**TTN:** if the neutral is directly connected to the ground **($Z_N$ = 0)**

**ITN:** if the neutral is not connected to the ground **($Z_N$ =∞)**

*Figure 3-22 Model of the TTN and ITN systems by two separate ground connections.*

TTN and ITN models are depicted in Figure 3-22. These systems require two distinct ground connections: one for the loads' ground and another for the transformer body and the neutral. On the other hand, in TNR and ITR systems, the grounds are linked to each other, and thus, the input ground is connected to the frame, the neutral, and the loads' ground, as demonstrated in Figure 3-23.

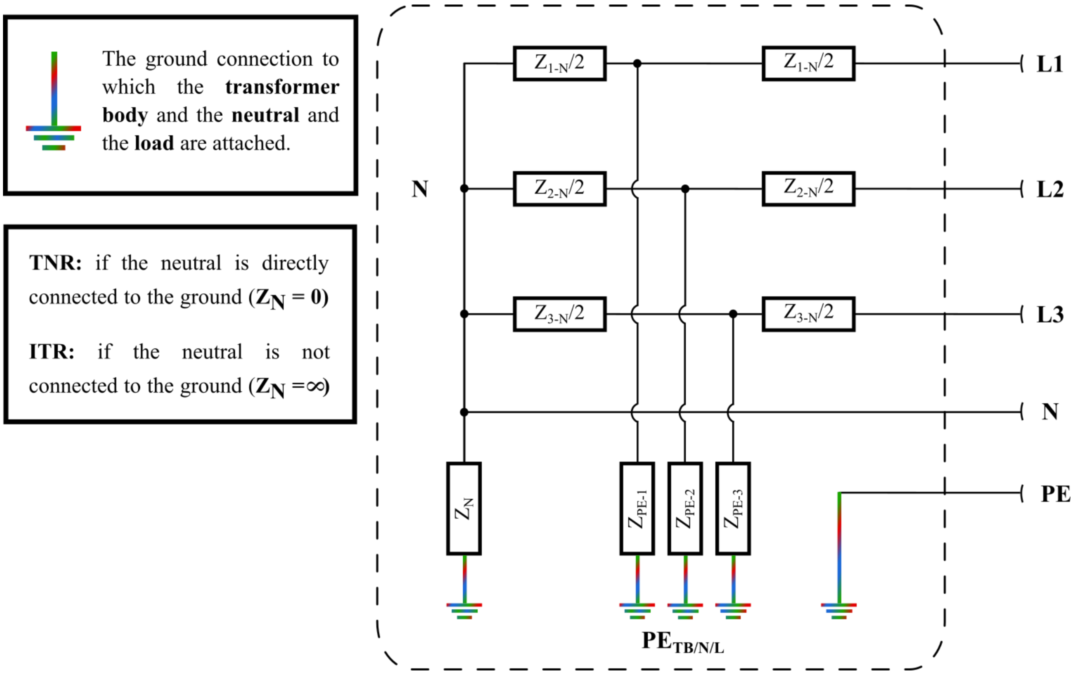

*Figure 3-23 Model of the TNR and ITR systems by a single ground connection.*

Each grounding system is modeled based on the measured impedance of the utilized resistors, the Isolation Monitoring Device (IMD), and the wire used to connect the neutral to the ground. Consequently, all models were added to our model library, which includes all the possible states of the realized microgrid.

### 3.2.1.4 Circuit breakers modeling

The circuit breaker mechanism generally relies on a latch to maintain contacts in the closed position. When the contacts are closed, the current flows through a solenoid. This solenoid is designed so that when its current surpasses the circuit breaker's rating, the solenoid's pull releases the latch, causing the contacts to open due to the spring action. Consequently, when the contacts are closed, they exhibit inductive characteristics due to the solenoid, while in the open state, they display capacitive properties. The impedance of the circuit breakers in both open and closed states is measured, modeled, and included in our library. The open-state impedances of the circuit breakers are presented in Figure 3-24, where their capacitive properties can be observed. The capacitance values for the two Miniature Circuit Breakers (MCBs) – C10 and C16 – are the same, approximately 3.1 pF, while for the Residual Circuit Breaker with Overload protection (RCBO) – C40 – a capacitance value of roughly 5.6 pF.

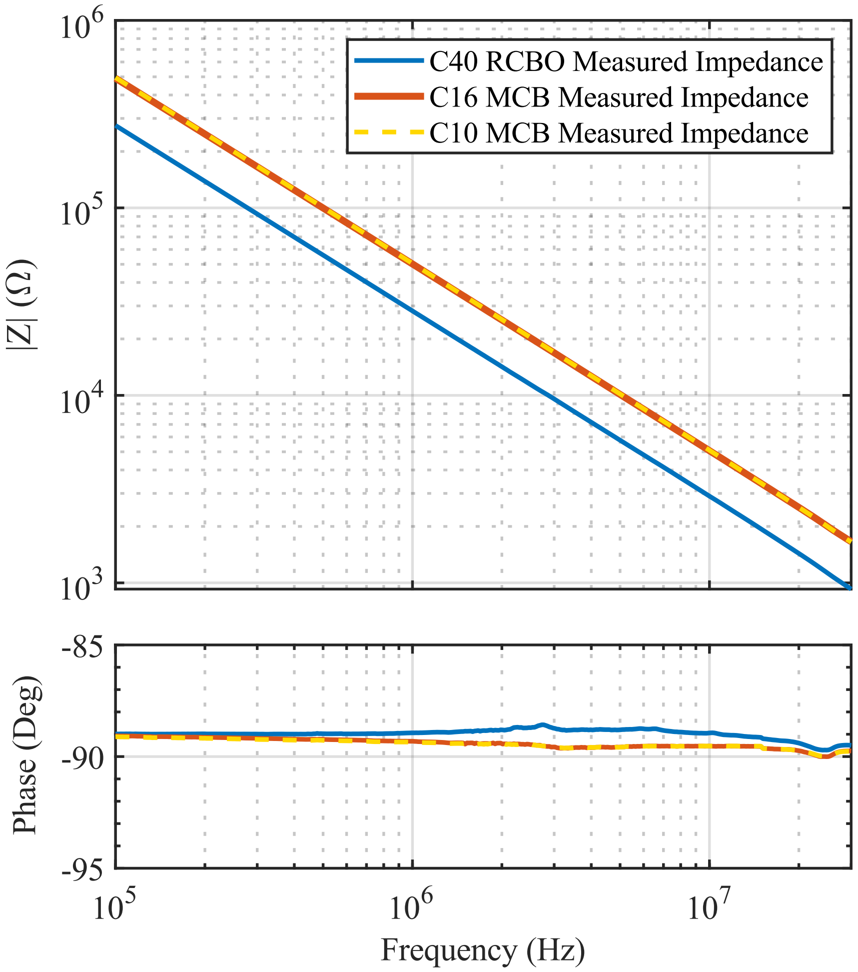

*Figure 3-24 Measured impedances of circuit breakers in the off state with different limitation currents.*

It is worth mentioning that in the case of the RCBO, measuring the on-state impedance of each phase separately is not possible due to differential protection. Therefore, by connecting three breakers in parallel and injecting between the fourth breaker and the other three, the equivalent impedance was measured, and then the impedance for each phase was calculated.

As presented in Figure 3-25, the impedance of a circuit breaker in the closed state increases when its limitation current is lower. This can be due to the fact that as the limitation current decreases, a higher number of turns are required in the solenoid to generate the same level of magnetic field according to Ampere’s law. Therefore, an increased number of turns leads to higher resistance and inductance for the winding. The approximate inductance values for C10, C16, and C40 breakers are 360 µH, 140 µH, and 110 µH, respectively.

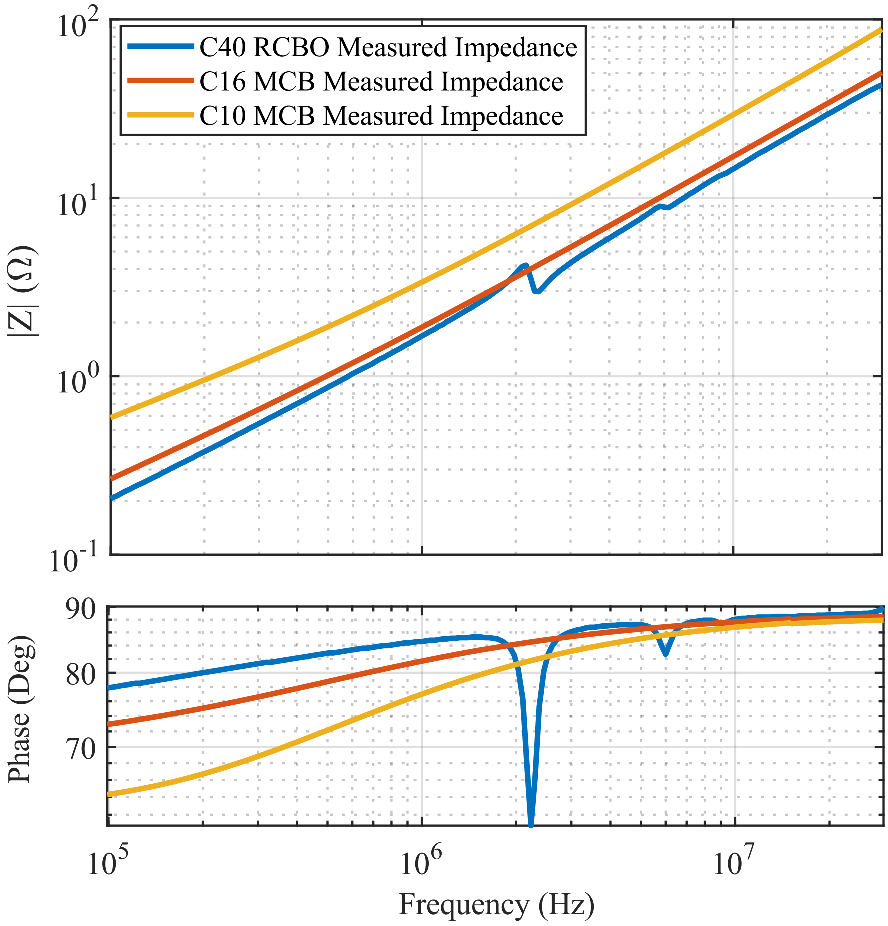

*Figure 3-25 Measured impedances of circuit breakers in the on state with different limitation currents.*

#### 3.2.1.5 Microgrid model verification

In order to assess the performance of our model, a series of impedance measurements were conducted using the E4990A impedance analyzer and the 42941A impedance probe from different points of the microgrid, with and without the presence of the loads. These measurements were performed while the primary side of the autotransformer was short-circuited, as shown in Figure 3-26-b. Moreover, all the verification measurements were conducted when the sliding brush of the autotransformer was set to the nominal voltage, and the ITR system was implemented within the transformer. The numbering of outlets is also presented in Figure 3-26-b. Furthermore, the loads are characterized by their impedance, as detailed in Appendix D, and then incorporated into the model.

It is worth mentioning that the wiring inside the electric panel is also accounted for in the model, whether it involves 3-wire cables for single-phase outlets or 5-wire cables for three-phase outlets. The cable lengths from the input to an outlet vary, ranging from 130 cm for outlet #6 to 161 cm for outlet #3, depending on the placement of the outlet and the circuit breakers. Afterward, the measured data are compared to the simulated results, as presented in Figure 3-27, Figure 3-28, and Figure 3-29, to verify the model's validity in the frequency range of interest.

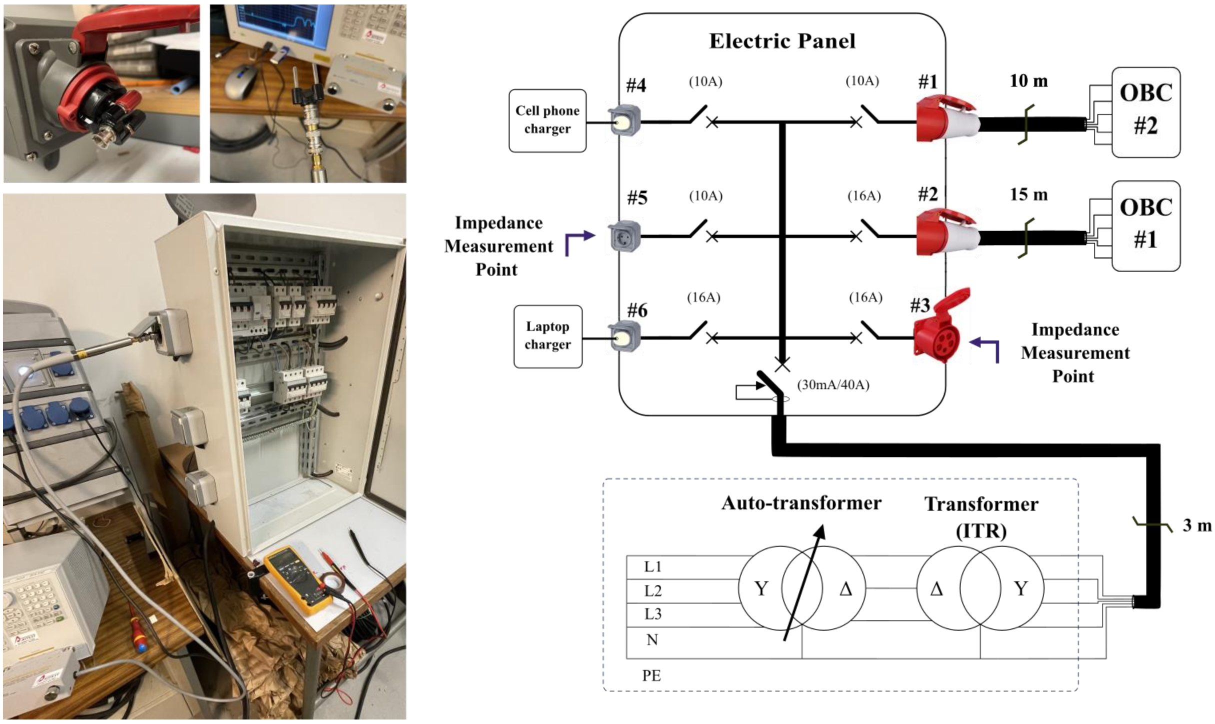

(a) (b)

*Figure 3-26 Microgrid model verification: (a) measurement setup and connections; (b) The microgrid diagram with all the loads connected.*

Figure 3-27 provides a comparison between line-to-ground impedance results from outlet #3 in two scenarios – without loads and with the two OBCs – derived from the model and measurements. In the case where no load is connected to the microgrid, the deviation between simulated and measured data is more noticeable, as can be seen in Figure 3-27-b, which is partly due to the simplifications made during the microgrid modeling process. For instance, cable wires are assumed to stay inside their isolation as a cable all along even inside the electric panel. However, in practice, the insulation of the cable was removed, and wires were separated in certain sections within the electric panel where they were connected to circuit breakers. However, a lesser discrepancy can be observed when a few loads are attached.

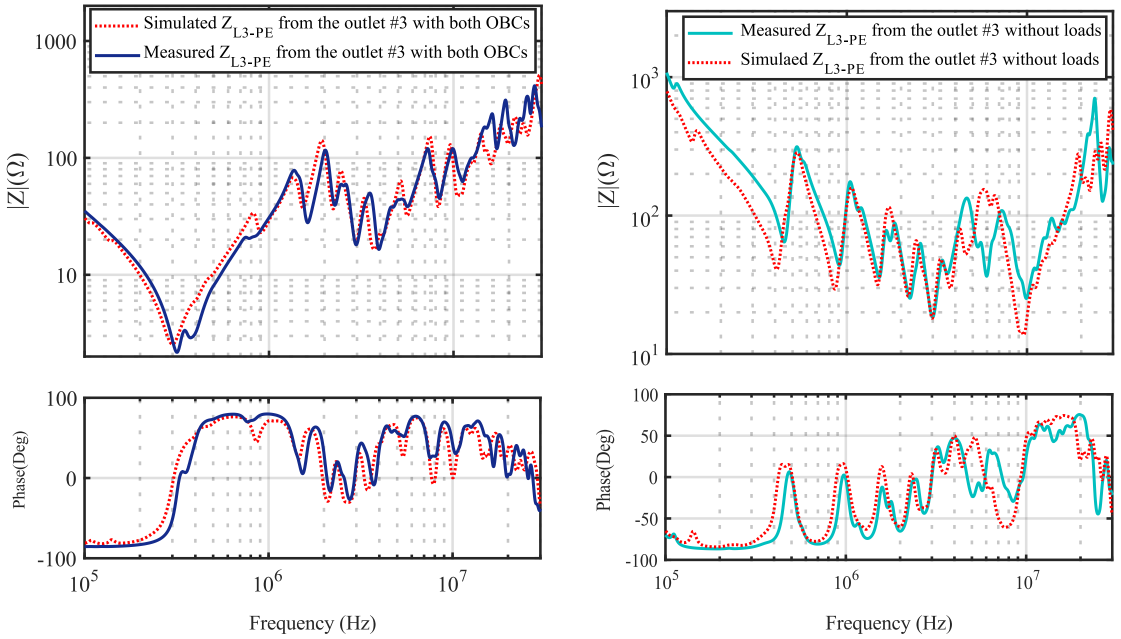

(a) (b)

*Figure 3-27 Measured and simulated line-to-ground impedance comparison: (a) with both OBCs, (b) without loads.*

The line-to-line impedance from outlet #3 with and without loads, and DM impedance from single-phase outlet #5, are also presented in Figure 3-28 and Figure 3-29, respectively. Despite the complexity of the presented impedances, the presented simulated results derived from the developed model exhibit an overall acceptable agreement with measured data.

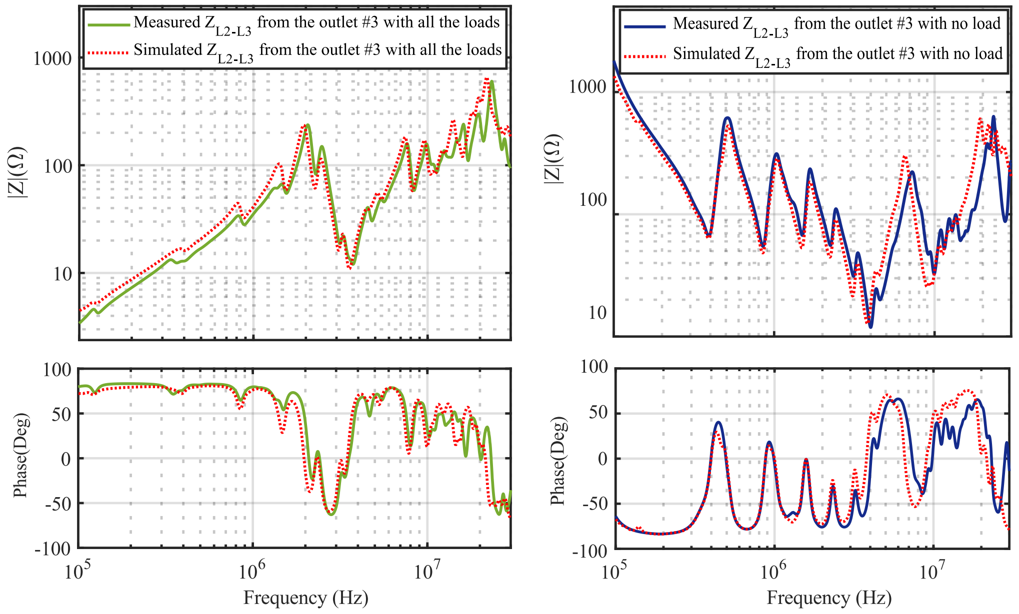

(a) (b)

*Figure 3-28 Measured and simulated line-to-line impedance comparison: (a) with all the loads, (b) without loads.*

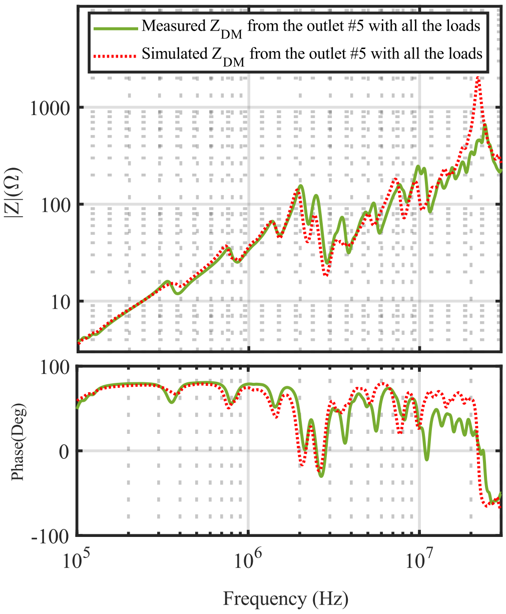

*Figure 3-29 Comparison of measured and simulated DM impedance from outlet #5 with all the loads.*

Now that the model has been validated, we can determine any impedance – DM or CM – from any point within the microgrid using the developed model. For instance, Figure 3-30 demonstrates the difference between CM impedance from outlet #2 in ITR and TNR grounding systems when no load is connected to the microgrid.

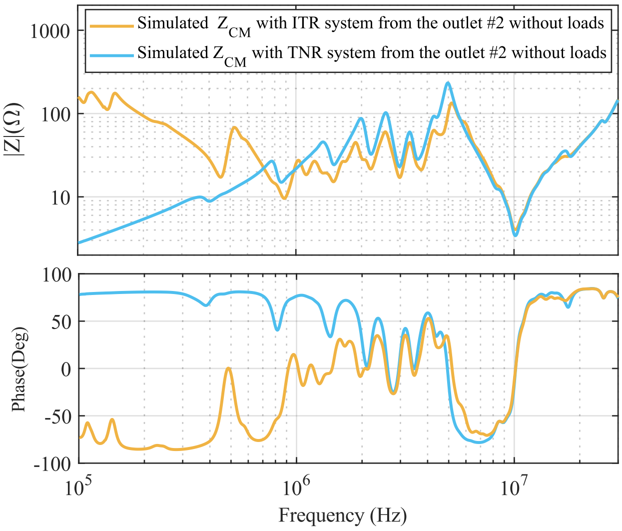

*Figure 3-30 Comparison of the simulated CM impedance in ITR and TNR systems.*

This model can serve as an efficient tool for observing the impedance from any desired location within the system with a user-friendly interface provided by LTspice. Moreover, the simulation time for the mentioned case, with all the loads connected to the microgrid, does not exceed 20 seconds, which allows for facilitated and quick HF impedance analysis in large-scale systems.

### 3.2.2 HF Model of the Bi-directional OBC

This section is dedicated to the definition of an HF model for the bi-directional OBC as the perturbation source. This model enables the prediction of conducted emissions at any point within the microgrid when integrated into the microgrid model. As mentioned earlier, the behavioral modeling approach for the converter is selected due to its alignment with our objectives and constraints, including prototype confidentiality and the ability to simulate a large-scale system with a reduced calculation time.

In the following section, a brief overview of the state of the art in the black box modeling approach for converters will be presented, followed by the development of the black box model for the OBC.

#### 3.2.2.1 State of the art in HF behavioral modeling of a converter

The black box modeling approach is based on the multi-port network representation of the power converters including independent sources and an associated impedance matrix. By linearizing the non-linear system – the power converter that incorporates power switches – around an operating point this method offers a simplified model of the system, which can be used to predict the conducted emissions in the frequency domain.

This modeling approach is employed in many research works. In [89] and [40], two-port black box models have been proposed to represent the high-frequency behavior of DC/DC converters. As presented in Figure 3-31, the equivalent circuit of these black box models can be different depending on preferences of using voltage or current sources.

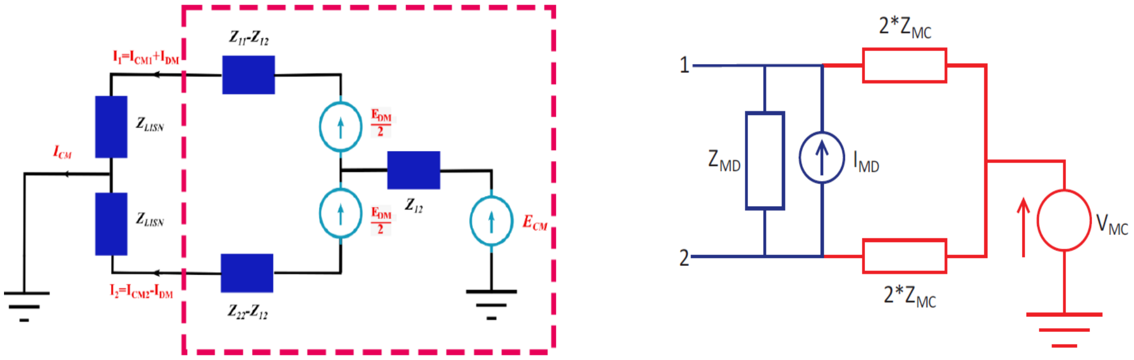

(a) (b)

*Figure 3-31 Two different equivalent models for DC/DC converters based on two-port black box network proposed by: (a) [40], (b) [89].*

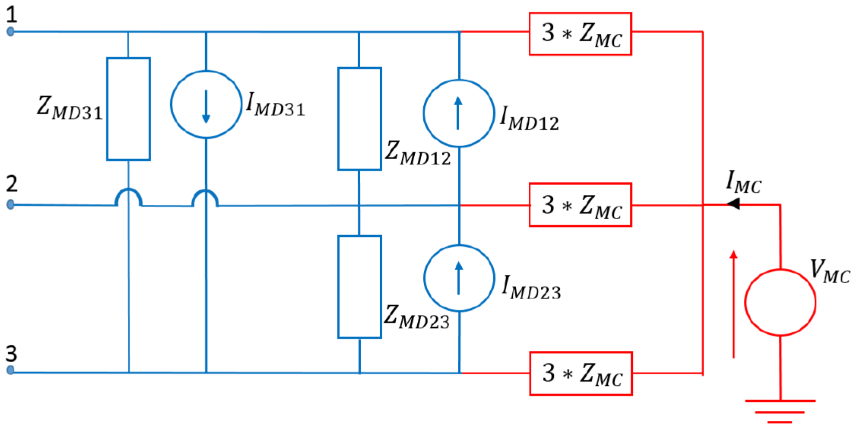

*Figure 3-32 Black box model for the AC side of a three-phase inverter [90].*

In [90], a three-port black box model, presented in Figure 3-32, is developed for the AC side of a three-phase inverter. In order to find the parameters of the model's equivalent circuit, first, the CM and DM impedances must be measured, and this should be followed by the calculation of the perturbation sources. Figure 3-33 presents the proposed measurement configurations for each of the impedances defined in the model, which were done with an impedance analyzer in offline mode.

For the perturbation sources calculations, the superposition theorem is applied, and four different configurations, each time by considering that one of the independent sources is active and by turning off the three other sources, are analyzed.

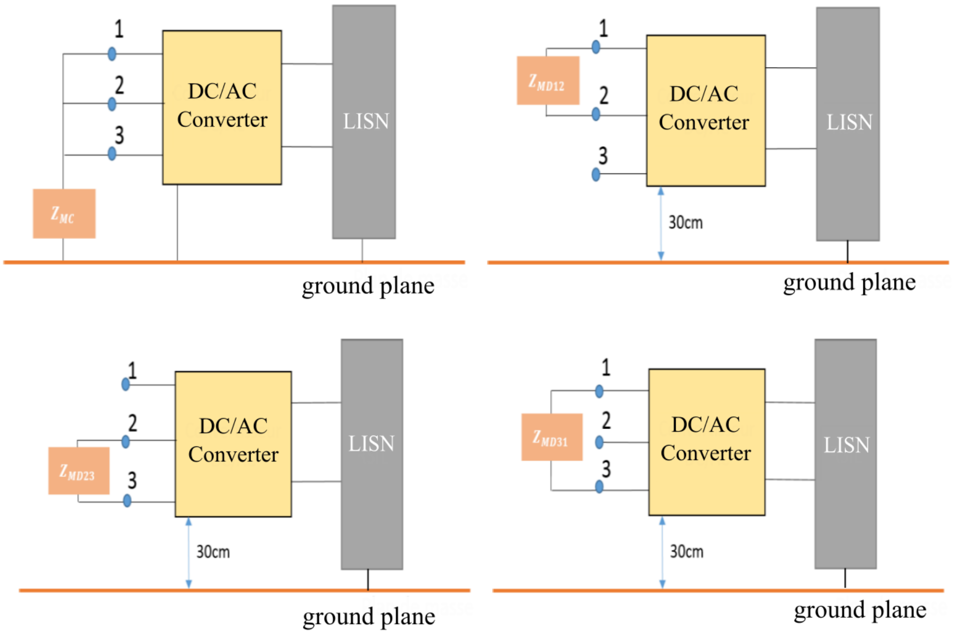

*Figure 3-33 DM and CM impedance measurement configurations in a 3-phase converter using an impedance analyzer [90].*

In [90], like all other studies mentioned earlier, the analytic approach is employed to calculate the perturbation sources by employing the superposition theorem. However, in three-port models the analytic calculation is much more complicated than in two-port. Particularly in the case of DM sources calculation, the analytic approach is notably lengthy. As described for one of the DM configurations in detail in Appendix E, using Norton theorem, the relation of the differential current source between lines 1 and 2, depicted in Figure 3-32, and the output currents can be expressed:

$$\boldsymbol{I_{DM12}} = \frac{\boldsymbol{I_1 - I_2}}{\boldsymbol{3\,\alpha}} \tag{3-11}$$

where $\boldsymbol{I_1}$ and $\boldsymbol{I}_2$ are output currents for lines 1 and 2, and $\boldsymbol{\alpha}$ is defined as

$$\boldsymbol{\alpha} = \frac{\boldsymbol{Z_N\,Z_P}}{\boldsymbol{(Z_N + Z_{charge})(Z_P + Z_{charge})}} \tag{3-12}$$

where $Z_{\mathrm{charge}}$ is the impedance of the symmetric load connected to the model and $Z_P$ and $Z_N$ are

$$\boldsymbol{Z_P} = \frac{\boldsymbol{9Z_{MD}\,Z_{MC}}}{\boldsymbol{Z_{MD} + 9Z_{MC}}} \tag{3-13}$$

$$\boldsymbol{Z_N} = \frac{\boldsymbol{(((2Z_{charge} + Z_P)||\,Z_{charge}) + (Z_P||\left(2Z_P + \frac{Z_P^2}{Z_{charge}}\right))).\,(2Z_{charge} + Z_P)}}{\boldsymbol{2Z_{charge} + Z_P + \left((2Z_{charge} + Z_P\right)||\,Z_{charge}) + (Z_P||\left(2Z_P + \frac{Z_P^2}{Z_{charge}}\right))}} \tag{3-14}$$

In this calculation, the assumption for simplification is that the system is completely symmetric, including load impedances, CM impedances, and DM impedances. Due to the complexity of the circuit, the analytic approach is extremely time-consuming and challenging for non-symmetric systems with more than three ports, such as the system that we are analyzing in our study.

#### 3.2.2.2 Black box model of the OBC under the nominal voltage

In order to model the three-phase OBC from the AC side, a four-port black box model is proposed, as illustrated in Figure 3-34. The differential mode is represented by six non-identical DM impedances and three current sources, while the common mode is modeled by three identical impedances, supposing that the total CM impedance is evenly distributed.

Although we refer to it as a black box model, it is not entirely opaque since we know there is no fourth switching leg on the neutral, so instead of six DM sources, three DM sources are considered for our model, and this way, we simplified the model.

Due to the presence of relays in the entry of the OBC prototype, in order to measure the CM and DM impedances the measurement must be conducted under operational voltage conditions, allowing the relays to close. This implies that measurements cannot be done with off-line methods such as an impedance analyzer. Therefore, the TP method that was developed in section 2.1.2 can be employed once more to perform impedance measurements.

The OBC is controlled via the CAN interface and using CANalyzer software. Once the appropriate voltage level is achieved, the command to close the relays can be executed.

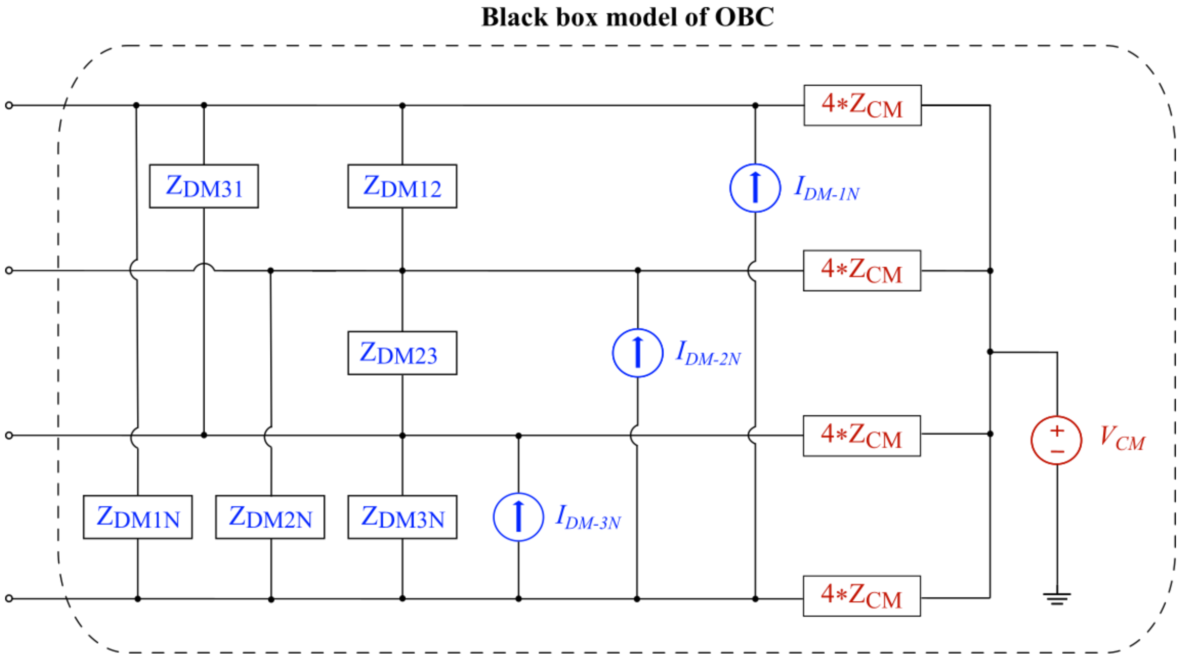

*Figure 3-34 Proposed black box model for the OBC.*

In order to measure the parameters of the proposed model under voltage, the NNLK 8121 three-phase LISN is inserted in the circuit in both impedance measurement and source identification processes. This LISN includes four identical 50 µH/50 Ω networks used only for AC power mains based on CISPR 16 standard with a frequency range from 9 kHz to 30 MHz. It is essential to mention that the BNC socket must be terminated with 50 Ω if it is not directly connected to the EMI test receiver. The measured impedance between the line and the ground from the LISN output is presented in Figure 3-35. The LISN line-to-ground impedances were modeled directly by the measurement data in LTspice.

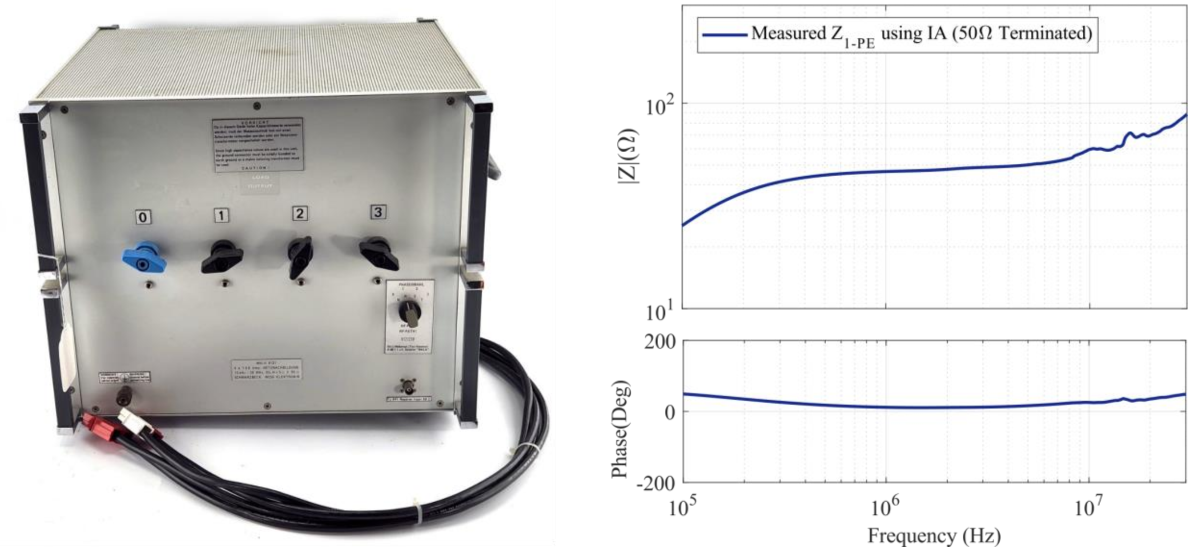

(a) (b)

*Figure 3-35 NNLK 8121 three-phase LISN and its line-to-ground impedance.*

##### 3.2.2.2.1 Impedance Measurement Procedure

The TP impedance measurement method that was used in Chapter 2 for grid impedance measurement is again employed in this section, but this time in order to conduct in-circuit measurements using configurations similar to what is proposed in [61].

The CM impedance measurement configuration, using the TP method, is presented in Figure 3-36. The measurements with the TP method involve the same VNA, amplifier, and injection probe that were described in Chapter 2. However, for the current monitor, Pearson 8585C was selected as the Pearson 2877 area was smaller than the sum of the cross-section area of the four wires.

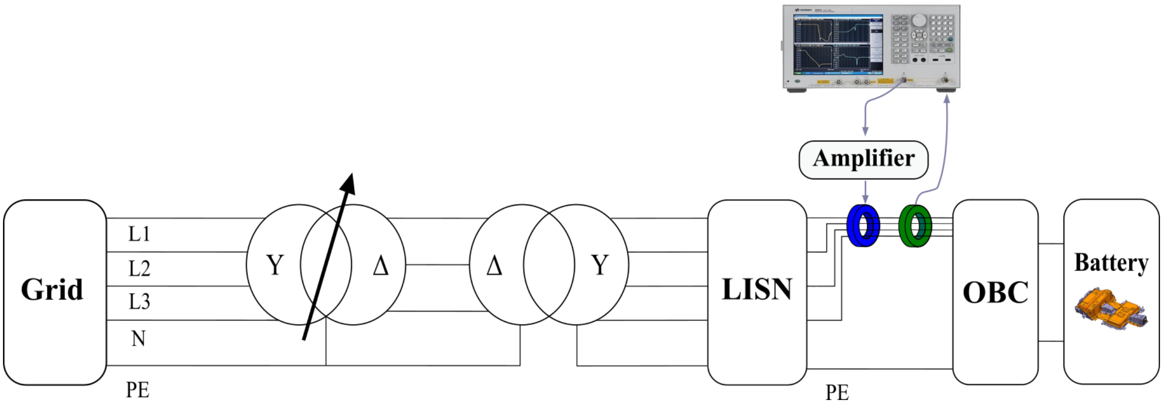

*Figure 3-36 Diagram of CM impedance measurement configuration under nominal voltage.*

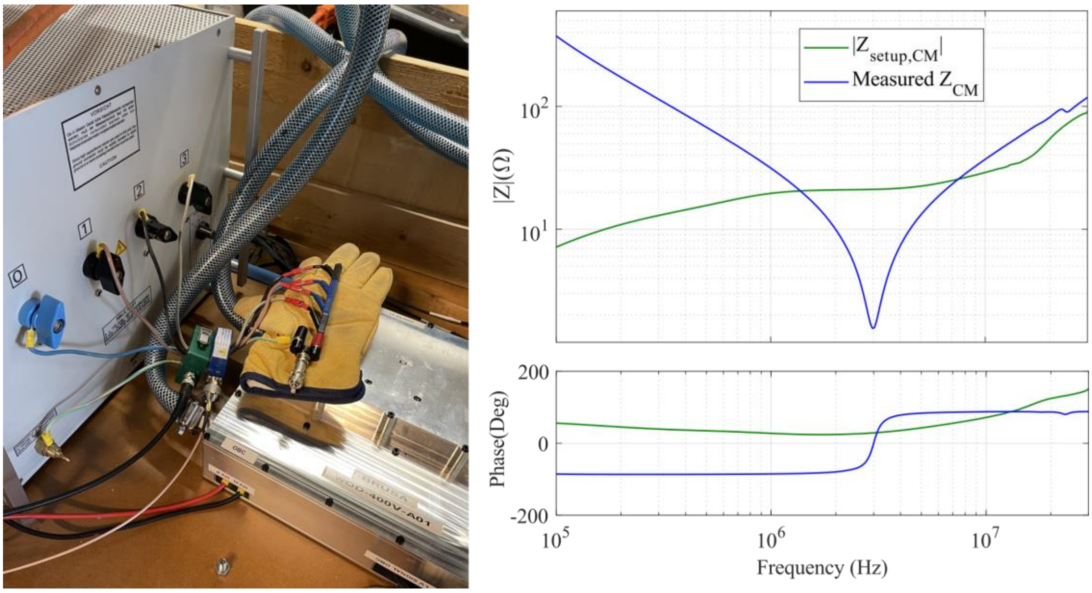

(a) (b)

*Figure 3-37 Common mode impedance: (a) calibration configuration, (b) measured results.*

The results for measured CM impedance alongside the calibration setup are presented in Figure 3-37. The $Z_{setup,CM}$ here includes the LISN Impedance as well as the impedances of wires, probes, and the connections. Since the TP method accuracy depends on the order of the impedance of the loop, which includes the impedance of the targeted device and the impedance of the setup, meaning the rest of the impedances within the loop, setup impedance is also presented in Figure 3-37-b along with the results for CM impedance.

As an example of the DM impedance measurement configurations, Figure 3-38 presents the configuration for measuring the impedance between ports 1 and 2, which can be applied to other differential mode impedances as well. It is essential to mention that DM impedances are calculated from the measured impedances between the two ports that they are connected to by subtracting the other impedances seen in parallel. For instance, the $Z_{DM12}$ is calculated from the impedance measured between ports 1 and 2 by subtracting the impedances seen in parallel.

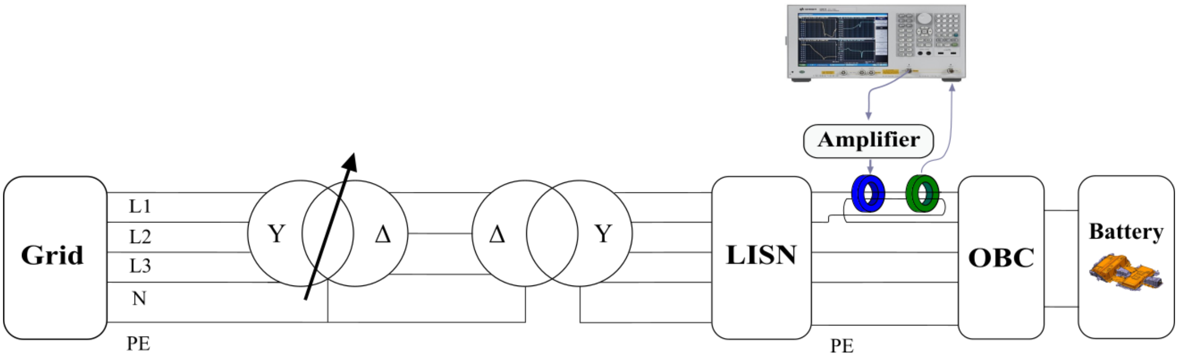

*Figure 3-38 Diagram of $Z_{DM12}$ measurement configuration under nominal voltage.*

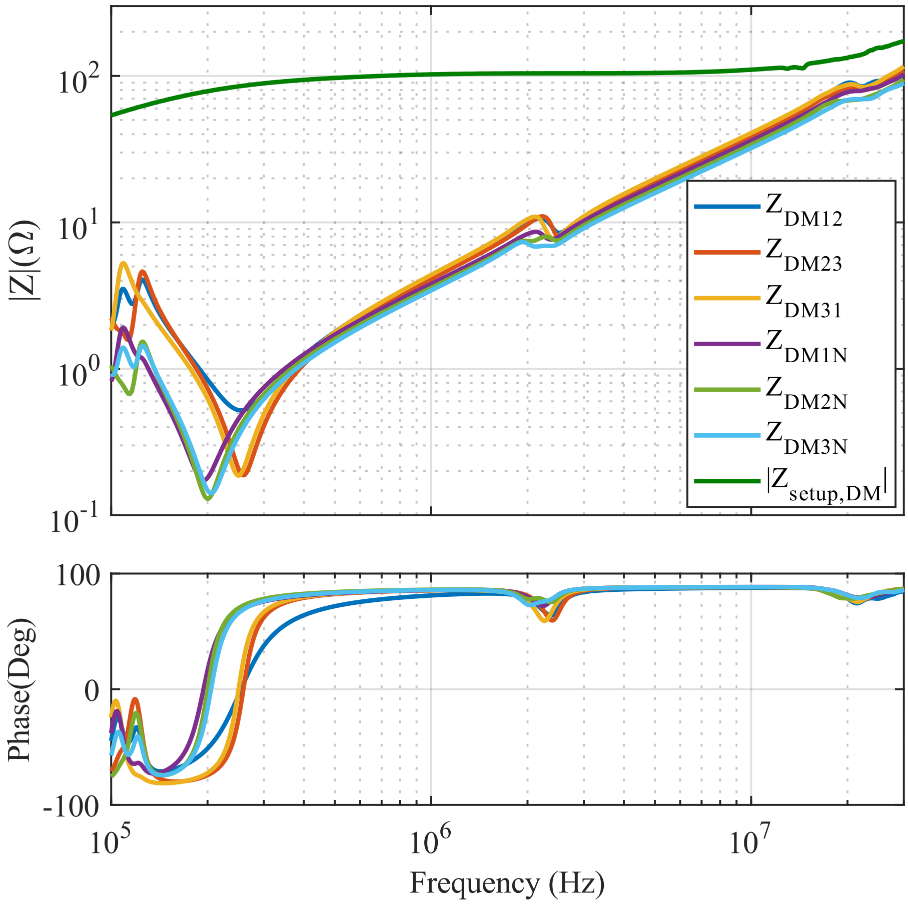

*Figure 3-39 Measured results for differential mode impedances and the setup impedance.*

The DM impedances are presented in Figure 3-39. As can be seen, the impedances are not identical, which means the system is not symmetric. Particularly in lower frequencies and between line-to-line and line-to-neutral impedances, the difference is more pronounced. Finally, the CM and DM impedances are modeled using the same approach as microgrid elements, which is detailed in Appendix C.

#### 3.2.2.2.2 Calculation of Perturbation Sources

The objective is to derive the noise sources based on the currents measured at the output and the internal impedances in order to be able to forecast the output current when alterations such as adding a filter at the output or modifying the external noise termination impedance occur.

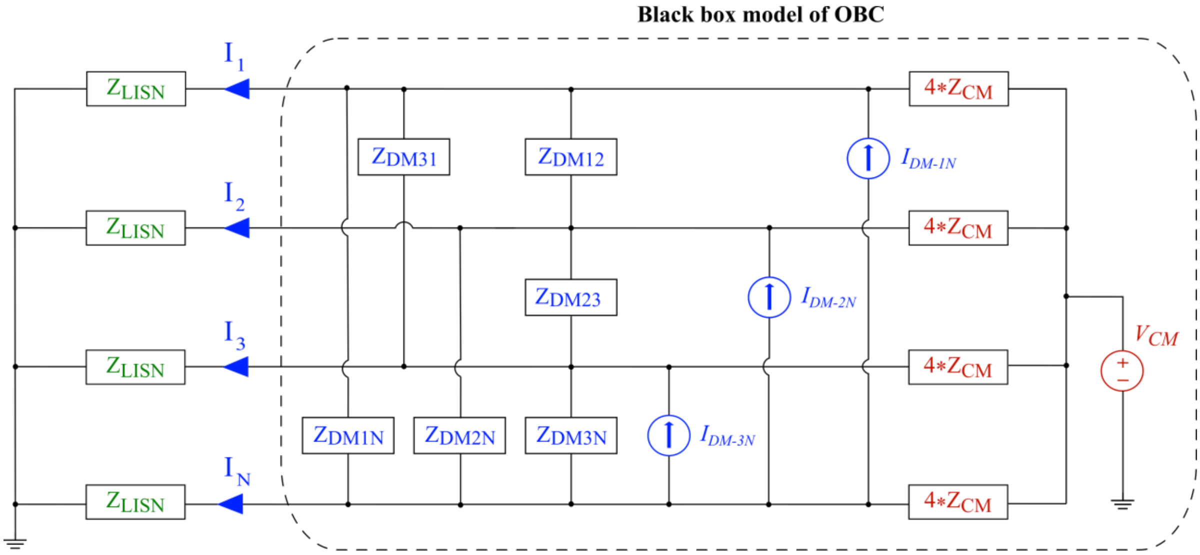

*Figure 3-40 The complete EMC model of the AC side of the OBC connected to the LISN.*

Given that the system is regarded as linear time-invariant (LTI) around an operating point, the superposition theorem can be applied. Since our model has four independent sources, four distinct cases can be considered and analyzed:

- Configuration (1): by turning off all independent sources except the CM voltage source, as presented in Figure 3-41-a.
- Configuration (2): by turning off all independent sources except the DM current source between neutral and line 1, as depicted in Figure 3-41-b.
- Configuration (3): by turning off all independent sources except the DM current source between neutral and line 2, as depicted in Figure 3-41-c.
- Configuration (4): by turning off all independent sources except the DM current source between neutral and line 3, as depicted in Figure 3-41-d.

Therefore, in the complete model, when all the sources are active, each line current can be expressed by the sum of each source’s contribution to the total current as follows:

$$\boldsymbol{I_1 = I_1^{(1)} + I_1^{(2)} + I_1^{(3)} + I_1^{(4)}} \tag{3-15}$$

$$\boldsymbol{I_2 = I_2^{(1)} + I_2^{(2)} + I_2^{(3)} + I_2^{(4)}} \tag{3-16}$$

$$\boldsymbol{I_3 = I_3^{(1)} + I_3^{(2)} + I_3^{(3)} + I_3^{(4)}} \tag{3-17}$$

$$\boldsymbol{I_N = I_N^{(1)} + I_N^{(2)} + I_N^{(3)} + I_N^{(4)}} \tag{3-18}$$

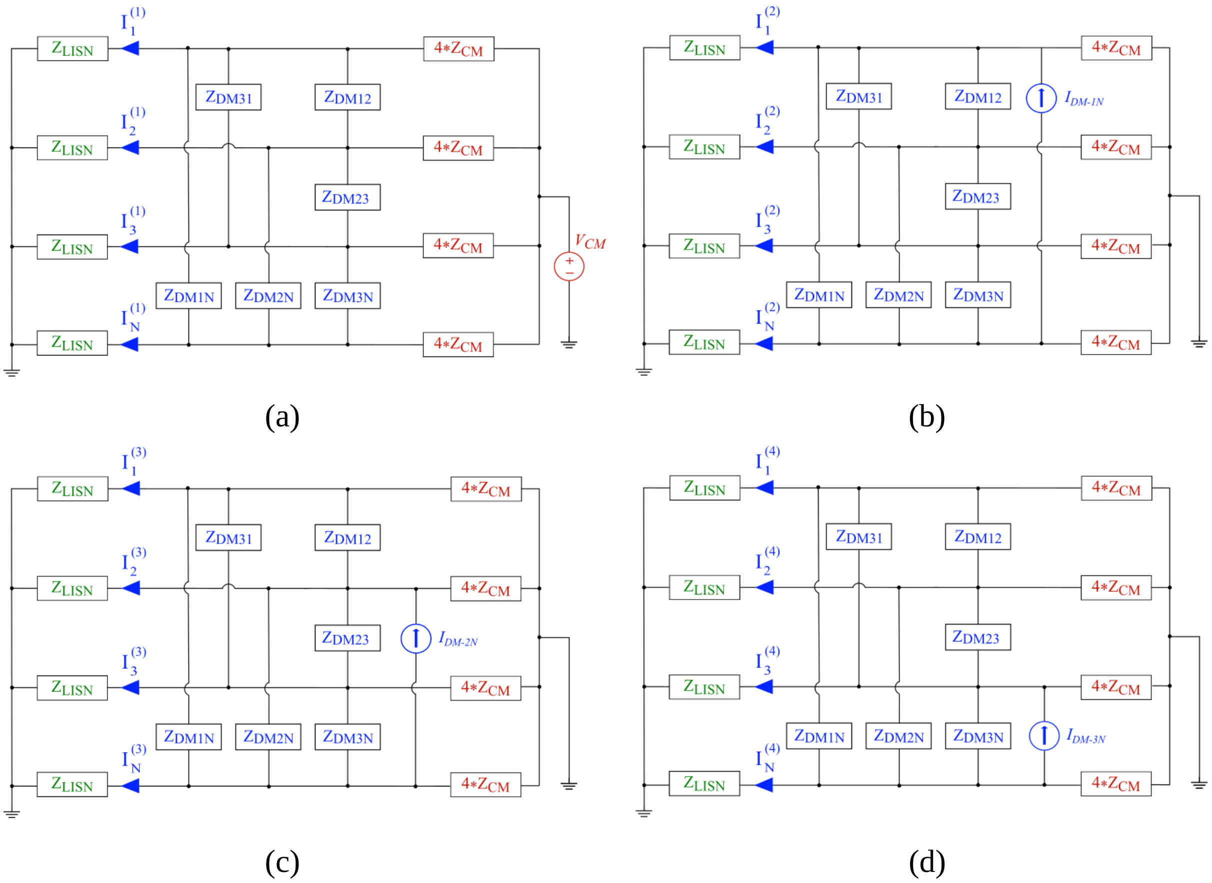

*Figure 3-41* *The four possible configurations by applying the superposition theorem and turning off all independent sources except (a) $V_{CM}$, (b) $I_{DM1N}$, (c) $I_{DM2N}$, (d) $I_{DM3N}$.*

In these equations, each current contribution can be defined with a frequency-dependent coefficient as follows:

$$\boldsymbol{I_1 = \alpha_{11}V_{CM} + \alpha_{12}I_{DM1N} + \alpha_{13}I_{DM2N} + \alpha_{14}I_{DM3N}} \tag{3-19}$$

$$\boldsymbol{I_2 = \alpha_{21}V_{CM} + \alpha_{22}I_{DM1N} + \alpha_{23}I_{DM2N} + \alpha_{24}I_{DM3N}} \tag{3-20}$$

$$\boldsymbol{I_3 = \alpha_{31}V_{CM} + \alpha_{32}I_{DM1N} + \alpha_{33}I_{DM2N} + \alpha_{34}I_{DM3N}} \tag{3-21}$$

$$\boldsymbol{I_N = \alpha_{41}V_{CM} + \alpha_{42}I_{DM1N} + \alpha_{43}I_{DM2N} + \alpha_{44}I_{DM3N}} \tag{3-22}$$

These coefficients can be expressed by the impedances of the model using the analytic approach. Nonetheless, as previously discussed, this approach would be exceedingly time-consuming and challenging. Furthermore, in this study, it is unnecessary to determine the exact expression for these coefficients since they can be computed numerically thanks to the simulation method employed. Since the system is considered to be LTI, by simulating each of the four configurations separately with impedances that are modeled based on the experimental data in LTspice using AC analysis, in each case, four transfer functions of the system can be numerically calculated by considering the noise source as the input and the four lines currents as the outputs. This method facilitates the source calculation even for more complicated black box models with a high number of ports and enhances accuracy as well for asymmetric systems, as it requires fewer assumptions and circuit simplifications regarding system symmetry. The results for coefficients from the numerical approach are presented in Figure 3-42. We can express Equations *3-19*, *3-20*, *3-21*, and *3-22* in a matrix form as follows:

$$\begin{bmatrix} \boldsymbol{I_1} \\ \boldsymbol{I_2} \\ \boldsymbol{I_3} \\ \boldsymbol{I_N} \end{bmatrix} = [\boldsymbol{\alpha}] \begin{bmatrix} \boldsymbol{V_{CM}} \\ \boldsymbol{I_{DM1N}} \\ \boldsymbol{I_{DM2N}} \\ \boldsymbol{I_{DM3N}} \end{bmatrix} \tag{3-23}$$

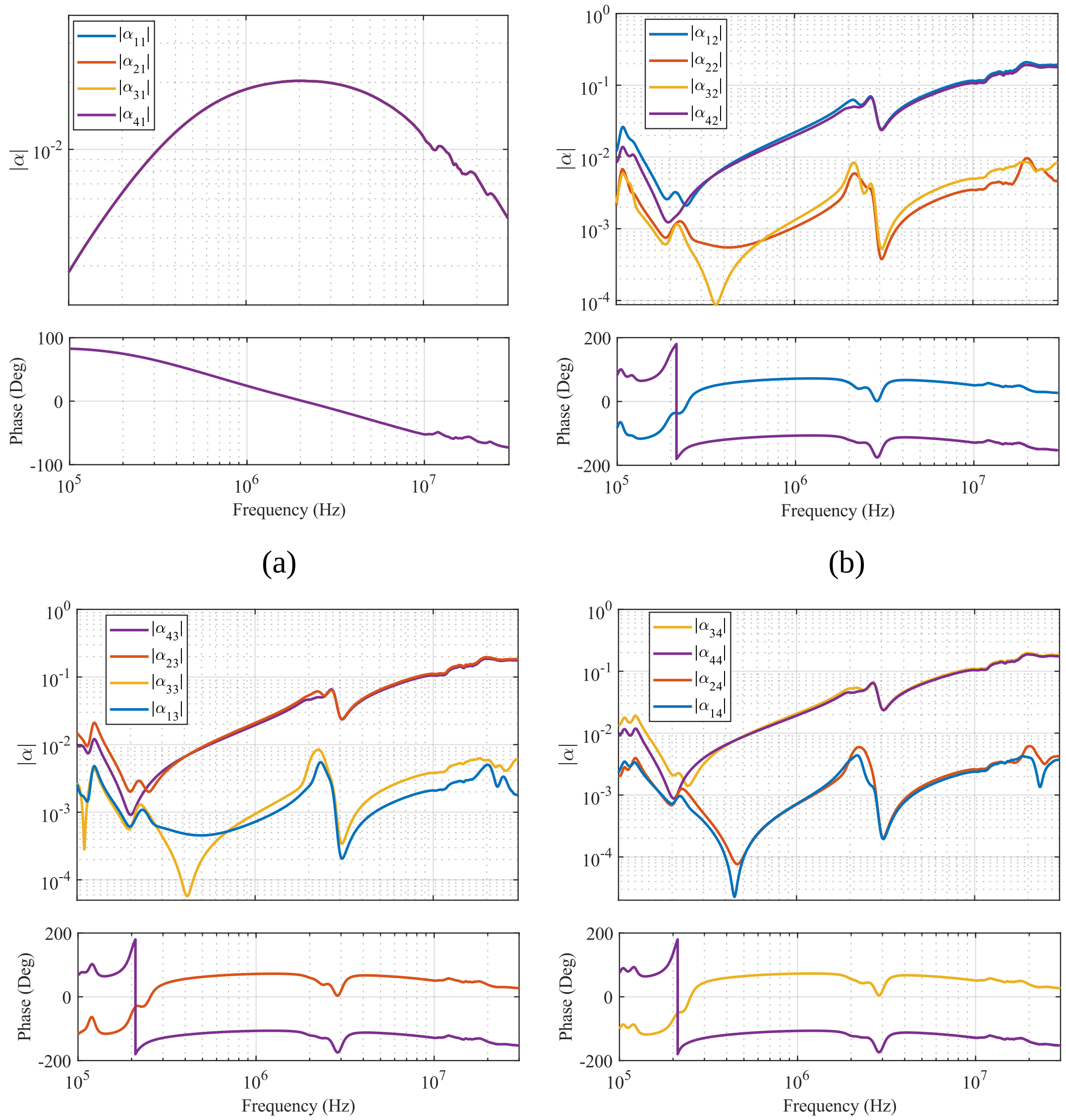

(a) (b)

(c) (d)

*Figure 3-42 Coefficients results obtained from the numerical approach using LTspice from (a) configuration 1, (b) configuration 2, (c) configuration 3, (d) configuration 4.*

The matrix $\boldsymbol{\alpha}$ is the coefficients matrix, and it can be defined as:

$$[\alpha] = \begin{bmatrix} \alpha_{11} & \alpha_{12} & \alpha_{13} & \alpha_{14} \\ \alpha_{21} & \alpha_{22} & \alpha_{23} & \alpha_{24} \\ \alpha_{31} & \alpha_{32} & \alpha_{33} & \alpha_{34} \\ \alpha_{41} & \alpha_{42} & \alpha_{43} & \alpha_{44} \end{bmatrix} \tag{3-24}$$

therefore, the perturbation sources can be determined using Equation *3-25* if the square matrix $\boldsymbol{\alpha}$ is invertible.

$$\begin{bmatrix} V_{CM} \\ I_{DM1N} \\ I_{DM2N} \\ I_{DM3N} \end{bmatrix} = [\alpha]^{-1} \begin{bmatrix} I_1 \\ I_2 \\ I_3 \\ I_N \end{bmatrix} \tag{3-25}$$

In our case, since the coefficient matrix was not invertible for most of the frequencies, we needed to implement some simplifications to perform perturbation sources calculations across all frequencies. These simplifications were not only necessary for calculating the perturbation sources in our specific case but also aimed to introduce a robust and generic method that works consistently, regardless of the invertibility of the matrix $\boldsymbol{\alpha}$. Since in this model the CM current comes from the contributions of the $V_{CM}$ source, it can be expressed as

$$\boldsymbol{I_{CM} = I_1^{(1)} + I_2^{(1)} + I_3^{(1)} + I_N^{(1)}} \tag{3-26}$$

As shown in Figure 3-42-a, by supposing that the total CM impedance is evenly distributed and by having the identical LISN impedance in each line, we have

$$\boldsymbol{\alpha_{11} = \alpha_{12} = \alpha_{13} = \alpha_{14} = \alpha_{CM}} \tag{3-27}$$

thus, by applying Equation ***3-27*** in ***3-26***, the CM current can be expressed as

$$\boldsymbol{I_{CM} = 4\,\alpha_{CM} V_{CM}} \tag{3-28}$$

finally, the CM voltage source can be calculated using Equation ***3-30***.

$$\boldsymbol{V_{CM} = \frac{I_{CM}}{4\,\alpha_{CM}}} \tag{3-29}$$

On the other hand, the CM current can be described as the sum of the currents flowing in the four lines.

$$\boldsymbol{I_{CM} = I_1 + I_2 + I_3 + I_N} \tag{3-30}$$

thus, by measuring the sum of the four currents at the output, the Model's CM perturbation source can be calculated.

The assumption for DM sources is that the current from the source between neutral and one line flows only in neutral and that line. This can be expressed as

$$\boldsymbol{I_2^{(2)} = I_3^{(2)} = 0} \qquad 3\text{-}31$$

$$\boldsymbol{I_1^{(3)} = I_3^{(3)} = 0} \qquad 3\text{-}32$$

$$\boldsymbol{I_1^{(4)} = I_2^{(4)} = 0} \qquad 3\text{-}33$$

Therefore, the equations for line current can be simplified as follows:

$$\boldsymbol{I_1 = \alpha_{11} V_{CM} + \alpha_{12} I_{DM1N}} \qquad 3\text{-}34$$

$$\boldsymbol{I_2 = \alpha_{21} V_{CM} + \alpha_{23} I_{DM2N}} \qquad 3\text{-}35$$

$$\boldsymbol{I_3 = \alpha_{31} V_{CM} + \alpha_{34} I_{DM3N}} \qquad 3\text{-}36$$

$$\boldsymbol{I_N = \alpha_{41} V_{CM} + \alpha_{42} I_{DM1N} + \alpha_{43} I_{DM2N} + \alpha_{44} I_{DM3N}} \qquad 3\text{-}37$$

As the current for each source is assumed to flow through the related line and the neutral, we have

$$\boldsymbol{\alpha_{42} = \alpha_{43} = \alpha_{44} = -\alpha_{12} = -\alpha_{23} = -\alpha_{34} = -\alpha_{DM}} \qquad 3\text{-}38$$

The accuracy of this assumption depends on the degree of symmetry within the system. As can be seen in Figure 3-39 and Figure 3-42, in the frequencies where the difference between DM impedances is more significant, discrepancies between coefficients become evident. The convenience of the simulation method lies in its ability to easily detect the effects of asymmetry in the system. It helps to identify the frequency bands where these simplifications become invalid and thus predicts distortions in the final results of the model.

As an example, the $I_{DM1N}$ coefficients are presented in Figure 3-43 along with the DM impedances. It can be observed that before around 300 kHz, due to the deviations in the DM impedances, when $I_{DM1N}$ source is the only active source in the system, its current cannot be assumed to flow only in line 1 ($\boldsymbol{\alpha_{12}}$) and neutral ($\boldsymbol{\alpha_{42}}$). The amplitude of currents in line 2 ($\boldsymbol{\alpha_{22}}$) and line 3 ($\boldsymbol{\alpha_{32}}$) also become relatively significant and cannot be neglected (less than a 10-fold difference).

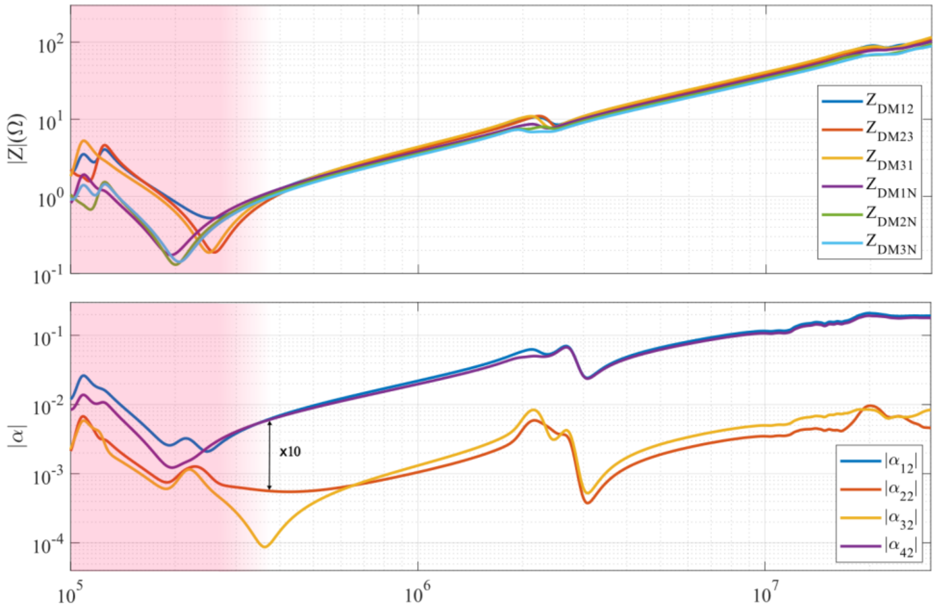

*Figure 3-43 The effect of the asymmetry in the system on the $I_{DM1N}$ coefficients.*

By applying Equations *3-27* and *3-38* to the output currents equations, they can be expressed as

$$\boldsymbol{I_1 = \alpha_{CM} V_{CM} + \alpha_{DM}\, I_{DM1N}} \tag{3-39}$$

$$\boldsymbol{I_2 = \alpha_{CM} V_{CM} + \alpha_{DM}\, I_{DM2N}} \tag{3-40}$$

$$\boldsymbol{I_3 = \alpha_{CM} V_{CM} + \alpha_{DM}\, I_{DM3N}} \tag{3-41}$$

$$\boldsymbol{I_N = \alpha_{CM} V_{CM} - \alpha_{DM}\,(I_{DM1N} + I_{DM2N} + I_{DM3N})} \tag{3-42}$$

Finally, from *3-39*, *3-40*, and *3-41*, the DM current sources can be determined as follows:

$$\boldsymbol{I_{DM1N} = \frac{I_1 - \alpha_{CM}\, V_{CM}}{\alpha_{DM}}} \tag{3-43}$$

$$\boldsymbol{I_{DM2N} = \frac{I_2 - \alpha_{CM}\, V_{CM}}{\alpha_{DM}}} \tag{3-44}$$

$$\boldsymbol{I_{DM3N} = \frac{I_3 - \alpha_{CM}\, V_{CM}}{\alpha_{DM}}} \tag{3-45}$$

On the other hand, supposing that

$$\boldsymbol{I_{DM1N} + I_{DM2N} + I_{DM3N} = 0} \tag{3-46}$$

the neutral current from Equation *3-42* can be expressed as

$$\boldsymbol{I_N = \alpha_{CM} V_{CM} = \frac{I_{CM}}{4}} \qquad 3\text{-}47$$

This was verified experimentally, and the results within the range of interest (150 kHz-30 MHz) show approximately a 12 dB difference (factor of 4) between the related peaks of the two currents, as presented in Figure 3-44.

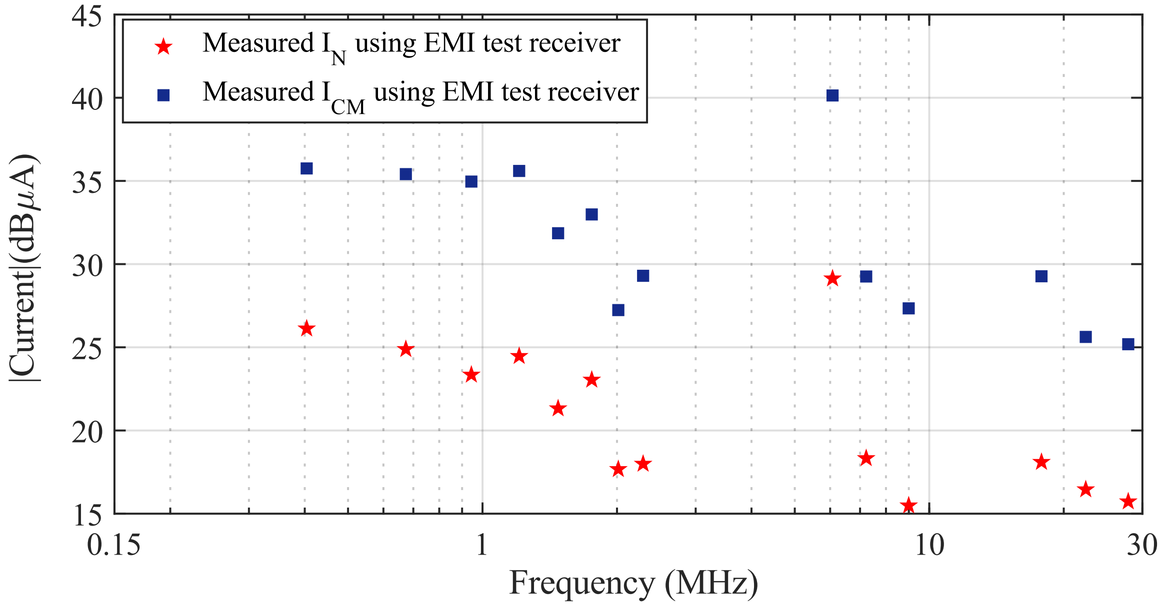

*Figure 3-44 Comparison between measured data for the neutral current and for the CM current.*

Currents were measured in both time and frequency domains using a 6595 Pearson current monitor with the setup presented in Figure 3-45-b. For time-domain measurements, a Tektronix 3 Series MDO oscilloscope was employed, offering a vertical resolution of 11 bits. The oscilloscope sampled at a rate of 250 MHz, acquiring $10^7$ samples to cover two complete periods of the fundamental current at 50 Hz. The frequency-domain measurements are conducted using an R&S ESU EMI Test Receiver with a resolution bandwidth (RBW) of 2 kHz, a video bandwidth (VBW) of 1 kHz, and a peak detector. The operating point for the model perturbation source identification was fixed on 2 A at the DC side in G2V mode.

Figure 3-45-a presents results for "$I_1+I_2+I_3$" and a comparison between direct acquisition using an EMI test receiver and the calculated FFT of the data measured in the time domain, demonstrating that the results from both methods are aligned with each other.

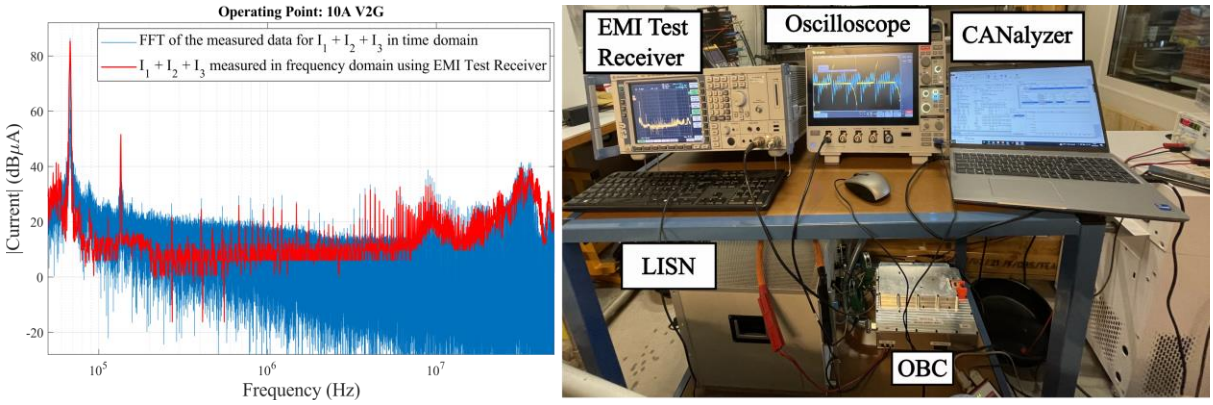

(a) (b)

*Figure 3-45 (a) Comparison of the measured data in the frequency domain obtained through two methods: direct acquisition using an EMI test receiver and FFT of the data measured in the time domain. (b) The current measurement setup.*

By applying Equation *3-28* to Equations *3-43*, *3-44*, and *3-45*, we can rewrite the DM sources' expressions as

$$\boldsymbol{I_{DM1N}} = \frac{\boldsymbol{4\,I_1 - I_{CM}}}{\boldsymbol{4\,\alpha_{DM}}} = \frac{\boldsymbol{3\,I_1 - (I_N + I_3 + I_2)}}{\boldsymbol{4\,\alpha_{DM}}} \quad 3\text{-}48$$

$$\boldsymbol{I_{DM2N}} = \frac{\boldsymbol{4\,I_2 - I_{CM}}}{\boldsymbol{4\,\alpha_{DM}}} = \frac{\boldsymbol{3\,I_2 - (I_N + I_3 + I_1)}}{\boldsymbol{4\,\alpha_{DM}}} \quad 3\text{-}49$$

$$\boldsymbol{I_{DM3N}} = \frac{\boldsymbol{4\,I_3 - I_{CM}}}{\boldsymbol{4\,\alpha_{DM}}} = \frac{\boldsymbol{3\,I_3 - (I_N + I_1 + I_2)}}{\boldsymbol{4\,\alpha_{DM}}} \quad 3\text{-}50$$

therefore, the DM sources can be determined from the DM coefficient, which was calculated numerically, and the currents that can be measured using configurations such as the one illustrated in Figure 3-46 for $I_{DM3N}$.

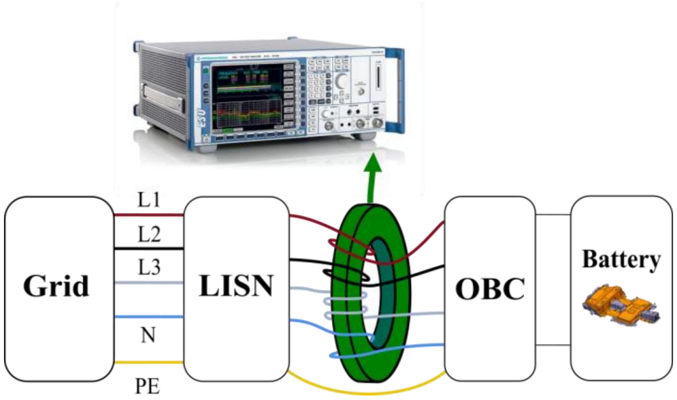

*Figure 3-46 Current measurement configuration in order to calculate the DM current source between neutral and line 3 for the black box model.*

Initially, for the calculation of perturbation sources, the FFT of the output current data measured in the time domain was utilized. However, due to a lack of access to the converter clock and, consequently, an unknown exact switching frequency, as well as the low-level signals from an already filtered prototype, a distortion in current phases was observed during the FFT calculation. Unfortunately, as a result, precise phase information was unavailable, necessitating assumptions regarding the phases of the sources. The phases were assumed to be balanced for DM current sources, supposing 0, -120, and 120 degrees for $I_{DM1N}$, $I_{DM2N}$, and $I_{DM3N}$, respectively, across the entire frequency range. The $V_{CM}$ phase was also assumed to be 60 degrees in order to form a phase shift between DM and CM sources.

This modeling limitation introduces a more significant deviation between the results derived from the model and the measured data, particularly in neutral current, which will be discussed in the following section.

Furthermore, for the final model, the amplitude data obtained by the EMI test receiver were utilized for calculation of the perturbation sources, since it offered a lower noise floor, as can be seen in Figure 3-45-a.

#### 3.2.2.3 OBC model verification

After calculating the perturbation sources for an operating point – 2 A at the DC side in G2V mode – and determining the DM and CM impedances, all these model elements were modeled by employing the methodology outlined in Appendix C. In order to verify the OBC black box model, the circuit presented in Figure 3-40 was simulated in LTspice using AC analysis mode.

It is worth mentioning that since only the current peaks need to be analyzed, in order to reduce the simulation time, the noise sources were calculated using envelopes that pass through the peaks of the signals. Therefore, simulating the black box model when connected through the LISN, as demonstrated in Figure 3-40, requires only 164 ms for 625 points per decade in a range from 135 kHz to 30 MHz.

The results for measured currents and the simulated currents are presented in Figure 3-47. The results indicate a close match between empirical and simulated data, except for the neutral current. The deviation between the measured and simulated data in the case of neutral current can be largely a result of the assumptions regarding the phases, as mentioned earlier, given its consistency throughout the spectrum.

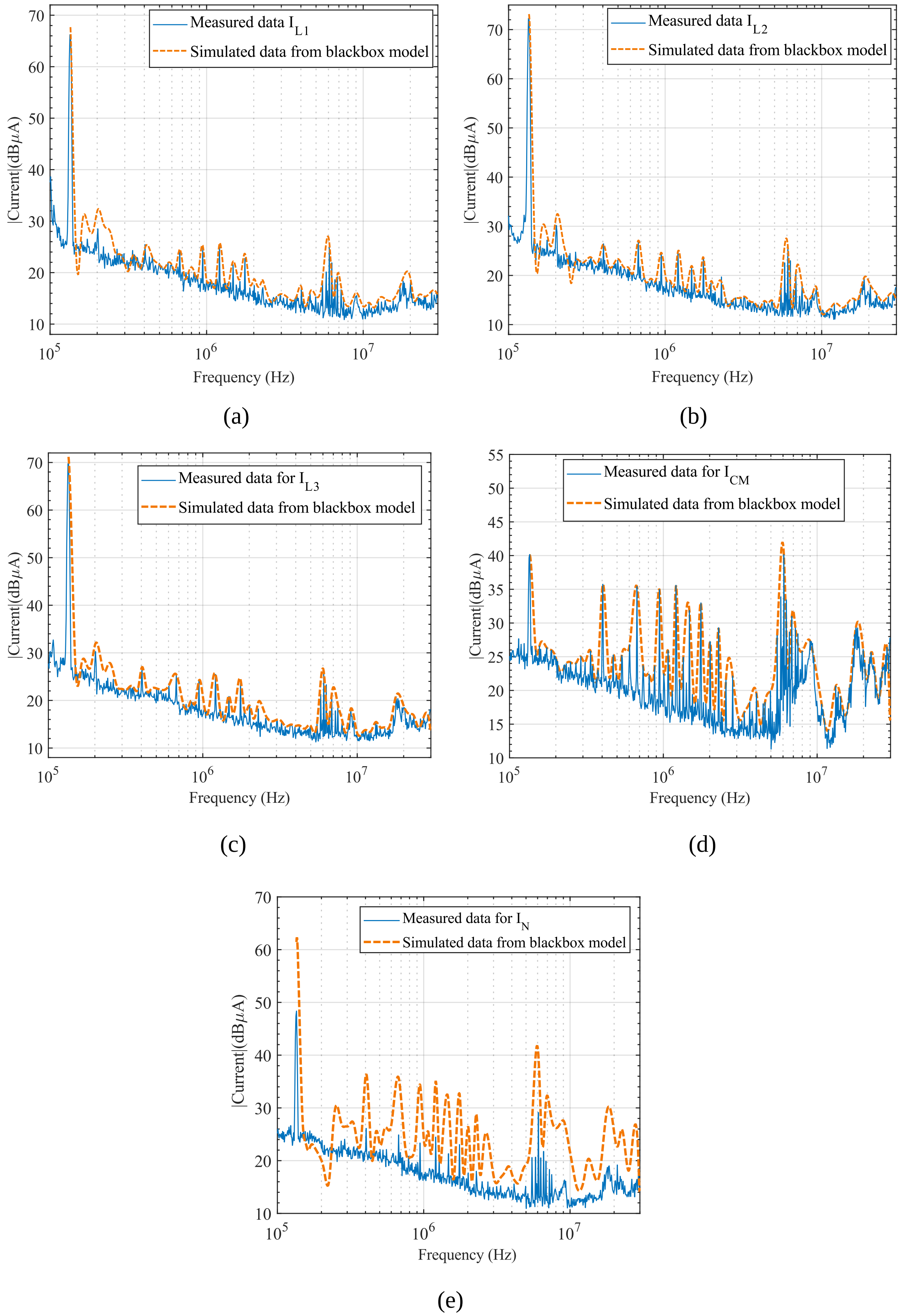

(a)

(b)

(c)

(d)

(e)

*Figure 3-47* *Comparison between measured data and simulated data from black box model: (a) Line 1 current, (b) Line 2 current,(c) Line 3 current, (d) CM current, (e) Neutral current.*

In line currents such as line 3, as shown in Figure 3-47-b, around 250 kHz, a relatively significant difference is observed. However, this discrepancy arises due to the fact that the assumptions for the DM sources (Equations *3-31*, *3-32*, and *3-33*) are not valid around this frequency band due to the asymmetric DM impedances, as demonstrated in Figure 3-43.

Due to unsatisfactory results for the neutral current, it will not be discussed further in the following chapter. Instead, our focus will be on lines and CM currents, which demonstrated more accurate results.

One of the inconveniences of this modeling approach is that it is only applicable to a single operating point, necessitating the definition of a new model and perturbation sources for each distinct operating point. However, with the developed code, simply changing the input measured currents allows for the generation of new circuit elements based on the newly calculated perturbation sources. Therefore, this capability facilitates the analysis of multiple operating points.

## 3.3 Conclusion

In this chapter, firstly, the OBC prototype under test was introduced. Then, in order to examine the conducted emissions caused by our prototype bidirectional on-board charger in a controlled environment without LISN, a grid-connected microgrid was established that offers the following advantages:

- The HF impedance and, consequently, conducted emissions will be less affected by undesired changes in the loads in the neighborhood outside the microgrid.
- Impedance and noise measurements can be conducted at any desired point in the system regarding the distance from the last transformer.
- Various grounding systems can be implemented on the transformer, and therefore, their influence on the measured impedance and conducted emissions can be analyzed.

Moreover, an innovative approach was proposed to develop a frequency model of the charging environment, including the microgrid and the converter, based on a SPICE-type solver by directly utilizing the data from the experimental acquisition of impedances and currents. This method allows for faster simulations of large-scale systems. Therefore, the proposed method is beneficial for both black box and white box models, where the internal components of the system and its operation are fully known. To ensure the model’s accuracy and reliability, rigorous verification procedures were conducted. Overall, the results demonstrated good agreement with the measured data, with some exceptions attributable to insufficient knowledge about the signal phases.

In the following chapter, the conducted emissions due to the OBC will be measured and analyzed when the OBC is connected to a microgrid with different parameters, such as different grounding systems and cable lengths, in the presence or absence of the loads. In addition, the black box model of the OBC and the microgrid model will be utilized in order to predict the level of conducted emissions.

# CHAPTER 4

# OBC Conducted Emission Analysis

In this chapter, the conducted emissions generated by the OBC prototype are investigated under different scenarios to study the impact of the operating point, the grounding systems, the cables lengths, and the loads connected to the microgrid. In the next step, the developed model for the microgrid is employed in order to analyze the HF impedance of the grid. Finally the entire developed charging environment model is utilized to predict the conducted emissions levels in the system. Employing this model enables the simulation of parasitic currents level at any point within the microgrid, regardless of the connected loads. We also took it a step further by creating a model for an extended version of the implemented system to examine the conducted emissions in a larger charging setting.

## 4.1 The Grid and Operation Parameters Impact on Conducted Emissions

The objective of this section is to examine the influence of system parameters on the levels of parasitic currents. Initially, the focus is on analyzing the impact of the operating point with the LISN, and with a particular emphasis on V2G mode. Subsequently, the investigation shifts to the influence of microgrid parameters. The primary goal is to evaluate the high-frequency behavior of the OBC prototype in terms of its generated conducted emissions when the LISN is removed. In the absence of the LISN, the fixed impedance, previously provided by the LISN as the external noise termination, is replaced by the impedance of the grid. The grid impedance is variable and depends on several factors, such as the connected loads and the grounding system. These variations in HF impedance can alter the levels of conducted emissions and, in certain scenarios, lead to malfunctions in other devices. Therefore, it is crucial to study the behavior of the OBC without the LISN to understand these implications.

### 4.1.1 Operating Point Impact

The level and direction of the DC current flowing to the battery are the prototype controllable parameters. Accordingly, the parasitic currents were measured at the AC side of the OBC in various operating points when it was connected to the panel through the LISN. Conducted emission measurements were conducted with the LISN to ensure a symmetric external noise termination impedance. All current measurements in this chapter were performed in the frequency domain using a Pearson 8585C current monitor and the R&S ESU EMI test receiver, adhering to the settings detailed in the previous chapter. However, the frequency range is limited to 2 MHz in most cases because this range is more important for filter design, and most variations in different scenarios occur within this frequency band. At higher frequencies, the current levels are observed to be generally more stable.

Figure 4-1 illustrates the currents for lines 1, 2, and 3 at 2 A and 10 A in G2V mode. In this chapter, we will be conducting numerous comparisons; thus, the focus will primarily be on the peak amplitudes comparing, as this approach provides more visible data presentation and, therefore, clearer insights. The spectral characteristics of the currents across the three lines are notably similar, particularly at higher frequencies. As discussed in the previous chapter, this similarity is due to the symmetric DM impedances at high frequencies, although this symmetry does not hold below 300 kHz, as shown in Figure 3-43. This is evident in the first peak, which are located within this frequency band. This asymmetry affects the first peak of the neutral current as well, leading to a neutral current higher than CM current at 135 kHz.

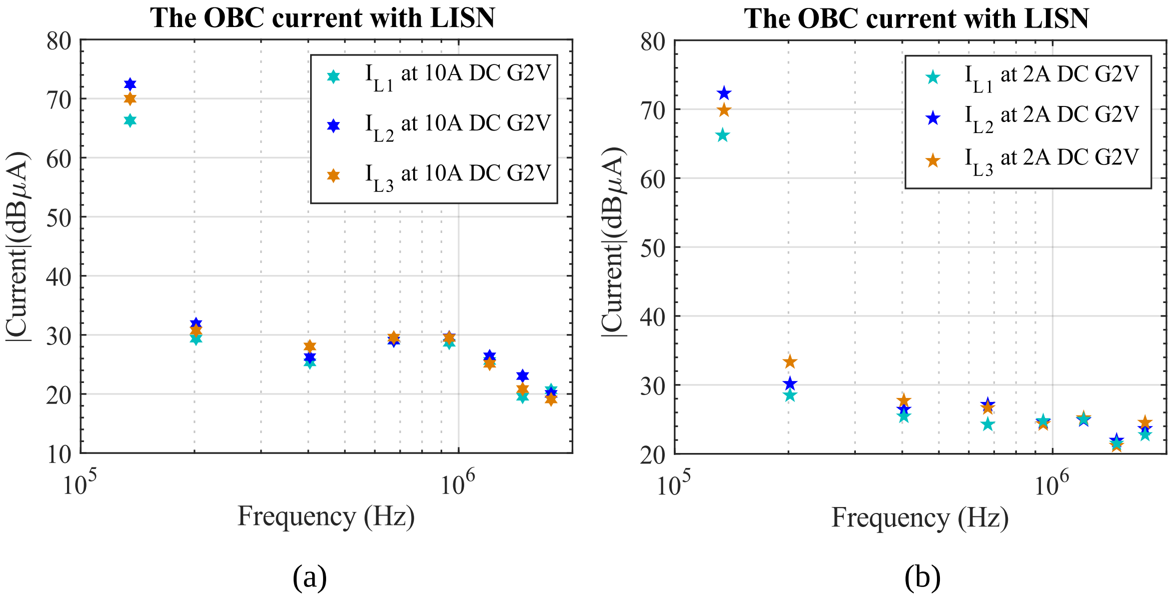

*Figure 4-1 Lines currents in two different operating points: (a) 2A G2V, (b) 10A G2V.*

As the line currents are approximately at the same level, we will henceforth consider one of the lines, the neutral, and the common mode (CM) current for future comparisons.

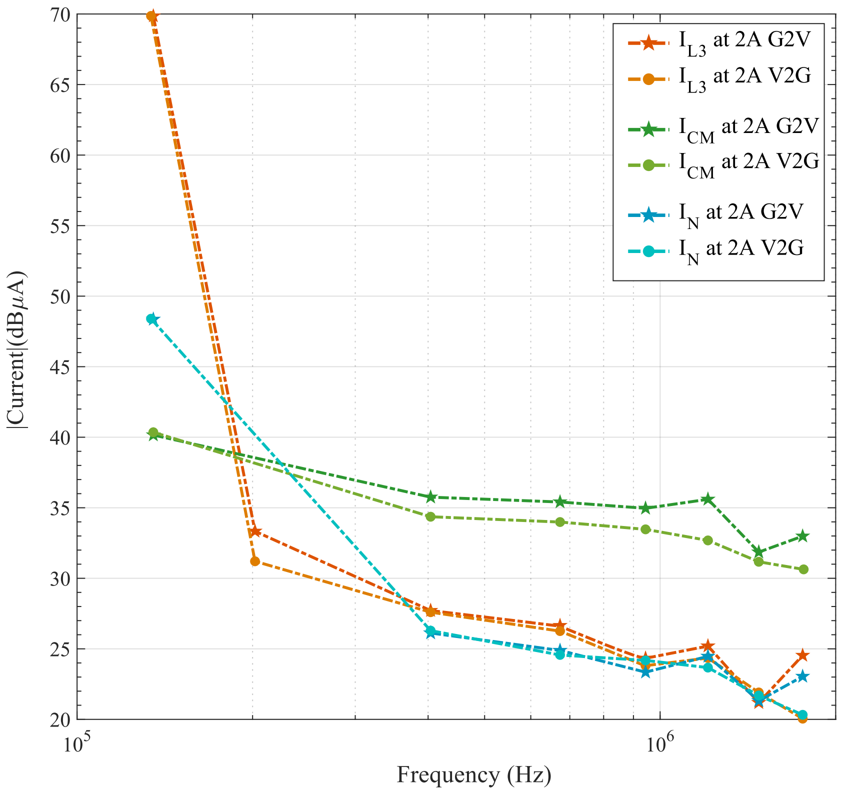

*Figure 4-2 The comparison between G2V and V2G operating modes in the CM, neutral, and line 3 currents.*

Figure 4-2 presents a comparison between G2V and V2G modes at 2A. It can be observed that since the switching frequency remains constant across all operating points in our prototype, unlike in resonant converters, the frequency of the peaks does not shift depending on the operating point. Moreover, the amplitude of the peaks between G2V and V2G modes shows approximately the same level, with a maximum difference of 4 dB in the frequency band under study.

It is worth mentioning that although both modes display similar levels of emissions in the EMC frequency range, we observed that the low-frequency current (50 Hz) waveform in V2G mode is more distorted compared to G2V mode and exhibits a higher THD. This indicates that the PFC block does not perform equally well in G2V and V2G modes.

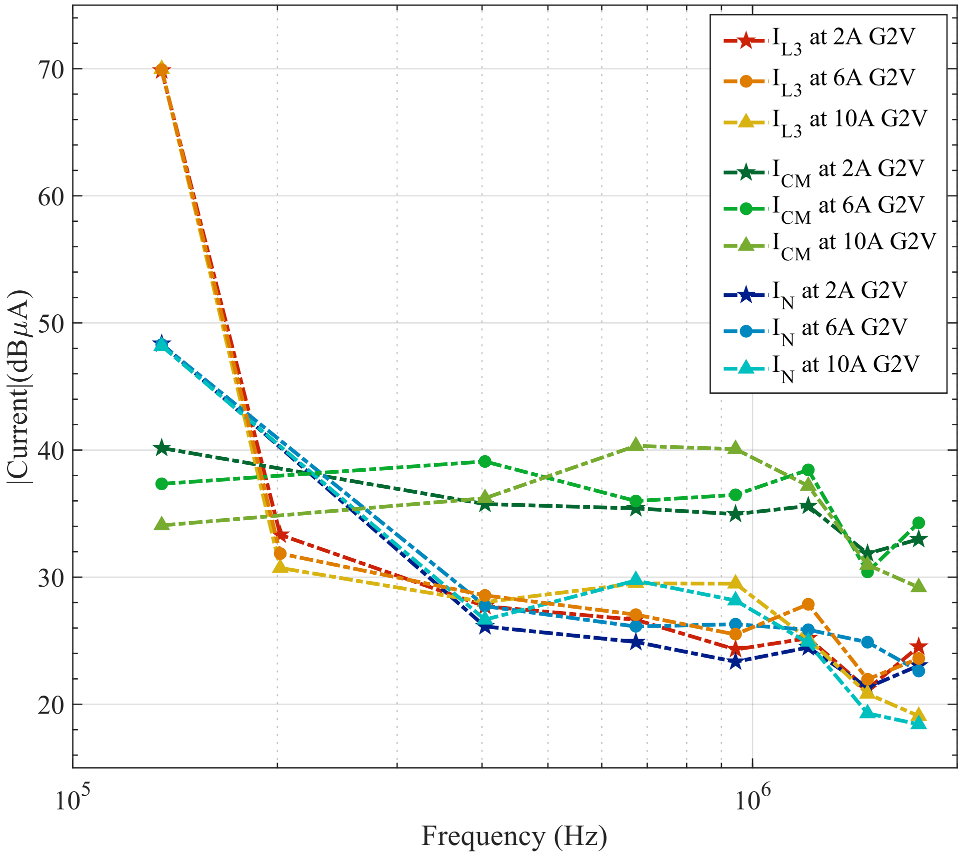

*Figure 4-3 The comparison between three operating points in G2V mode in line 3, CM, and neutral currents.*

Figure 4-3, on the other hand, illustrates a comparison between three different operating points in G2V mode. As can be seen, similar to the comparison between V2G and G2V modes, the same level of parasitic currents is observed across different operating points. This demonstrates that a higher DC level on the battery side, and consequently a higher current at 50 Hz on the AC side, does not necessarily result in higher levels of conducted emissions. This outcome is due to the specific conversion structure of the OBC used, which includes a PFC stage followed by a DAB, as detailed in the previous chapter. This result is likely generalizable to all converter structures of the same type.

### 4.1.2 Grounding Systems and Cable Length Impact

This section aims to analyze the impact of grounding systems on conducted emissions. Therefore, current measurements were conducted with the OBC connected to the microgrid without the LISN, as depicted in Figure 4-4. The configuration and the realization of different grounding systems on the transformer are detailed in section 3.2.1.3 and thus will not be reiterated here.

It must be noted that the results that will be discussed here pertain specifically to our OBC prototype with its unique internal noise termination impedances. The conclusions, trends, and effects observed in this study may not be applicable, or may vary in degree, for a converter with a different EMC filter and, thus, different internal noise termination impedances.

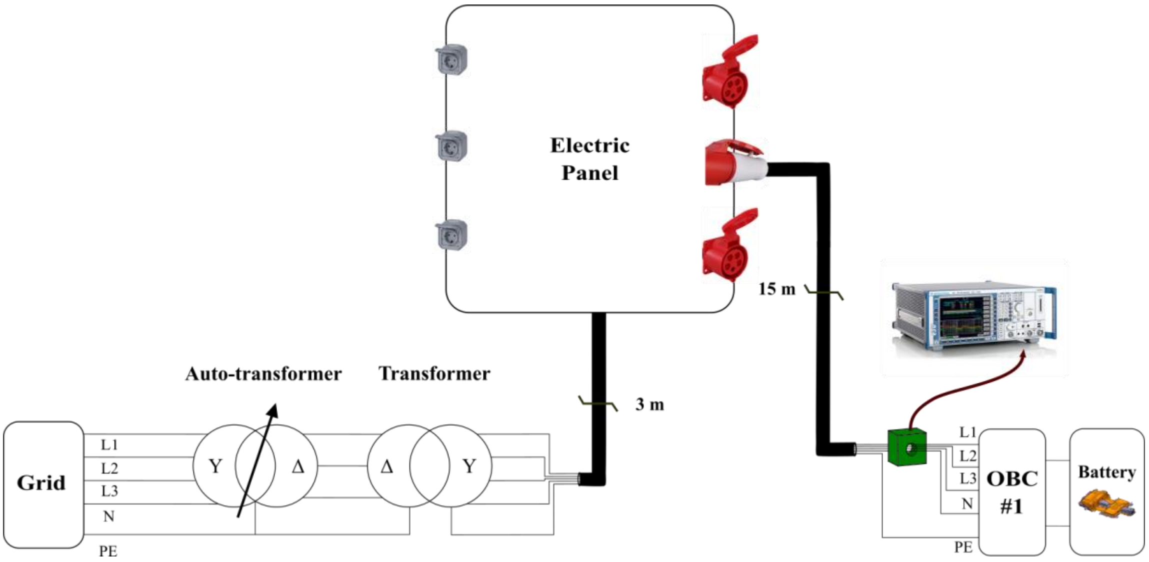

*Figure 4-4 The configuration used for conducted emissions measurements for different grounding systems.*

The comparison of CM current results across various grounding systems and in the case with the LISN, as illustrated in Figure 4-5, reveals that TNR, TTN, and TTS systems exhibit highly similar spectra, with some exceptions notably at the third harmonic of switching frequency. This similarity may stem from the implementation and emulation of ground connections using resistors, which effectively work for low frequencies (50 Hz) but do not entirely replicate the high-frequency behavior of a genuine ground connection.

In addition, the spectrum can be divided into three zones, as demonstrated in Figure 4-5. In the first zone, the IT system generally displays a lower level of CM current compared to the other systems. In the second zone, this trend reverses, and the IT system exhibits a higher level of CM current. However, in the third zone, the CM current is approximately the same level regardless of the grounding system. The explanation for this behavior lies in the CM impedance observed from the OBC, presented in Figure 3-30.

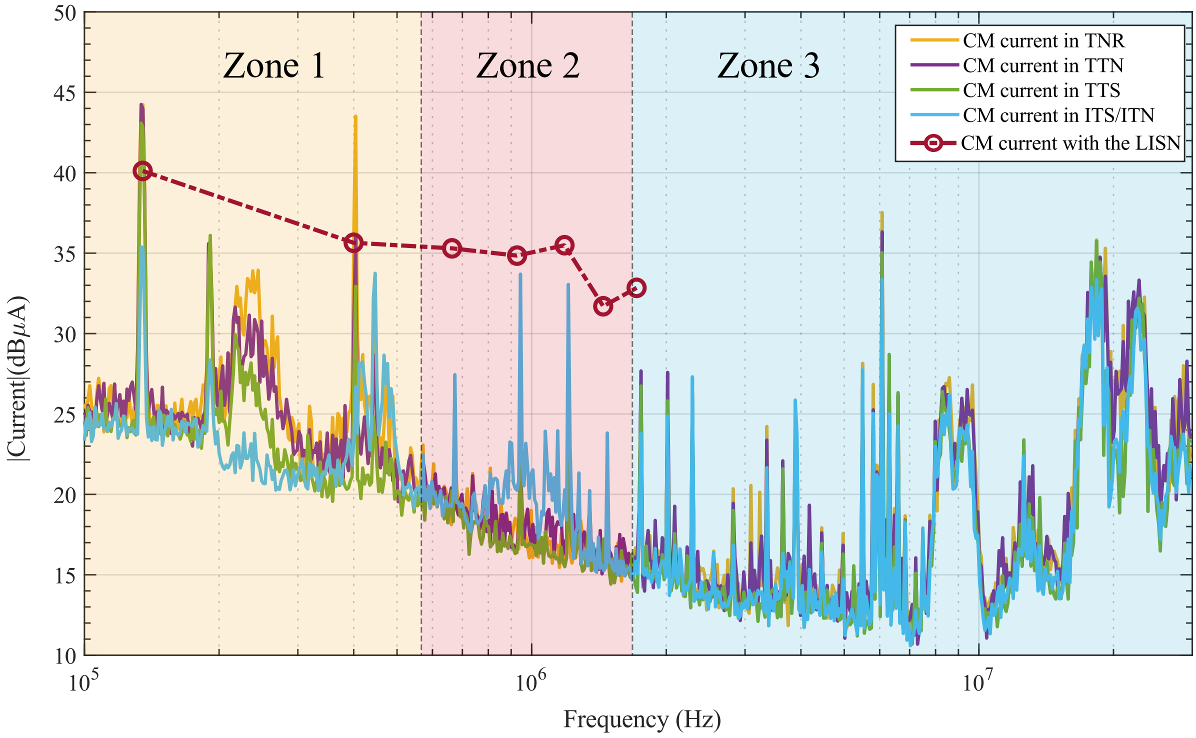

*Figure 4-5 Measured CM current comparison between cases with LISN and without LISN in different grounding systems.*

In order to investigate the effect of cable length, we altered the length of the cable connecting the OBC to the grid from 15 meters to 5 meters. The results indicated that this modification caused the first zone to expand and the second zone to shift to higher frequencies, from approximately 600 kHz–1.6 MHz to roughly 1.1 MHz–2.9 MHz. This shift is due to the influence of cable impedance on the overall impedance seen by the OBC, which will be discussed in more detail in section 4.3.

Figure 4-5 also shows that the CM current with the LISN is greater in amplitude compared to the IT system across the entire spectrum. However, in the first zone, which is the most important frequency band for EMC filter design, the CM current with the LISN is lower than that of the other grounding systems than IT.

The only impedance that changes across different grounding systems is the neutral-to-ground impedance, resulting in consistent lines' currents across all grounding systems. Additionally, the neutral current exhibits a similar trend to the CM current, albeit with not the same amplitudes. Hence, for the sake of brevity, lines and neutral currents are not presented.

### 4.1.3 Loads Impact

Loads connected to the microgrid modify the impedance observed from the noise source – OBC prototype – thereby influencing the level of conducted emissions. In order to investigate the magnitude of these variations in parasitic currents, measurements are performed with the IT system at various points within the microgrid, such as the RCBO output at the electric panel entry and the OBC AC side, as indicated in Figure 4-6. A synthesis of the obtained results is presented in this section.

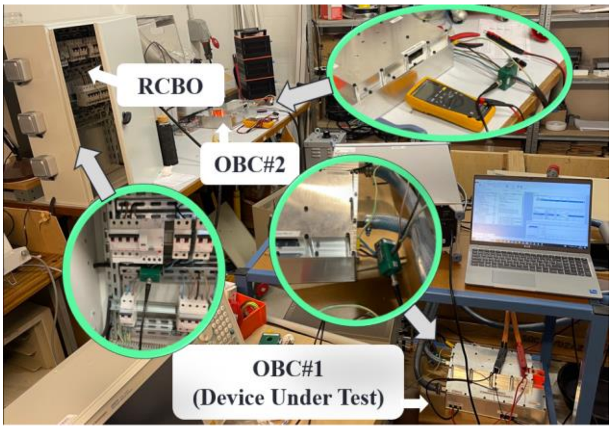

*Figure 4-6 The conducted emissions measurment setup for investigating the loads effect.*

The conducted emissions measurements are executed in four states: first, with only one OBC – the noise source – connected to the microgrid; second, after adding the second OBC (OBC#2, which acts as a passive load since it is not connected to a battery) to the microgrid; third, by plugging the laptop charger into a single-phase outlet which is connected between the second line (L2) and the neutral without connecting the laptop itself; and finally, by connecting the charger to the laptop.

The system diagram for determining the loads' impact on L2 current with all the loads – the fourth state – is indicated in Figure 4-7. It is worth noting that the loads are characterized by their impedance in Appendix D. Figure 4-8 presents a comparison between the measured data for L2 current across the four states and the scenario where the OBC is connected through the LISN. From the first to the fourth state, there is an observed increase in the amplitude of the L2 current across all frequencies within the range as well as in noise floor levels, particularly at lower frequencies.

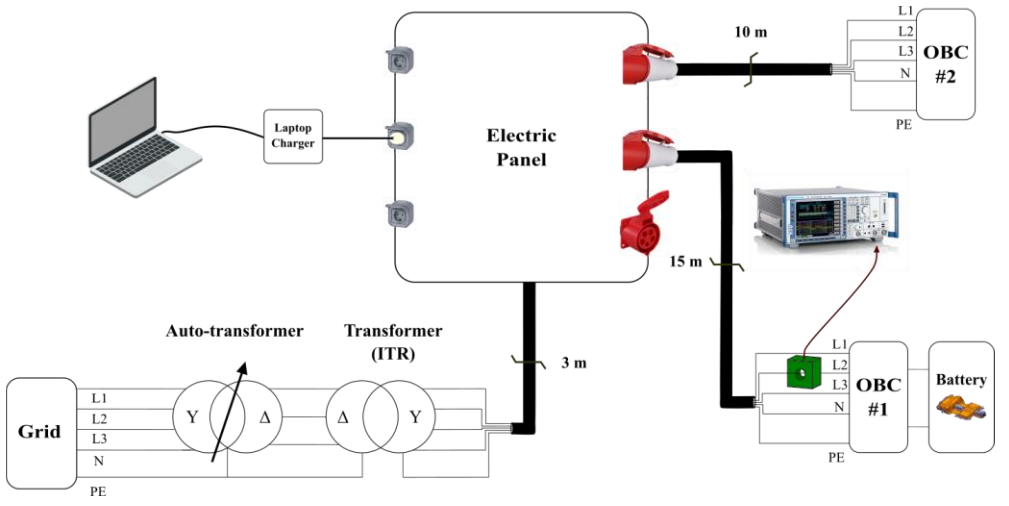

*Figure 4-7 The diagram of the system used for investigating the load impact on L2 current.*

This increase is attributed to the lower impedance that the loads provide in this frequency band from the noise source's point of view, as these impedances are in parallel. The second OBC exhibits a resonance and, therefore, a minimum impedance of around 200 kHz, while for the laptop charger, this occurs at around 250 kHz.

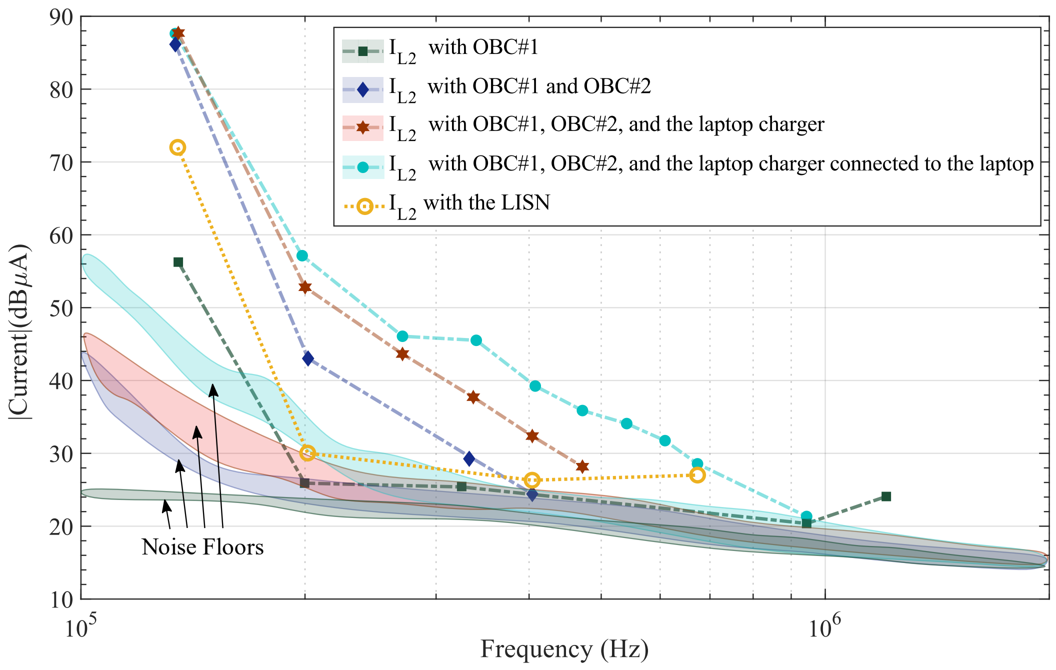

*Figure 4-8 The L2 current measured at the OBC#1 point and its evolution by connecting loads to the microgrid.*

Moreover, comparing the results of the second, third, and fourth states to the case with the LISN present indicates a significant amplitude difference of more than 15 dB at 135 kHz. This disparity worsens at the second peak (around 200 kHz), where the difference between the fourth state and the LISN case reaches a staggering 28 dB.

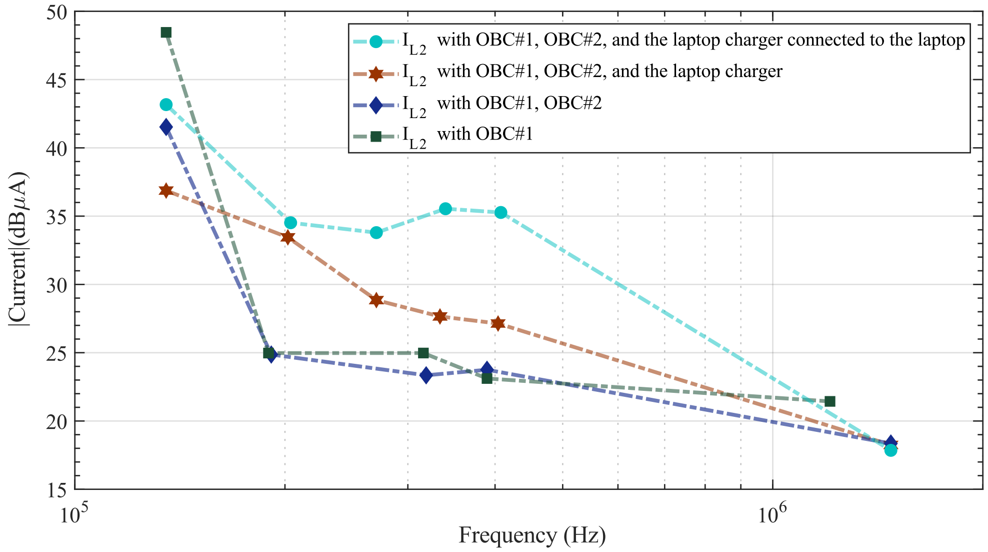

*Figure 4-9 The L2 current measured at the RCBO output – the electric panel entry – and its evolution by connecting loads to the microgrid.*

In addition, the measured L2 current for the four states at the RCBO output – the electric panel entry – is illustrated in Figure 4-9. It can be observed that when OBC#2 is added to the system, the noise level going toward the transformer decreases as the noise current can now circulate between the noise source and the loads as well.

When the laptop charger is plugged into the microgrid, some new peaks appear in the L2 current spectra that were previously obscured by the noise floor. However, even with the laptop connected to the charger and introducing a new source of perturbation into the system, the emission level at the first peak does not reach the level of current observed when only OBC#1 is connected. This is because the noise flows between the loads and does not reach the transformer side. It is important to mention that our discussion on the impact of the grounding system considered only one active load (the perturbation source) connected to the grid. When no other load is connected, the grounding system serves as the sole noise termination for the CM current, making the effect of the grounding system more pronounced. However, it is uncommon to have only one load connected or to have more loads all of them possessing very high impedance. Therefore, the impact of the grounding system in reality is likely less intense than what is depicted in Figure 4-5.

For the CM current, the same trend as L2 was observed from the first to the second state, increasing from 36 dBµA to 50 dBµA. However, unlike the L2 current, the CM current did not change across all frequencies when the laptop charger was added due to its very high CM impedance, as detailed in Appendix D.

## 4.2 Application of Charging Environment Model to Predict Conducted Emissions Level

In this section, the objective is to predict the level of parasitic currents generated by the OBC prototype when connected to the microgrid with the presence of LISN. This can be achieved by employing the black box model developed in Chapter 2, where the OBC was connected through the LISN, and integrating it into our microgrid model to establish the complete charging environment model.

In the following sections, we first apply the black box model of the converter to the realized microgrid model to compare the simulated data with the data from conducted emissions measurements presented earlier in this chapter. Subsequently, the developed converter model is employed in an extended version of the realized setup to analyze the conducted emissions in a larger-scale system.

### 4.2.1 Conducted Emissions Prediction in the Realized Microgrid

The model of the charging environment was formed by integrating the converter model for 2A G2V with the microgrid model, both developed in the previous chapter. In this section, two distinct setups are selected for the conducted emissions prediction. Within these two cases, we compare the measured results for the parasitic currents with the predicted level obtained from our model. The first setup under examination is depicted in Figure 4-4, where OBC#1 is connected to the microgrid without the LISN and without any other loads. All the current results indicated in this section are measured or simulated at the AC side of OBC#1.

It is essential to note that during some scenarios, such as connecting OBC#1 to the microgrid without the LISN and with the OBC#2 and laptop charger, presented in Figure 4-8, new peaks appear that were obscured by the noise floor previously when the measurements were done with the LISN. Since the black box model was developed based on the peaks observed when the LISN was in the circuit, the simulation results at the new peaks' frequency points are not comparable with the measured data. Therefore, we only compare the measured data and the simulated data at the frequency points where peaks were previously identified with the LISN.

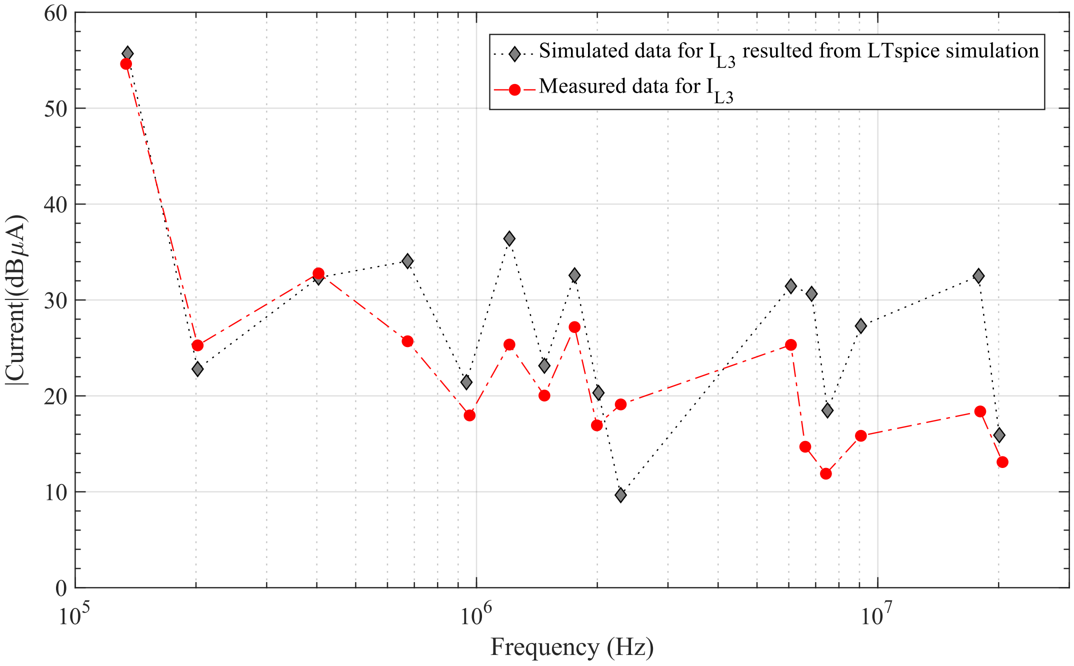

*Figure 4-10 The comparison between the measured and simulated data on the L3 current at the AC side of the OBC#1 when it is the only load connected to the microgrid with the ITR grounding system.*

The comparison between measured and simulated data obtained for the L3 and CM currents in this case are presented in Figure 4-10 and Figure 4-11, respectively. Moreover, the grounding system is selected to be ITR in both setups under study.

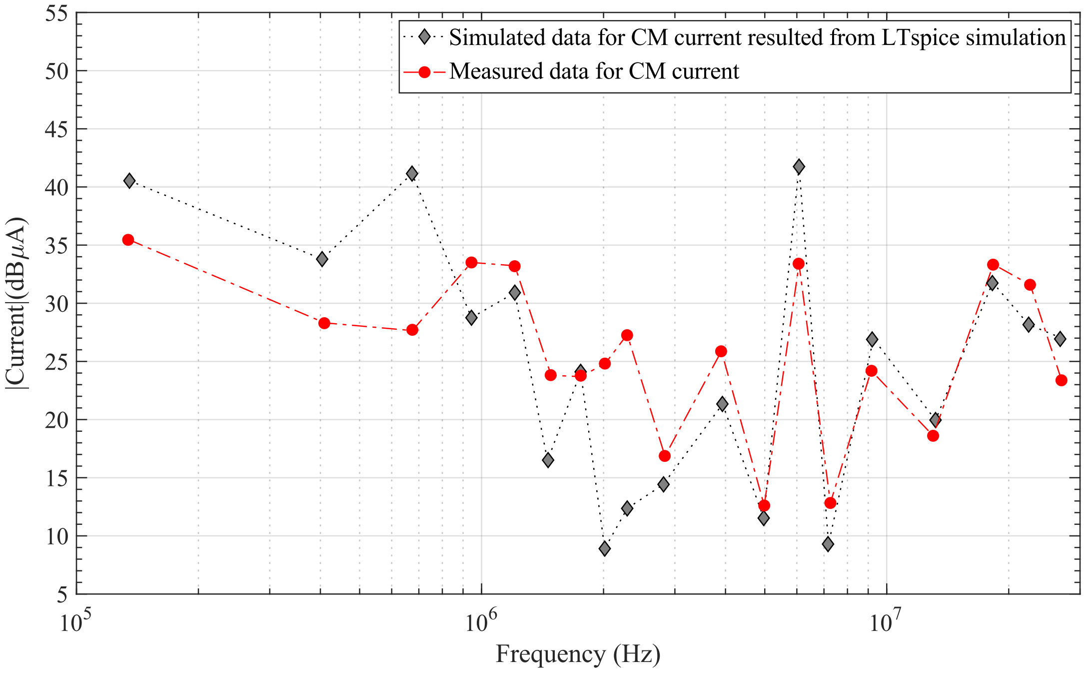

*Figure 4-11 The comparison between the measured and simulated data for the CM current at the AC side of the OBC#1 when it is the only load connected to the microgrid with the ITR grounding system.*

The second setup consists of OBC#1 and OBC#2 on the microgrid – by removing the single-phase load from the setup presented in Figure 4-7 – and the current simulations and measurements are performed at the OBC#1 input. The peak amplitudes for L3 and CM currents are presented in Figure 4-12 and Figure 4-13, respectively.

In all cases, there are some frequencies where the discrepancy between the simulated and measured results becomes significant. This discrepancy can be attributed mainly to three factors. First, there is the difficulty in phase extraction for the noise current and the assumptions regarding the phase of the perturbation sources, as discussed in Chapter 3. Second, the asymmetry present in the microgrid impedance contributes to this issue. Unlike the LISN, the microgrid impedance is not symmetric, particularly the difference between line-to-ground and neutral-to-ground impedances, which varies across different grounding systems and can cause a conversion of modes between DM and CM. The third factor lies in the error inherent in the microgrid impedance model. As presented in Section 3.2.1.5, the comparison between measured and simulated impedance at certain frequencies can be significant due to the simplifications made during the modeling stage, which are discussed in detail in the previous chapter. The relationship between the error in external noise termination impedance—the impedance of the microgrid from the OBC's perspective—and the level of parasitic current depends on the internal noise terminations (notably the EMC filter at the AC side) as well, and thus cannot be easily generalized or predicted.

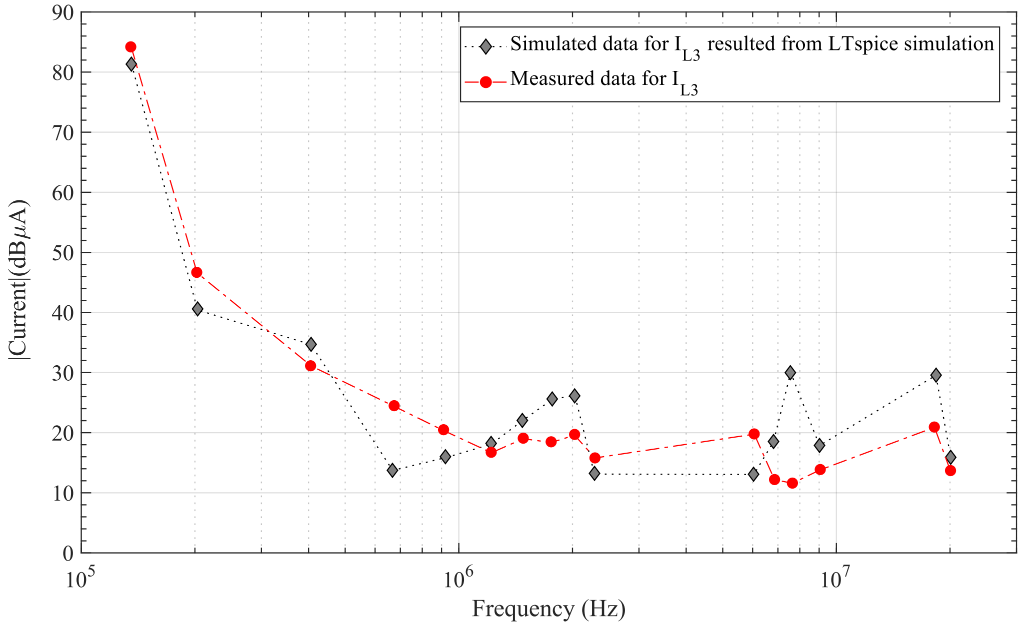

*Figure 4-12 The comparison between the measured and simulated data for the L3 current at the AC side of the OBC#1 when both OBCs are connected to the microgrid with the ITR grounding system.*

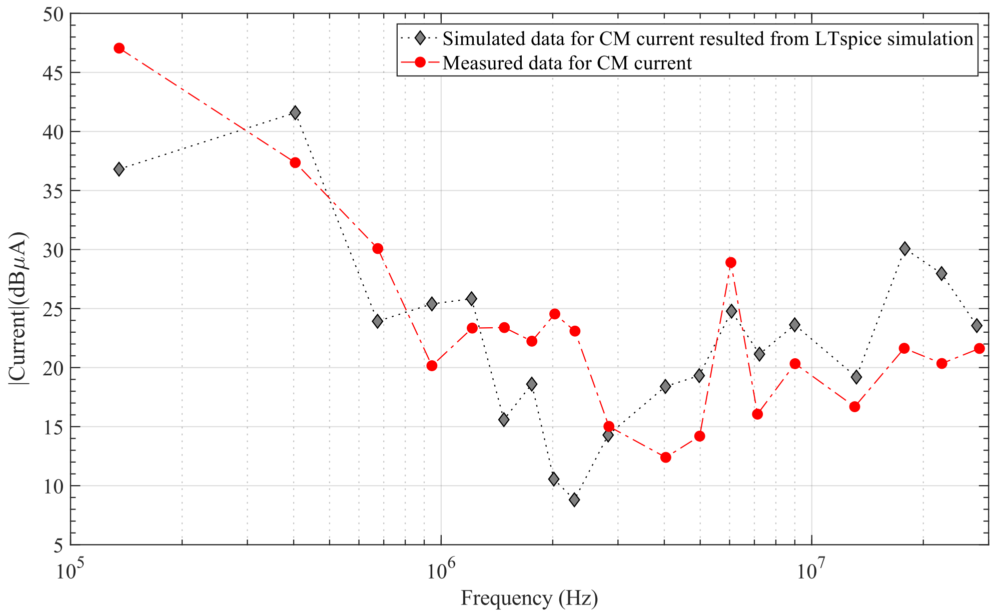

*Figure 4-13 The comparison between the measured and simulated data for the CM current at the AC side of the OBC#1 when both OBCs are connected to the microgrid with the ITR grounding system.*

Although deviations of up to approximately 10 dB exist between the measured and simulated results at some frequency points in both setups and across the four presented current spectra, the overall trend is accurately predicted. Within the EMC context, especially for complex systems with numerous parameters like ours, this level of deviation is acceptable. Additionally, some peaks are precisely forecasted. For instance, the first peak (at 135 kHz) of the L3 current, shown for three cases in Figure 4-14, demonstrates a deviation of less than 2 dB across the cases.

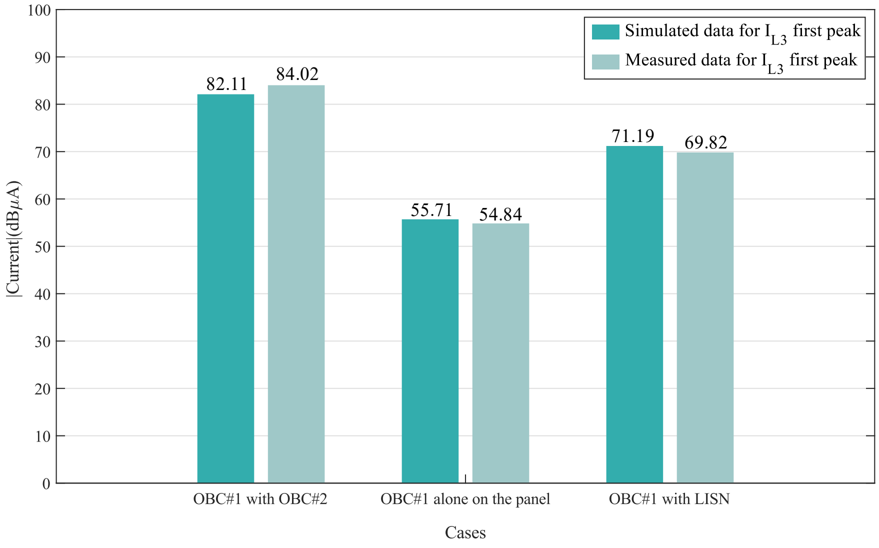

*Figure 4-14 The comparison between measured and simulated data for the first peak of L3 current at the AC side of the OBC#1 in different cases.*

This implies that by understanding the potential connected loads and employing this type of modeling, we can prevent potential malfunctions or overdesign. This is achieved by predicting the current levels in real-world situations and designing the filter based on these predicted currents instead of those measured by the LISN.

Given that the first peak, corresponding to the switching frequency, is particularly crucial for filter design, and also the fact that simulated results for the L3 current at this frequency showed minimal deviation from the measured data, in the following section, we will focus on the evolution of these first peaks as the system scales and the number of loads on the microgrid increases.

### 4.2.2 Conducted Emissions in an Extended System Model

In this section, we present the simulation results obtained from a larger-scale version of the realized system. To simplify the interpretation of the results, we begin with only one active OBC – displayed connected to the battery – and four similar passive OBCs, which are represented by the developed black box model with the perturbation sources turned off. This setup illustrates the distribution of parasitic current due to a single active OBC when five OBCs are connected to a microgrid with the structure presented in Figure 4-15.

The locations where the currents are simulated are indicated with a color code, and the cable lengths are fixed during this test. We start the simulation with OBC#1, then proceed by adding OBC#2, and continue until OBC#5.

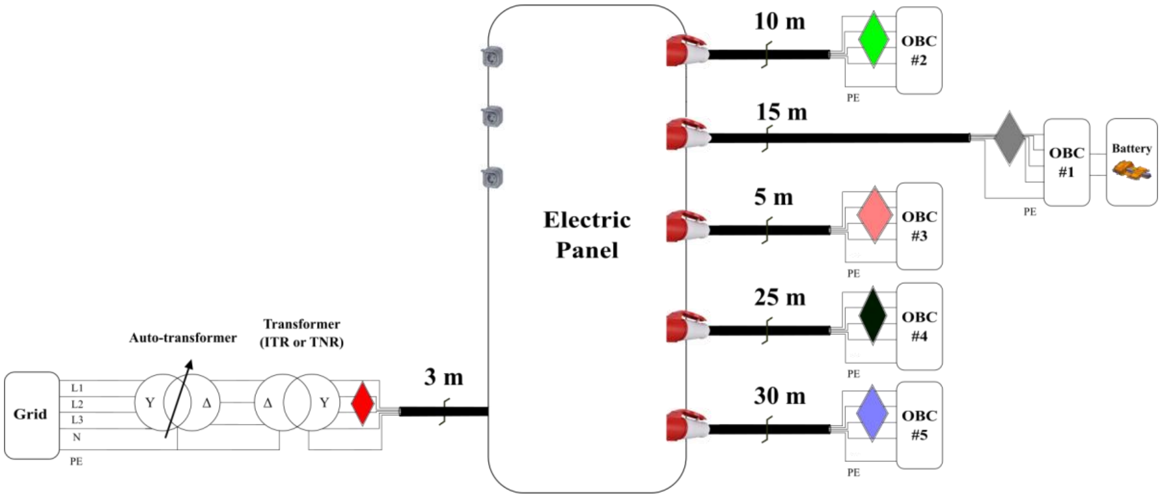

Figure 4-15 *The diagram of the extended system model with one noise source.*

The simulation results for L3 and CM currents at various locations within the microgrid with the ITR grounding system are presented in Figure 4-16 and Figure 4-17, respectively.

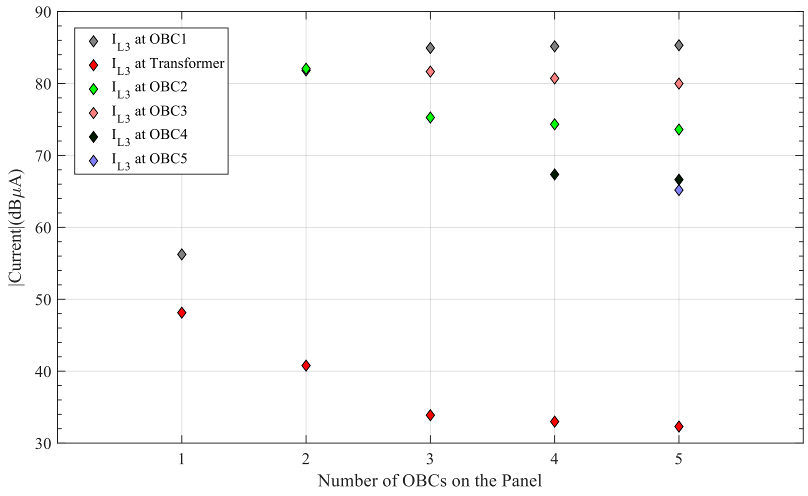

*Figure 4-16 L3 current first peak (at 135 kHz) evolution by increasing number of OBCs connected to the microgrid with ITR system.*

The L3 current results show that by adding OBCs to the microgrid, the current level at the transformer decreases while it increases at OBC#1. This occurs because the equivalent impedance seen from the noise source decreases as additional loads, which are in parallel, are added. When five OBCs are connected, the L3 current at each OBC is proportional to the length of the cable connecting the OBC to the microgrid. However, this observation is specific to this frequency and cannot be generalized as the effect of cable length at each frequency point may vary depending on the cable impedance and its impact on the equivalent impedance seen by the noise source.

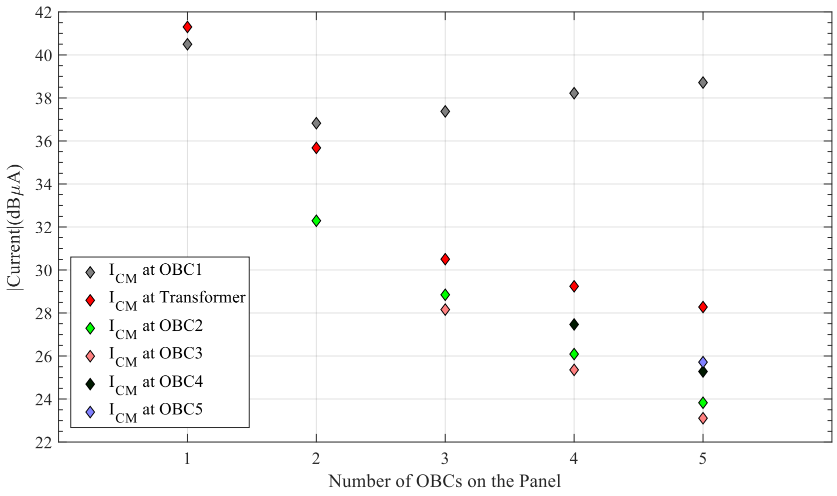

*Figure 4-17 CM current first peak (at 135 kHz) evolution by increasing number of OBCs connected to the microgrid with ITR grounding system.*

The results for the CM current at the transformer exhibit a similar trend as the L3 current. However, in the case with five OBCs on the panel, the effect of the cable length is reversed compared to the L3 current, with OBC#5 showing a higher level of noise. Nonetheless, the deviation between the CM currents at the passive OBCs is not significant in this case.

The first scenario illustrates the contribution of OBC#1 to the total current in the situation when all the OBCs are operating using the superposition theorem. It also represents a situation where the four other OBCs are not operating (simply because their respective batteries are fully charged) and are merely connected to the microgrid, presenting only their impedance.

The same test was repeated, this time with the microgrid simulated using the TNR grounding system. The results revealed identical peak amplitudes for the L3 current in both the TNR and ITR systems, which aligns with the measurement results discussed earlier in this chapter. However, in the CM current case, as presented in Figure 4-18, we observe a significant increase in CM current level across the microgrid compared to the ITR system, particularly at the transformer level, due to the lower impedance at this frequency in the TNR system.

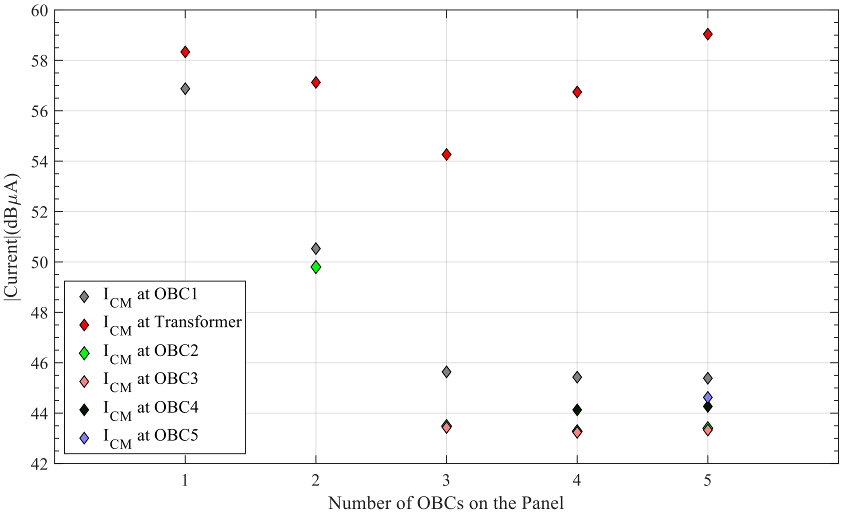

*Figure 4-18 CM current first peak (at 135 kHz) evolution by increasing number of OBCs connected to the microgrid with TNR grounding system.*

It is worth noting that the CM current did not drop below the levels observed in the case with the LISN (around 40 dBμA) in any of the cases or locations in the TNR system.

In the second scenario, two active OBCs are defined, and the CM current is analyzed across five states. Initially, only OBC#5 is connected to the microgrid. Subsequently, the other OBCs are added one by one, starting from OBC#4 and proceeding to OBC#1. The simulations were conducted in two different cases. In the first case, the active OBCs are identical. In the second case, a 30-degree phase shift is added to the CM voltage source of OBC#5.

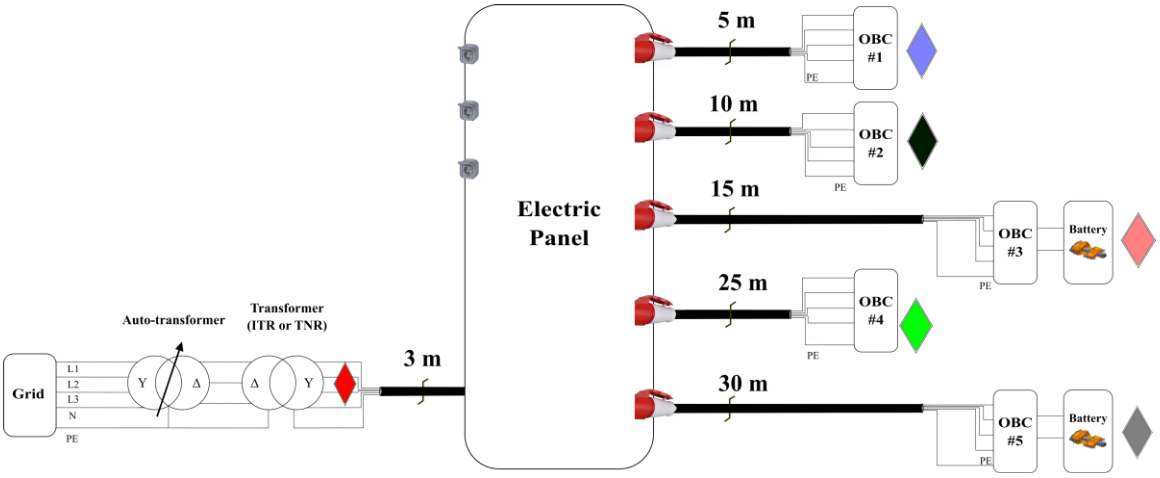

*Figure 4-19 The diagram of the extended system model with two noise sources.*

The results for both cases are illustrated in Figure 4-20. Comparing the first state – only one OBC in the system – between the two cases – one with and one without phase shift – shows 3 dB difference in CM currents at OBC#5 and around a 7 dB difference at the transformer. This highlights the phase definition importance and the limitation of this model, as discussed earlier.

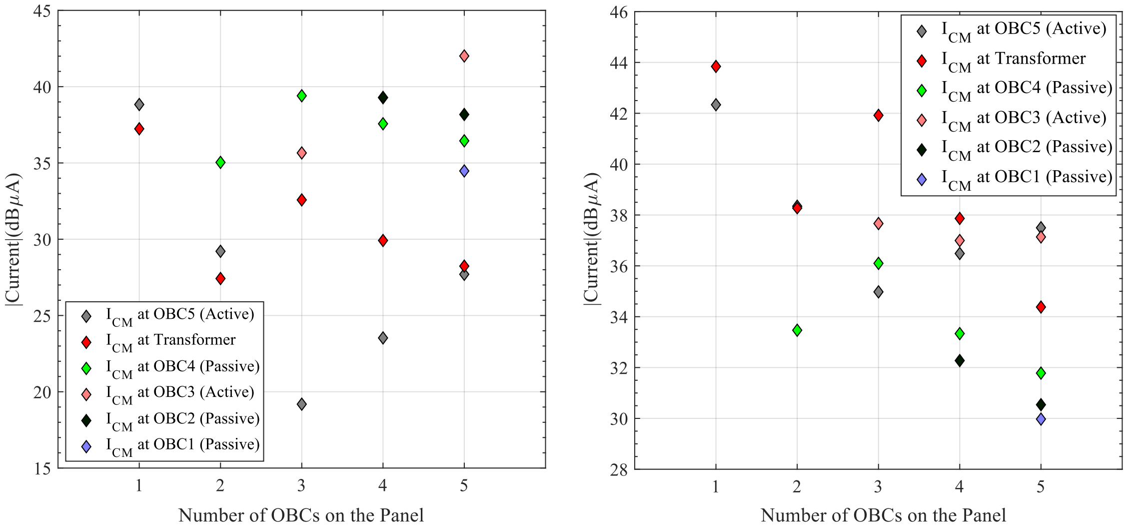

(a) (b)

*Figure 4-20 CM current first peak (at 135 kHz) evolution by increasing number of OBCs connected to the microgrid with ITR grounding system when two active OBCs are present: (a) OBCs with the same phases, (b) OBCs with a 30-degree shift in CM sources.*

Furthermore, when the second active OBC is added, the current at OBC#5 drops drastically if both OBCs have the same phase, as depicted in Figure 4-20-a. However, this impact is less pronounced when there is a phase shift between them. In practical scenarios, if the OBCs have the same switching frequency and are produced by the same company, they can exhibit random phase shifts relative to each other, as they are not synchronized. Consequently, their contributions to the current can either add up or cancel each other out.

On the one hand, the difficulty in exact phase identification of a single OBC, and on the other hand, the random variation in phase relationships when multiple OBCs are connected to the grid makes the accurate prediction of conducted emissions challenging. Consequently, this variability suggests that the model is well-suited to a statistical approach, given its reasonable computation time. Instead of providing deterministic results, the model can yield statistical outcomes in the form of probability surfaces of current levels, offering a more comprehensive understanding of potential variations in conducted emissions behavior in a complex system.

The simulation time of the model is highly dependent on the total length of the cables. Comparing the simulations for the realized system and the extended version, the number of elements increased from 9,425 to 25,111, resulting in an increase in simulation time from 20.9 seconds to 169.7 seconds, using the same frequency range and number of points.

## 4.3 Microgrid Model Application for Analyzing the Grid HF Impedance

In this section, we continue to exploit our developed microgrid model by analyzing the grid HF impedance, acknowledging the limitations posed by the noise source phase identification difficulties in the converter model. While we cannot precisely determine the impact of variations in this impedance on conducted emissions – since it depends on the noise source impedance and internal termination impedances – the trends in the external noise termination impedance generally dictate the trend of changes in conducted emissions. This is because the noise source impedances and internal noise termination impedances are usually fixed.

The microgrid model enables the exploration of various scenarios to identify the worst-case situations by finding the minimum impedance that can result from certain grid architectures through changes in grid model parameters. It can also be used to design a specific LISN tailored for particular types of grids, such as EV parking grids, with an impedance that better represents the grid's potential impedance than a typical LISN used for all grid types. We will analyze the impedance seen by the OBC in different scenarios with different parameters using our microgrid model.

The impedance seen from the measurement point was simulated, as indicated in Figure 4-21, under five conditions where OBCs were successively connected to the microgrid, from OBC#1 to OBC#4, for two distinct grounding systems.

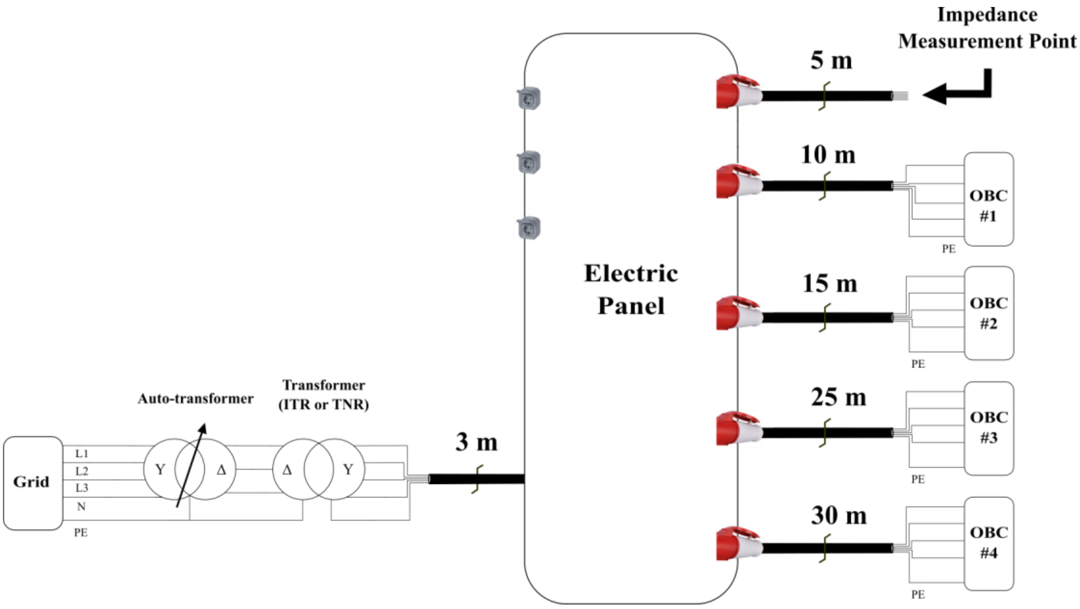

*Figure 4-21 The digram of the system used for the HF impedance investigation.*

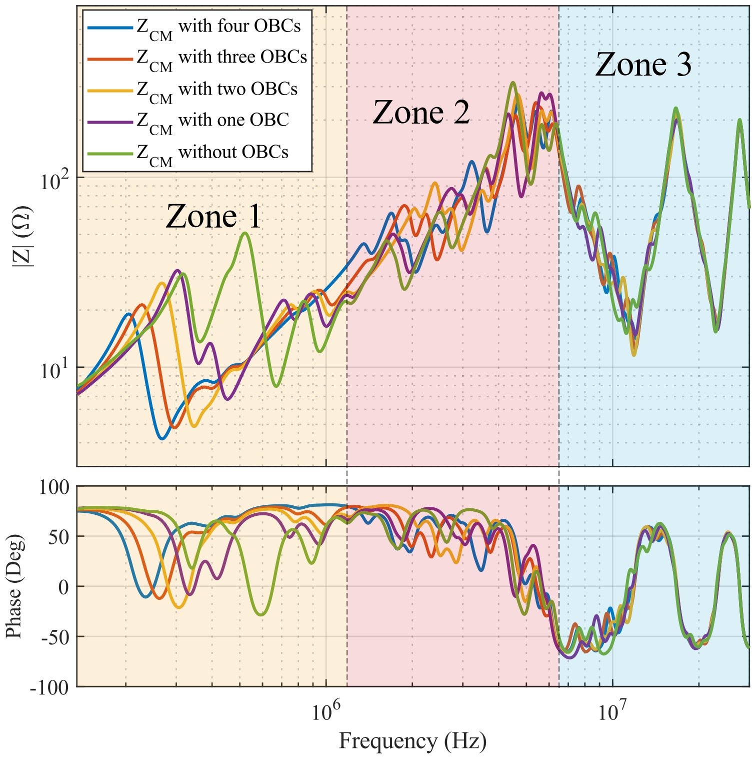

*Figure 4-22 The CM impedance evolution by increasing the number of OBCs connected to the microgrid with the TNR grounding system.*

The results for CM impedance in TNR and ITR systems are presented in Figure 4-22 and Figure 4-23, respectively.

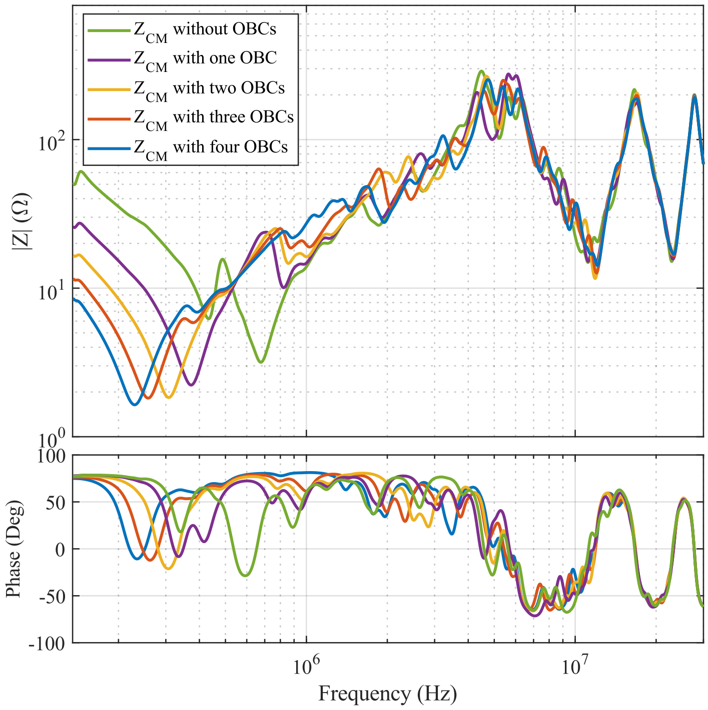

*Figure 4-23 The CM impedance evolution by increasing the number of OBCs connected to the microgrid with the ITR grounding system.*

As indicated in Figure 4-22, the impedance spectrum can be categorized into three zones. In the first zone, impedance exhibits significant variation across different loading scenarios and is relatively predictable. The second zone is characterized by impedances starting to converge, although notable deviations still exist among them, rendering the behavior unpredictable. In the third zone, impedances are nearly fully converged, with minimal deviation observed. Notably, after exploring various parameters, it was determined that changes primarily occur when adjusting the length of the final cable connecting the OBC to the microgrid. This behavior is consistent across both the case of ITR, depicted in Figure 4-23, and measurements conducted at the ENS parking grid, as presented in Chapter 2, such as in Figure 2-17.

The impedance between line 1 and neutral is also simulated for these cases and the obtained results for the ITR system are presented in Figure 4-24. The model with the TNR system yielded nearly identical results, and therefore, it is not presented here.

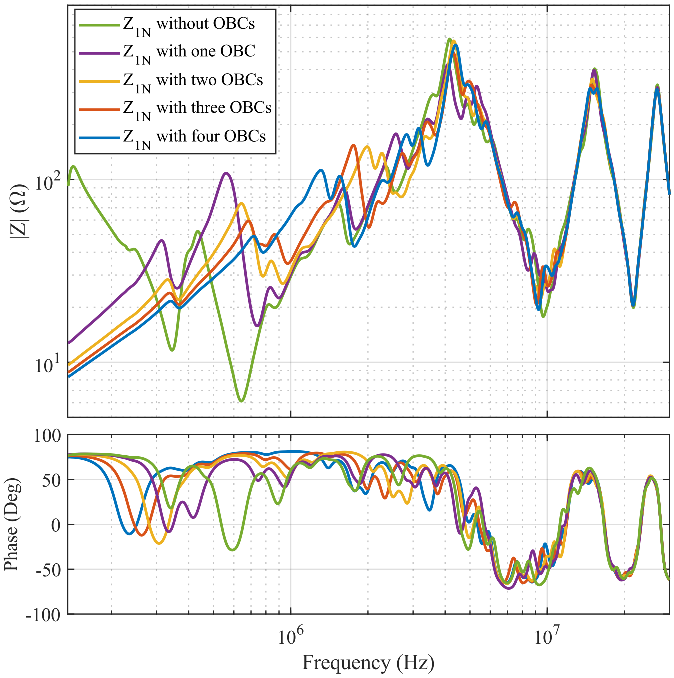

*Figure 4-24 The DM impedance ($L_1$-N) evolution by increasing the number of OBCs connected to the microgrid with the ITR grounding system.*

This impedance study provides explanations for the trends observed in conducted emissions throughout this chapter under different scenarios and configurations. It also indicates the importance of external noise termination impedance in EMC designs, which is often undermined by using the LISN.

## 4.4 Conclusion

This chapter was first dedicated to studying the conducted emissions within our realized charging environment to understand the impact of various parameters on the parasitic current. We investigated the influence of operating points, grounding systems, cable lengths, and connected loads on the emissions generated by the OBC prototype.

The focus then shifted to the exploitation of the developed model. In the first step, we predicted the level of conducted emissions under different conditions, comparing these predictions to measured results. The results were then interpreted, showing trends and explanations for deviations. The analysis revealed that although the model could accurately predict some peaks and overall trends, deviations existed due to complexities such as phase identification of the perturbation sources. This makes accurate phase-dependent predictions challenging specially in situations when mulitple OBCs operating in the system. However, a significant advantage of the model is its low computation time, making it suitable for statistical studies.

The focus then shifted to exploiting the developed model. Initially, we predicted the level of conducted emissions under various conditions and compared these predictions to measured results. The analysis showed that while the model could accurately predict some peaks and overall trends, deviations existed due to complexities such as the phase identification of perturbation sources. These complexities make accurate phase-dependent predictions particularly challenging in situations where multiple OBCs are operating within the system. However, a significant advantage of the model is its low computation time, which makes it well-suited for statistical studies.

Finally, the impedance study justified the variations observed in conducted emissions under different scenarios and configurations. It underlined the importance of the external noise termination impedance in understanding and predicting conducted emissions propagation in complex electrical systems.

In conclusion, the chapter highlighted the critical role of detailed impedance analysis and accurate modeling in predicting and mitigating conducted emissions in EV charging environments. It also stressed the limitations of relying solely on LISN for EMC designs and the necessity of considering the grid's characteristics for comprehensive EMC management.

# GENERAL CONCLUSION AND PERSPECTIVES

The research presented in this dissertation has provided significant insights into the propagation of conducted emissions generated by OBCs in grids with various grounding systems and in different scenarios. By implementing an online HF impedance measurement technique, we were able to measure and analyze the HF impedance of the grid. Moreover, by employing this technique, we were able to model a prototype under its operating condition with a black box modeling approach.

We conducted an impact analysis on the volume and mass of EMC filters. This involved a quantitative assessment of how these volumes vary under different scenarios, particularly focusing on the effects of including or excluding an LISN in the measurement setup, as well as the implications of adjusting the stringency of EMC standards.

A microgrid was first established to allow parameter modifications, followed by the development of a detailed model with automatic generation of circuit elements based on experimental acquisitions. This flexible model permits quick and easy parameter adjustments, making it well-suited for analyzing various scenarios and conducting statistical studies, while also ensuring the accuracy and relatively short simulation times.

By integrating the black-box model of the OBC prototype with the detailed microgrid model, we have successfully simulated and analyzed the impact of different parameters, such as grounding configurations, on conducted emissions. The comparison between simulated and measured results has highlighted the challenges in predicting precise emission levels, particularly due to the phase identification difficulties and asymmetries in microgrid impedance.

Key findings of this study include the identification of trends in the external noise termination impedance and their influence on the conducted emissions and the EMC filter volume. In conclusion, this dissertation contributes to the field of EMC by providing a methodology for assessing conducted emissions in realistic grid scenarios and offers valuable perspectives for enhancing the effectiveness of EMC filtering and reducing the potential for interference in practical applications.

## Perspectives

The limitations identified in this work, such as the phase extraction challenges, suggest areas for further research. Future studies could focus on the following list.

- A critical perspective for further study is the measurement of the phase of parasitic currents with more advanced configurations. Utilizing a signal analyzer capable of providing both the phase and amplitude of the signal will improve the accuracy of noise characterization and result in a more predictive model.
- Developing a converter model based on more accurate phase data and fewer assumptions with improved performance when connected to asymmetric systems such as the microgrid model discussed in this research. This advancement could enhance the accuracy of the model in predicting conducted emissions under various operating conditions, particularly in complex electrical environments.
- Employing the developed model for conducting a statistical analysis of conducted emissions in scenarios with multiple OBCs with random phases connected to the grid. This approach would involve establishing probability surfaces for current levels, offering a more comprehensive understanding of the variability and potential extremities in conducted emissions in complex systems.
- The developed microgrid model can be instrumental in designing and fabricating specialized LISNs tailored for particular grid types, such as domestic or public EV parking facilities. In environments where there is general knowledge about the types of loads, cable lengths, and grounding systems, a specialized LISN can predict worst-case scenarios for that specific grid and avoid malfunctions; it can also help in avoiding overdesign in some cases. To go beyond that, we can imagine new standards that introduce a set of specialized LISNs, each related to a specific grid in which parameters such as maximum cable length, a cap on the number of EVs, and a specific grounding configuration are imposed. This provides a more accurate basis for EMC testing and compliance, especially in less general settings with unique characteristics and load configurations.
- To date, there are no EMC standards that specifically dictate an amplitude range of the input HF impedance (in the EMC frequency range) of a device seen by the grid, which is mostly the impedance of the grid-side EMC filter. Using the model, a study about the

optimum amplitude range for this impedance can be conducted. If applied, this can significantly limit the overall conducted emission in the system.

These perspectives aim to enhance the precision of conducted emissions modeling and measurement, leading to better design practices and compliance strategies in evolving electrical systems and infrastructures.

## Published Papers

M. Seddighi, F. Costa and M. Petit, "Influence of Modifying Standard Emission Levels on the sizing of EMC Filters," 2021 23rd European Conference on Power Electronics and Applications (EPE'21 ECCE Europe), 2021, pp. P.1-P.9.

M. Seddighi, F. Costa, P. -E. Levy and D. Oustad, "Impact of Standardized Methods Applied for Conducted EMI Estimation on the Volume of an EMC Filter in a DC Supplied Single-leg Inverter," 2022 IEEE 7th Southern Power Electronics Conference (SPEC), Nadi, Fiji, 2022, pp. 1-4, doi: 10.1109/SPEC55080.2022.10058449.

# Appendix A

## ***Scattering parameters***

The general solution for the voltage and current wave equations for a lossless transition line can be expressed as

$$V(x) = Ae^{-j\beta x} + Be^{j\beta x} \qquad \text{A-1}$$

$$I(x) = \frac{A}{Z_0}e^{-j\beta x} - \frac{B}{Z_0}e^{j\beta x} \qquad \text{A-2}$$

where A and B are complex constants calculated using the boundary conditions and $Z_0$ is the characteristic impedance of the transmission line, and $\beta$ is the propagation constant.

Introducing the following notations for incident voltage wave:

$$V^+(x) = Ae^{-j\beta x} \qquad \text{A-3}$$

and for reflected voltage wave:

$$V^-(x) = Be^{j\beta x} \qquad \text{A-4}$$

we can rewrite A-1 by replacing

$$V(x) = V^+(x) + V^-(x) \qquad \text{A-5}$$

and A-2 in form

$$I(x) = I^+(x) - I^-(x) = \frac{V^+(x)}{Z_0} - \frac{V^-(x)}{Z_0} \qquad \text{A-6}$$

By introducing the normalized notation for voltage and current as follows

$$v(x) = \frac{V(x)}{\sqrt{Z_0}} \qquad \text{A-7}$$

$$i(x) = \sqrt{Z_0}\, I(x) \qquad \text{A-8}$$

The normalized incident and reflected waves can be defined as

$$a(x) = \frac{V^{+}(x)}{\sqrt{Z_0}} \qquad \text{A-9}$$

$$b(x) = \frac{V^{-}(x)}{\sqrt{Z_0}} \qquad \text{A-10}$$

By replacing A-9 and A-10 inside A-5 and A-6, we can write

$$v(x) = a(x) + b(x) \qquad \text{A-11}$$

$$i(x) = a(x) - b(x) \qquad \text{A-12}$$

For a two-port network, as shown in Figure A-1, incident and reflected waves at port 1 and port 2 as

$$b_1(l_1) = S_{11}\, a_1(l_1) + S_{12}\, a_2(l_2) \qquad \text{A-13}$$

and

$$b_2(l_2) = S_{21}\, a_1(l_1) + S_{22}\, a_2(l_2) \qquad \text{A-14}$$

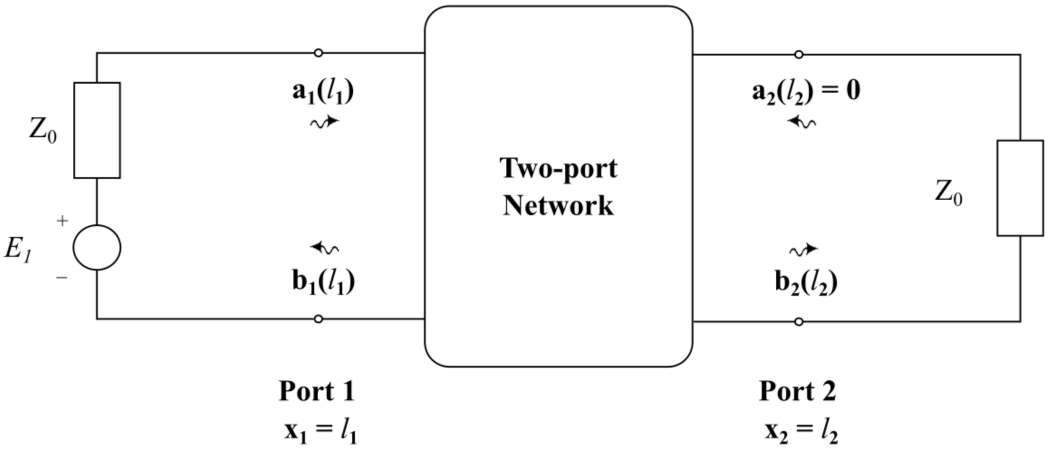

*Figure A-1 Incident and reflected waves in a two-port network with one source*

where the $S_{11}$, $S_{12}$, $S_{21}$, $S_{22}$ are called scattering parameters or S-parameters and represent reflection and transmission coefficients. They are usually presented in matrix form for a two-port network:

$$[S] = \begin{bmatrix} S_{11} & S_{12} \\ S_{21} & S_{22} \end{bmatrix} \qquad \text{A-15}$$

Therefore, each of them can be defined as follows:

- $S_{11}$: Input reflection coefficient with output properly terminated

$$S_{11} = \left.\frac{b_1(l_1)}{a_1(l_1)}\right|_{a_2(l_2)=0} \qquad \text{A-16}$$

- $S_{21}$: Forward transmission coefficient with output properly terminated

$$S_{21} = \left.\frac{b_2(l_2)}{a_1(l_1)}\right|_{a_2(l_2)=0} \qquad \text{A-17}$$

- $S_{22}$: Output reflection coefficient with input properly terminated

$$S_{22} = \left.\frac{b_2(l_2)}{a_2(l_2)}\right|_{a_1(l_1)=0} \qquad \text{A-18}$$

- $S_{12}$: Reverse transmission coefficient with input properly terminated

$$S_{12} = \left.\frac{b_1(l_1)}{a_2(l_2)}\right|_{a_1(l_1)=0} \qquad \text{A-19}$$

For finding the relation between the voltages ratio and S-parameters, we can write the A-11 for both input and output voltages:

$$\frac{v_2}{v_1} = \frac{a_2 + b_2}{a_1 + b_1} \qquad \text{A-20}$$

as there is no source in the output $a_2$ is equal to zero, and by dividing the numerator and denominator by $a_1$ we can rewrite A-20 as follows:

$$\frac{v_2}{v_1} = \frac{b_2}{a_1 + b_1} = \frac{\frac{b_2}{a_1}}{1 + \frac{b_1}{a_1}} \qquad \text{A-21}$$

then, by replacing A-16 and A-17 inside A-21, the output and input voltage ratio can be written in the function of S-parameters as follows:

$$\frac{v_2}{v_1} = \frac{S_{21}}{1 + S_{11}} \qquad \text{A-22}$$

# Appendix B

## *RF current injection and monitor probes*

The wideband probes that were characterized in probe selection procedure for TP method are listed in Table B-1. Among them, probes such as Pearson 6595 and 8585C, were also employed in conducted emission measurement. The transfer functions of the probes were measured using the configuration presented in Figure 2-5. For instance, Figure B-1 exhibits the transfer function of the Pearson 6595.

*Table B-1 List of clamp probes characterized during the probe selection process.*

| | **Nominal Frequency Range** | **Nominal Sensitivity** | **Type** |
|---|---|---|---|
| Pearson 2877 | 300 Hz – 200 MHz | 1 Volt/Ampere | Current Monitor |
| Pearson 8585C | 1500 Hz – 200 MHz | 1 Volt/Ampere | Current Monitor |
| Pearson 6595 | 100 Hz – 150 MHz | 0.5 Volt/Ampere (on 1 MΩ) | Current Monitor |
| Pearson 441C | 25 Hz – 20 MHz | 0.1 Volt/Ampere | Current Monitor |
| Tektronix CT2 | 1200 Hz – 200 MHz | 1 Volt/Ampere | Current Monitor |
| Prana IP-DR250 | 10 kHz – 400 MHz | N/A | BCI |
| Com-Power CLCE-400 | 10 kHz – 400 MHz | N/A | BCI |

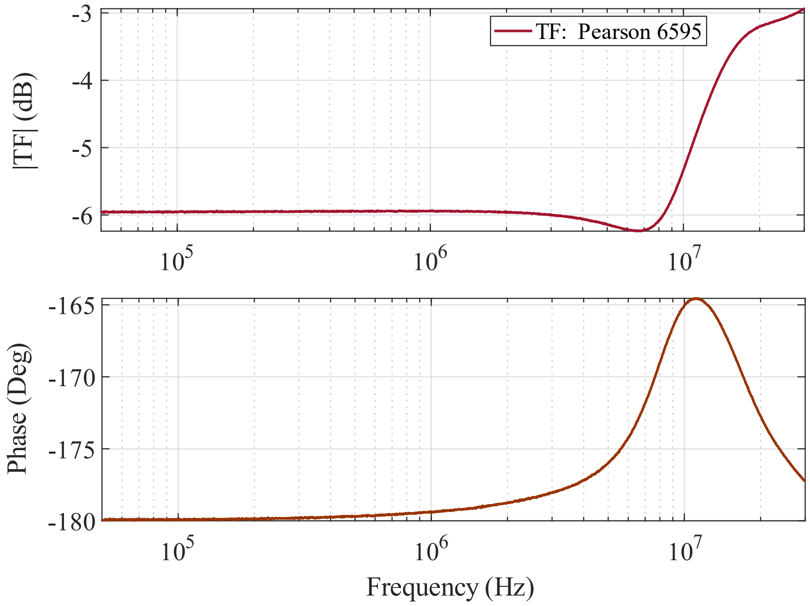

*Figure B-1 The measured transfer function of the Pearson 6595.*

# Appendix C

## *Circuit element definition in LTspice*

LTspice AC analysis introduces the possibility of defining a complex impedance or source based on measured data by defining the data – amplitude and phase – at all the frequency points. This capability enables the creation of more accurate and simpler models for complex systems and consequently lowers the simulation time. Although time-domain analysis is not possible with this method, it is highly useful for cases like ours where frequency-domain analysis is required, even if the simulation is done in the time domain. To accomplish this, we need to create a netlist that specifies all the frequency points using arbitrary behavioral voltage or current sources and then associate it with a symbol, as shown in Figure C-1.

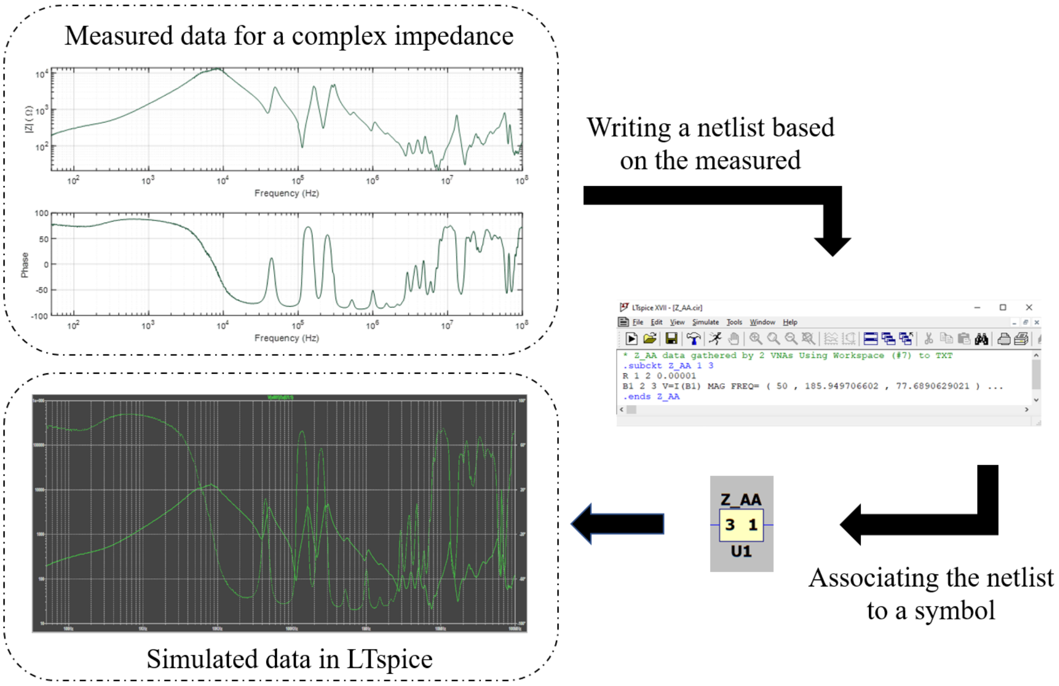

```
* Z_AA data gathered by 2 VNAs Using Workspace (#7) to TXT
.subckt Z_AA 1 3
R 1 2 0.00001
B1 2 3 V=I(B1) MAG FREQ= ( 50 , 185.949706602 , 77.6890629021 ) ...
.ends Z_AA
```

*Figure C-1 Definition of a circuit element for a complex impedance in LTspice based on measured data.*

This can be done for a complex voltage or current source as well with a similar approach using two arbitrary behavioral sources. As an example, for a current source the netlist and the results are presented in Figure C-2.

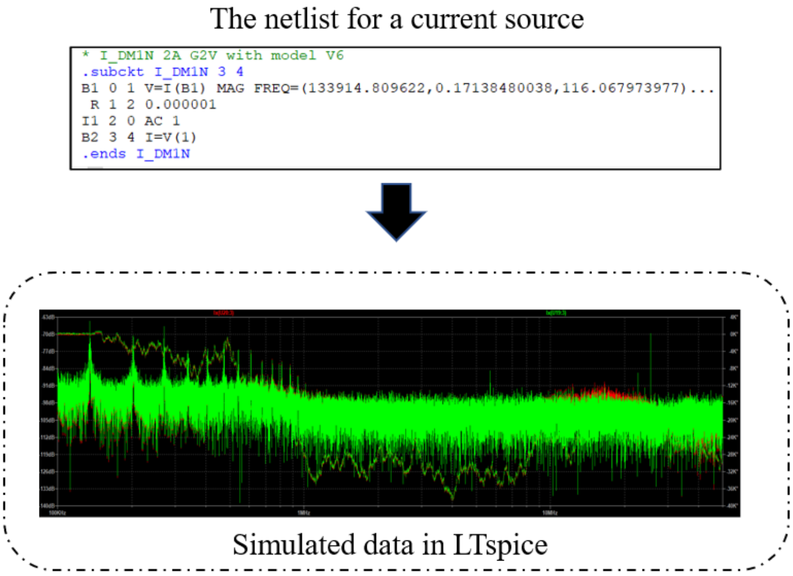

```
* I_DM1N 2A G2V with model V6
.subckt I_DM1N 3 4
B1 0 1 V=I(B1) MAG FREQ=(133914.809622,0.17138480038,116.067973977)...
 R 1 2 0.000001
I1 2 0 AC 1
B2 3 4 I=V(1)
.ends I_DM1N
```

*Figure C-2 Definition of a circuit element for a complex current source in LTspice based on measured data.*

It is worth mentioning that in this method, the simulation time varies significantly with the simulation number of points as well as the number of points used to define the impedance or the source. This is because LTspice performs interpolation twice: once to find the appropriate data for the circuit element at the analysis frequency points and again to interpolate between the result data.

In the results presented in Figure C-2, the current source is defined by $10^7$ frequency points coming from FFT on the time-domain measurements and $10^5$ simulation points per decade, and the simulation time is around 6 minutes for analysis in the range from 100 kHz to 50 MHz. However, it is not an efficient way to define the noise source, as we are interested only in peak points and not in the points of the noise floor. Therefore, by defining an envelope for the signal, the simulation time and the needed simulation points can be significantly reduced. In the final simulation done in section 3.2.2.3, 625 simulation points per decade are used, and the circuit elements are defined using a maximum of 2000 points, which results in a simulation time of 164 ms for a frequency band from 135 kHz to 30 MHz.

# Appendix D

## Modeling of the loads connected to the microgrid during the model verification

In the microgrid model verification procedure, the measured and simulated impedance of the microgrid were compared under various conditions, both with and without loads, from different points within the microgrid. For the model verification, two single-phase loads – a laptop charger and a phone charger – along with two three-phase OBCs of the same model were utilized. These components were measured offline and then modeled with the method explained in Appendix C.

The laptop charger model, along with the offline CM impedance measurement, is presented in Figure D-1. Similar to other offline impedance measurements in this study, the E4990A impedance analyzer was employed for measuring the impedance of the loads.

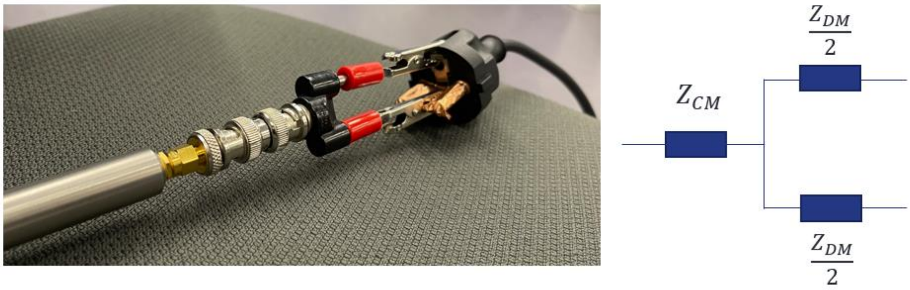

*Figure D-1 CM impedance measurement and the model of the laptop charger.*

As demonstrated in Figure D-2, the results show a capacitive CM impedance and a DM impedance with a resonance at around 450 kHz.

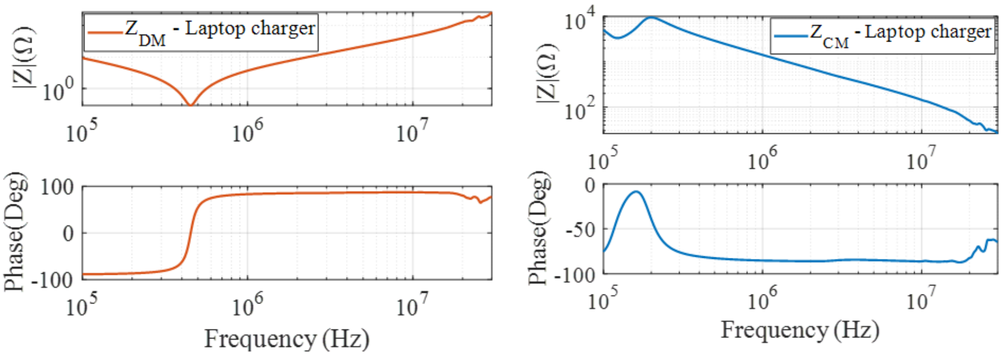

*Figure D-2 The measured data for laptop charger CM and DM impedances.*

However, it must be mentioned that for the fourth Chapter, the previously used laptop charger was replaced with a new charger. For this charger, the same model was employed, presented in Figure D-1, and its CM and DM impedances are demonstrated in Figure D-3.

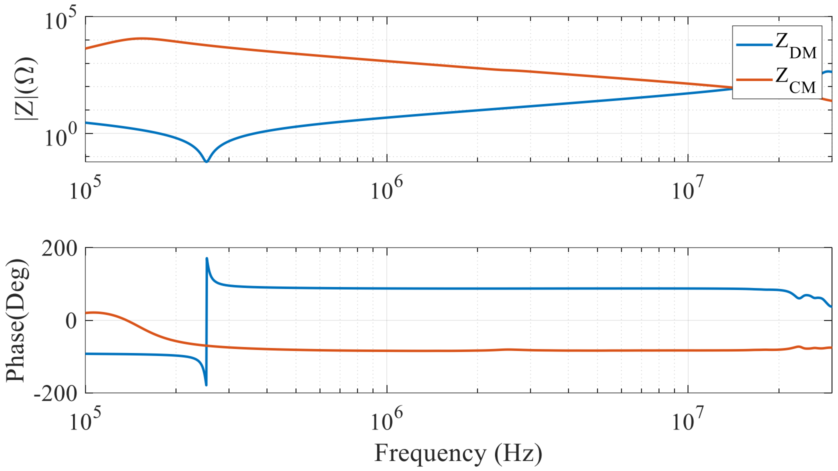

*Figure D-3 The measured data for CM and DM impedances of the laptop charger used in the fourth Chapter.*

The phone charger, on the other hand, does not have a protective earth connection due to its lower power compared to the laptop charger. Therefore, it can be simply modeled by a single impedance, as depicted in Figure D-4.

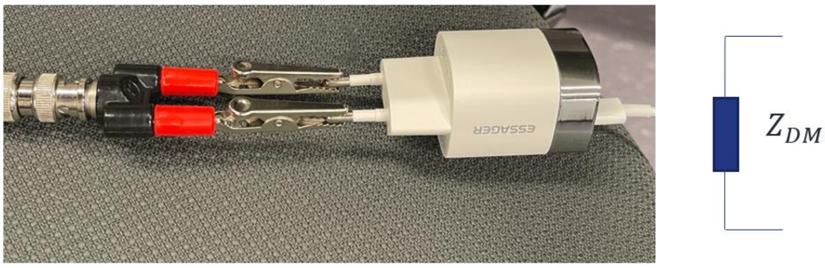

*Figure D-4 DM impedance measurement and the model of the phone charger.*

The measured data for the phone charger is presented in Figure D-5. In addition, the OBCs have identical impedances, and their offline impedances match their online impedances, which are presented in Chapter 3. This is due to the fact that the relay is placed between the EMC filter and the converter, with the EMC filter dominating the impedance seen from the AC output, even when the relay is closed. Therefore, the passive model of the OBCs is obtained by just turning off the perturbation sources of the developed black box model. All these measured data were used directly to create the circuit elements, as explained in Appendix C.

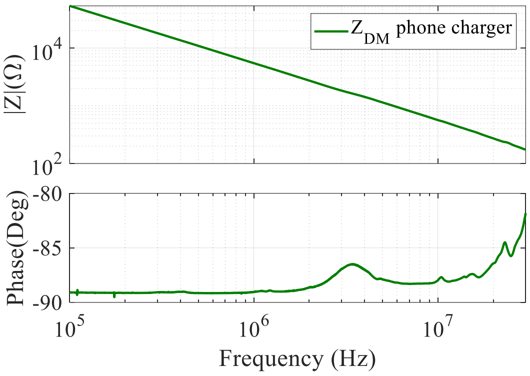

*Figure D-5 The measured data for the phone charger DM impedance.*

# Appendix E

## ***DM source calculation using an analytic approach for a three-port black box model***

In [90], the analytic approach is employed to calculate the perturbation sources of a three-port black box model by employing the superposition theorem. Given that the model proposed by [90], presented in Figure 3-32, includes four independent noise sources, the superposition theorem allows us to consider four distinct configurations. Each configuration is analyzed by turning off all sources except the one under examination. Since the procedure is identical for all three DM sources, we will focus on the DM current source between lines 1 and 2, corresponding to the second configuration presented in Figure E-1. In this section, we will discuss a part of the calculation process of DM sources, which involves the determination of $\boldsymbol{I_{DM12}}$ contribution to the output currents ($\boldsymbol{I_1^{(2)}}$ and $\boldsymbol{I_2^{(2)}}$) in function of the system impedances.

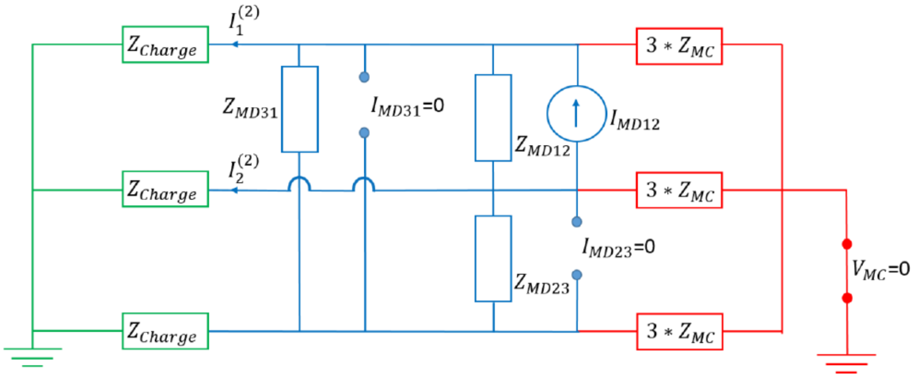

*Figure E-1 The equivalent model of the second configuration [90].*

In order to determine the $\boldsymbol{I_{DM12}}$ in function of $\boldsymbol{I_1^{(2)}}$ and $\boldsymbol{I_2^{(2)}}$, the schematic in Figure E-1 is simplified and replaced with the equivalent Norton model presented in Figure E-2.

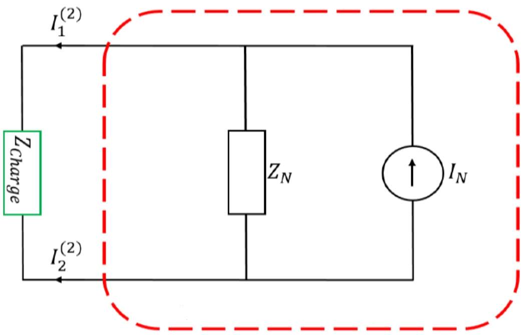

*Figure E-2 The equivalent Norton model [90].*

This involves calculating the equivalent Norton current source by short-circuiting the $Z_{Charge}$ impedance and determining the $Z_N$ impedance by disconnecting the $Z_{Charge}$ impedance and deactivating the $I_N$ current source. Therefore, from the model presented in Figure E-2, the currents $\boldsymbol{I_1^{(2)}}$ and $\boldsymbol{I_2^{(2)}}$ can be calculated from equation E-1.

$$\boldsymbol{I_1^{(2)} = -I_2^{(2)} = \frac{I_N\, Z_N}{Z_N + Z_{Charge}}} \tag{E-1}$$

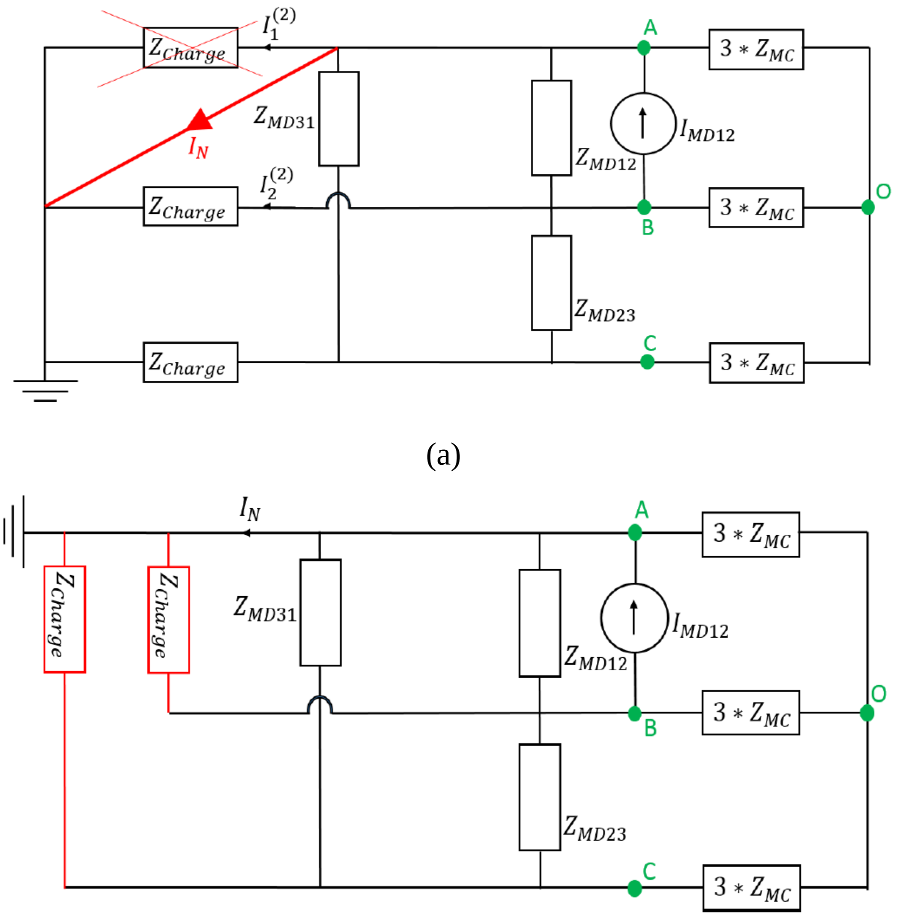

(a)

(b)

*Figure E-3 Converter equivalent diagrams for determining Norton current [90].*

In order to determine the Norton current, the $Z_{Charge}$ is short-circuited, as depicted in Figure E-3-a. Therefore, the diagram presented in Figure E-3-b can be obtained. By applying the KENNELLY theorem, the star (OABC) can be transformed into a triangle (ABC), as presented in Figure E-4, using the following Equation:

$$\boldsymbol{Z'_{MC} = \frac{3(3Z_{MC})^2}{3Z_{MC}} = 9Z_{MC}} \tag{E-2}$$

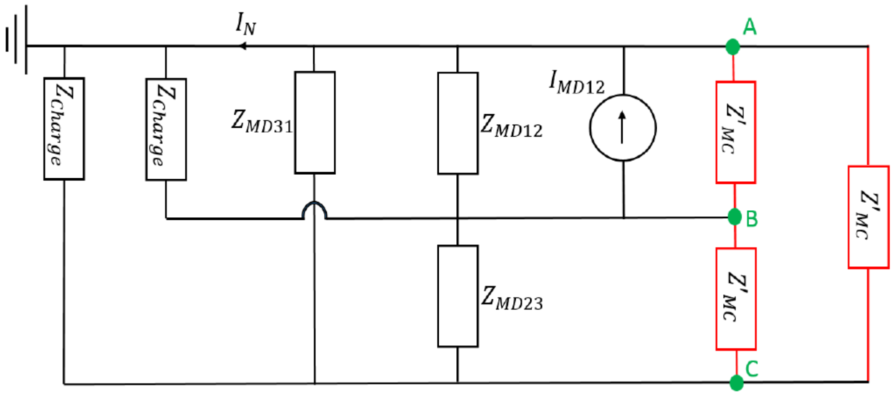

*Figure E-4 Equivalent diagram after applying the KENNELLY theorem [90].*

The DM impedances are assumed to be identical and equal to $Z_{MD}$ for the sake of simplification, which allows for simplifying the diagram as presented in Figure E-5 by defining $Z_p$ as

$$Z_p = Z_{MD} \,||\, Z'_{MC} = \frac{Z_{MD}\ Z'_{MC}}{Z_{MD} + Z'_{MC}} = \frac{9\ Z_{MD}\ Z_{MC}}{Z_{MD} + 9Z_{MC}} \qquad \text{E-3}$$

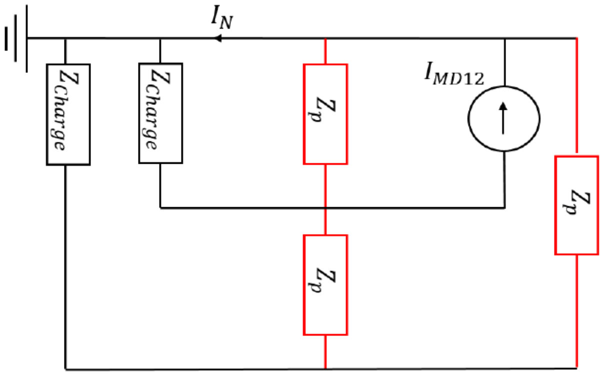

*Figure E-5 Equivalent diagram after using the parallel equivalent of the impedances [90].*

Therefore, the Norton current can be expressed as:

$$I_N = \frac{I_{MD12}\, Z_p}{Z_p + Z_{Charge}} \qquad \text{E-4}$$

In order to determine the Norton impedance ($Z_N$), $Z_{Charge}$ is eliminated along with the current source, as presented in Figure E-6. In order to simplify the diagram presented in Figure E-6, first, by applying again the KENNELLY theorem, the $Z'_{MC}$ can be calculated as described in Equation E-2. Then, by assuming the identical DM impedances, $Z_p$ can be defined by Equation E-3. Therefore, the simplified diagram can be obtained as demonstrated in Figure E-7.

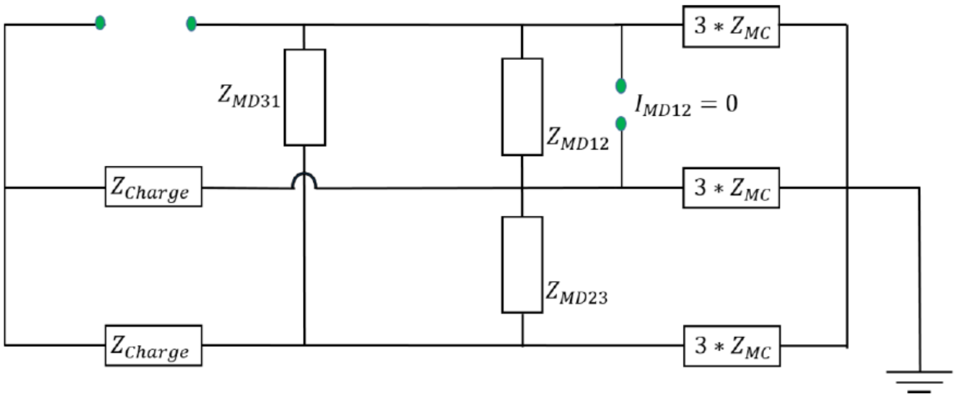

*Figure E-6 Equivalent diagram used for the calculation of the Norton impedance [90].*

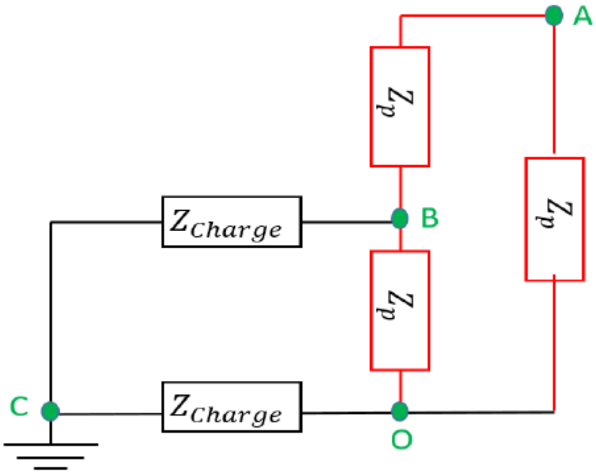

*Figure E-7 The obtained equivalent diagram after applying the KENNELLY theorem and using the equivalent for parallel impedances [90].*

In order to simplify further, for the second time, the KENNELLY theorem is applied to transform from the star structure (OABC) to the triangle structure (ABC). This results to the simplified diagram illustrated in Figure E-8 where the $Z_{k1}$, $Z_{k2}$, and $Z_{k3}$ impedances are defined as:

$$\boldsymbol{Z_{k1} = \frac{Z_{Charge}\, Z_p + Z_{Charge}\, Z_p + Z_p\, Z_p}{Z_p} = 2Z_{charge} + Z_P} \quad \text{E-5}$$

$$\boldsymbol{Z_{k2} = \frac{Z_{Charge}\, Z_p + Z_{Charge}\, Z_p + Z_p\, Z_p}{Z_{Charge}} = 2Z_P + \frac{Z_P^2}{Z_{charge}}} \quad \text{E-6}$$

$$\boldsymbol{Z_{k3} = \frac{Z_{Charge}\, Z_p + Z_{Charge}\, Z_p + Z_p\, Z_p}{Z_p} = 2Z_{charge} + Z_P} \quad \text{E-7}$$

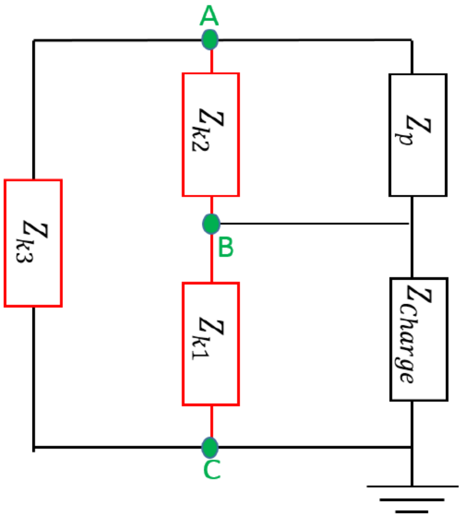

*Figure E-8 The obtained equivalent diagram after transformation to the triangle structure [90].*

Finally, the Norton impedance can be determined as follows:

$$\boldsymbol{Z_N = ((Z_{Charge}||\,Z_{k1}) + (Z_p||\,Z_{k2}))\,||\,Z_{k3}}$$
$$= \frac{\boldsymbol{(((2Z_{charge} + Z_P)||\,Z_{charge}) + (Z_P||\left(2Z_P + \frac{Z_P^2}{Z_{charge}}\right))).\,(2Z_{charge} + Z_P)}}{\boldsymbol{2Z_{charge} + Z_P + ((2Z_{charge} + Z_P)||\,Z_{charge}) + (Z_P||\left(2Z_P + \frac{Z_P^2}{Z_{charge}}\right))}} \qquad \text{E-8}$$

Therefore, from the Norton equivalent circuit and by replacing Equation E-4 inside E-1, the $\boldsymbol{I_1^{(2)}}$ and $\boldsymbol{I_2^{(2)}}$ currents can be expressed as:

$$\boldsymbol{I_1^{(2)} = -I_2^{(2)} = \frac{Z_p Z_N}{(Z_N + Z_{Charge})(Z_p + Z_{Charge})}\,I_{MD12}} \qquad \text{E-9}$$

# REFERENCES

[1] M. R. Khalid, I. A. Khan, S. Hameed, M. S. J. Asghar, and J.-S. Ro, “A Comprehensive Review on Structural Topologies, Power Levels, Energy Storage Systems, and Standards for Electric Vehicle Charging Stations and Their Impacts on Grid,” *IEEE Access*, vol. 9, pp. 128069–128094, 2021, doi: 10.1109/ACCESS.2021.3112189.

[2] “Policy developments – Global EV Outlook 2023 – Analysis,” IEA. Accessed: Oct. 27, 2023. [Online]. Available: https://www.iea.org/reports/global-ev-outlook-2023/policy-developments

[3] *Technologies des voitures électriques: motorisations, batteries, hydrogène, recharge et interactions réseau*. Malakoff: Dunod, 2021.

[4] Q. Li, Y. Yang, X. Yu, and H. Li, “A 700 W·h·kg $^{-1}$ Rechargeable Pouch Type Lithium Battery,” *Chinese Phys. Lett.*, vol. 40, no. 4, p. 048201, Mar. 2023, doi: 10.1088/0256-307X/40/4/048201.

[5] A. A. Naqvi, A. Zahoor, A. A. Shaikh, F. A. Butt, F. Raza, and I. U. Ahad, “Aprotic lithium air batteries with oxygen-selective membranes,” *Mater Renew Sustain Energy*, vol. 11, no. 1, pp. 33–46, Apr. 2022, doi: 10.1007/s40243-021-00205-w.

[6] “EV-Volumes - The Electric Vehicle World Sales Database.” Accessed: Oct. 26, 2023. [Online]. Available: https://www.ev-volumes.com/

[7] M. S. Mastoi *et al.*, “An in-depth analysis of electric vehicle charging station infrastructure, policy implications, and future trends,” *Energy Reports*, vol. 8, pp. 11504–11529, Nov. 2022, doi: 10.1016/j.egyr.2022.09.011.

[8] H. Kilicoglu and P. Tricoli, “Technical Review and Survey of Future Trends of Power Converters for Fast-Charging Stations of Electric Vehicles,” *Energies*, vol. 16, no. 13, p. 5204, Jul. 2023, doi: 10.3390/en16135204.

[9] M. Nour, J. P. Chaves-Ávila, G. Magdy, and Á. Sánchez-Miralles, “Review of Positive and Negative Impacts of Electric Vehicles Charging on Electric Power Systems,” *Energies*, vol. 13, no. 18, p. 4675, Sep. 2020, doi: 10.3390/en13184675.

[10] B. A. Rayan, U. Subramaniam, and S. Balamurugan, “Wireless Power Transfer in Electric Vehicles: A Review on Compensation Topologies, Coil Structures, and Safety Aspects,” *Energies*, vol. 16, no. 7, Art. no. 7, Jan. 2023, doi: 10.3390/en16073084.

[11] I. Okasili, A. Elkhateb, and T. Littler, “A Review of Wireless Power Transfer Systems for Electric Vehicle Battery Charging with a Focus on Inductive Coupling,” *Electronics*, vol. 11, no. 9, Art. no. 9, Jan. 2022, doi: 10.3390/electronics11091355.

[12] C. C. Lee, H. Ouyang, and G. Che, “Development of New Wireless Charging System with Improved Energy Efficiency for Electric Vehicles,” in *IECON 2020 The 46th Annual Conference of the IEEE Industrial Electronics Society*, Oct. 2020, pp. 3617–3621. doi: 10.1109/IECON43393.2020.9255192.

[13] B. Shi, F. Yang, S. Wang, and M. Ouyang, “Efficiency Improvement of Wireless Charging System Based on Active Power Source in Receiver,” *IEEE Access*, vol. 7, pp. 98136–98143, 2019, doi: 10.1109/ACCESS.2019.2928623.

[14] Y. Bu, S. Endo, and T. Mizuno, “Improvement in the Transmission Efficiency of EV Wireless Power Transfer System Using a Magnetoplated Aluminum Pipe,” *IEEE Transactions on Magnetics*, vol. 54, no. 11, pp. 1–5, Nov. 2018, doi: 10.1109/TMAG.2018.2840109.

[15] “10 Billion Kilometers of Driving Reveals NIO’s Users Preference in Battery Swapping | NIO.” Accessed: Nov. 04, 2023. [Online]. Available: https://www.nio.com/news/10-Billion-Kilometers

[16] Hybrid - EV Committee, “SAE Electric Vehicle and Plug in Hybrid Electric Vehicle Conductive Charge Coupler,” SAE International. doi: 10.4271/J1772_201710.

[17] P. G. Pereirinha, “Electric vehicles,” in *Encyclopedia of Electrical and Electronic Power Engineering*, Elsevier, 2023, pp. 350–387. doi: 10.1016/B978-0-12-821204-2.00112-4.

[18] J. A. Sanguesa, V. Torres-Sanz, P. Garrido, F. J. Martinez, and J. M. Marquez-Barja, “A Review on Electric Vehicles: Technologies and Challenges,” *Smart Cities*, vol. 4, no. 1, Art. no. 1, Mar. 2021, doi: 10.3390/smartcities4010022.

[19] R. Pradhan, N. Keshmiri, and A. Emadi, “On-Board Chargers for High-Voltage Electric Vehicle Powertrains: Future Trends and Challenges,” *IEEE Open J. Power Electron.*, vol. 4, pp. 189–207, 2023, doi: 10.1109/OJPEL.2023.3251992.

[20] “SAE International Announces Standard for NACS Connector, Charging PKI and Infrastructure Reliability.” Accessed: Nov. 06, 2023. [Online]. Available: https://www.sae.org/site/news/press-room/2023/06/sae-international-announces-standard-for-nacs-connector

[21] “J3400 (WIP) SAE J3400: NACS Electric Vehicle Coupler - SAE International.” Accessed: Nov. 06, 2023. [Online]. Available: https://www.sae.org/standards/content/j3400/

[22] H. Kim, J. Park, S. Kim, R. M. Hakim, H. P. Kieu, and S. Choi, “Single-Stage EV On-Board Charger with Single- and Three-Phase Grid Compatibility,” in *2021 IEEE Applied Power Electronics Conference and Exposition (APEC)*, Phoenix, AZ, USA: IEEE, Jun. 2021, pp. 583–589. doi: 10.1109/APEC42165.2021.9487195.

[23] S.-G. Jeong, Y.-S. Jeong, J.-M. Kwon, and B.-H. Kwon, “A Soft-Switching Single-Stage Converter With High Efficiency for a 3.3-kW On-Board Charger,” *IEEE Trans. Ind. Electron.*, vol. 66, no. 9, pp. 6959–6967, Sep. 2019, doi: 10.1109/TIE.2018.2877093.

[24] N. Sakr, D. Sadarnac, and A. Gascher, “A review of on-board integrated chargers for electric vehicles,” in *2014 16th European Conference on Power Electronics and Applications*, Lappeenranta, Finland: IEEE, Aug. 2014, pp. 1–10. doi: 10.1109/EPE.2014.6910865.

[25] B. Briane and S. Loudot, “Rapid reversible charging device for an electric vehicle,” US20110254494A1, Oct. 20, 2011 Accessed: Nov. 16, 2023. [Online]. Available: https://patents.google.com/patent/US20110254494A1/en

[26] J. Yuan, L. Dorn-Gomba, A. D. Callegaro, J. Reimers, and A. Emadi, “A Review of Bidirectional On-Board Chargers for Electric Vehicles,” *IEEE Access*, vol. 9, pp. 51501–51518, 2021, doi: 10.1109/ACCESS.2021.3069448.

[27] M. Schweizer and J. W. Kolar, “Design and Implementation of a Highly Efficient Three-Level T-Type Converter for Low-Voltage Applications,” *IEEE Trans. Power Electron.*, vol. 28, no. 2, pp. 899–907, Feb. 2013, doi: 10.1109/TPEL.2012.2203151.

[28] D. Oustad, “Etude de l’intérêt de la montée en tension du bus DC pour minimiser les pertes dans l’onduleur d’un véhicule électrique.”

[29] S. S. Ravi and M. Aziz, “Utilization of Electric Vehicles for Vehicle-to-Grid Services: Progress and Perspectives,” *Energies*, vol. 15, no. 2, p. 589, Jan. 2022, doi: 10.3390/en15020589.

[30] J. R. Pillai and B. Bak-Jensen, “Integration of Vehicle-to-Grid in the Western Danish Power System,” *IEEE Trans. Sustain. Energy*, p. 5560848, Jan. 2010, doi: 10.1109/TSTE.2010.2072938.

[31] R. Smolenski, M. Jarnut, G. Benysek, and A. Kempski, “AC/DC/DC Interfaces for V2G Applications—EMC Issues,” *IEEE Trans. Ind. Electron.*, vol. 60, no. 3, pp. 930–935, Mar. 2013, doi: 10.1109/TIE.2012.2188876.

[32] J. García-Villalobos, I. Zamora, J. I. San Martín, F. J. Asensio, and V. Aperribay, “Plug-in electric vehicles in electric distribution networks: A review of smart charging approaches,” *Renewable and Sustainable Energy Reviews*, vol. 38, pp. 717–731, Oct. 2014, doi: 10.1016/j.rser.2014.07.040.

[33] H. Shareef, Md. M. Islam, and A. Mohamed, “A review of the stage-of-the-art charging technologies, placement methodologies, and impacts of electric vehicles,” *Renewable and Sustainable Energy Reviews*, vol. 64, pp. 403–420, Oct. 2016, doi: 10.1016/j.rser.2016.06.033.

[34] M. Nour, J. P. Chaves-Ávila, G. Magdy, and Á. Sánchez-Miralles, “Review of Positive and Negative Impacts of Electric Vehicles Charging on Electric Power Systems,” *Energies*, vol. 13, no. 18, Art. no. 18, Jan. 2020, doi: 10.3390/en13184675.

[35] O. Sundstrom and C. Binding, “Flexible Charging Optimization for Electric Vehicles Considering Distribution Grid Constraints,” *IEEE Trans. Smart Grid*, vol. 3, no. 1, pp. 26–37, Mar. 2012, doi: 10.1109/TSG.2011.2168431.

[36] C. R. Paul, R. C. Scully, and M. Steffka, *Introduction to electromagnetic compatibility*, Third edition. Hoboken, NJ, USA: Wiley, 2022.

[37] J. Genoulaz, “Contribution à l’Étude du Rayonnement des Câbles Soumis aux Signaux de l’Électronique de Puissance dans un Environnement Aéronautique,” 2008.

[38] A. R. Ekon, “Contribution à la montée en performance des alimentations DC-DC bipolaires des électroaimants de correction rapide du Synchrotron SOLEIL,” 2023.

[39] “Electromagnetic compatibility (EMC).” Accessed: Dec. 08, 2023. [Online]. Available: https://single-market-economy.ec.europa.eu/single-market/european-standards/harmonised-standards/electromagnetic-compatibility-emc_en

[40] A. Gahfif, “Contribution à l’étude et la réalisation d’un filtre CEM actif hybride destiné à un convertisseur DC-DC à base de transistors GaN,” phdthesis, Université Paris-Saclay, 2023.

[41] P. S. Niklaus, M. M. Antivachis, D. Bortis, and J. W. Kolar, “Analysis of the Influence of Measurement Circuit Asymmetries on Three-Phase CM/DM Conducted EMI Separation,” *IEEE Transactions on Power Electronics*, vol. 36, no. 4, pp. 4066–4080, Apr. 2021, doi: 10.1109/TPEL.2020.3025122.

[42] T. Hegarty, “An overview of conducted EMI specifications for power supplies,” Texas Instruments, 2018.

[43] J. R. Nicholson and J. A. Malack, “RF Impedance of Power Lines and Line Impedance Stabilization Networks in Conducted Interference Measurements,” *IEEE Trans. Electromagn. Compat.*, vol. EMC-15, no. 2, pp. 84–86, May 1973, doi: 10.1109/TEMC.1973.303254.

[44] K.-R. Li, K.-Y. See, and R. M. Sooriya Bandara, “Impact Analysis of Conducted Emission Measurement Without LISN,” *IEEE Trans. Electromagn. Compat.*, vol. 58, no. 3, pp. 776–783, Jun. 2016, doi: 10.1109/TEMC.2016.2533539.

[45] M. Seddighi, F. Costa, P.-E. Levy, and D. Oustad, “Impact of Standardized Methods Applied for Conducted EMI Estimation on the Volume of an EMC Filter in a DC Supplied Single-leg Inverter,” in *2022 IEEE 7th Southern Power Electronics Conference (SPEC)*, Nadi, Fiji: IEEE, Dec. 2022, pp. 1–4. doi: 10.1109/SPEC55080.2022.10058449.

[46] A. S. De Beer, G. N. Wooding, and J. D. Van Wyk, “Problematic aspects when using a LISN for converter EMI characterisation,” in *2013 IEEE International Conference on Industrial Technology (ICIT)*, Cape Town: IEEE, Feb. 2013, pp. 633–637. doi: 10.1109/ICIT.2013.6505745.

[47] Schneider Electric, “Guide de l’Installation Electrique 2017,” 2017.

[48] R. Calvas and B. Lacroix, “Cahier technique no. 172: Earthing systems in LV.” Schneider Electric, 2002.

[49] F. Jullien and I. Héritier, “Cahier technique no. 178: The IT earthing system (unearthed neutral) in LV,” Schneider Electric.

[50] D. Dorr, “Determining voltage levels of concern for human and animal response to AC current,” in *2009 IEEE Power & Energy Society General Meeting*, Calgary, Canada: IEEE, Jul. 2009, pp. 1–6. doi: 10.1109/PES.2009.5275848.

[51] B. Lacroix and R. Calvas, “Cahier technique no. 173: earthing systems worldwide and evolutions,” Schneider Electric.

[52] J.-F. REY, “Infrastructures de Recharge VE - Règles d’intégration dans une installation électrique BT — Guide de l’Installation Electrique,” Schneider Electric. [Online]. Available: https://fr.electrical-installation.org/frwiki

[53] H. Gu, X. Guo, D. Wang, and W. Wu, “Real-time grid impedance estimation technique for grid-connected power converters,” in *2012 IEEE International Symposium on Industrial Electronics*, May 2012, pp. 1621–1626. doi: 10.1109/ISIE.2012.6237333.

[54] L. Asiminoaei, R. Teodorescu, F. Blaabjerg, and U. Borup, “A digital controlled PV-inverter with grid impedance estimation for ENS detection,” *IEEE Transactions on Power Electronics*, vol. 20, no. 6, pp. 1480–1490, Nov. 2005, doi: 10.1109/TPEL.2005.857506.

[55] L. Asiminoaei, R. Teodorescu, F. Blaabjerg, and U. Borup, “Implementation and test of an online embedded grid impedance estimation technique for PV inverters,” *IEEE Transactions on Industrial Electronics*, vol. 52, no. 4, pp. 1136–1144, Aug. 2005, doi: 10.1109/TIE.2005.851604.

[56] M. Ciobotaru, R. Teodorescu, P. Rodriguez, A. Timbus, and F. Blaabjerg, “Online grid impedance estimation for single-phase grid-connected systems using PQ variations,” in *2007 IEEE Power Electronics Specialists Conference*, Jun. 2007, pp. 2306–2312. doi: 10.1109/PESC.2007.4342370.

[57] M. Liserre, F. Blaabjerg, and R. Teodorescu, “Grid Impedance Estimation via Excitation of LCL -Filter Resonance,” *IEEE Transactions on Industry Applications*, vol. 43, no. 5, pp. 1401–1407, Sep. 2007, doi: 10.1109/TIA.2007.904439.

[58] I. Fernández *et al.*, “Comparison of Measurement Methods of LV Grid Access Impedance in the Frequency Range Assigned to Nb-Plc Technologies,” *Electronics*, vol. 8, no. 10, Art. no. 10, Oct. 2019, doi: 10.3390/electronics8101155.

[59] I. Fernández *et al.*, “Measurement System of the Mean and Sub-Cycle LV Grid Access Impedance From 20 kHz To 10 MHz,” *IEEE Trans. Power Delivery*, vol. 38, no. 3, pp. 2204–2212, Jun. 2023, doi: 10.1109/TPWRD.2023.3238647.

[60] V. Tarateeraseth, K. Y. See, F. G. Canavero, and R. W.-Y. Chang, “Systematic Electromagnetic Interference Filter Design Based on Information From In-Circuit Impedance Measurements,” *IEEE Transactions on Electromagnetic Compatibility*, vol. 52, no. 3, pp. 588–598, Aug. 2010, doi: 10.1109/TEMC.2010.2046419.

[61] V. Tarateeraseth, B. Hu, K. Y. See, and F. G. Canavero, “Accurate Extraction of Noise Source Impedance of an SMPS Under Operating Conditions,” *IEEE Transactions on Power Electronics*, vol. 25, no. 1, pp. 111–117, Jan. 2010, doi: 10.1109/TPEL.2009.2024675.

[62] X.-M. Li, S.-Q. Hu, K.-Y. See, and K.-R. Li, “Improved two-probe approach for in-circuit measurement based on three-port network pre-calibration,” in *2015 Asia-Pacific Symposium on Electromagnetic Compatibility (APEMC)*, May 2015, pp. 60–63. doi: 10.1109/APEMC.2015.7175264.

[63] F. Fan, K. Y. See, K. Li, J. K. Banda, X. Liu, and A. K. Gupta, “Efficient inductive coupled in-circuit impedance extraction with enhanced SNR and instrument protection,” in *2018 IEEE International Symposium on Electromagnetic Compatibility and 2018 IEEE Asia-Pacific Symposium on Electromagnetic Compatibility (EMC/APEMC)*, May 2018, pp. 1288–1292. doi: 10.1109/ISEMC.2018.8393996.

[64] K.-R. Li, K.-Y. See, and R. M. Sooriya Bandara, “Impact Analysis of Conducted Emission Measurement Without LISN,” *IEEE Transactions on Electromagnetic Compatibility*, vol. 58, no. 3, pp. 776–783, Jun. 2016, doi: 10.1109/TEMC.2016.2533539.

[65] “IEC 61557-3:2019 | IEC Webstore.” Accessed: Mar. 26, 2024. [Online]. Available: https://webstore.iec.ch/publication/60893

[66] “E4990A Impedance Analyzer,” Keysight. [Online]. Available: https://www.keysight.com/fr/en/assets/7018-04256/data-sheets/5991-3890.pdf

[67] F. Costa, C. Gautier, E. Labouré, and B. Revol, *Electromagnetic compatibility in power electronics*. in Electronics engineering series. London: ISTE, 2014.

[68] K. Raggl, T. Nussbaumer, and J. W. Kolar, “Guideline for a Simplified Differential-Mode EMI Filter Design,” *IEEE Trans. Ind. Electron.*, vol. 57, no. 3, pp. 1031–1040, Mar. 2010, doi: 10.1109/TIE.2009.2028293.

[69] M. J. Nave, “On modeling the common mode inductor,” in *IEEE 1991 International Symposium on Electromagnetic Compatibility*, Cherry Hill, NJ, USA: IEEE, 1991, pp. 452–457. doi: 10.1109/ISEMC.1991.148275.

[70] J. Brombach, T. Schroter, A. Lucken, and D. Schulz, “Optimized cabin power supply with a +/- 270 V DC grid on a modern aircraft,” in *2011 7th International Conference-*

*Workshop Compatibility and Power Electronics (CPE)*, Tallinn, Estonia: IEEE, Jun. 2011, pp. 425–428. doi: 10.1109/CPE.2011.5942274.

[71] A. Mariscotti, “Power Quality Phenomena, Standards, and Proposed Metrics for DC Grids,” *Energies*, vol. 14, no. 20, Art. no. 20, Jan. 2021, doi: 10.3390/en14206453.

[72] C. Vermaelen, “Contribution à la modélisation et à la réduction des perturbations conduites dans les systèmes d’entraînement à vitesse variable,” phdthesis, École normale supérieure de Cachan - ENS Cachan, 2003.

[73] M. D. Lauretis, “Transmission line theory for cable modeling: a delay-rational model based on Green’s functions.”

[74] H. Hoffmann sathler, “Optimization of GaN-based Series-Parallel Multilevel Three-Phase Inverter for Aircraft applications,” These de doctorat, université Paris-Saclay, 2021. Accessed: Apr. 18, 2024. [Online]. Available: https://theses.fr/2021UPAST108

[75] “Analysis of Multiconductor Transmission Lines | IEEE eBooks | IEEE Xplore.” Accessed: Apr. 19, 2024. [Online]. Available: https://ieeexplore.ieee.org/book/5271237

[76] V. D. Santos, N. Roux, B. Revol, B. Sareni, B. Cougo, and J.-P. Carayon, “Unshielded cable modeling for conducted emissions issues in electrical power drive systems,” in *2017 International Symposium on Electromagnetic Compatibility - EMC EUROPE*, Angers: IEEE, Sep. 2017, pp. 1–6. doi: 10.1109/EMCEurope.2017.8094736.

[77] N. Idir, Y. Weens, and J.-J. Franchaud, “Skin effect and dielectric loss models of power cables,” *IEEE Transactions on Dielectrics and Electrical Insulation*, vol. 16, no. 1, pp. 147–154, Feb. 2009, doi: 10.1109/TDEI.2009.4784562.

[78] V. Dos Santos, “Modélisation des émissions conduites de mode commun d’une chaîne électromécanique : Optimisation paramétrique de l’ensemble convertisseur filtres sous contraintes CEM,” These de doctorat, Toulouse, INPT, 2019. Accessed: Apr. 19, 2024. [Online]. Available: https://theses.fr/2019INPT0021

[79] A. F. Moreira, T. A. Lipo, G. Venkataramanan, and S. Bernet, “High frequency modeling for cable and induction motor overvoltage studies in long cable drives,” in *Conference Record of the 2001 IEEE Industry Applications Conference. 36th IAS Annual Meeting (Cat. No.01CH37248)*, Sep. 2001, pp. 1787–1794 vol.3. doi: 10.1109/IAS.2001.955774.

[80] “Multiconductor cable modeling for EMI simulations in power electronics | IEEE Conference Publication | IEEE Xplore.” Accessed: Apr. 19, 2024. [Online]. Available: https://ieeexplore.ieee.org/document/6388958

[81] H. Akagi and I. Matsumura, “Overvoltage Mitigation of Inverter-Driven Motors With Long Cables of Different Lengths,” *IEEE Transactions on Industry Applications*, vol. 47, no. 4, pp. 1741–1748, Jul. 2011, doi: 10.1109/TIA.2011.2154294.

[82] L. Wang, Y. Zhang, M. S. Ali, G. Chen, J. M. Guerrero, and J. C. Vasquez, “High-Frequency Modeling and Filter Design for PWM Drives with Long Cables,” *Energies*, vol. 14, no. 4, Art. no. 4, Jan. 2021, doi: 10.3390/en14041155.

[83] C. Marlier, “Modélisation des perturbations électromagnétiques dans les convertisseurs statiques pour des applications aéronautiques,” These de doctorat, Lille 1, 2013. Accessed: Apr. 19, 2024. [Online]. Available: https://theses.fr/2013LIL10145

[84] H. De Paula, D. A. De Andrade, M. L. R. Chaves, J. L. Domingos, and M. A. A. De Freitas, “Methodology for Cable Modeling and Simulation for High-Frequency

Phenomena Studies in PWM Motor Drives," *IEEE Trans. Power Electron.*, vol. 23, no. 2, pp. 744–752, Mar. 2008, doi: 10.1109/TPEL.2007.915759.

[85] C. Marlier, A. Videt, N. Idir, H. Moussa, and R. Meuret, "Modeling of switching transients for frequency-domain EMC analysis of power converters," in *2012 15th International Power Electronics and Motion Control Conference (EPE/PEMC)*, Novi Sad, Serbia: IEEE, Sep. 2012, p. DS1e.1-1-DS1e.1-8. doi: 10.1109/EPEPEMC.2012.6397241.

[86] M. Moreau, N. Idir, and P. Le Moigne, "Modeling of Conducted EMI in Adjustable Speed Drives," *IEEE Trans. Electromagn. Compat.*, vol. 51, no. 3, pp. 665–672, Aug. 2009, doi: 10.1109/TEMC.2009.2025269.

[87] Y. Weens, "Modélisation des câbles d'énergie soumis aux contraintes générées par les convertisseurs électroniques de puissance," These de doctorat, Lille 1, 2006. Accessed: Apr. 19, 2024. [Online]. Available: https://theses.fr/2006LIL10104

[88] M. Moreau, N. Idir, and P. Le Moigne, "Modeling of Conducted EMI in Adjustable Speed Drives," *IEEE Transactions on Electromagnetic Compatibility*, vol. 51, no. 3, pp. 665–672, Aug. 2009, doi: 10.1109/TEMC.2009.2025269.

[89] M. Ali, "Nouvelles architectures intégrées de filtre CEM hybride," These de doctorat, Cachan, Ecole normale supérieure, 2012. Accessed: May 06, 2024. [Online]. Available: https://theses.fr/2012DENS0009

[90] M. Amara, "Maîtrise des émissions conduites des électroniques de puissance.," These de doctorat, Lyon, 2019. [Online]. Available: https://theses.fr/2019LYSEC047